Remote Sensing of the Temperature during Magnetic Hyperthermia

Fang-Yu Lin

"A report submitted in partial fulfilment of the requirements for the degree of PhD in Medical Physics and Bioengineering."

University College London

2020

Prof Quentin Pankhurst
Dr Paul Southern

Report Declaration Form

I, Fang-Yu Lin, confirm that the work presented in this report is my own. Where information has been derived from other sources, I confirm that this has been indicated in the report.

Signature:

Name:

Date:

Abstract

The cancer therapy, magnetic hyperthermia, was proposed 60 years ago. Despite decades of efforts, this technique is still in its research stage. An *ex-vivo* experiment presented in Chapter 1 shows that one of the main barriers lies in its temperature measurement. The current gold standard is to insert a thermal probe into the target tumour. The measurement of which is invasive and point measurement only. Because of the inhomogeneous particle distribution, the accuracy of point measurement relies on accurate placement of the thermal probe, which is difficult to achieve.

Thus, this study investigates two alternatives of point measurement. The first alternative is an existing technique, i.e., infra-red thermography and the second is a thermometry proposed in this study. The latter is termed as magnetic particle thermometry (MPT). Before discussing these two methods of temperature sensing, Chapter 2 reviews concepts such as the biological effects of heat, the mechanism of magnetic heating, and other remote sensing methods.

Subsequent to this, Chapter 3 and Chapter 4 respectively present *in-vitro* and *in-vivo* experiments to evaluate the implementation of infra-red thermography in magnetic hyperthermia. In which, the effects of particle distribution and the thermal doses on hyperthermia are discussed. The result suggests that the infra-red thermography is applicable to studies involving subcutaneous tumours. When treating a deep-seated tumour, another sensing method is still desired.

Chapter 5 then describes the principles of proposed MPT. The MPT assesses the average temperature of the target tumour by detecting the average temperature of the deposited magnetic nanoparticles. The MPT is possible because the temperature of magnetic nanoparticles would interfere the resonant frequency of the field applicator. By tracking the shift in resonant frequency of the field applicator, the average temperature of particles is estimated. The theory of which is carefully validated through a series of experiments presented in Chapter 6.

Impact Statement

The study has three impacts in magnetic hyperthermia research. Firstly, a framework of the procedure has been presented. For cross-disciplinary research, a framework provides a guide to correlate different researches. Based on the framework, four *in-vivo* studies have been designed, performed and discussed. Part of the *in-vivo* studies will potentially be published.

Secondly, novel remote thermometry, i.e., MPT, has been proposed. The MPT detects the average temperature of a target area into which where magnetic particles are injected; therefore, it avoids the disadvantages of conventional spot measurement. Based on which, the thermometry can improve the thermal management of magnetic hyperthermia. The theory of MPT and its validation will potentially be published.

Thirdly, the proposed sensing technique is a cost-effective way to measure the magnetic susceptibility of a material. The measurement of susceptibility can be used to accurately measure the quantity of magnetic material when diluting the suspension during the synthesis of particles. Furthermore, this sensing technique can potentially be deployed in other measurements. Take the viscosity measurement as an example, the proposed technique can also be used as a viscosity meter, because the susceptibility of magnetic nanoparticles depends on the viscosity of the medium.

The proposed MPT has been presented in the form of oral presentation as well as a poster in **the 11th International Conference on the Scientific and Clinical Applications of Magnetic Carriers**. The presentations were titled as:

1. Remote Monitoring of Magnetic Particle Temperature During Hyperthermia: the Ideal Dose-Response Metric?

2. Temperature and AC Field Dependence of Magnetic Susceptibility and its use in Magnetic Hyperthermia.

Part of the presented work has contributed to two publications:

1. J. C. Bear et al., “Magnetic hyperthermia controlled drug release in the GI tract: Solving the problem of detection,” Scientific Report, 2016.

2. T. Carter et al., “Potential of Mmgnetic Hyperthermia to simulate an immune response in glioblastoma,” Neuro-Oncology, 2017.

Acknowledgement

It has been five years since I first met Prof Quentin Pankhurst and Dr Paul Southern in a small room on the third floor of Royal Institute. This meeting was the starting point of my PhD journey. It was the first time that I learned the concept of treating by heating with tiny magnets. I thank them for leading me into this fascinating field of research. Their knowledge of magnetic hyperthermia is indeed the most important pillar of this study. Moreover, I would like to thank Simon Hattersley, whose ability to see through things with fundamental principles of physics has greatly helped me to interpret some of the experimental results.

Thank to Dr Stephen Nesbitt for his efforts in nicely managing the laboratory. His extensive experimental experience also did a great support when I set up the *ex-vivo* experiment. I would like to express my appreciation to Dr Richard Jackson for his technical suggestions on the construction of moulds. I am also grateful to Dr Lara Bogart, whose expertise in nanoparticle characterisation had solved some of my confusion when I went through theories in this field.

Additionally, I want to thank Prof Neil Telling and Dr Kenneth Tong for being my viva examiners. Their invaluable feedback has helped me to improve the quality and presentation of this thesis.

I also have to mention Prof Tzong-Shi Liu and Prof Ching-Yao Chen here; without their encouragement, I would not have stepped out my comfort zone and started a PhD journey outside of Taiwan. And this journey could be extremely difficult to me, if I did not have supports from Dr Christos Bergeles, Prof Li-Chen Fu and Prof Quentin Pankhurst. It was through their supports, I had the opportunity to receive UCL research scholarships (GRS and ORS).

This journey would not be so enjoyable without a company of friends. I was lucky to meet many kind colleagues from Prof Thanh Nguyen's group. I would like to especially thank Andreas Sergides, Dr Alec Lagrow, Dr Bengi Ozkahraman, Geogios Kaspanis, Lilin Wang, Matej Sebek, Dr Simone Famiani and Dr Stefanos Mourdikoudis. Thank

them for sharing some of the most important moments in my life.

Five years may just be part of my life, but I can foresee this particular five-year journey is one of the most importance across my life. I am grateful to those people I met who stayed and became good friends of mine during this journey. I debated on a verity of topics with and Raymond Shih, Dr George Peng, Dr Henry Wu. Through their perspectives, I expanded my view of the world. It is inevitable that one may feel upset at some moment, I thank Dr Denny Han for always being a patient one to listen to me and to feedback with wise suggestions. I regard them as my family.

And there was a friend actually became my family. I thank to her not only for sharing her life together with me but also for taking care of our daughter on the other side of earth alone in the past two years. Without my wife Tiffany's efforts, this thesis would not have been completed.

I only realised at the end of this journey that a PhD study is indeed a collective work. It is not only an academically collective collaboration, but also a collective contribution of my family. Therefore, I would like to say some words to my beloved family to express my appreciation to them. It is written in Mandarin and presented in the next page.

Before that, please allow me to thank Prof Quentin Pankhurst once again. Through those questions he threw at me in the past few years, I gradually started to understand how a scientist thinks differently from an engineer. I used to think once a practical problem is tackled, it is good enough to close the project and move on. But a scientist would not let it go like this, a scientist would tend to dig out the actual mechanism underneath a phenomenon. Only when one can explicitly describe it, one understands it. The whole chapter 6 would not exist if I was not questioned (hardly) by Prof Quentin Pankhurst on how the magnetic particle thermometry works.

Lastly, I want to thank him for the note he gave to me, that says, *perfect is the enemy of good*. The ambition to make things perfect does not guarantee a good performance or a good result. Oppositely, this ambition has sometimes made me fail to delivery an average performance. Learning how to balance my ambition, practical limitations and my own abilities may be my lifelong homework.

謹以此論文獻給我敬愛的爸爸、媽媽以及在天上的阿嬤， 林慶波 先生、黃(王民)伶 女士以及林方燕雀 女士。

萬物皆有源。若我有一絲的理解事物的能力，這是源自於他們。每個人身上都有著不同人的影子，屬於我的，來自於他們。在求學的路上，他們處世的智慧惠我良多。沒有他們三十餘年來的持續努力，我未能有此機會遠赴英國，在倫敦學習如何將科學用於醫療，學習如何透過自身的努力為周遭的人做出些微的、正向的影響。一如他們數十年來每日所做的努力。

此外，我想感謝我的哥哥、姊姊，林芳誠以及林芳亞，若未有他們時常照顧在父母左右，為父母分憂，我不能如此任性地、專注地在一個特定的領域揮霍近五年的時間。我至英國求學的想法更是源自於姊姊先前於英國的求學經歷。

任何一段旅程，只要它的時間夠長，它必然是個人的。這段學術研究的旅程之於我個人也極其重要。我與妻子，鄭宇庭，的相識、相戀、結婚、生子，皆在這五年之內。研究之路，跌跌撞撞，一如在無垠的黑暗之中試圖去找到一點指引道路的星光。我在這旅程中掙扎的時刻，感謝有她的陪伴。同時，我也想感謝她的體貼，當我在倫敦撰寫論文的時刻，她獨自一人在地球的另一側照顧著孩子，沒有她的付出，這本論文不可能會完成。

孩子，若你有一天無聊到不小心翻到爸爸的論文。爸爸想和你說，這個世界很有趣，同一個現象，我們用不同的角度觀察，會有不同的描述。一如我站在你的身邊，之於你我是靜止的，之於地球之外的太空人我則是快速地隨著地球而轉動。這也是論文裡面所提到為什麼會有超順磁性(superparamagnetism)的現象。爸爸還在努力試著了解世界，希望你也會覺得這一個世界是有趣的。

最後，一如那一棵在森林之中倒下的樹，沒有人聽到則沒有聲音。若這份關於磁性熱療的研究論文有幸被你翻閱，甚或於你對其中些許的內容感到有趣，我想感謝你找到無盡森林之中的這一棵樹，聽到它的聲音。這一棵樹，是在上述眾人的努力之下再經由我的手型塑而成的。

芳宇 貳零貳零年 三月 於倫敦

Contents

List of Figures

List of Tables

Acronyms

ABS Acrylonitrile Butadiene Styrene

AMF Alternating Magnetic Field

CAD Computer Aided Design

CEM Cumulative Number of Equivalent Minutes

FEA Finite Element Analysis

H and E Hematoxylin and Eosin

HSP70 Heat Shock Protein 70

HU Hounsfield Unit

ICP-MS Inductively Coupled Plasma Mass Spectrometer

IHC Immunohistochemistry

ILP Intrinsic Loss Power

MACH Magnetic Alternating Current Hyperthermia

MicroCT Micro Computed Tomography

MNP Magnetic Nanoparticle

MPI Magnetic Particle Imaging

MPT Magnetic Particle Thermometry

MRI Magnetic Resonance Imaging

SAR Specific Absorption Rate

SPM Superparamagnet

SQUID Superconducting Quantum Interference Device

WSI Whole Slide Images

Chapter 1

Hyperthermia - Fire and Cure

1.1 Introduction

Fire, or heat, has begun to be used to defeat diseases since the period of the ancient Greece. As Hippocrates (479 - 377 B.C.) once said, *"those who cannot be cured by medicine can be cured by surgery. Those who cannot be cured by surgery can be cured by fire. Those who cannot be cured by fire, they are indeed incurable."* Over time, using heat as a cure never leaves the stage of history; instead, its mechanisms have been studied and revealed. The evidence of its ability to cure was first recorded in the form of a modern scientific report in 1866 by Busch, who discovered the high temperature during fever has a positive relationship with tumour shrinkage [1]. This finding encourages clinicians to treat cancers by heating them, of which the procedures are termed as hyperthermia. The energy used to heat tissues can be derived from different forms of energy, e.g. ultrasound, radio frequency or magnetic field. This study focuses on the hyperthermia associated with the latter form of energy, often refers to magnetic hyperthermia. This technique was originally proposed by Gilchrist *et al.* in 1957 [2].

In magnetic hyperthermia, magnetic nanoparticles (MNPs) would be deposited into a tumour pre-operatively. Then, when the tumour is exposed to an external alternating magnetic field (AMF), MNPs absorb magnetic energy and convert it to heat based on effects of either hysteresis or relaxation loss of MNPs (see section 2.2). Because only the tumour is deposited with MNPs, while the temperature of the area in and around is elevated, healthy tissues away from the tumour remain unaffected. Magnetic hyperthermia is especially beneficial in treating deep-seated tumours, e.g. prostate cancer and glioblastoma, because conventional surgeries often require sacri-

ficing a large volume of healthy tissues around the deep-seated tumours to reach the pathological sites and perform the actual treatment. That is, the selective damage to a tumour in magnetic hyperthermia can potentially minimise the complications and thus is favourable.

Although the principle of magnetic hyperthermia is straightforward, practical challenges appear when applying it to clinical scenarios. The challenges lie in three perspectives, which are respectively in relation to the heating ability of MNPs, field generator and thermal management. As indicated in Fig. 1.1, magnetic hyperthermia can only be safely performed when issues in these three components are all addressed. Each component has its own limitations. For instance, the magnetic field is not harmful only at a certain range of strength and frequency (see section 2.3) [3]. Hence, a purpose designed field generator for hyperthermia is required. The first commercial field generator for clinical use is the NanoActivator, developed by MagForce (Berlin, Germany). While the NanoActivator is as large as a magnetic resonance imaging (MRI) scanner, another portable system, MACH (magnetic alternating current hyperthermia), also purpose designed for magnetic hyperthermia, is developed by its competitor, Resonant Circuits Limited (London, UK).

As to MNPs, the limitation lies in its dosage. The most common MNPs used in magnetic hyperthermia are superparamagnetic iron oxide nanoparticles (SPIONs). Despite the biocompatibility, applying a high dose of SPIONs to a patient can be toxic; i.e. the dose of MNPs has to be limited. As a result, to achieve the therapeutic temperature, the heating ability of MNPs needs to be optimised for the therapeutic range of magnetic field. Fortunately, over the past two decades, there was a rapid development in nanotechnology. The heating ability is determined by particle diameters, structures, and surface coatings [4]. By tuning these parameters of MNPs during synthesis, the heating ability of MNPs has been much improved. Current MNPs have nearly ten times stronger heating ability than what SPIONs could achieve a decade ago [5].

The improvement is Issues in field generator and MNPs, although there is still room for improvement, they have been sufficiently addressed to meet the requirements of clinical usages.

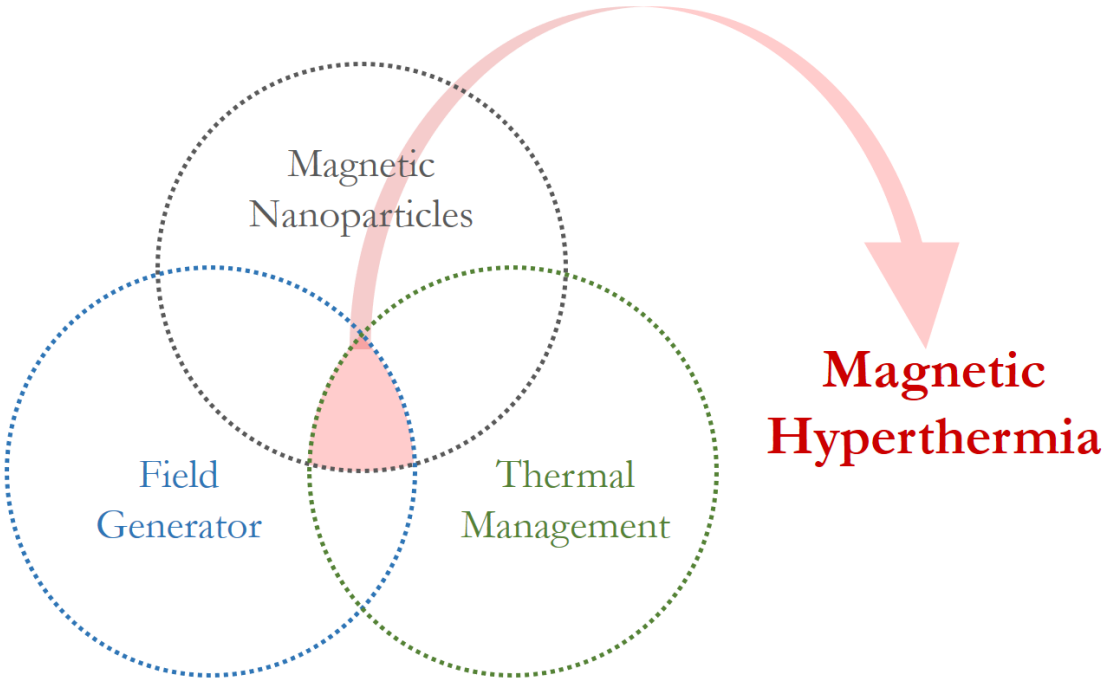

Figure 1.1: Three components that consist of magnetic hyperthermia.

The final piece of the jigsaw to complete magnetic hyperthermia is the thermal management. As the saying goes, fire is an excellent servant but a terrible master. While a not-high-enough temperature rise at the target site would lead to an ineffective treatment, excessive heating can cause danger to the patient. To manage the heating well, to turn the fire into a servant, we should understand the correlation between the dose of MNPs and the corresponded temperature variation, so that the clinician knows what dose of MNPs can raise the intra-tumoural temperature to the therapeutic level. Furthermore, it is essential to monitor the intra-tumoural temperature during the treatment. Because of the complexity of the human body, it is difficult to accurately predict the temperature elevation just based on the dose of MNPs. In other words, the success of temperature monitoring provides us with the opportunity to become the master of the fire.

Prior to the detailed discussion on temperature monitoring, it will be helpful if we can understand the magnetic hyperthermia in a practical aspect. Accordingly, a preliminary experiment has been conducted and will be presented in the following sections.

1.2 An Illustrative Example

To better understand a technique, there may be no better way than actually performing it. To understand the constraints of thermal management during magnetic hyperthermia, an *ex-vivo* experiment has been performed. The *ex-vivo* experiment presented here does not aim for showing the effectiveness of magnetic hyperthermia; instead, its purpose is to show the practical difficulties of this procedure.

The tissues used in this experiment were porcine prostates. Prostate cancer is one of the cancers which can benefit from magnetic hyperthermia, because of the minimal invasiveness. The sections below will further describe the details of apparatus, materials and the process of this illustrative experiment. A brief conclusion will be drawn in the end. The conclusion is the starting point of the research described in this thesis.

1.2.1 Apparatus and Setup

There were three apparatuses applied in this experiment, which were respectively a thermometer, a field generator and a simulation chamber.

Thermometer

The thermometer was LUXTRON FOT Lab Kit (LumaSense Technologies Inc., California, USA). The LUXTRON is a fibre optic multi-channel thermometer, which supports simultaneous readings of four thermal probes. The precision of which is 0.5 °C, and its sensing range covers from 0 °C to 295 °C. The LUXTRONN thermometer was calibrated before the experiment. To calibrate the thermometer, the temperature of a beaker filled with distilled water and ices was regarded as the reference temperature, i.e., 0 °C. For the calibration, the thermometers were then placed in the beaker, the temperature of which was set to be 0 °C.

Field generator - MACH pre-clinical coil

The MACH provided by Resonant Circuits Limited (London, UK) was deployed to generate an AMF in this study. The working principle of this field generator is based on the LC (Inductor-Capacitor) resonant effect.

The magnetic field depends on what coil was used in an experiment. For the illustrative experiment, the MACH pre-clinical coil was used. The MACH pre-clinical

coil consists of a split pair of double-turn coils. An AMF was generated at the split pair of double-turn coils when an alternating current is running through the coil. The adjustable range of field strength was between 2 kA/m and 6 kA/m (at the centre of the coil) and the operational frequency is up to 1 MHz.

The diameter and height of this coil is 52 mm and 40 mm respectively (see Fig. 1.2a). The field distribution of the coil is simulated based on the geometry of the coil and Biot-Savart law. The field distribution is calculated based via a Python package magpylib [6]. The implementation of magpylib is presented in Appendix A. The result is shown in Fig. 1.2b. When the coil current is 113 A, the field intensity at the centre of coil would be 5 kA/m.

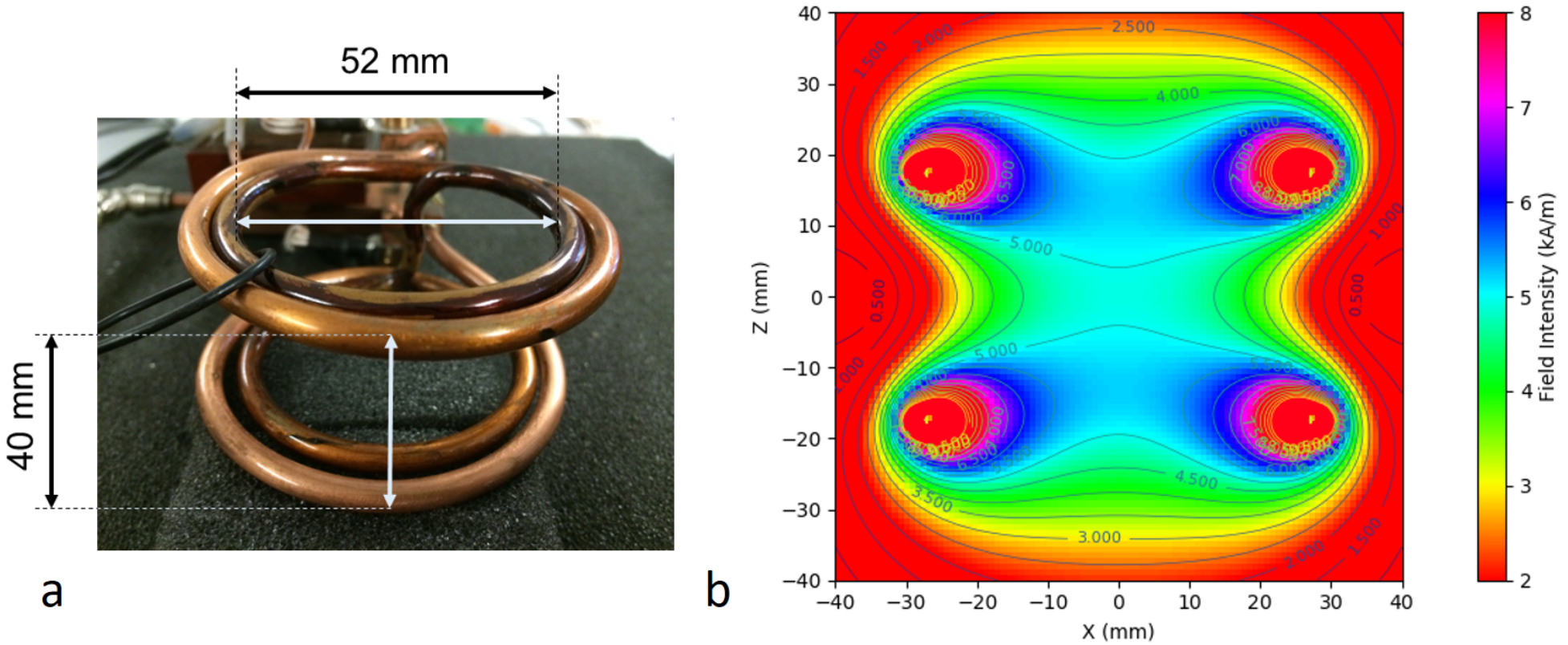

Figure 1.2: (a) The dimension of MACH pre-clinical coil. The inner diameter of the coil is 52 mm, and the height of the coil is 40 mm. (b) The field distribution of the MACH pre-clinical coil. The origin, i.e., X = 0 mm; Z= 0 mm, represents the centre of the coil. The Z and X are associated with the height and the radius of the coil (see Appendix A for the details of the calculation).

Simulation Chamber

Furthermore, to simulate the biological thermal environment, a simulation chamber was designed and built. The main components of this chamber were a bespoke-built enclosure and a fan heater from World Precision Instrument (Sarasota, USA). The inside of the enclosure was layered with a bubble wrap, which enhanced the thermal insulation between the surroundings and the chamber. The air inside the enclosure was heated up and gently circulated by the fan heater. The fan heater has its own thermocouple which provides temperature feedback that allows it to hold the temperature at a certain level. However, the accuracy of that thermocouple was not high. Hence, another fibre optic probe was inserted into the enclosure for monitoring its temperature. The latter was calibrated with ice water before the experiment and the value of which was seen as the ground truth. To keep the temperature at the coil region to be the normal body temperature, i.e., 37 °C [7], the target temperature of the fan heater was set to be 41 °C. Both the enclosure (the white box) and the fan heater are shown in Fig. 1.3. The same figure also presents a pair of split double coils (a component of MACH). Once the MACH is switched on, an alternating current with the frequency of hundreds of kHz would oscillate in the coil, causing an AMF to appear around the coil.

Setup

The overall experimental setup is depicted as a schematic diagram in Fig. 1.4. The signal of the thermometer was recorded and visualised through a computer, as shown on the right-hand side. On the left-hand side, it shows the air circulation inside the simulation chamber as well as the positions of a sample and the coil.

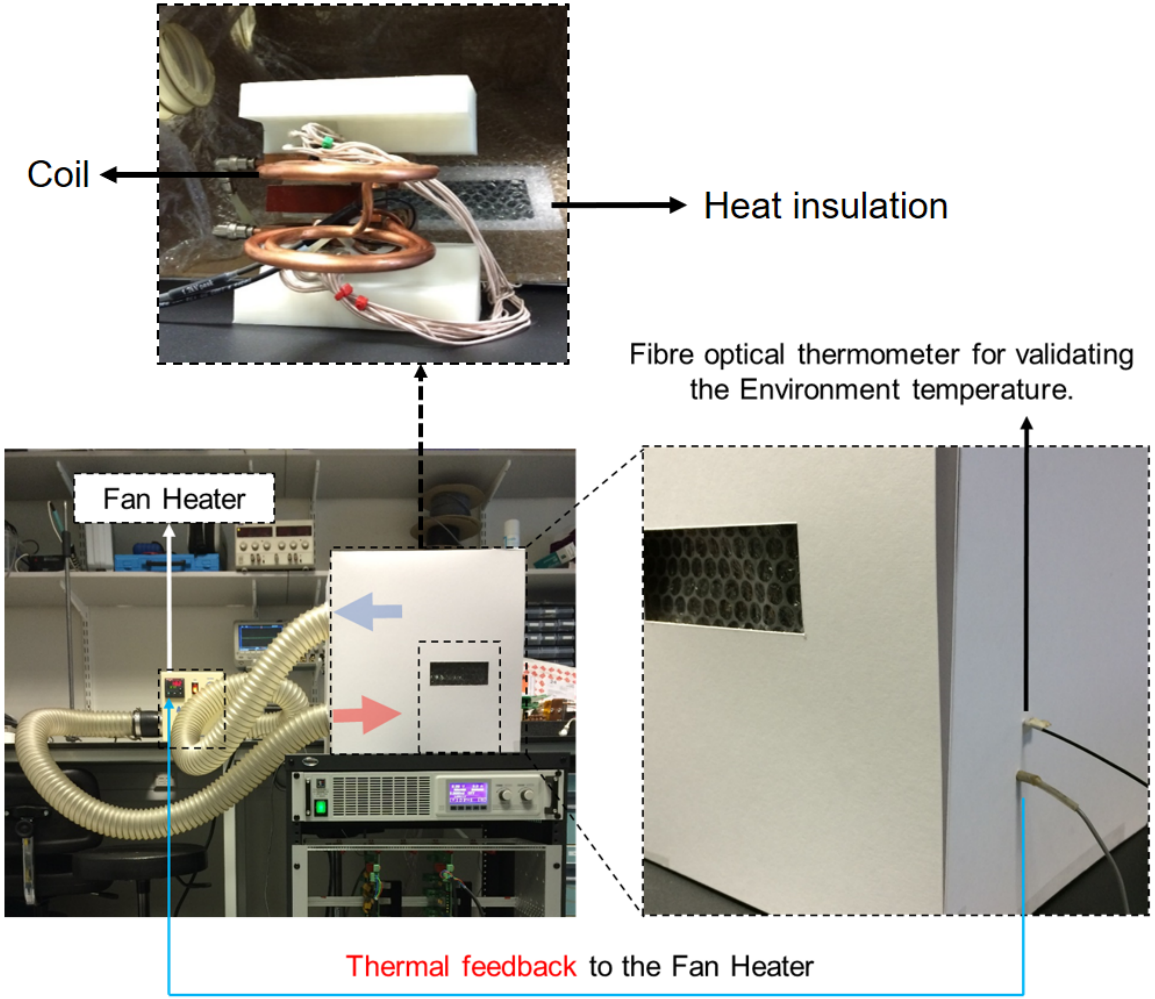

Figure 1.3: Components of the simulation chamber

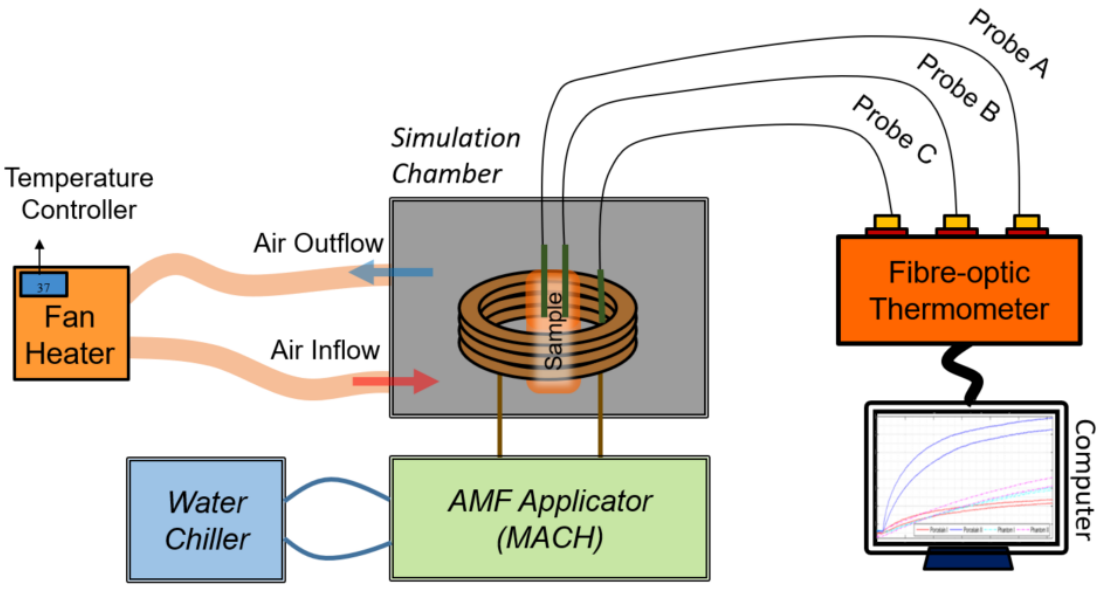

Figure 1.4: The experimental setup of the *ex-vivo* experiment

1.2.2 Materials

Two main materials in this experiments were the tissues to be heated and the MNPs.

Porcine prostate

A donation of 11 porcine prostate tissues was received. After removing adjacent tissues, two prostates with the similar size were selected for the experiment. They were kept in a freezer of which the temperature was maintained at -80 °C. Porcine tissues were placed at the room temperature for more than 4 hours until they achieved the thermal equilibrium with the environment, then the experiment started.

Magnetic nanoparticles

In terms of MNPs, two MNP suspensions were applied. One MNP suspension was provided by Endomagnetics Limited (Cambridge, UK), the name of which is Sienna$^+$, the core of which consists of magnetite (Fe_3O_4) and maghemite (γFe_2O_3). The other MNP suspension was Nanomag®, which was provided by micromod Partikeltechnologie GmbH (Rostock, Germany). The core Nanomag® is magnetite. The size of Sienna$^+$ and Nanomag® are 60 nm and 100 nm. Both suspensions are water-based. The neat concentration of Sienna$^+$ and Nanomag® are 28.0 mg_{Fe}/ml and 73.0 mg_{Fe}/ml (a list of MNP used in this study is presented in Appendix C).

As to the heating performance, the intrinsic loss power (ILP) is a common indi-

cator for quantifying the heating ability of MNPs (see section 2.2.6). The ILP is a concentration-independent indicator. The ILP of Sienna$^+$ is 2.60 $\pm$ 0.1 nHm^{2}kg^{-1} (measured in the concentration of 28.0 mg$_{Fe}$/ml). Nanomag® responses better to an AMF and it has the ILP of 5.50 $\pm$ 0.3 nHm^{2}kg^{-1} (measured in the concentration of 35.5 mg$_{Fe}$/ml), which is roughly twice as high as Sienna$^+$ has (The method for ILP measurement can be found in Appendix B).

To be more comparable to Sienna$^+$, the concentration of Nanomag® was diluted to be 35.5 mg$_{Fe}$/ml before being injected into a porcine prostate.

1.2.3 Experimental Procedure

Both prostates were injected with a 0.5 *ml* MNP suspension. Because the porosity of each prostate is different, the distribution of MNP suspensions was difficult to be predicted. Some flowed back from the injection site, and some leaked from the ureter, as shown in Fig. 1.5. In the figure, the prostate injected with Sienna$^+$ suspension was labelled as *Porcine I*, and the one injected with Nanomag® suspension was labelled as *Porcine II*.

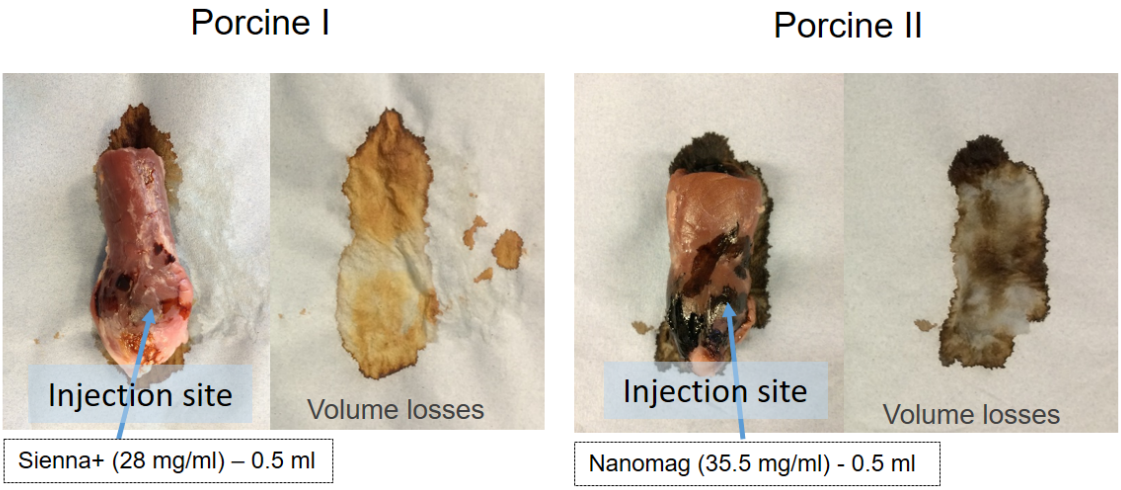

Figure 1.5: The volume loss during the injection of MNP suspension. The *Porcine I* and *Porcine II* were injected with Sienna$^+$ and Nanomag® respectively.

Twenty minutes after the injection, each tissue was covered by a cling film to avoid possible contamination of the coil. Then, an AMF with the intensity of 4 kA/m and the frequency of 968 kHz was applied. Their temperatures were constantly measured by the fibre optic thermometer during the magnetic heating. Three optic thermal probes were used in each heating experiment. While two (Probe A and Probe B in Fig. 1.4) recorded the temperature of a sample, one (Probe C) monitored the chamber

temperature. More precisely, the Probe A monitored the temperature at the injection site, and the Probe B measured the temperature at 5 mm away (see Fig. 1.6). Both porcine tissues were magnetically heated for 30 minutes.

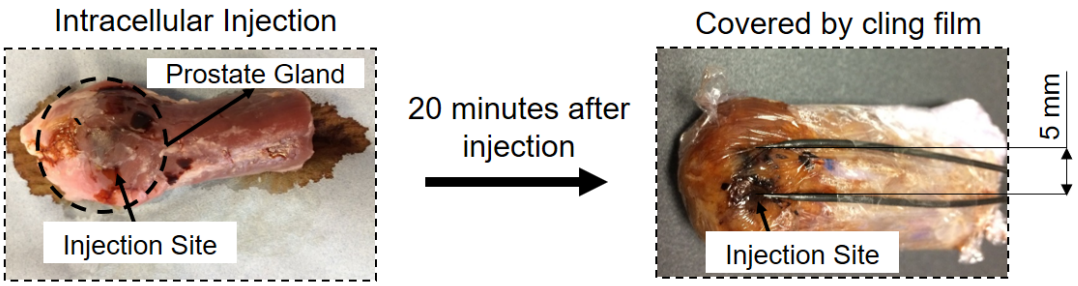

Figure 1.6: The placement of thermometers on a porcine prostate.

1.2.4 Results and Discussion

The heating curves of *Porcine I* and *Porcine II* are presented in Fig. 1.7 (a) and (d). The red and blue lines respectively indicate the temperature of the injection site and the temperature of 5 mm from the injection site. After 30 minutes of magnetically heating, the temperature of the injection site of *Porcine I* was elevated for ca. 6 °C, while the temperature increase in *Porcine II* was ca. 38 °C. The temperature rise in the latter was nearly 6 times of the increase in the former.

However, the ratio of their heating powers, i.e., the ratio of ILPs [1], was only 2.15, which suggests that the ratio of temperature rises in two tissues would be around 2 instead of 6, when the heating period, the volume loss during the injection, the injected volume and the iron concentration of MNP suspension were similar, if not identical, in both cases.

A possible explanation of this inconsistency is the inhomogeneous distribution of MNP suspension. By observing the Fig. 1.5, one can notice that the Sienna$^+$ suspension was deposited more deeply in *Porcine I*, while much of the Nanomag® suspension flowed back from the injection site and remained on the surface of *Porcine II*. This difference in distribution pattern can cause the misreading of the representative temperature, as the injection site did not necessarily have the largest amount of MNPs, but the placement of the thermal probe was based on the position of the injection site. That is, because much of the suspension retained inside *Porcine I*, the thermal

[1] The intrinsic loss power (ILP) is a parameter that represents the heating power of an MNP which is normalised to the field parameters and the iron content. See section 2.2.6)

probe might only contact with a small portion of the Sienna$^+$ suspension. On the other hand, the thermal probe could easily touch much of the Nanomag® suspension as the suspension flowed back to the surface of *Porcine II* during the injection. Hence, we may say the unexpected high ratio of temperature rises as a result of the dissimilarity of MNP distributions. Alternatively, from another perspective, one may also claim that the thermal probe failed to detect a representative temperature due to misplacement of the probe.

The importance of the placement of thermal probes was once again emphasised in Fig. 1.7(b) and Fig. 1.7(e). In these two plots, the difference between the red and blue lines in Fig. 1.7(a) and Fig. 1.7(d) are presented. A temperature difference of 1.5 °C was found in *Porcine I*, and the temperature difference of its counterpart was 4 °C after 400 seconds of the heating period. Then, the difference remained nearly constant. These two plots suggest that the higher the temperature at which the heat source was raised, the higher the temperature gradient would be. In other words, for well-heated subjects, a slight shift in the placement of the thermal probe can result in a large difference in measured values. The shift of the thermal probe was already difficult to be controlled to be 5 *mm* away from the injection site in this *ex-vivo* experiment because the tissue is deformable. It can be even more challenging to precisely control the position of thermal probes in *in-vivo* environment.

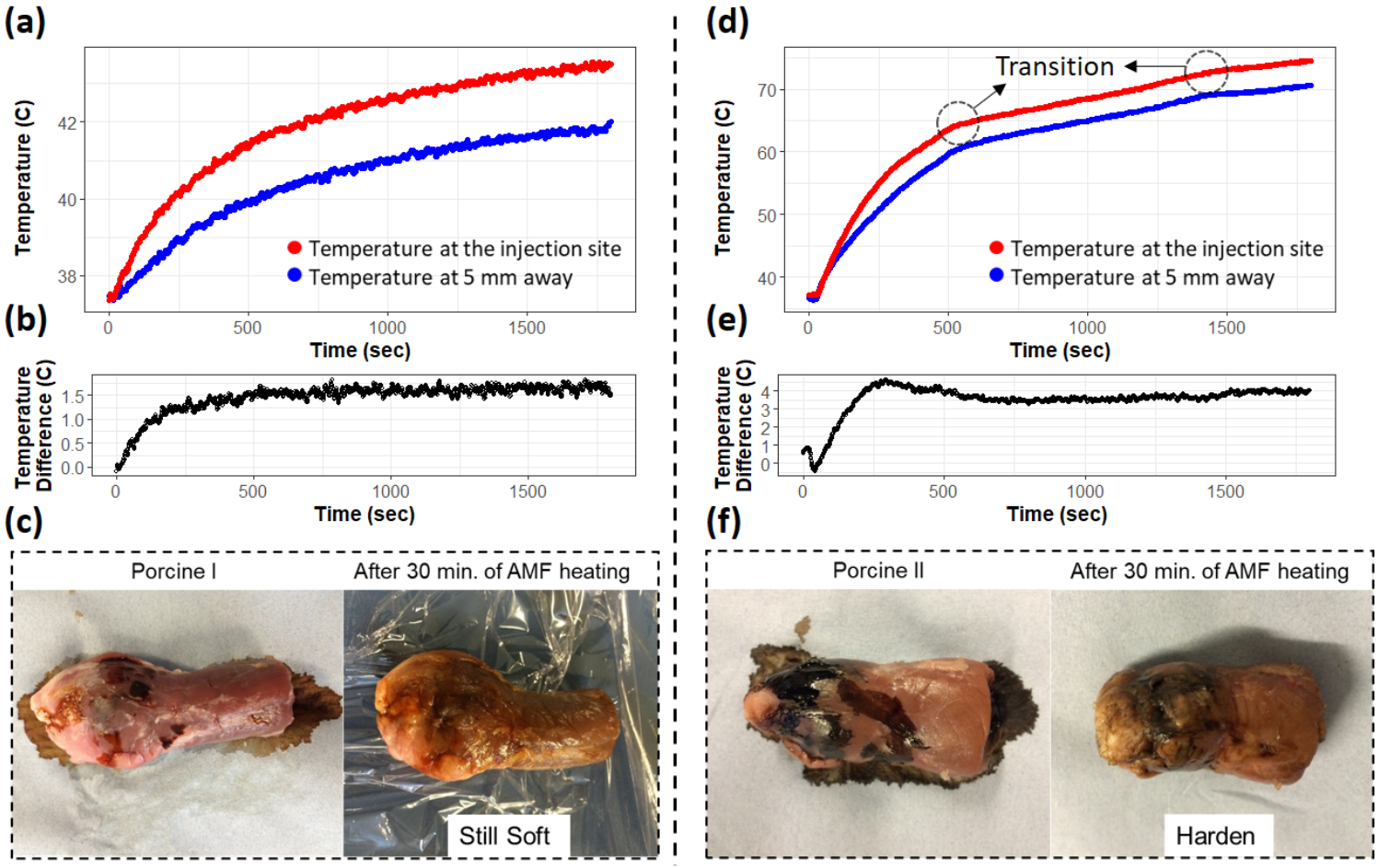

Figure 1.7: The *Ex-vivo* results for *Porcine I* and *Porcine II*. (a) and (d): the temperatures of the injection site (measured by Probe A and indicated with the red line) and the temperature 5 mm away from the injection site (measured by Probe B and indicated with the blue line). (b) and (e): the temperature difference between Probe A and Probe B. (c) and (f): The images of porcine tissues before and after the magnetic heating.

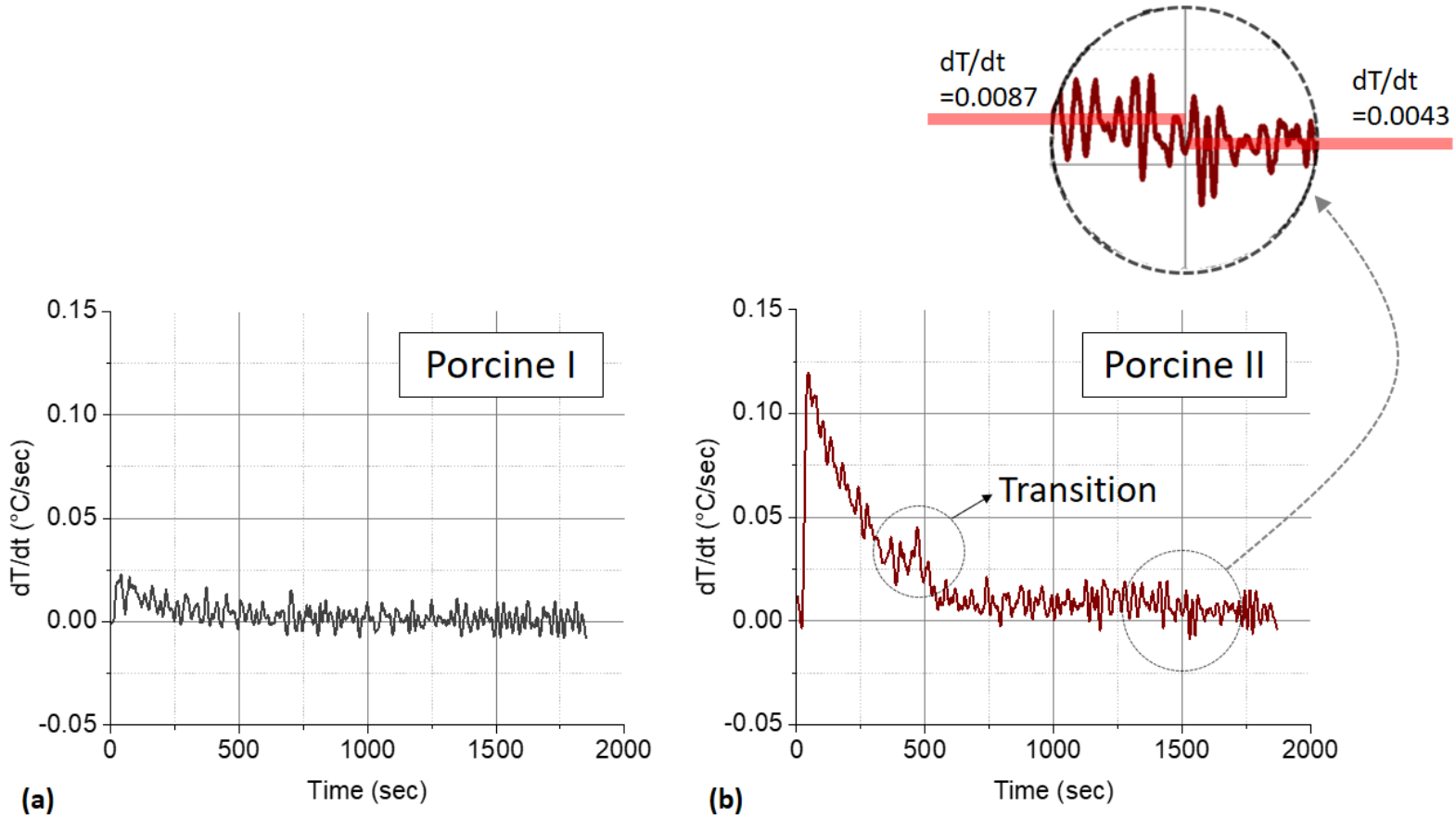

Figure 1.8: (a) The derivative of *Porcine I*'s heating curve (Probe A). The slope, i.e., the derivate of heating curve, decreased for the first 500 second. It then became more or less constant. (b) The derivative of *Porcine II*'s heating curve (Probe A). A spike appeared just before the 500th second, which suggests there was a sudden change in the slope of heating curve. No evident spike was observed at the 1500th second, but a change in the slope of heating curve happened at the 1500th second. The values before and after the 1500th second were 0.0087 °C/sec and 0.0043 °C/sec.

Lastly, it is worth mentioning how the heat affects the tissue structure. Once the temperature is a few degrees above the biological temperature, *i.e.,* 37 °C for the human being, the protein begins to denature. Interestingly, the denaturation is not a one-off action; instead, the protein gradually denatures with the increase in temperature. Furthermore, different types of proteins reacts to the heat differently. Generally speaking, if a tissue is mildly heated, and the heating does not last for long, the protein is often repairable, and it will be self-healed as long as the temperature returns to the biological temperature, the process of which is termed as renaturation. However, if the tissue is excessively heated and its temperature is above 55 °C, then in most situations, the protein denaturation would be unrecoverable. Denaturation means deformation of protein structure. Deformation of protein structure would result in the deformation of tissue structure. Deformation of tissue structure would then lead to a change in its thermal properties. This suggests that by observing the transition in the thermal property of the tissue, it can be found whether degeneration occurs. By sensing the change in thermal conductivities of chicken tissues, Kijowski and Mast found denaturation happened more than once when the tissue temperature was raised from 57 °C to 78 °C [8]. A similar result was found in the present experiment. For the excessively heated *Porcine II*, two transitions in the heating curve was found (see Fig. 1.7(d)). The transitions lie in 64 °C and 73 °C respectively, and this implies the protein denatured to different extents at these two temperatures. On the other hand, no observable transition was found in the heating curve of *Porcine I*. This was reasonable because, unlike *Porcine II*, *Porcine I* was only mildly heated. The temperature of the injection site was 43.5 °C after 30 minutes of heating period. The degree of denaturation of the two cases can also be qualitatively observed in Fig. 1.7(c) and (g). The figure shows that *Porcine I* was still soft but the *Porcine II* was much hardened (because of denaturation) after the magnetic heating.

To more clearly observe the transition of tissue structure caused by heating, one can take the derivative of *Porcine I*'s and *Porcine II*'s heating curves. Their derivatives or slopes are presented in Fig. 1.8. In the figure, only the slopes of heating curves measured by Probe A are calculated. Because the heatings measured by Probe A were at the injection site, the transition of tissue structure here would be more evident than that at the location of Probe B.

Fig. 1.8a and Fig. 1.8b respectively represent the slopes of *Porcine I*'s and *Porcine II*'s heating curves. The change in the slope of *Porcine I* was mild. Its

slope decreased for the first 500 seconds and became stable afterwards. The trend is consistent with the heating curve presented in Fig. 1.7(a). For *Porcine II*, a spike in its heating curve slope was observed just before the 500th second. A spike indicates that there was a sudden change in its heating curve, which should caused by the transition of tissue structure. Moreover, although no spike was observed at the 1500th second, there was a observable change in the slope. The slope of *Porcine II*'s heating curve changed from 0.0087 °C/sec to 0.0043 °C/sec at the 1500th second. This sudden change in the slope should be caused by another transition that altered the thermal property of *Porcine II*. The time when these two transitions happened was in consistent with that observed in Fig. 1.7(b).

It is also worth noting that the aforementioned effect is bidirectional, not only does temperature cause denaturation, but also the thermal properties of the tissue after denaturation change, which in turn affects temperature variations during magnetic heating. This increases the uncertainty of the temperature prediction during hyperthermia. To eliminate the effect of this uncertainty on thermal management, reliable temperature monitoring is required.

1.2.5 A Brief Conclusion

The above discussion indicates that point measurement of temperature through thermal probes can be unreliable because of the uncertainty of particle distribution. For example, it is difficult to ensure the reading of the thermal probe at the injection site represents the highest temperature during the treatment. Interestingly, the more information does not necessarily lead to the better the results. In many cases, false information is worse than no information. In the case of magnetic hyperthermia, the misreading of temperatures elevation may result in over-treatment. This will not only kill malignant tumours, but also cause undesired damage on benign tissues. For treatment of sensitive areas such as the brain, over-treatment can result in serious consequences.

1.3 Three Actions and Five Elements

Before moving on to the discussion on temperature sensing methods, let's take a step back and have a more comprehensive look at magnetic hyperthermia. As described previously, the thermal management is like a jigsaw that completes the whole picture

of magnetic hyperthermia. This study tends to improve the thermal management, but limited by the time and resources, only a part of the issues in thermal management has been addressed. However, the jigsaw consists of more than one element. To more clearly state the position of this study, it is essential to understand what elements are included in the jigsaw of thermal management.

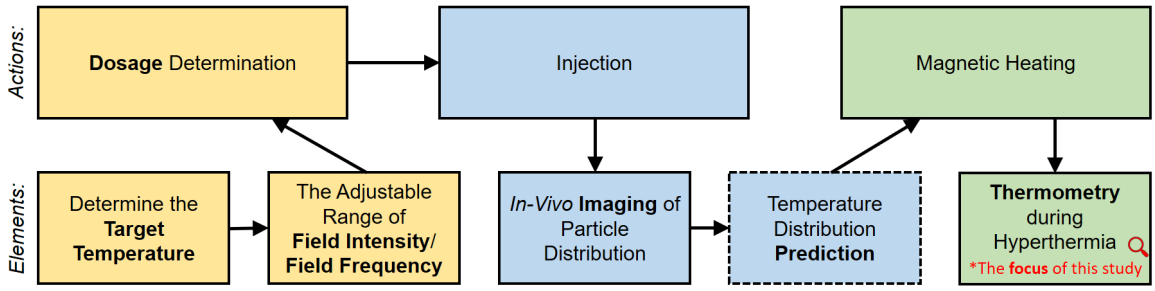

Figure 1.9: The actions in magnetic hyperthermia and elements of thermal management. The research focus of this study is the last element, thermometry.

Broadly speaking, the procedure of magnetic hyperthermia can be divided into three actions, which are respectively the *dosage determination*, the *injection* and the *magnetic heating*. From the experience in the *ex-vivo* experiment, the author concludes five elements that should be taken into consideration in order to ensure the quality of thermal management. The five elements are presented in Fig. 1.9. Each element is in relation to one of the three actions. The details are described as below.

Firstly, when a clinician receives an MNP suspension and a field generator, the clinician would be provided with the ILP of the MNP suspension as well as the adjustable ranges of field intensity and frequency. Before a treatment, the clinician would need to set a target temperature and a desired heating period, *i.e.,* the target thermal dose (see Section 2.1.2). The target temperature may be determined by clinicians through *ex-vivo* or pre-clinical experiments before the actual treatment. With the above parameters in mind, the clinician determines what dose of MNPs should be applied to the patient. Even if this determined dose does not guarantee that the temperature of the tumour rises to the target temperature, it provides good guidance to the clinician. Secondly, once the dose is determined, the MNP suspension is injected to the target tumour. Unfortunately, the particle distribution is uncertain, which leads to uncertainty in the temperature distribution. A way to manage the effect of this uncertainty is to image the particle distribution, based on which the heating protocols can then be more appropriately adjusted. Increasing studies have begun to use micro-computed tomog-

raphy (MicroCT) to visualise *in-vivo* distribution of MNPs [9] [10]. With the MicroCT intervention, results with improving therapeutic effectiveness have been reported in Zhu's group and Hilger's group respectively [11] [12]. The image of particle distribution together with field parameters, thermal properties of tissues and the ILP of MNPs provide an opportunity to predict the temperature distribution. The temperature distribution can be estimated based on the particle distribution through finite element analysis (FEA), as reported in [13]. This is another element of thermal management. However, it is dangerous to merely rely on this prediction, because many factors that are not included in the prediction, such as the heat taken by the blood flow or the aforementioned denaturation, would affect the temperature variation; hence, the last element, a reliable thermometry during hyperthermia, is necessary. The thermometry is a key element of thermal management and it is the research focus of this thesis. However, it does not reduce the importance of other elements. Although the *in-vivo* imaging is not the main focus of this study, from the author's perspective, the *in-vivo* imaging of particle distribution is essential for improving the thermal management. More discussion on *in-vivo* imaging can be found in Section 4.5. As to the temperature distribution prediction, depending on the pattern of particle distribution, it may or may not be important. If the particle distribution is homogeneous, one can probably avoid the complex FEA but still be able to manage the temperature profile well through sensing the representative temperature of the target tumour, e.g. the average temperature of the target site.

1.4 Conclusion

1.4.1 Focus on Remote Temperature Sensing

Overall, a brief conclusion can be drawn here: *A more reliable temperature sensing method than point measurement, e.g., measuring by a thermometer, is needed for improving the thermal management of magnetic hyperthermia.* As mentioned previously, this conclusion is brief, but this is the starting point of this study.

This thesis includes the discussion of two remote temperature sensing methods. One is the infra-red thermography. Infra-red thermography has been applied to different aspects of the medical field because of its ability to monitor the temperature of multipoint. Another advantage of it is the non-invasiveness. Unlike thermal probes,

the infra-red thermography does not require direct contact with an object; hence, the measurement does not affect the temperature of the object. Although infra-red rays have a limited ability to penetrate the skin, the infra-red thermometry has been reported as an effective method for monitoring the temperature change of subcutaneous tumours during magnetic hyperthermia [14].

In addition to infra-red thermometry, this study proposes another thermometry, which is termed as magnetic particle thermometry. Rather than a point measurement, the magnetic particle thermometry detects the average temperature of the region of interest and regards it as a representative temperature. In this method, MNPs are not only seen as heat sources but also regarded as thermal probes. This thermometry is possible because the presence of MNPs causes a shift in the resonant frequency of the field generator. Moreover, the resonant frequency changes as the temperature of MNPs changes. More discussion can be found in Section 5.1.

1.4.2 Thesis Outline

This chapter has explained the reason and the purpose of this research. More detailed discussion on the infra-red thermometry can be found in Chapter 3 and Chapter 4. The former and the latter will respectively present an *in-vitro* experiment and an *in-vivo* experiment. The infra-red thermometry was applied in both experiments. Moreover, the physical phenomena of the proposed magnetic particle thermometry will be described in Chapter 5. The validation of the magnetic particle thermometry will be presented in Chapter 6. This will be followed by another chapter describing how magnetic properties affect the performance of this thermometry. The last chapter will then conclude the findings of this study and discuss about potential applications of these findings. These discussions will all begin from the literature survey presented in the next chapter. In which, the literature on the biological effects of heat, the fundamental magnetism and the remote sensing thermometry will be covered.

Chapter 2

Literature Review

This chapter covers the foundations of the magnetic hyperthermia. The first section briefs the biological effects of heat, which includes the cell death mechanism and a special protein called heat shock protein. The latter is an interesting protein whose amount tends to increase with temperature. In another section, the magnetic properties will be introduced before the explanation of the mechanism of magnetic heating. In which, the quantification of magnetic heating power is also presented. Afterwards, another section discusses the safety concerns of magnetic fields and the dose limitation of MNPs. The final section of this chapter focuses on the remote sensing techniques for temperature monitoring during magnetic hyperthermia. This section includes both the application of the infra-red thermometry and the development of magnetic particle thermometry.

2.1 Biological Effects of Heat

2.1.1 Cell Death in Hyperthermia

Heat can lead to two forms of cell death. On the one hand, at the high dose of heat, the cellular membranes would be directly damaged due to the high temperature. Cells die because the intracellular content is released through the damaged cellular membranes. This sort of cell death is called necrosis. On the other hand, at a milder elevated temperature, the cellular membranes remain undamaged; however, the heat can still trigger another type of cell death, which is known as apoptosis [15]. Unlike necrosis as a passive process, apoptosis is an active process. Once the apoptosis is triggered, a cell starts to form belbs. Later, the belbs detach and become apoptotic

bodies. These apoptotic bodies would gradually be swallowed by phagocytes. The morphology of necrosis and apoptosis is shown in Fig 2.1.

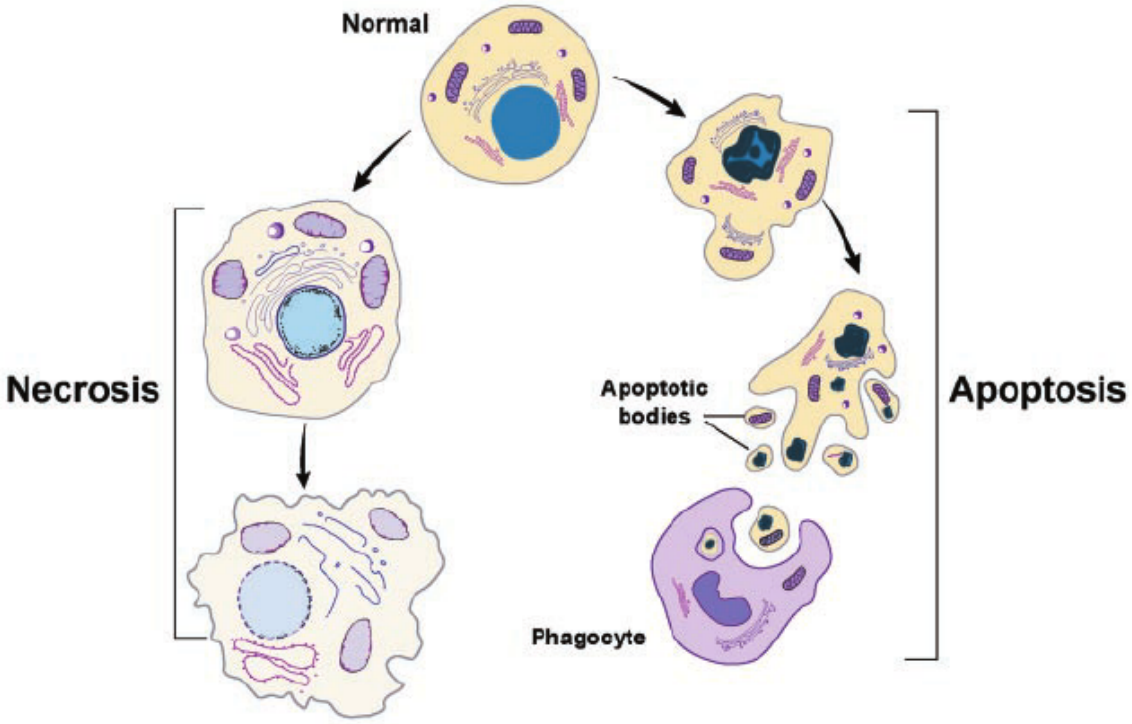

Figure 2.1: Morphology of necrosis and apoptosis (adapted from [16]).

Heat is one of the main factors that causes necrosis or triggers apoptosis. The effect of heat on these two cell death mechanisms were studied in an interesting experiment conducted by Song et al. [17]. In the experiment, human prostate cancer cells were cultured and the temperature of which was elevated by a temperature-controlled chamber. Twenty four hours after the heating, the proportion of each form of cell death was measured through flow cytometry based on two different stains. The reported results indicate that apoptosis is the primary mechanism leading to cell death for mildly heated cells, and when the temperature was further elevated, the cells become necrotic. More specifically, for those cells that were heated to 52 °C for 10 minutes, apoptosis was detected, and necrosis only emerged when the temperature was elevated above 60 °C for the same duration. Interestingly, even if the temperature of cells was only a few degree above the biological temperature, it could still trigger apoptosis or cause necrosis as long as the heating duration is long enough. In this specific experiment, after keeping the cells' temperature at 44 °C for 120 minutes, apoptosis was found to be the main mechanism that led to cell death; by increasing the temperature with just 1 °C to 45 °C, with the same heating duration, necrosis became the dominant effect.

Although there are two forms of cell death, in the context of hyperthermia, one may be more concerned with the result of cell death rather than the mechanism that leads to it. From the above discussion, we have learnt that not only the applied temperature but also the heating duration have a significant effect on heat-induced cell death. To facilitate the discussion on the cell damage during hyperthermia, a parameter called thermal dose has been suggested in the literature, which will be described in the next section.

2.1.2 Thermal Dose

The previous section describes a phenomenon, the biological response of cells to heat. It is one thing to understand a phenomenon. It is quite another to utilise or control this phenomenon. The concept of thermal dose was established for the latter purpose. From the previous section, we have concluded that the lower the heating intensity is, the longer the heating duration is required to cause the same degree of cell damage. The thermal dose was defined to be an indicator of cell damage. When one states that the thermal dose in case A is identical to that in case B, this means that one expects the degree of cell death is the same in both cases if the tissue properties in both cases are identical. In other words, a thermal dose is not a term that was mathematically deduced from physic theories. Instead, the thermal dose is a defined parameter that correlates the heat-induced cell damage with both the intensity and the duration of heating.

This correlation was carefully discussed in a highly cited paper by Sapareto and Dewey [18]. In their report, the thermal dose was mathematically described as an equivalent number of minutes at a reference intensity. To elaborate the concept more clearly, we may take a look at the following example: if a target tissue was heated and its temperature retains at 45 °C for 5 minutes and an empirical examination shows that the tissue has the same degree of cell damage to another tissue of which the temperature held at the reference value, e.g. 43 °C, for 20 minutes, then one may claim that the applied thermal dose is equivalent to 20 minutes heating at the reference temperature. In short, what makes 5 minutes at 45 °C be equivalent to 20 minutes at 43 °C is the equivalent degree of cell death from empirical studies. Based on an *in-vivo* study, Sapareto and Dewey proposed the equation for modelling the thermal dose as below:

$$t_{reference} = \sum_{n=1}^{N} \Delta t R^{T_{reference} - T_n} \tag{2.1}$$

In which, the Δt represents the interval of exposure time, T_n means the average temperature during the n^{th} interval, N indicate the number of intervals in the procedure and the value of R reflects the rate of cell killing. The value of R is supposed to be a function of temperature, but for the range of interest (37-46 °C), R can be approximated to be two constants, which respectively are 0.5 and 0.25 when T is above and below 43 °C. Although this approximation would introduce a 2% error, it is tolerable and acceptable in later studies [19] [20]. Because the reference temperature is commonly selected to be 43 °C, in the literature, this equation is often written as:

$$CEM43 = \sum_{n=1}^{N} \Delta t R^{43 - T_n} \tag{2.2}$$

The CEM43 is the abbreviation of a cumulative number of equivalent minutes at 43 °C [21]. This conversion makes two factors into one so that clinicians are able to expect the level of cell damage or to evaluate the intensity of hyperthermia based on the value of CEM43.

The Eq. 2.2 converts the temperature of a single point to the thermal dose. However, the temperature distribution in a tumour is not homogeneous during the magnetic hyperthermia. To better evaluate the condition of the treatment, Dewey later introduced a regional indicator **CEM43-Tx** [22]. The indicator indicates that the x% of the tumour region receives a certain amount of thermal dose. For instance, if the thermal dose is 25 minutes of CEM43-T90, it represents the 90% of the tumour region receives the thermal dose higher than 25 minutes of CEM43. *In-vivo* reports have shown the positive correlation between **CEM43-T90** and clinical outcomes [23] [24] [25]. This regional indicator of thermal dose will be discussed in Section 4.4.

Based on the empirical observation of heat-induced cell death, CEM43 was created for modelling the concept of thermal dose. Apoptosis or necrosis occurs only when the thermal dose is above a threshold [1]. Another question to ask is, what happens if the thermal dose is below the threshold? Does the cell still react to heat? To address this question, the following section will introduce another interesting heat-induced

[1] Dewhirst et al. have made efforts on building databases of the thermal dose thresholds, which are presented in the table 3 in [21] and the table 2 in [26].

response of the cell, which is known as heat shock response.

2.1.3 Heat Shock Response

The term *heat shock response* explains itself. Heat shock response is a phenomenon that specific proteins form after cells are shocked by heat. Although the term *heat shock response* does not reflect the whole picture of the phenomenon, it does illustrate the history of its discovery. This effect was firstly discovered by Ritossa in 1962 [27]. In the report, Ritossa presented two images which indicate that certain bands of a chromosome of drosophila (fruit flies) expanded after being applied with a thermal dose of 30 minutes at 30 °C. This expansion is later referred to chromosome puffing. The chromosome puffing was found to be associated with an increase in specific proteins after a decade [28]. Since the stimulus in both studies was heat, the induced protein has been named as heat shock protein (HSP), even if subsequent studies have found that stimuli other than heat can also induce the formation of HSP. That is, when exposed to stimuli like heat, amino acid analogues, glucose analogues, heavy metals and etc., the amount of HSPs in cells increases [29]. The nomenclature of HSP is only based on the first discovered stimuli that induces its synthesis.

There are more than one type of HSPs. As the function of a protein is often decided by its length, the HSPs are categorised by their sizes. A protein constitutes amino acids, and thus a way to determine the size of a protein is to directly state the number of amino acids. Another way used more frequently is quantifying the protein size based on its molecular weight. The unit of the molecular weight is Dalton, abbreviated as Da, also known as the atomic mass unit, which is defined as one-twelfth of the carbon atom mass [2]. A protein is a macromolecule, which means the molecular weight of most proteins is above one kilo-Dalton, abbreviated as kDa. As the structure of a protein directly affect its function, HSPs are categorised to a variety of families based on their molecular weights. For instance, the HSPs which have the molecular weights of 60 kDa, 70 kDa and 90 kDa are respectively grouped and termed as HSP60, HSP70 and HSP90.

An object often processes more than one nature, but one often describes an object based on a single nature. For example, water can be described as a liquid based on its phase and it can also be described as an inorganic matter based on its chemical

[2]The molecular weight of a amino acid is about 110 Da.

compound. Similarly, the term HSP only illustrates that its synthesis is induced by heat shock, but it does not describe what is its function. When discussing on the function of HSPs, a large group of HSPs is regarded as molecular chaperones. Molecular chaperone is another interesting term. The term was first used by Laskey et al. in 1978 [30]. They used this term to metaphorise the auxiliary role of a specific protein, nucleoplasmin, in the process of nucleosome assembly. During the assembly, nucleoplasmins temporarily bind with histones. This binding neutralises the positive charges on the histones, thereby promoting the combination of histones and DNAs, the assembly of which is a nucleosome. Despite the important role of nucleoplasmins, they are not a component of the final product. Nucleoplasmins are detached after the assembling process. Like nucleoplasmins, other proteins have the similar effect that contributes to different biological responses without being a part of the final product. Later, Ellis et al. summarised this phenomenon and extended the term *molecular chaperone* to describe all the molecules that have similar properties [31]. In their report, a molecular chaperone was defined as "a family of unrelated classes of protein that mediate the correct assembly of other polypeptides, but are not themselves components of the final functional structure" [32]. Not all HSPs, but a large group of HSP families, e.g., HSP70 and HSP90, behave as molecular chaperones. Many HSPs were found to play an important role in preventing the unfolding of proteins and some of them are even able to assist in refolding proteins [33–36]. In short, HSPs would be induced in cells for the purpose of preventing or recovering the damages when exposed to harmful stimulus.

Heat is undoubtedly an effective stimulus to induce the synthesis of HSPs. One of the most frequently studied HSP family is HSP70, mainly because its quantity is easy to be measured and it is ubiquitous in most types of cells. Didomenico *et al.* presented a study that shows positive correlation between the severity of heat shock and the quantity of induced HSP70 in [37]. There is no quantitative description on the heat shock mentioned here, but its context is qualitatively identical to the aforementioned thermal dose (i.e. CEM43). Both are related to the severity of cell damage. Morris *et al.* pointed out that it is not the external stimulus, e.g. heat shock, that activates HSP synthesis; it is the increase in macromolecular damage that activates HSP synthesis [38]. Since the synthesis of HSPs is associated with the environmental temperature, Craig and Gross proposed a concept of using the level of HSP70 induction as the cellular thermometer [39]. This appealing concept was

later used for monitoring the effect of the change in environmental temperature on biological species at different locations [40]. In the context of thermal treatment, the induction of HSP70 is sometimes seen as an indicator of the severity of sub-lethal cell damages [41].

While the CEM43 is an indicator that derived from the temperature and the duration of heating, the quantity of HSP70 indicates the actual biological response to the environmental stimulus, i.e., the heat shock in the context of this thesis. Both indicators were compared and discussed in the *in-vivo* experiment presented in Section 4.4.

2.2 Heating Mechanisms of Magnetic Nanoparticles

The previous section has introduced the biological effect of heat, a way of quantifying thermal dose and an indicator, i.e., HSP70, for monitoring sub-lethal cell damages. This section will focus on how the heat is generated magnetically. To explain the mechanism of magnetic heating, a few components will be included in the following subsections. The first component is the description of a magnetic field, *i.e.,* what parameters we can use to describe an invisible field? Then, another subsection will illustrate a specific parameter called magnetic susceptibility. Susceptibility is one of the main parameters that defines the magnetic property of a material. As the term suggests, the susceptibility quantifies how easily a material would be affected by an external field. Furthermore, the effect of dimension, *i.e.,* the particle size, on the magnetic properties will be elaborated prior to the discussion on the magnetic heating. For small-dimension magnetic materials, the dominant heating mechanism is relaxation heating, which will be described in Section 2.2.5. The following subsection will describe the method of quantifying the magnetic heating, which is widely used in the literature. At the end of this section, the safety concern on the magnetic field and the limitation of MNP dosage will both be addressed.

2.2.1 Magnetic Field Intensity, Flux Density and Permeability

A concept often evolves over time. To better illustrate a concept, one should probably not ignore the impact of its development history on it, which is also the case when describing an invisible magnetic field. About 200 years ago, scientists were unsure how to describe a magnetic field. Two methods were proposed to calculate the intensity of a magnetic field.

Those two parameters were denoted as B and H. They are proportional to each other. When in vacuum, their relationship is as shown in the Eq. 2.3,

$$B = 4\pi \times 10^{-7} H \tag{2.3}$$

Although this mathematical relationship has been accepted as a fact, the interpretation of B and H is sometimes confusing. One of the main interpretation is from William Thomson (1824 - 1907). In his perspective, B and H have the equivalent statuses and both represent magnetic field intensity. The only difference between them is how they are derived. On the one hand, B as a magnetic field is derived based on Ampere's law: a law describing the fact that a conductor with current passing through it generates a magnetic field. Because this derivation is associated with electricity, Thomson termed B as the "electromagnetic definition" of magnetic field intensity. On the other hand, another definition of magnetic field, now termed as H, was originally built by Poisson (1781 - 1840). In Poisson's model, a layer of imaginary monopole magnetic material rather than the real dipole medium is used to derive H. Thomson found these two forms of magnetic field intensity would be quantitatively the same by multiplying a constant, as shown in Eq. 2.3.

Another interpretation, originated in Faraday (1791 - 1867) and Maxwell (1831 - 1879), distinguishes B and H. The concept of this interpretation is adopted from hydrodynamics. While the magnetic field intensity, H, is viewed as the gradient pressure of flow, the volumetric flow rate per unit area is analogous to so-called magnetic flux density, B (see Appendix D) [42] [43]. The latter interpretation is commonly used in modern engineering. This might because that the analogy of hydrodynamics is beneficial when considering the magnetic properties of matters. Similar to the permeability of a porous medium in the hydrodynamics, the constant $(4\pi \times 10^{-7})$ in the Eq. 2.3 can now be given a new physical meaning, the magnetic permeability in vacuum, termed as μ_0. Hence, the Eq. 2.3 is represented as below:

$$B = \mu_0 H \tag{2.4}$$

2.2.2 Magnetic Properties of Materials and Hysteresis Heating

Different mediums possess different magnetic permeabilities. As a result, even though the intensity of the primary magnetic field, H, remains unchanged, the flux density, B, varies in different mediums. The reason is because all matters are magnetisable

to some extent, i.e. when a matter exposed to a magnetic field, the matter itself is induced a magnetic field and thereby affects the flux density. This phenomenon is called magnetisation. Consider this phenomenon, the Eq. 2.4 is modified to become:

$$B = \mu H \tag{2.5}$$

In this equation, the constant, μ_0, is substituted by a variable, μ, which means the magnetic permeability of a matter. The Eq. 2.5 is still not convenient enough for examining the magnetic properties of a matter, because the flux density, B, in this equation is influenced by both primary and the induced magnetic fields. For analysing the magnetic property of a matter, the Eq. 2.5 is further divided into two terms and becomes:

$$B = \mu_0 H + \chi_0 \mu_0 H \tag{2.6}$$

In which the $\mu_0 H$ and $\chi_0 \mu_0 H$ are flux densities associated with primary and induced magnetic field, respectively. By dividing the second term by μ_0, the strength of the induced magnetic field, M, is obtained:

$$M = \chi_0 H \tag{2.7}$$

The variable of χ_0 is defined as (static) magnetic susceptibility, which indicates how likely a matter would be influenced by an external field. This is a key parameter when considering magnetic properties of materials. The susceptibility is sometimes visualised in the form of a M-H curve (see Fig. 2.2). If the χ_0 of a matter is positive and the value of which is between 10^{-6} and 10^{-1}, then the matter is termed as a paramagnetic material (e.g. aluminium), in which the direction of the induced magnetic field is the same as the primary magnetic field. A diamagnetic material (e.g. water), on the other hand, has an induced magnetic field with opposite direction to the primary magnetic field, and its χ_0 ranges from -10^{-6} to -10^{-3} [44].

To understand the magnetic property of material, we can observe it from both the macro and micro scales. The above description of the induced magnetic field is described from a macro perspective. As mentioned, the phenomenon of a magnetic field induced in a matter is called magnetisation.

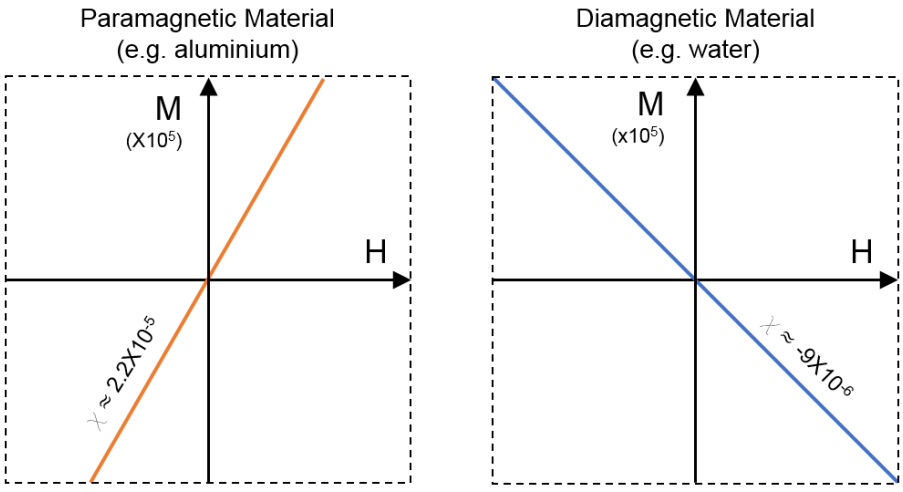

Figure 2.2: M-H curves of diamagnetic and paramagnetic materials (the figure is prepared by the author).

The macroscopic description illustrates the phenomenon but does not explain the formation of magnetisation. To further interpret magnetisation, one may take another look at the micro scale. If one slices a matter in half again and again, one would find that all matters are consists of elementary particles such as protons and electrons [3]. Due to the electricity, the spin and orbital movement of elementary particles would form magnetic fields. These inherent magnetic fields are termed as magnetic moments or magnetic dipoles. In the absence of an external magnetic field, the magnetic dipoles in paramagnets and diamagnets are unordered, and their moments are evened to be (nearly) zero. However, within an external field, these dipoles would be aligned with the external magnetic field to a certain extent, which results in a non-zero net magnetic moment. This is how an induced magnetic field forms, as depicted in the Fig. 2.3. The figure provides us with microscopic aspect of the magnetisation. In addition, if a matter with the volume of V is induced a net magnetic moment m by an applied field, we can define the magnetisation (strength of induced magnetic field), termed as M, to be: $M = m/V$.

[3]To avoid being too complicated, we do not consider substructures such as quarks discovered in the second half of the 20th century.

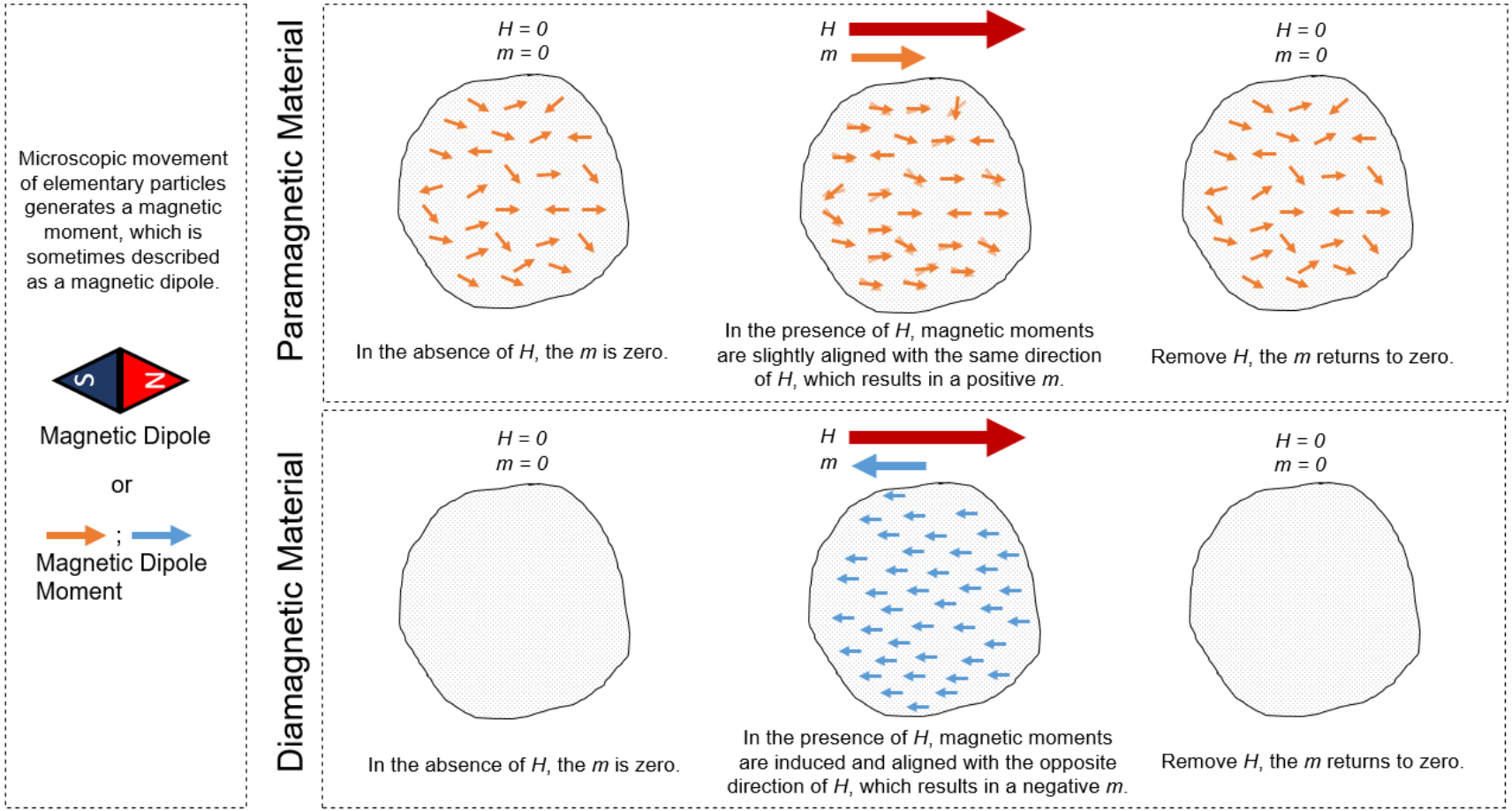

Figure 2.3: Magnetisations of paramagnets and diamagnets. H: the strength of an external magnetic field; m: the net magnetic moment (the figure is prepared by the author)

2.2.3 Magnetic Materials - Ferromagets, Ferrimagnets and Antiferromagnets

Every material is magnetic to some extent, but only certain materials are considered as magnetic materials. Magnetic materials are much easier to be attracted or repelled by an external magnetic field than others. Unlike paramagnets and diamagnets, even though an external magnetic field does not be applied, the magnetic dipoles in magnetic materials, such as ferromagnets, ferrimagnets and antiferromagnets, would align with their adjacent dipoles. The region where the magnetic dipoles are oriented to the same direction is called a domain, as shown in Fig. 2.4a. Because of the comparatively ordered magnetic moments, ferromagnets have stronger magnetisation than others; furthermore, as the rotation of domains requires less energy than the rotation of unordered dipoles, ferromagnets are easier to be magnetised, which means ferromagnets has higher susceptibility. In particular, the ferromagnet typically has its susceptibility 10,000 times larger than others [44].

Interestingly, because of the pinning of the domain walls at defects within the material, the ferromagnet tends to stay magnetised even when the applied field is switched off. This phenomenon is the well known magnetic hysteresis, which can be observed in its M-H curve as shown in Fig. 2.4b. In the figure, the magnetisation is saturated at M_S when the magnetic dipoles are aligned to a certain extent with the applied field; even if the field intensity increases further, the alignment does not improve further. When the applied field is removed, the magnetisation remains at a non-zero value, M_R. To demagnetise the M_R, it requires an additional magnetic field, coercivity (H_C), to be applied to the material. Due to the existence of M_S, M_R and H_C, a reversal of the magnetisation behaves as the hysteresis loop shown on the M-H graph. The area of the hysteresis loop represents the heat dissipation per unit volume (Q_{FM}) during a reversal of the magnetisation, which can be

described as:

$$Q_{FM} = \mu_0 \oint H dM \tag{2.8}$$

If the reversal of the magnetisation continues due to the external time-varying magnetic field. The power of heat generation becomes [44]:

$$P_{FM} = \mu_0 f \oint H dM \tag{2.9}$$

This heat generation often causes problems in electrical engineering yet in the context of magnetic hyperthermia, this heat generation is the core. Hysteresis heating is one

mechanism of energy loss during magnetisation. However, the dimension matters. When the diameter of a ferromagnet downs to tens of nanometres, the ferromagnet acts like a paramagnet which means one no longer observes the hysteresis effect. This phenomenon is termed as superparamagnetic, and it is the topic of the next section. Not surprisingly, energy would also dissipate as heat during the magnetisation of superparamagnet, the mechanism of which is called relaxation heating. This relaxation heating will be elaborated in more detail in Section 2.2.5.

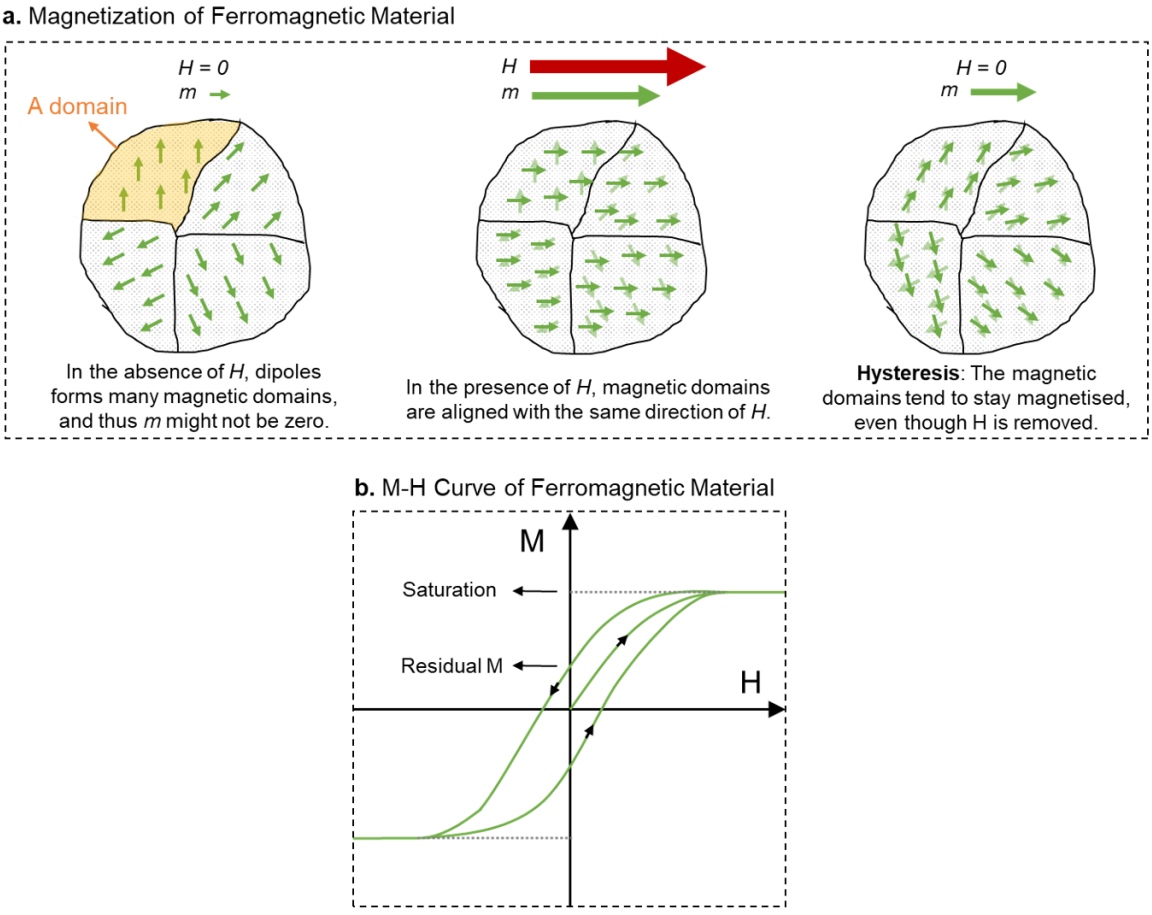

Figure 2.4: (a) The magnetisation of ferromagnets. H: the strength of an external magnetic field. m: the net magnetic moment. (b) The hysteresis curve of a ferromagnetic material. M_S: saturation magnetisation; M_R: remanent magnetisation; H_C: coercivity (the figure is prepared by the author).

2.2.4 Single-Domain Ferromagnet and Superparamagnet

When the dimension of ferromagnet declines, the domain walls become thinner. The thinner the domain wall is, the larger the energy for the formation is required (the detail of domain theory can be found in [45]). Thus, once the dimension of ferromagnets is below a critical value (e.g. approximate 80 nm for magnetite), it is energetically

unfavourable to form a domain wall. At this dimension scale, all the magnetic dipoles would orient in the same direction rather than being subdivided by domain walls. This small ferromagnet becomes a so-called single-domain ferromagnet. Place this single-domain ferromagnet in a time-varying magnetic field; similar to a multi-domain ferromagnet, heat would be generated due to the hysteresis loss during reversals of magnetisation. However, their mechanisms of generating hysteresis loss are slightly different. The difference is from the way they flip their magnetic dipoles. While a multi-domain ferromagnet flips dipole direction through the movement of its domain walls, a single-domain ferromagnet directly rotates its dipoles, which requires sufficient energy to overcome its intrinsic energy barrier, ΔE. As the direct rotation of dipoles needs more energy than the movement of domain walls, the hysteresis loss are comparatively large in single-domain ferromagnets, i.e. the hysteresis loop becomes wider (see Fig. 2.5a). In addition, its energy barrier, ΔE, depends on both the anisotropy energy density, K, and the volume, V of the ferromagnet, i.e. $\Delta E = KV$. This implies that the dipoles become looser when the volume of the single-domain ferromagnet continues to decrease. In consequence, the demagnetisation becomes easier when the applied field is removed. When the volume drops below another critical value, the associated hysteresis effect becomes less evident and vanishes eventually. Without the hysteresis effect, the matter acts like the paramagnet but has much stronger magnetisation (or higher susceptibility) and thus is termed as superparamagnet.

The vanishing of hysteresis effect is due to the thermal fluctuation. For a superparamagnet, its energy barrier is comparable to the thermal energy in the environment. As a result, without an applied field, the dipoles would be easily fluctuated by the background thermal energy. That is, after a very short period, the time-average net magnetisation of dipoles (i.e., the remanent magnetisation in Fig. 2.4) becomes zero. Generally speaking, because of the thermal fluctuation, the remanent magnetisation in a all matter tends to vanish within a particular period. This phenomenon is called relaxation and the particular period is denoted as τ, termed as relaxation time. In fact, the environmental thermal energy affects all magnetic materials; nevertheless, since the energy barrier in ferromagnet is much larger than the environmental thermal energy, its remanent magnetisation vanishes so slowly that the hysteresis effect is easily observable. On the other hand, the hysteresis is unobservable in superparamagnets due to the rapid relaxation of remanent magnetisation [4].

[4]One can argue that the hysteresis effect still exists in a superparamagnet; it is just that we do

For a single-domain magnetic material (e.g., either a superparamagnet or a single domain ferromagnet), provided that the material itself is immobilised, then the relaxation would be dominated by so-called Néel relaxation, which describes that the relaxation is achieved by the rotation of magnetic dipoles rather than physical rotation of the matter. This relaxation can be seen as a battle between the energy barrier that stops the dipoles from rotating and the thermal fluctuation that tends to randomise dipoles. As a consequence, the Néel relaxation time, τ_N, is described as below [46]:

$$\tau_N = \tau_0 e^{KV/K_B T} \tag{2.10}$$

In which, K_B means the Boltzmann constant, and T is the environmental temperature. The unit of the factor, τ_0, is *second* and is of the order 10^{-9} - 10^{-12} [44] [5]. That is, when the energy barrier (KV) is comparable to (or smaller than) the thermal energy ($K_B T$), the net magnetisation would vanish, i.e., the relaxation would be completed, within 10^{-9} - 10^{-12} seconds.

As indicated in the equation, this relaxation would also be affected by the temperature. When the temperature is extremely low, the thermal energy ($K_B T$) would be too weak to rotate magnetic moments. This situation is often described as: those magnetic moments are blocked, and the temperature that is just low enough to cause the block is termed as blocking temperature. The blocking temperature is not constant for a material; instead, its value is dependent on the volume of the material. After all, it is all about the balance or battle between the thermal energy and the energy barrier. Therefore, the larger volume the particle, the higher the blocking temperature.

Due to the different reasons mentioned above, a ferromagnet acts differently when its size varies. The Fig. 2.5b shows the size-dependence of transitions from the multi-domain to single-domain ferromagnet and to the superparamagnet. In the figure, the coercivity, H_C, is used to roughly represent the width of the hysteresis loop [47].

---

not observe it through our perspectives or through the applied measurement instrument. However, if one blinks his or her eyes fast enough, one would be able to capture the hysteresis effect in that matter and that matter actually behaves like a ferromagnet. In this case, we may no longer classify that matter as a superparamagnet from the new perspective. After all, observation is based on a perspective. If the perspective is no longer the same, the world we see can be very different.

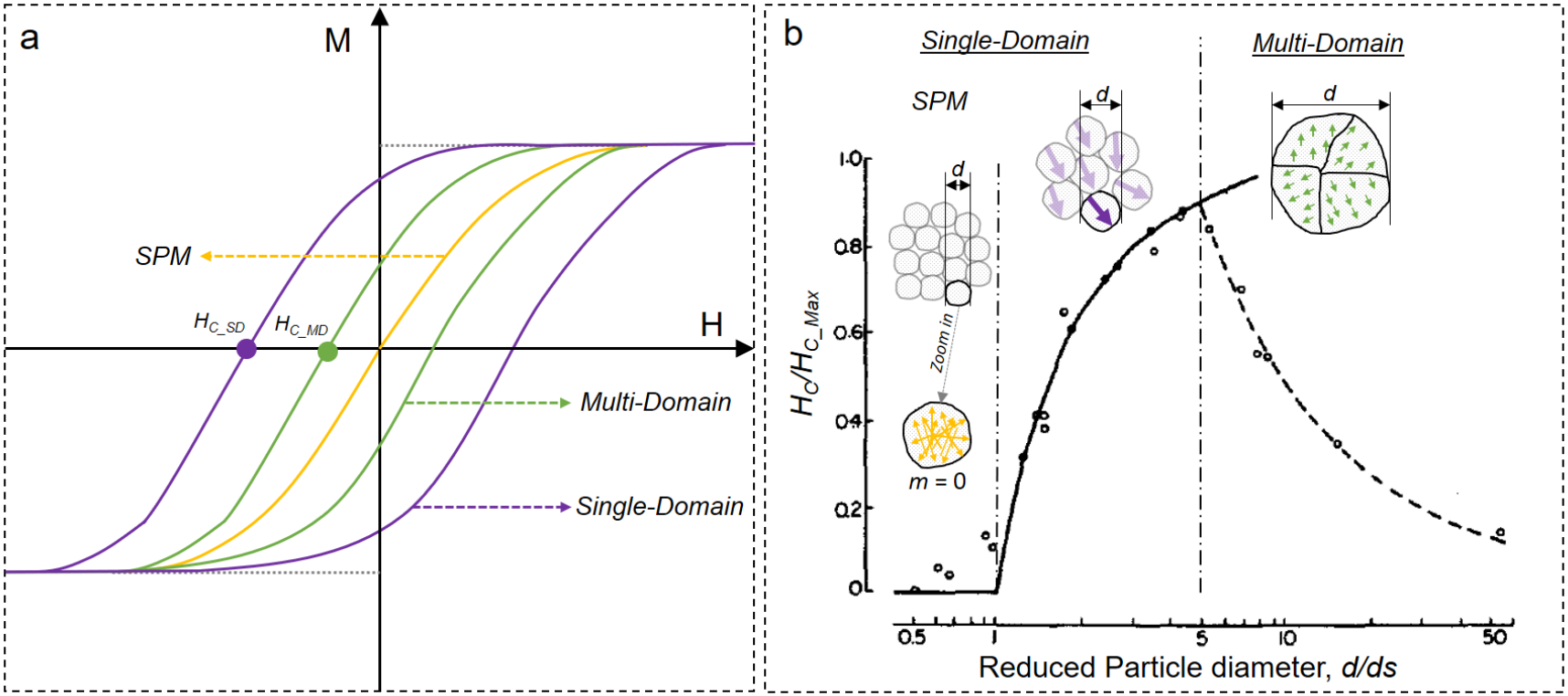

Figure 2.5: (a) M-H curves of a superparamagnet (SPM), single-domain and multi-domain ferromagnets. H_{C_SD}: the coercivity of the single-domain ferromagnet. H_{C_MD}: the coercivity of the multi-domain ferromagnet. (b) Measurement of spherical iron particles at 207 K in different diameters of particles. H_C: coercivity. d: diameter of particles. d_S: the critical diameter of particles, below which it becomes a superparamagnet. m: net magnetic moment. Adapted from [47]. Note that, in addition to size dependence, the SPM is also frequency dependent. A material behaves like a SPM is only because its relaxation is so fast that the hysteresis effect is not observed. If an field oscillates quicker than the relaxation of magnetic moments, then the hysteresis effect would be observed again; that is, in this case, the material behaves like a ferromagnet.

2.2.5 Magnetic Relaxation Heating

For ferromagnets, hysteresis loss can be easily quantified, as the hysteresis loop area is measurable. In contrast, for superparamagnets, since the hysteresis loop is unobservable, its energy loss cannot be quantified through the same method. As a consequence, Rosensweig proposes another method for quantifying energy loss in superparamagnets during relaxation and has been widely adopted in the literature. [48]. The result of which is often referred to as relaxation loss or relaxation heating. The relaxation loss are due to the lagging of magnetisation. Even though it is not seen on a M-H graph, it is reasonable to assume that the induced magnetisation, $M(t)$, has a finite time delay to the alternating applied field, $H(t)$. Consider this lagging and assume the phase lag is θ. Assume that $H(t)$ is a sinusoidal signal; let's say $H(t) = H_0 cos(\omega t) = Re\{H_0 e^{j\omega t)}\}$, in which the t is time, the H_0 is its amplitude and the ω is its angular frequency; then the Eq. 2.7 can be rewritten as:

$$M(t) = \chi_0 Re\{H_0 e^{j\omega t}\ e^{-j\theta}\} \tag{2.11}$$

Note that, the Eq. 2.11 is correct only when the fundamental assumption is considered. The fundamental assumption here is that the magnetisation is in its linear region. Only if the magnetisation responses linearly to the AMF, then its signal would also be as a sinusoidal signal like the AMF. To be more specific, the field intensity of the applied field should be small enough to keep the magnetisation in its linear region.

Now, let us expand the Euler's formula of Eq. 2.11, and the equation becomes:

$$M(t) = Re\{\chi_0(cos\theta - jsin\theta)H_0(cos\omega t + jsin\omega t)\} \tag{2.12}$$

In which, θ represents the phase difference between $H(t)$ and $M(t)$. For the convenience, the term, $\chi(cos\theta - jsin\theta)$, is often referred to as $\chi' - j\chi''$ in the literature. Thus, the Eq. 2.12 becomes:

$$M(t) = \chi' H_0(cos\omega t) + \chi'' H_0(sin\omega t) \tag{2.13}$$

In this way, the real susceptibility, χ', is associated with the in-phase magnetisation, while the imaginary susceptibility, χ'', determines the quantity of out-of-phase magnetisation. The latter is the main source that accounted for the relaxation heating. Based on the Debye model, the power of relaxation heating is derived by

Rosensweig [48], written as [5] [6]:

$$P = \mu_0 \pi \chi'' f H^2 \tag{2.14}$$

The neat equation above indicates that only the out-of-phase magnetisation contributes to relaxation heating. Furthermore, the power of the relaxation heating is proportional to the frequency and square intensity of the applied field. In the same paper, Rosensweig interprets the relationship between the χ'' and the relaxation time, which can be concluded by the equation below:

$$\chi'' = \chi_0 sin\theta = \chi_0 \frac{2\pi f\tau}{1 + (2\pi f\tau)^2} \tag{2.15}$$

While the χ_0 means the static susceptibility, the τ is the overall relaxation time. This equation implies that when $2\pi f\tau$ equals to 1, the imaginary susceptibility is at its maximum, and thus has better heating performance. The relaxation time is dominated by the Néel relaxation (i.e. $\tau = \tau_N$) only when the MNPs are immobilised. However, MNPs are generally carried by a medium such as water. In the aqueous medium, the MNPs can freely rotate, which results in another mechanism known as Brownian relaxation. In addition to the thermal energy in the environment, the viscosity coefficient of the medium, η, and the hydrodynamic volume of the MNPs, V_H, are both essential factors to the Brownian relaxation. As a consequence, the Brownian relaxation time, τ_B, is expressed as [49]:

$$\tau_B = \frac{3\eta V_H}{K_B T} \tag{2.16}$$

Consider both the Brownian and Néel relaxation, the effective relaxation time, τ, in the Eq. 2.15, is then given by [48]:

$$\frac{1}{\tau} = \frac{1}{\tau_B} + \frac{1}{\tau_N} \tag{2.17}$$

So far, we have theoretically introduced the principle of relaxation heating. However, the heating depends on not only the internal factor, such as the mass of material, but also external factors, such as the properties of magnetic field. In order to compare the heating performance between materials from different laboratories, it is necessary

[5] This equation is only true for linear magnetisation. To meet the requirement, the field strength needs to be weak enough so that $M(t)$ has the same type of waveform of $H(t)$; that is, if $H(t)$ is a sinusoidal wave, $M(t)$ is a sinusoidal wave. The difference between the two is the phase delay.

[6] To the author's knowledge, there is a typo in the Eq.5 in [48]. The term before the integration should be: $\omega\mu_0 H_0^2 \chi''$ instead of $2\mu_0 H_0^2 \chi''$.

to standardise the heating power in order to compare all materials on the same page. Hence, the following section will continue to describe the quantification of heating performance.

2.2.6 Quantification of Heating Performance

The heating performance of MNPs are generally reported in the form of specific absorption rate (SAR), which is defined by the equation below:

$$SAR = P/m_{MNP} \tag{2.18}$$

In which, the rf and m_{MNP} represent the heating power (unit: watt) and unit mass of MNPs (unit: g) respectively. The heating power of superparamagnets is described in Eq. 2.14. The equation indicates that the heating power is proportional to the imaginary susceptibility of the material, which is dependent on its mass. Thus, the mass normalisation is essential for internally quantifying the heating performance of a material. From the same equation, one can see that the heating power is actually affected by other extrinsic factors such as the frequency (f) and intensity (H) of applied field. For the convenience of comparison, another parameter is suggested to represent the heating ability of an MNP suspension by [50]. The parameter is known as intrinsic loss power (ILP). Based on SAR, the ILP further considers the influence of applied field (note that the assumption of Eq. 2.14 should also be applied to the ILP calculation, i.e., Eq. 2.19; that is, the applied field should not be so large that the magnetisation responses to the field non-linearly). The definition of ILP is described as the equation:

$$ILP = SAR/fH^2 \tag{2.19}$$

In relation to the calculation method, based on a study by Wildeboer *et al.* [51], Resonant Circuits Limited developed a MATLAB script for the calculation of SAR and ILP, which can be found in [52]. This algorithm was adopted and a script in R has been built and applied in this study.

The above discussions have elaborated how MNPs are heated up in an external AMF and how one can quantifying the heat ability of a material. Factors such as susceptibility and relaxation time have also been interpreted. The above discussion is from the perspective of physicists. The next section will examine magnetic hyperther-

mia from the perspective of clinicians. That is, the safety concerns on the magnetic hyperthermia.

2.3 Safety Concerns

The magnetic hyperthermia consists of MNPs and an external AMF. For medical applications, it is essential to understand their potential risks to a patient.

2.3.1 Safety Concerns of Magnetic Field

In terms of the safety of the magnetic field, its risk is associated with the currents magnetically induced in a patient. The generation of currents is due to the eddy current effect: a conductor generates circular currents when exposed to an AMF. Because the tissue fluid is conductive, an eddy current may be induced in the area of tissues where exposed to the applied field. There are two concerns about the currents. The first concern is that the current may activate physiological effects, such as stimulation of peripheral nerves, skeletal or cardiac muscles, as discussed in Reilley's work [53]. The improper excitation can probably affect the rate of heart beating (arrhythmia) or even lead to death.

Another concern is the non-specific heating caused by the eddy currents, which is discussed in a study done by Atkinson et al. [54]. In their study, the power of eddy current heating per unit tissue for a cylinder body (e.g. arm or torso) is concluded to be an equation as below:

$$P_{eddy} = \sigma_t(\pi\mu_0)^2(Hf)^2r^2 \tag{2.20}$$

The σ_t and r respectively represent the conductivity and radius of the cylinder tissue. The experiments in the same study also suggested that maximum values of the intensity and frequency of the applied field that a patient can tolerate, which are: H = 35.8 A/m; f = 13.56 MHz. Later, Brezovich proposed to use their production as the safe limit for applying an AMF to human bodies [55]. Although this safe limit, $Hf < 4.85 \times 10^8 \mathrm{Am}^{-1}\mathrm{s}^{-1}$, has been widely used in many studies, this value is still an on-going debate. According to the Eq. 2.20, eddy current heating is also affected by other factors such as the radius of the applied tissue. Thus, Dutz and Hergt suggested a safe limit of $5 \times 10^9 \mathrm{Am}^{-1}\mathrm{s}^{-1}$ due to the smaller coil they applied [5]. Additionally, other tolerated values of applied fields were presented in studies lead by Andreas Jor-

dan [23] [56] [57] as well as the report by Matsumine *et al.* [58]. These safe limits are listed in Table 2.1. It is important to be aware that these Brezovich criteria are unsuitable to low-frequency fields because the field with a frequency lower than hundreds of kHz is likely to active the physiological effects mentioned previously (see the figure 3 in [3]).

The Part of A Body	Brezovich Criterion ($Am^{-1}s^{-1}$)	Ref.
Thoracic Region	4.85×10^8	Atkinson *et al.* [54]
Pelvic Region	5.0×10^8	Johannsen *et al.* [57]
Pelvic Region	6.0×10^8	Wust *et al.* [23]
Thoracic Region	7.5×10^8	Wust *et al.* [23]
Head	13.5×10^8	Maier-Hauff *et al.* [56]
Leg	23.9×10^8	Matsumine *et al.* [58]
-	5.0×10^9	Dutz and Hergt [5]

Table 2.1: Safe limits for the intensity and frequency of an applied magnetic field to a patient.

2.3.2 Dose Limitation of Magnetic Nanoparticles

The toxicity of MNPs is likely to depend on its coating, but the detailed discussion on which is beyond the scope of this thesis. Although the coating of MNPs is an essential research topic, its issues would usually be tackled with by MNP manufacturers. As an end user, clinicians would be more concerned with dose limits.

About a decade ago, the maximal dosage of the MNP was carefully suggested to be between 5 mg_{Fe} and 10 mg_{Fe} per cm^3 of tissues in general [44]. Over the past decade, with the results reported in the emerging clinical studies, researchers have had a chance to further refine that suggestion. Based on the administration method, Southern and Pankhurst suggested two dosage limitations [59]. For intravenous injection, the dose should not exceed 8.5 mg_{Fe} per kg of a human. For intratumoural injection, the dose is suggested to be up to 40 mg_{Fe} per cm^3 of tissues. Since the *in-vivo* studies presented in this thesis are based on pre-clinical models (see Chapter 4), the following discussion illustrates how to define pre-clinical dosage limits based on recommendations from Southern and Pankhurst.

The dose limitation of the intravenous injection is mainly restricted by the metabolic

system. The higher the metabolic rate, the higher the dose that the organism can withstand. Interestingly, the metabolic rate is inversely proportional to the size of an organism [60]. Small organisms have larger surface to volume ratio. The volume of an organism decides its heat capacity, i.e., its ability to store heat, while the surface area decides the rate of heat dissipation from the organism to the surroundings. An organism's volume is like the size of a tank that filled with water, and its surface area is like the area of the hole at the bottom of the tank; thus, the surface to volume ratio indicates the ability of the tank to keep water. It is, however, an imbalance system. To balance it, one needs to open the tap above and let the water fill the tank. For the thermal homeostasis of an organism, the tap is like the heat source, and the biological heat is generated through the metabolic process. Overall, because of high surface to volume ratio, small organisms have low ability to retain heat; hence, their metabolic rate is high for the purpose of regulating body temperature. The comparably high metabolic rate in pre-clinical models such as mice allows them to stand with higher dose, which has led the US Food and Drug Administration (FDA) to recommend a dose conversion rate of approximately 12.3 between mice and humans. This implies that the aforementioned dose limitation for a human when injected intravenously, i.e., 8.5 $\mathrm{mg_{Fe}/kg}$ (single dose), can now be converted to 104.6 $\mathrm{mg_{Fe}/kg}$ (single dose) for a mouse. Provided that the weight of a mouse is 0.020 kg, then the maximum amount of iron that allows to be injected intravenously would be 2.09 $\mathrm{mg_{Fe}}$.

The discussion about intravenous doses is fairly straightforward. Nevertheless, it is not the case for the intratumoural doses. Provide that the upper limit of the intratumoural dose the tissues can withstand is 40 $\mathrm{mg_{Fe}/cm^3_{tissue}}$, there is still a need to find out the upper limits of the concentration and volume at which the MNP suspension can be applied.

To address this, two factors should be taken into consideration. One is the diffusion rate, which indicates the phenomenon that the MNP suspension is dispersed at the target site after injection. The other is the retention rate. The retention rate is important because not all MNPs remains at the target site; instead, some MNPs are carried away from the target site through the body's circulation system. Once MNPs enter in the circulation system, one should take the intravenous dose limitation into consideration. These two factors respectively determine the upper limits of the **concentration** and the **mass** of MNPs for intratumoural injection.

Let us elaborate effects of these two factors with an example. On the one hand,

if the diffusion rate is 3, then the density of MNP in the tissue will be one-third of the concentration of MNP suspension after injection. That is, say the dose limit is 40 mg_{Fe}/cm^3_{tissue}, the diffusion rate of 3 makes the **maximum acceptable concentration** of the MNP suspension to be 120 mg_{Fe}/ml. On the other hand, since only a part of MNPs remains at the injection site, it is necessary to consider whether the amount of MNPs entering the bloodstream exceeds the intravenous dose limits, i.e., 104.6 mg_{Fe}/kg for mice model. As a consequence, a formula has been suggested in [59] for calculating the intratumoural injected dose limit:

$$D_{max} = (F \times D_0)/(1 - R) \tag{2.21}$$

In which, D_0 is the maximum intravenous dose limit, i.e., 104.6 mg_{Fe}/kg for a mouse, the R is the retention rate, and F is the factor of maximum allowable systemic dose. For instance, if there are 50 % of MNPs retained at the injection site and the allowable systemic dose is 80 % of the maximum intravenous dose limit, then the R and F would be 0.5 and 0.8. Hence, for mice model with an adequate retention rate ($R = 0.5$) and good systemic tolerance ($F = 0.8$), the intratumoural injection dose limit D_{max} becomes 167.73 mg_{Fe}/kg. Hence, the mass limit of MNPs is 3.35 mg_{Fe} for a 0.020 kg mouse.

When performing either clinical or pre-clinical studies, the upper limits of concentration and the mass of MNPs should both be taken into consideration. More discussion on dose limits can be found in Chapter 4.

Apart from the aforementioned safety concerns, i.e., the concern of dosage and field parameters, another critical parameter a clinician needs to be extremely careful about is the temperature elevation during the magnetic hyperthermia. Thus, how to measure the change in temperature is essential, and two remote sensing methods applied in this study will be reviewed in the following section.

2.4 Current Methods for Remote Monitoring of Temperature

2.4.1 Infra-red Thermometry

As described earlier, one of the main issues on thermal management in magnetic hyperthermia is the thermometry. The current gold standard is invasively placing optic

thermometers into a target tumour for sensing. This point measurement, however, depends on the accurate placement of thermal probes, which is difficult and thus the reading can be unreliable. As a result, emerging studies began to use infra-red thermometry as the temperature sensing method for hyperthermia studies. This is mainly because this non-invasive thermometry can simultaneously detect the temperature at multiple points, which gives researchers a broader picture of the situation.

Infra-red radiation is one of the 3 forms of heat transfer. That is, any object with the temperature above 0K would emits infra-red radiations to some extent. An infra-red thermal imaging camera measures the temperature by detecting the infra-red radiation emits from an object. A thermal camera passively receives these infra-red radiations and converted them to temperatures based on the power of those radiations.

It will be interesting to review the features of infra-red here. The infra-red does not have a good ability to penetrate a subject, but in some scenarios, it is used to penetrate skins or even a skull to detect the biological activities inside a human body (e.g., functional near infrared spectroscopy for detecting brain activity). In these scenarios, they often required to emit a powerful an infra-red light to the target.

For example, the study given by Henderson et al. indicates that, for a near infra-red[7] with power of 15 W, it can penetrates the tissues to up to 3 cm. However, it also indicates that for a low energy level near infra-red light, it failed to penetrate a 2 mm skin [61]. Another example of emitting an infra-red to a target in a clinical scenario is called biogenetic radiation. Biogenetic radiation is a therapeutic modality that involves a procedure of letting the patient exposing to a far infra-red (The far infra-red refers to the infra-red with wavelengths between 3 mum and 100 mum.), which is normally generated by a powerful heat lamp. According to Vatansever et al., the penetration depth of a far infra-red to skin is up to 4 cm [62].

It will be useful to understand more about the infra-red, but because a thermal imaging camera only detects the infra-red naturally emits from an object, the penetration depth of an infra-red would not be a great concern here. In the scenario of magnetic hyperthermia, the heat source is underneath the skin and tissue. The heat transfer between the heat source and skin would be dominated by the heat conduction. What a thermal image camera detect is the infra-red emitted from the skin. Thus, an infra-red thermal camera can only detect the surface temperature.

Although it has an inherent limitation that it can only measure the surface temper-

[7]The near infra-red refers to the infra-red with wavelengths between 0.7 mum and 1.4 mum.

ature, it is still a powerful tool. Infra-red thermometry may not be suitable for monitoring the temperature of deep-seated tumours, such as prostate cancer and glioblastoma. But in most cases, the tumour is subcutaneously cultured in a pre-clinical model. Thus, the infra-red thermometry can be a ideal tool to detect the change in temperature in pre-clinical studies. *In-vivo* pre-clinical studies by Rodrigues et al. showed that the difference between the thermographic reading and the reading of the fibre optic probe inserted into the centre of the tumour was within 5 % [14]. Later, they reported an experimental configuration and a numerical model to further improve the precision [63]. Similarly, Padilla-Valverde et al. applied the infra-red thermometry to evaluate the temperature homogeneity during the procedure of the chemotherapy combined with hyperthermia on murine models [64]. This thesis utilized the infra-red thermometry to sense the temperature of phantoms *in-vitro*. Because the temperature of a phantom is more controllable than that of an actual organism, the *in-vitro* study provided us with a chance to evaluate the infra-red thermometry (see Chapter 3). Thereafter, the infra-red thermometry was used in pre-clinical studies to analyse the effect of particle diffusion on temperature distribution and the biological effect of heat, i.e., a comparison between HSP70 and CEM43 (see the Chapter 4).

Because of the inherent disadvantage, infra-red thermometry may only be suitable for pre-clinical studies. For clinical research, another thermometry that is able to sense the temperature of deep-seated tumour is still required. As a result, a novel magnetic particle thermometry has been proposed in this thesis, which will be further elaborated in Chapter 5. Prior to this, the next section will first review the associated concepts of magnetic particle thermometry.

2.4.2 Magnetic Particle Thermometry

Overall, the magnetic particle thermometry is a technique that detects the average temperature of a target at a distance. That is, with an appropriate configuration, the average temperature of a magnetically heated tumour can be detected.

In 2009, by coupling the temperature of MNPs into the ratio of the amplitudes of magnetisation harmonics, Weaver et al. described a technique for remote monitoring of temperature [65]. In this method, MNPs are regarded as thermal probes. There are different terminologies used to describe the similar technique in the literature. For the consistency, this thesis uses the term, magnetic particle thermometry (MPT), to

describe the technique that uses MNPs as thermal probes to monitor the temperature. Since Weaver et al. proposed the MPT, there is an increasing attention given to this technique. Apart from the progress made by Weaver and his colleagues [66–73], Zhong and his colleagues have started to investigate MPT since 2012 [74–78]. Because both MPTs are based on the Langevin equation, the operating frequencies of the two techniques are preferably as low as a few hundred Hz. These frequencies may be too low for magnetic hyperthermia, as the heating power generated in the MNP is proportional to the field frequency (see Eq. 2.14). Accordingly, Garaio et al. reported another MPT in 2015, which operates at the frequency used in magnetic hyperthermia, i.e., between 75 kHz and 1MHz. Garaio et al.'s MPT is based on the shifts in the phases of magnetisation harmonics, which was interpreted to be associated with the temperature dependence of SAR [79]. The theoretical bases, the devices and the methods used in these three MPTs are further briefed in the paragraphs below.

The MNPs used in Weaver et al.'s and Zhong et.al.'s MPTs are superparamagnetic. Both groups adopt the Langevin equation as their theoretical basis; hence, the frequency of the applied AMF is preferred to be lower than few kHz. The Langevin equation was first proposed to describe the paramagnetism. To deploy the same equation to describe the superparamagnetism, one should ensure that the magnetisation of the material is equilibrium all the time during the measurement. The equilibrium of magnetisation is very much dependent on measurement frequency. To achieve the equilibrium, the relaxation of magnetic dipoles in the material should be completed much faster than the measurement frequency; otherwise, undesired errors will occur because the Langevin equation fails to describe the phenomena. After all, the Langevin equation does not describe the dynamic status, i.e., the hysteresis effect, during the relaxation process. To avoid this relaxation error, both Weaver et al. and Zhong et al. used an AMF with frequency lower than few tens of kHz. Although the low magnetic frequency may not be an issue in many applications, the low magnetic frequency can limit the heat generated in MNPs during the magnetic hyperthermia. This issue was tackled to some extent by Garaio et al. In 2015, they reported another MPT based on the ratio of shifts in magnetisation phases [79], of which the phenomenon was interpreted to be associated with the temperature dependence of SAR (specific absorption rate) [80]. The operation frequency used in that study was between 75 kHz and 1030 kHz, which covers the most operation frequency range of magnetic hyperthermia.

Interestingly, the devices used in the aforementioned MPTs are fundamentally

identical. The only difference is how they withdraw the temperature information from the detected signal. All the MPTs are based on the change in magnetisation of the material, and thus the configurations of those MPT devices are similar to an AC magnetometer.

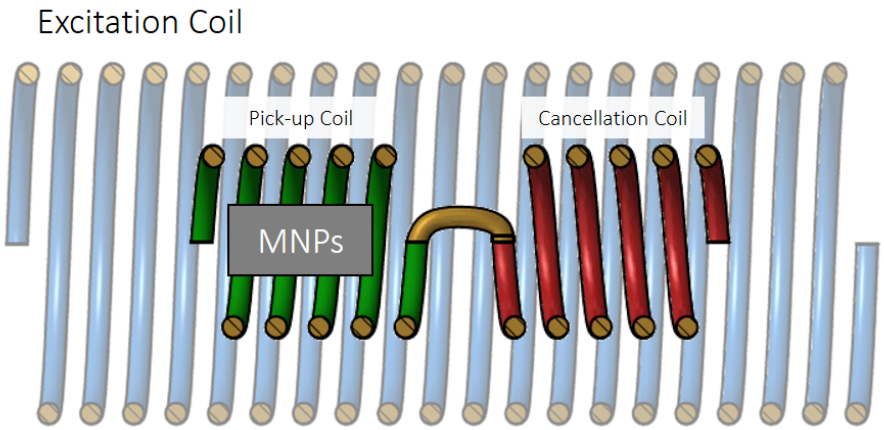

Figure 2.6: The schematic diagram of an AC magnetometer (the figure is prepared by the author).

The schematic diagram of an AC magnetometer is shown in Fig. 2.6. An AC magnetometer consists of an excitation coil and two oppositely wounded coils. The latter two are respectively a pick-up coil and a cancellation coil. The excitation coil generate an AMF during a measurement, while both the pick-up coil and the cancellation coil are used together to detect the magnetisation of a sample. The principle of operation is that, in the absence of a sample, the induced current in the pick-up coil caused by the excitation field is simultaneously balanced with the current induced in the cancellation coil. In the presence of a sample, because of the magnetisation of the material, the induced current would not be evened to zero. That is, the residual current is only associated with the magnetisation. With a calibration, the residual current can be converted to the magnetisation. The AC magnetometer has been widely used to analyse the dynamic magnetic properties of a material in the literature.

In addition, this method for detecting magnetisation is also deployed in the novel imaging device, magnetic particle image (MPI). This imaging device, proposed by Gleich and Weizenecker in 2005, is like a complex version of AC magnetometer [81]. Apart from a set of detecting coils (i.e., pick-up and cancellation coils) like those used in AC magnetometer, an MPI device has another set of coils for building an inhomogeneous static magnetic field. This magnetic field in most regions is strong

enough to saturate the applied MNPs, but there is a region called Field Free Point (FFP) where the effective static magnetic field is zero. On the one hand, placing MNPs in the FFP is like placing MNPs in an AC magnetometer. When applying an excitation AMF, the time-varying magnetisation induced in MNPs can be picked up by the detecting coils, the signals of which are demonstrated in Fig. 2.7a. On the other hand, for those MNPs not in the FFP, they would be saturated by the strong static magnetic field; the relatively small excitation AMF would not be able to alter their magnetisation status much. Hence, no time-varying signal would be detected (see Fig. 2.7b). The FFP is one of the cores of MPI. During the process of MPI, MNPs would first be distributed in a target of interest. Then, the FFP would be steered across the whole volume of the target. Based on the spatial information from FFP and the magnetisation from detecting coils, the distribution of MNPs can be reconstructed or say imaged. Additionally, MPI is attractive mainly because of its high imaging sensitivity. At present, MPI can detect nanograms of iron per millimeter [82]. This high sensitivity is contributed by another core of MPI, the data analysis method. In MPI, the detected time-varying magnetisation would be further converted to frequency domain through Fourier transformation. Because the nonlinearity of magnetisation, the waveform of the magnetisation is not as sinusoidal as the waveform of the excitation AMF; hence, there are magnetisation harmonics. These harmonics can be seen in a frequency spectrum (see the graph on the bottom right in Fig 2.7a). Because the fundamental frequency of magnetisation is known, which is the same as the frequency of excitation AMF, the harmonic frequencies can easily be attained. Therefore, by using extremely narrow bandwidth filters, one can avoid noises and obtain the signal of each magnetisation harmonic, even though the value of which may be quite small [83]. This data analysis technique boosts the imaging sensitivity of MPI.

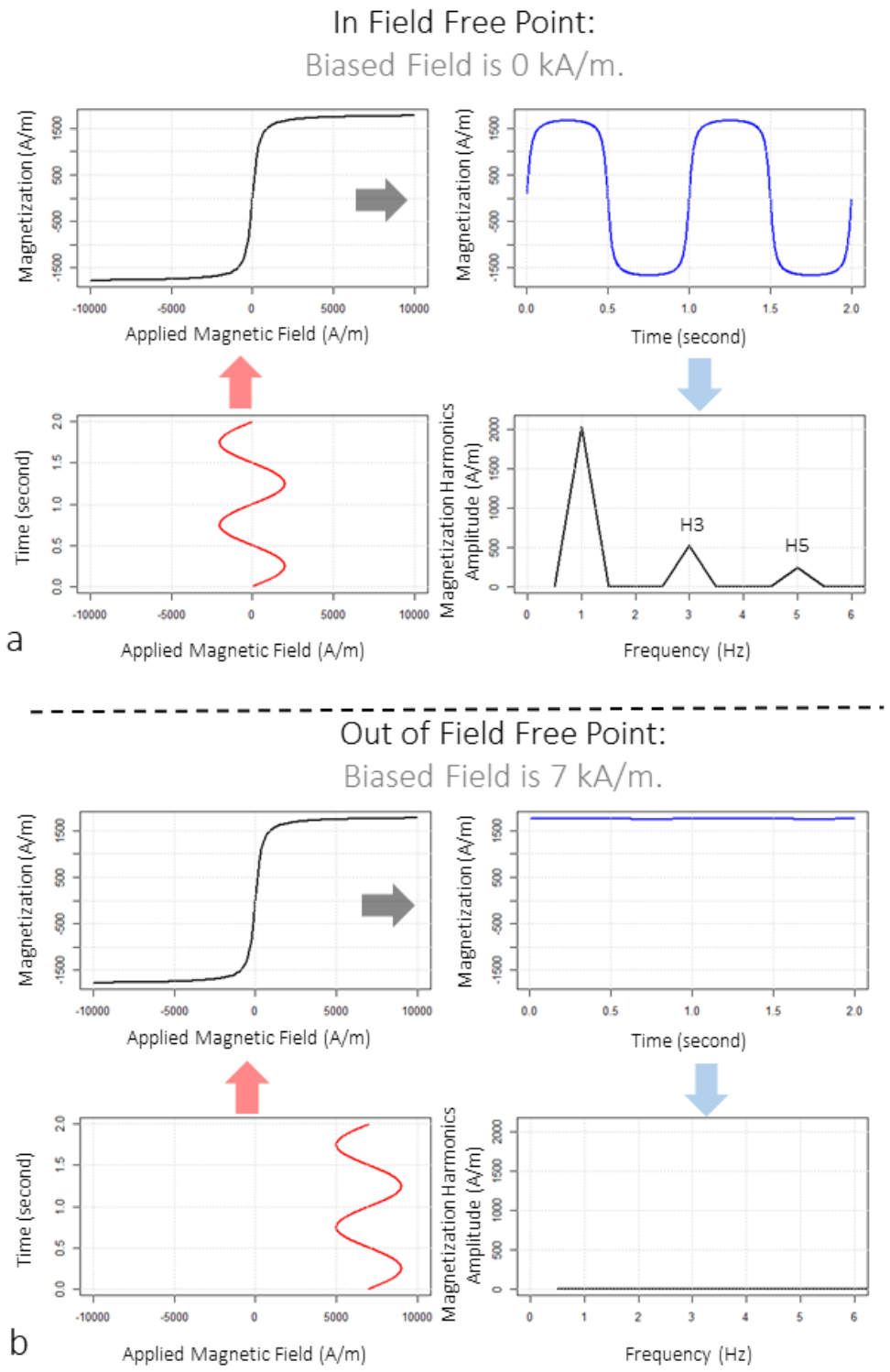

Figure 2.7: The signals in MPI. (a) The harmonics of magnetization would only appear in the Field Free Point. (b) No harmonics would be detected if the material is out of Field Free Point, in which region MNPs would already be saturated by the static magnetic field (the details of the simulation can be found in Appendix E).

Discussions on the principles of MPI is helpful for us to understand the MPT because the MPI is the predecessor of MPT. A year before Weaver et al. presented their MPT, they published a paper studying the effect of an additional bias field on MPI signals [83]. In which, they pointed out that the MPI signals are sensitive to the temperature of MNPs. This temperature dependence might be an issue in MPI but could also be an opportunity for a new thermometry. Weaver et al. noticed the potential and published another paper shortly after [83], in which they elaborated the temperature dependence of magnetisation with the Langevin equation [65]. The magnetisation M of superparamagnetic MNPs when exposing to an excitation field with the intensity of $H_0 cos(\omega t)$ can be expressed as:

$$M = \xi M_0 (coth(A_L) - (A_L)^{-1}) \tag{2.22}$$

in which,

$$\xi = \frac{n\nu}{V} \tag{2.23}$$

and

$$A_L = \frac{\nu M_0 H_0 cos(\omega t)}{4\pi K_B T_{MNP}} \tag{2.24}$$

where ξ is the volumetric concentration, A_L is the amplitude of Langevin equation, n is the number of MNPs, ν is the volume of each particle, M_0 is the bulk saturation magnetic moment per unit volume, V is the overall volume of the sample, H_0 and ω are the amplitude and the angular frequency of the excitation AMF, t is time, K_B is the Boltzmann constant and T_{MNP} is the absolute temperature of MNPs.

Although the amplitude of each magnetisation harmonic is different, Weaver et al. presumed that each harmonic amplitude varies proportionally with the change in magnetisation M. Interestingly, once the material and the concentration of the sample are determined, most variables in above equations are dependent variables. Only H_0 and T_{MNP} are independent variables. In short, not only the M but also the amplitudes of the harmonics are dependent on the ratio of H_0/T_{MNP}. Based on this dependence, Weaver et al. cleverly characterised the MNPs by recording the harmonic amplitudes when a variety of H_0 was applied to MNPs at a known and constant T_{MNP}. By doing so, a characterised curve is attained [8]. The characterised curve is depicted in Fig. 2.8. The X-axis and Y-axis of the characterised curve are the ratio H_0/T_{MNP}

[8] M_0 is assumed to be temperature independent here; the detailed discussion on the temperature dependence of M_0 can be found in [65].

and the amplitude of harmonic magnetisation respectively.

On the one hand, when characterising MNPs, a variety of H_0 is used, but the temperature of MNPs is a constant. On the other hand, when deploying the characterized curves in the MPT, a constant H_0 would be used. By fitting the detected harmonic amplitude to the characterized curve, the ratio of H_0/T_{MNP} can be determined and thus the T_{MNP} can be estimated since the H_0 is known. In theory, the characterized curve of a single harmonic amplitude can fulfil the purpose of temperature sensing. However, if one takes a closer look at Eq. 2.22, one can find that the magnetisation depends on not only the ratio of H_0/T_{MNP} but also the amount of MNPs n. To eliminate the effect of n, Weaver et al. further divided the characterized curve of 5th harmonic by that of 3rd harmonic. This additional step makes their MPT become independent of iron content. In short, the MPT proposed by Weaver et al. is based on the temperature dependent non-linearity of magnetisation. The temperature of this MPT is estimated based on the ratio of 5th and 3rd harmonics, as presented in Fig. 2.9.

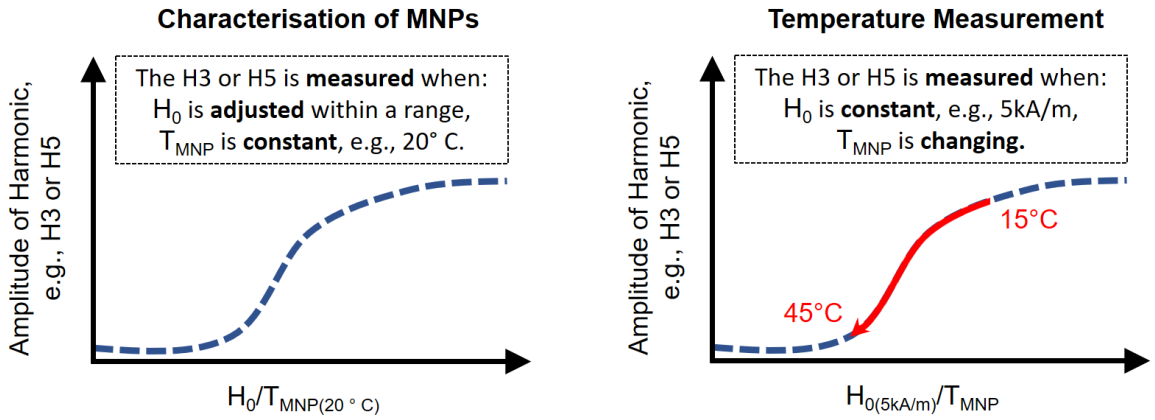

Figure 2.8: The characterised curve of Weaver et al.'s magnetic particle thermometry. The graph on the left hand side describes the conditions when characterising a magnetic material, while the graph on the right hand side describes the conditions during temperature measurement. H3 and H5 represent the amplitudes of the 3rd and the 5th harmonics.

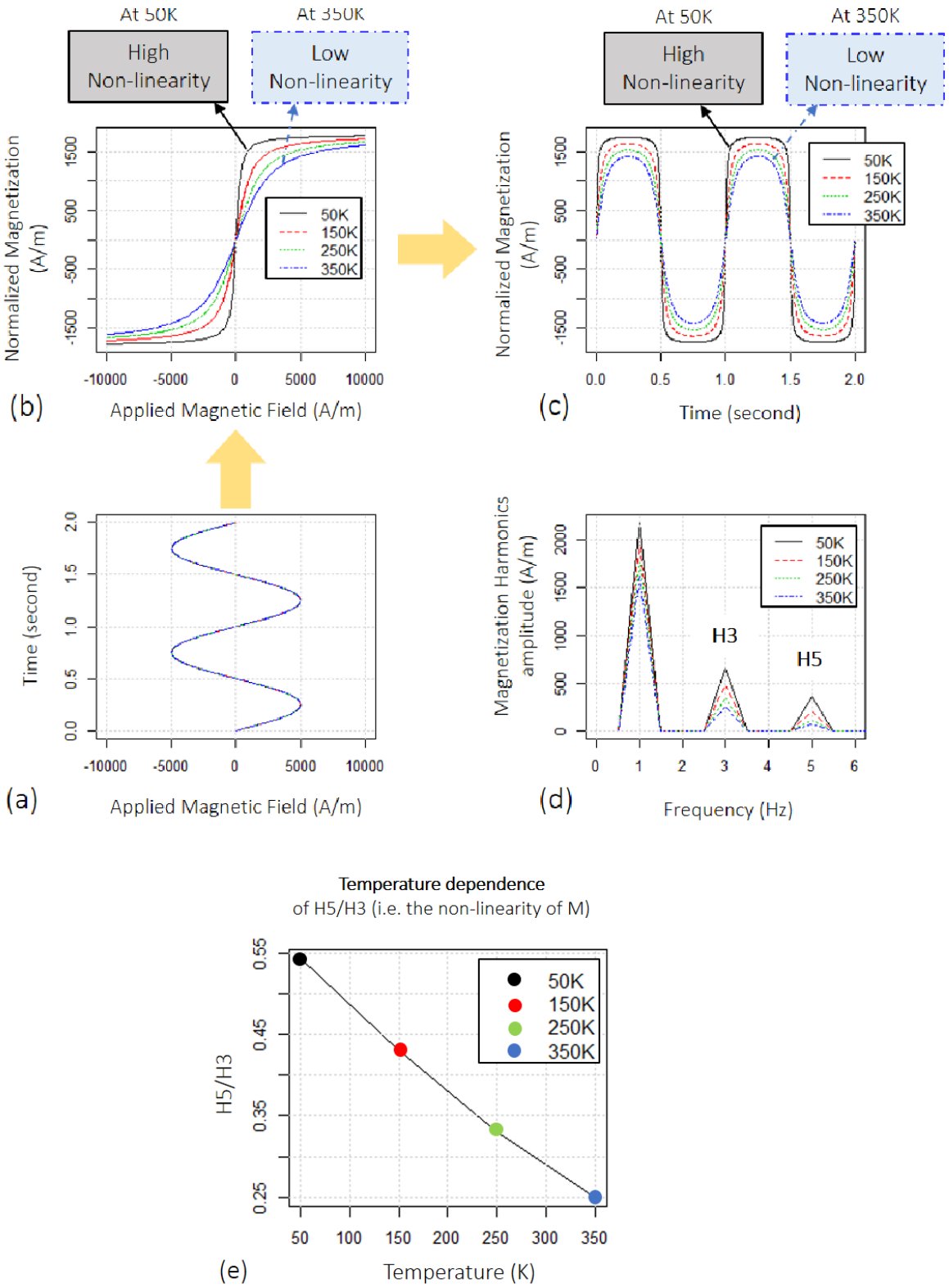

Figure 2.9: The temperature dependence of non-linearity of MH curves (see simulation details in Appendix E). (a) The field that applied to the magnetic material. The amplitude and the frequency of which are 2 kA/m and 1 Hz, respectively. (b) The MH curves of the magnetic material at temperatures ranges from 50 K to 350 K. (c) The simulated magnetisation of the magnetic material at different temperature. (d) The amplitude of magnetisation harmonics at different temperature. (e) The ration of 5th and 3rd harmonics of the magnetisation at different temperature. The higher the temperature, the smaller the ratio of H5 and H3.

Additionally, Fig. 2.9. presents another temperature dependence. One may notice that the initial susceptibility of MNPs, i.e., the initial slope of MH curve, decreases along with the increase in temperature. Zhong et al. interpreted this temperature dependence with the Langevin equation and used this phenomenon as the basis of their MPT [74]. If the applied field H_0 is weak enough, i.e., $coth(A_L) \approx coth(0)$, the Eq. 2.22 can be approximated by the first term of Taylor series and thus the volumetric susceptibility χ_0 for weak fields can be derived and it becomes:

$$\chi_0 \approx \frac{\xi M_0}{H_0 cos(\omega t)} \frac{A_L}{3} = \frac{n(\nu M_0)^2}{12\pi K_B T_{MNP} V} \tag{2.25}$$

This equation indicates that χ_0 is dependent on both n and T_{MNP} [9]. If one has enough information to solve the Eq. 2.25, one would be able to estimate both the amount and the temperature of MNPs, i.e., n and T_{MNP}. To fulfil the purpose, Zhong et al. deployed more than one term of Taylor series to approximate the Langevin equation. The higher order Taylor expansion shows that χ_0 depend on not only n and T_{MNP} but also H_0 [10]. Fortunately, H_0 is a known parameter and is controlled during the measuring process of MPT. By applying a variety of H_0 to MNPs, a series of χ_0 can be measured. Thereafter, by substituting the values of applied H_0 and measured χ_0 into the Taylor series of the Langevin equation, one would obtain an solvable overdetermined matrix equation. Thereby, the unknown parameters of n and T_{MNP} can be solved.

Despite Zhong et al. and Weaver et al. deploy similar devices and the same equation in their MPTs, it is interesting to note that the preferable operation frequencies are different. The operation frequencies of Zhong et al.'s and Weaver et al.'s MPTs are tens of Hz and tens of kHz respectively. The author infers that this result is due to the difference in their analytical methods. While Zhong et al. solve the theoretical equation to attain the temperature of MNPs, Weaver et al. attain the temperature based on characterisation. As a result, the preferable operation frequency of the former needs to be low to avoid the relaxation error, while the operation frequency of the latter can be higher as the relaxation error can be partially compensated by the empirical characterisation. It will be ideal if an AMF applicator can heat up MNPs and detect their temperature at the same time. However, the operation frequency of both MPTs above are too low for the heating purpose. In order to induce sufficient heat in MNPs, the magnetic hyperthermia usually requires an excitation AMF with

[9] Once again, the variation in M_0 is assumed to be ignorable here.

[10] For instance, the two order Taylor expansion is $\chi_0 \approx (\xi M_0 / H_0 cos(\omega t))(A_L/3 - A_L^3/45)$.

a frequency higher than hundreds of kHz, because the power dissipation of MNPs is proportional to the frequency of excitation field (see Eq. 2.14). This requirement makes Garaio et al.'s MPT more preferable in the scenario of magnetic hyperthermia since it can operate at as high as 1 MHz.

Garaio et al.'s MPT origins in their study on SAR measurement. While the AC magnetometer was used to measure the magnetisation and initial susceptibility by Weaver et al. and Zhong et al. respectively, Garaio et al. used it for measuring the SAR of MNPs [80]. In one of their reports, they pointed out that the SAR of a material is dependent on its temperature [84]. This phenomenon has also been described by other research groups [85] [86]. This phenomenon has become the foundation of another MPT proposed by Garaio et al. [79]. To understand the temperature dependence of SAR, one can substitute both Eq. 2.14 and Eq. 2.15 into Eq. 2.18 and obtain:

$$SAR = (\frac{\mu_0 \pi f H^2 \chi_0}{m_{MNP}}) sin\theta = (\frac{\mu_0 \pi f H^2 \chi_0}{m_{MNP}})(\frac{2\pi f \tau}{1 + (2\pi f \tau)^2}) \tag{2.26}$$

From one perspective, the above equation indicates that the SAR is a function of the relaxation time. Because the relaxation time is temperature dependent (see Eq. 2.10, Eq. 2.16 and Eq. 2.17), one can deduce that the SAR would vary with the temperature. From another perspective, the SAR is associated with the phase lag of magnetisation to the excitation field. That is, the phase lag of magnetisation varies with the temperature. Garaio et al. utilises this relation in their MPT, in which the phase shift of magnetisation was measured and converted to the temperature of MNPs after calibration. As the Langevin equation is not deployed in Garaio et al.'s MPT, it does not require to operate at low frequency.

In conclusion, MPT is a technique that converts the change in magnetic properties of MNPs to their temperature. Hence, the AC magnetometer is applied in current MPTs. Although the measurement devices are identical, their methods for withdrawing the information of temperature from the detected signal are different. While Weaver et al. quantify the temperature-dependent magnetisation with the non-linearity of MH curve, Zhong et al. and Garaio et al. derive the temperature from the initial susceptibility and the phase shift of magnetisation, respectively. The MPTs discussed above are ground-breaking, but they may not meet the requirement for magnetic hyperthermia. These MPTs require a different coil set from that used for applying hyperthermia. In the presence of the treatment field, large voltages tend

to be induced in the detecting coil. The large time-varying voltage can heat up the detecting coil very quickly and eventually damage the coil. Therefore, further research is still required. This study has made an effort to address this issue and a novel MPT has been proposed, which will be illustrated in Chapter 5.

Chapter 3

In-vitro Temperature Sensing with Infra-red Thermography

From the previous chapter, we have seen the theories of how heat kills cells and how heat is induced in MNP when exposed to an AMF. From this chapter towards to the end, discussions will be more practical. The objectives of following discussions are to understand, (1) the effect of particle distribution on thermal distribution during a magnetic hyperthermia, and (2) the feasibility of using an infra-red thermal camera to monitor a hyperthermia experiment.

To achieve these, *in-vitro* experiments on tissue-mimicking phantoms have been designed and performed. The phantoms were designed to simulate particle distribution. To be more specifically, the quantity of MNPs was controlled to be identical in each phantom, but its volume was varied from one case to another. The infra-red thermal camera was used throughout the experiment to monitor the thermal distribution on the surface of each phantom.

In contrast to a conventional thermometer, e.g., optic fibre thermometer, the infra-red thermal imaging is preferable because it can detect the temperature of multi-points on the phantom surface simultaneously.

This chapter is consist of 5 sections. The first section describes the phantom materials and the construction method. This is followed by another section that introduces the *in-vitro* experimental setup. The experimental results are presented, analysed and discussed in Section 3.3. In the discussion, the heating curves of phantoms are converted to a more clinically-related parameter, i.e., CEM43. Based on the values of CEM43, the treated area of each phantom are calculated. Then, at the end of this chapter, to evaluate the experimental results, FEA (Finite Element Analysis)

simulations have been conducted and compared to experimental results.

3.1 Phantom Construction

3.1.1 Materials of Phantom

Agarose

The material of phantom used in this study was agarose, which is a linear polymer derived from seaweeds. The fundamental unit of agarose is called agarobiose and its chemical formula is depicted in the Fig. 3.1. The agarose has an interesting property known as thermal hysteresis, which means that the agarose melts and gels at different temperatures. At about 100 °C, the agarose would start to melt and dissolve into water. Once the temperature drops to be lower than 45 °C, the linear polymers begin to cross-link to each other and thereby form helices, i.e., start to gel. The final status of the accumulation of helices determines the physical properties of agarose gel [87]. During the gelling process, holes are created among cross-linked helices. This porosity of agarose gel happens to resemble real tissues.

As a result, a water-based agarose gel is widely used in studies as a tissue-mimicking phantom. For example, the mixture of agarose and copper sulphate ($CuSO_4$) was successfully used as phantoms for the application of MRI. Because the relaxation time of protons can be adjusted by varying concentrations of agarose and copper sulphate, the MR images of different types of tissues can be simulated [88]. The dependence of mechanical properties on the concentration of agarose was presented in another report by Ross, *et al.* [89]. In their reports, the containers filled with agarose were rotated at different controlled speeds. These experiments indicate that the mechanical properties of agarose can be affected by mixing conditions, e.g., the rotating speed. As a tissue-mimicking phantom, agarose gels are common phantoms for studying the diffusion of suspension among tissues [90] [91].

More importantly, agarose gel is also used to mimic tissues in researches on hyperthermia, as reported in [92], [93], [94] and [95]. Because more than 95% of an agarose phantom consists of water, its thermal properties, i.e., thermal conductivity and specific heat capacity, are similar to water [93], which are 0.6 $\mathrm{W/m \cdot K}$ [96] and 4181 $\mathrm{J/kg \cdot K}$. The density of an agarose phantom is slightly higher than water, which was suggested to be 1070 $\mathrm{kg/m^3}$ in [97]. These properties are later used for the

simulation of thermal distribution on a phantom. (see Table 3.3).

Although agarose is widely used as a tissue mimicking phantom, because of the complex interactions among the blood flow, metabolic heat generation and non-uniform thermal conductivities of tissues, it is difficult to replicate the thermal conditions of real tissues by phantoms.

In other words, differences always exist between phantoms and real tissues. Despite the intrinsic differences, the work on a phantom is still essential because a phantom provides controllable and reproducible conditions, which helps to examine individual elements of magnetic hyperthermia.

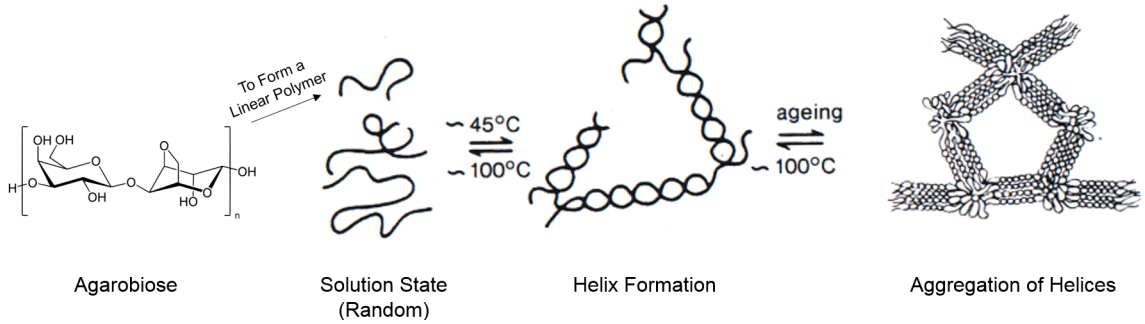

Figure 3.1: Gel formation of agarose (adapted from [98]).

In Gneveckow, *et al.*'s study, a phantom made up of agarose, $NaCl$ and $CuSO_4$ was used to calibrate an AMF applicator [99]. The addition of $NaCl$ is to mimic the electrical conductivity of tissues. Similarly, the agarose phantoms made in this study were also composed of these three ingredients. The concentrations of $NaCl$ and $CuSO4$ were 1.0 wt.% and 0.7 wt.%, respectively [100]. As to the concentration of agarose, to simulate a solid tissue like a prostate, 4.0 wt.% of agarose was used in the phantom fabrication. This formulation is listed in Table 3.1.

Weight Percentage (wt.%)		Function
Agarose	4.0	Porous Structure - Mechanical Property
$NaCl$	1.0	Electrical Conductivity
$CuSO_4$	0.7	Relaxation Time of Proton

Table 3.1: The formulation of agarose phantom for *in-vitro* experiments.

3.1.2 Process of Phantom Construction

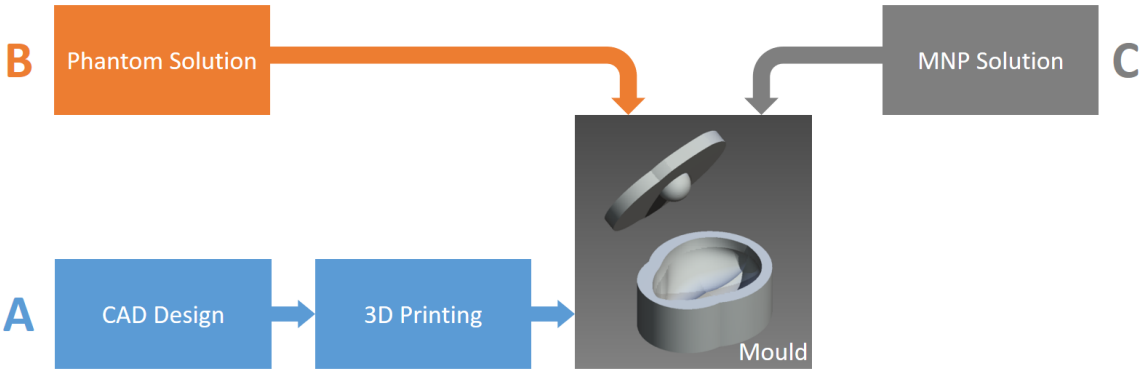

Figure 3.2: The process of phantom construction.

The process of phantom construction consists of 3 steps. As shown in the Fig. 3.2, they are, (A) the design of casting mould, (B) the preparation of phantom solution and (C) the preparation of MNP solution. The details of each step are described in the following subsections.

A. Design of casting mould

Because of the merit of minimal invasiveness, magnetic hyperthermia is beneficial to treat deep-seated cancers, such as prostate cancer. Thus, this study used the scenario of treating a prostate cancer as an example, and phantoms were made to become the anatomical shape of a prostate. Based on the real biological dimension, the width, length and height of the prostate phantom were designed to be 33 mm, 45 mm, and 35 mm, respectively (see Fig. 3.3a) [101].

For the convenience of observation, only a half prostate was made, so that the temperature distribution on the cross section could be recorded by a thermal image camera (the details of experimental setup can be seen in section 3.2).

The shape of a half prostate was then reversely engineered to define the shape of mould, which was later printed with ABS (acrylonitrile butadiene styrene) by a 3D printer. These tasks of mould design were done in the computer-aided design (CAD) environment, Autodesk Inventor (Autodesk Inc.,California, USA). The overall design process of casting mould is presented in Fig. 3.3b.

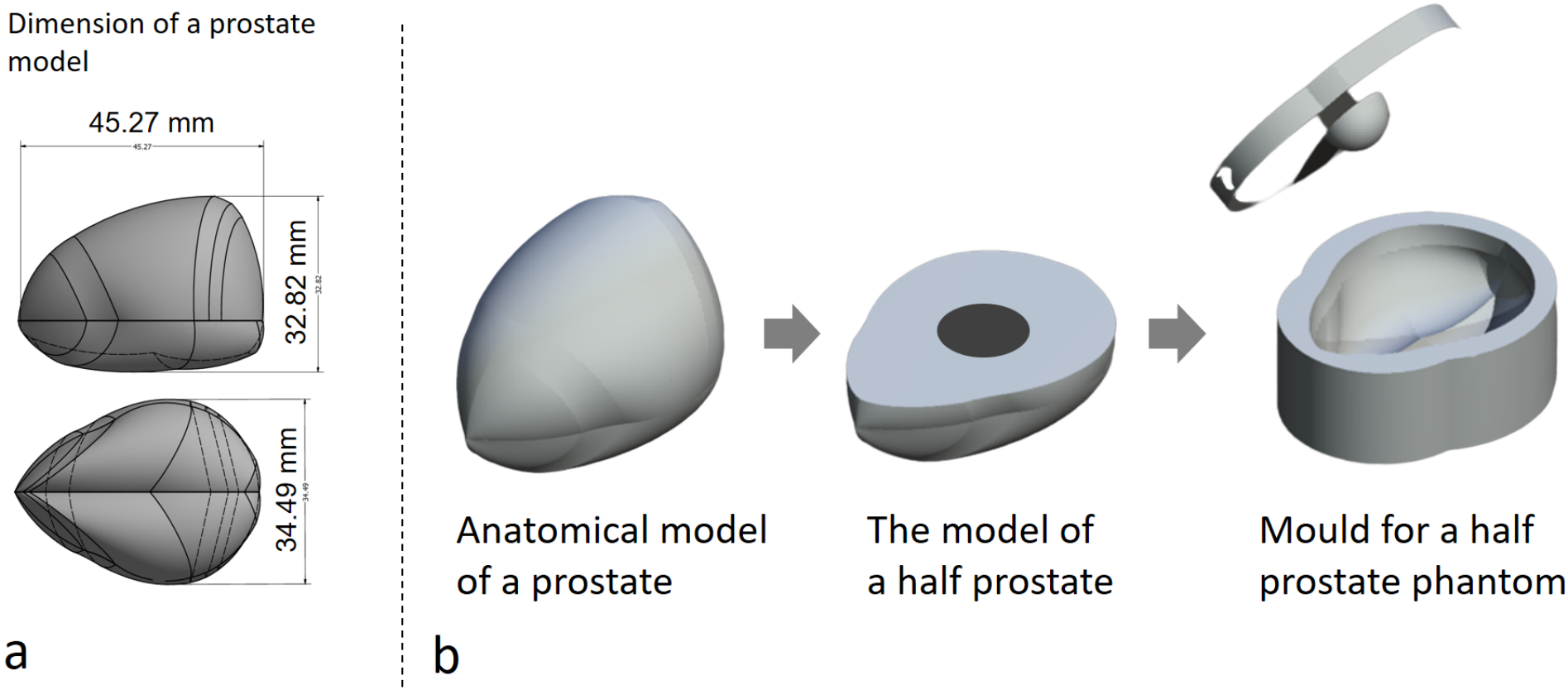

Figure 3.3: (a) The dimension of the prostate model designed in this study. (b) The design process of reverse engineering the prostate model to a mould.

B. Preparation of Phantom Solution

The phantom solution contained the ingredients listed in Table 3.1. As discussed in section 3.1.1, the agarose does not dissolve in water at room temperature, so the phantom solution was heated up to boiling by a laboratory-grade microwave oven. The heat melted the agarose powders, and thus the appearance of the phantom solution changed from cloudy to transparent.

After being heated by the microwave, the temperature of phantom solution was monitored by a mercury thermometer. This solution was not poured into the casting mould until its temperature dropped to be lower than 80 °C; otherwise, the plastic mould (made of ABS) would be deformed. In addition, the solution needed to be filled in the mould before it started to gel at 45 °C. Placing the mould filled with a phantom solution at room temperature for approximately 40 minutes (the settling time depends on the volume of the phantom), the polymers of agarose cross-linked and became a gel.

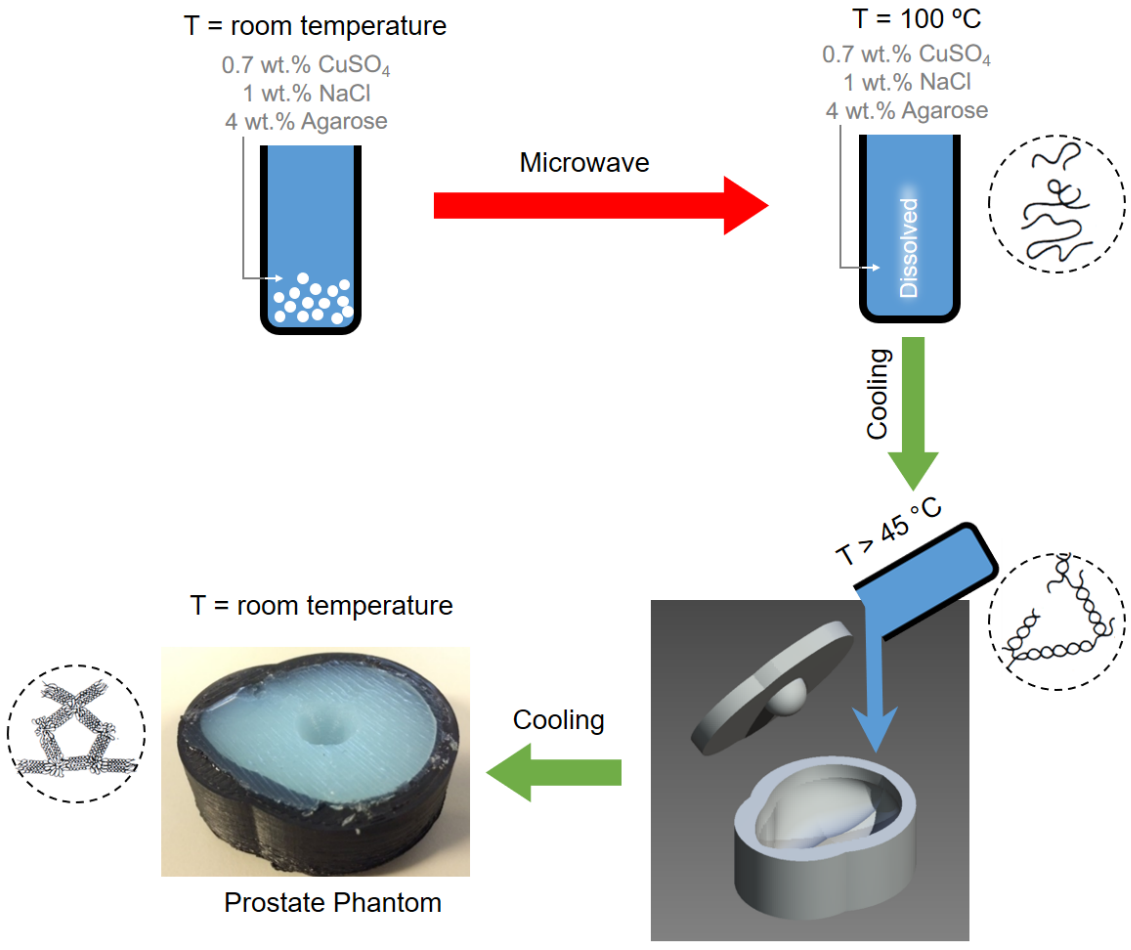

Figure 3.4: The process of manufacturing an agarose phantom.

C. Preparation of MNP Solution

Magnetic Nanoparticle The MNP suspension, Perimag®, was deployed in this study. It is a water-based MNP suspension, the core of which is magnetite. The size of Perimag® is 130 nm and it is coated with a layer of dextran. The ILP of Perimag® is 5.50 ± 0.3 $\mathrm{nHm^2kg^{-1}}$ and neat concentration is 20 $\mathrm{mg_{Fe}/ml}$ (see Table C.1).

Preparation Similar to the phantom solution, the MNP (Perimag®) solution was prepared by mixing MNP suspension with 4 % agarose powders. The MNP solution would also be heated to be nearly 100 °C by microwave for dissolving the agarose. Once the temperature of MNP solution cooled down to be a proper temperature, i.e., between 45 °C and 80 °C, the solution was poured into the hollow of the phantom (see Fig. 3.5). When the MNP solution became a gel, a phantom was completed.

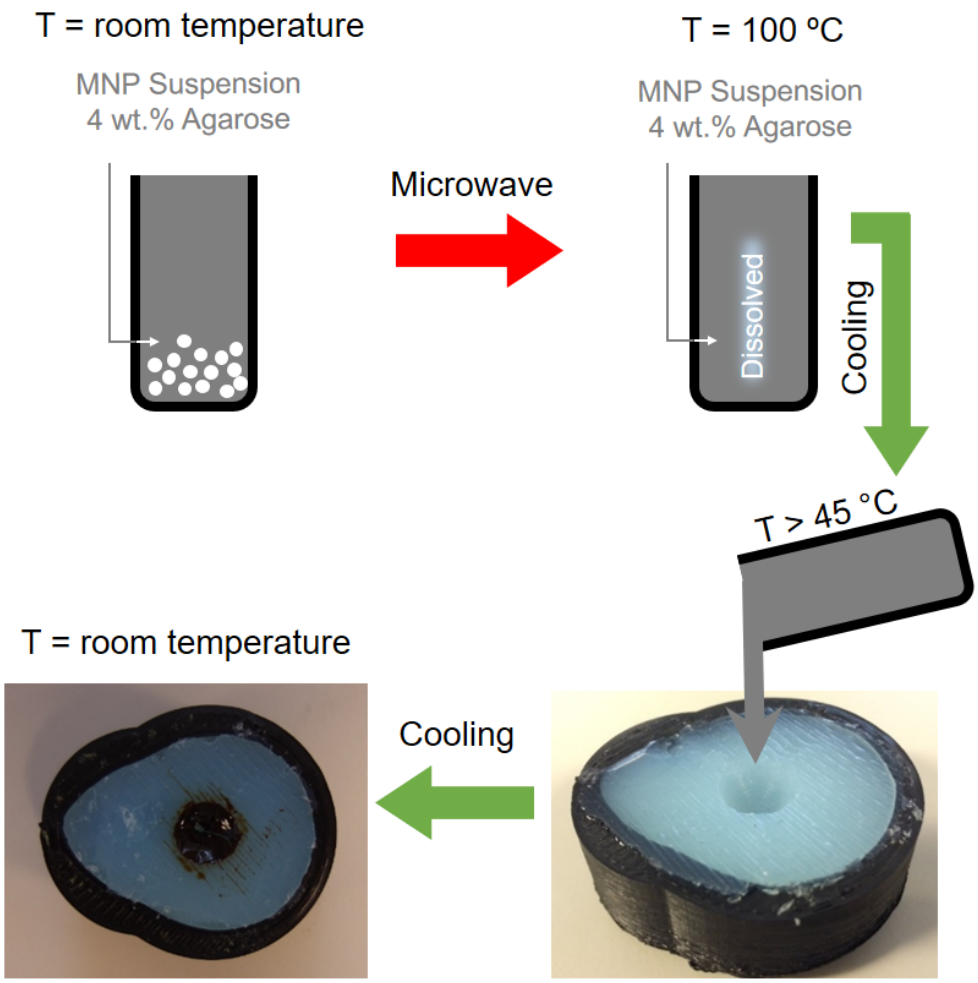

Figure 3.5: The process of manufacturing an MNP gel.

3.1.3 Handling of Phantom

There was another issue needed to be addressed before applying a phantom in an experiment. During the initial experiment, the author noted that the temperature of a phantom decreases over time, and it could not achieve thermal balance with its surroundings. To be more specific, the temperature of the phantom was always lower than the environmental temperature. In addition, a shrinkage in the phantom was observed. This might be because the water in the phantom was escaping from the phantom.

Hence, the phantom was wrapped with a cling film to prevent the evaporation, as shown in the Fig. 3.6a. Despite the simpleness, this method solved the problem. The other graph, Fig. 3.6b, indicates the temperature of the phantom in two situations. At the beginning, the phantom was covered with a cling film, so its temperature was able to thermally balance with the environment. Once the cling film was peeled off, its temperature began to decrease, even if the environmental temperature remained the same.

Through this handling of phantom, the phantom was ready for an experiment. The following section will further introduce how this phantom was used to help us understand the thermal distribution during a magnetic heating.

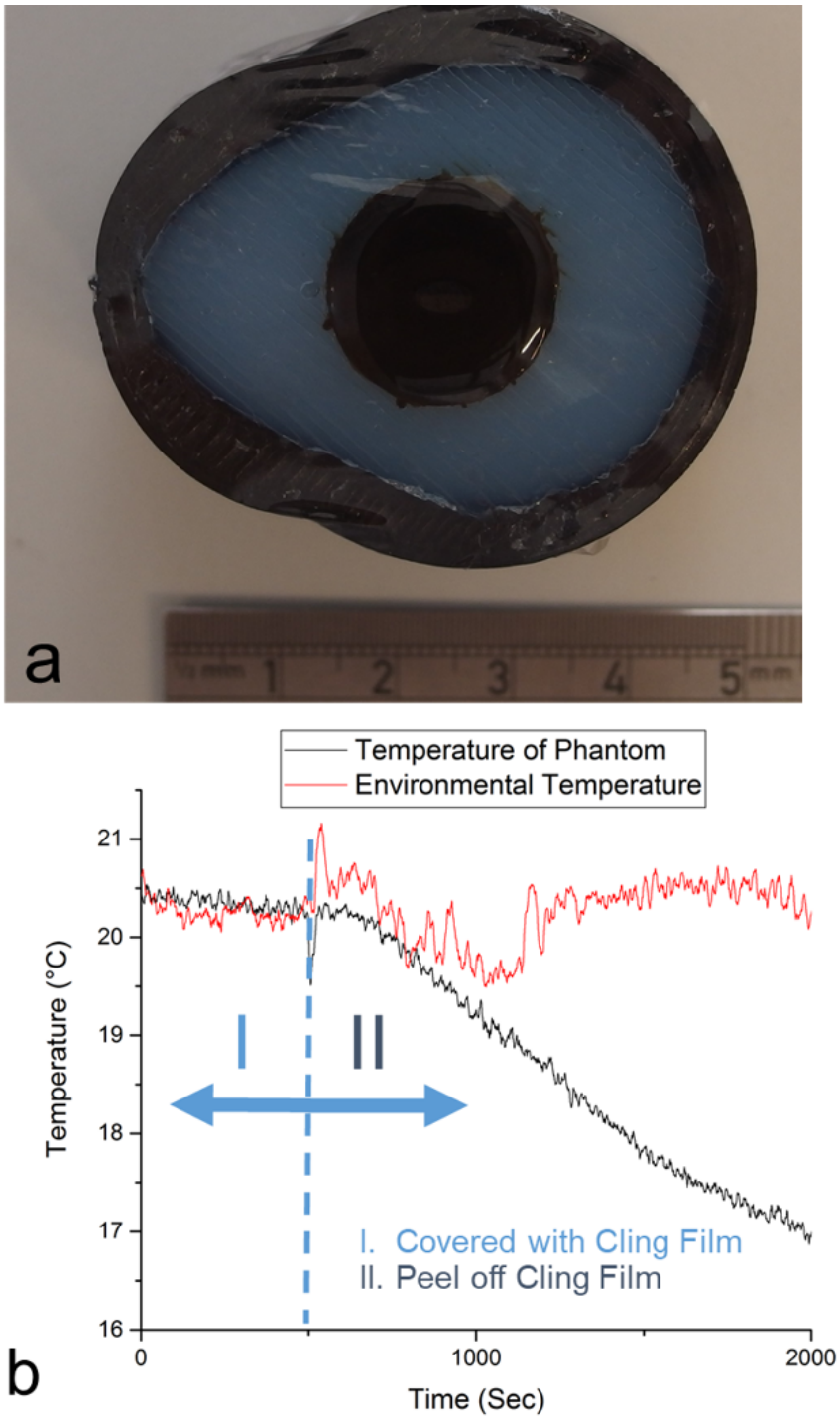

Figure 3.6: (a) A phantom covered with a cling film. (b) The temperature of a phantom compared with the environmental temperature at two periods: I. When the phantom was wrapped with a cling film, it thermally balanced with the environment. II. When the cling film was peeled off, the temperature of the phantom starts to drop due to the evaporation of water.

3.2 Experimental Setup

To simulate the thermal distribution during a magnetic hyperthermia, apart from the prostate phantom made of agarose, we would also need an AMF generator and a temperature recording device, i.e., a thermal imaging camera. In addition, to simulate the biological thermal environment, the author developed a simulation chamber to create a thermal environment as inside a human body (a revised version of the simulation chamber presented in Fig. 1.3).

Overall, the picture of the experimental Setup is presented in Fig. 3.7, and the block diagram of which is depicted in Fig. 3.8. The details of each equipment in this setup are described as below.

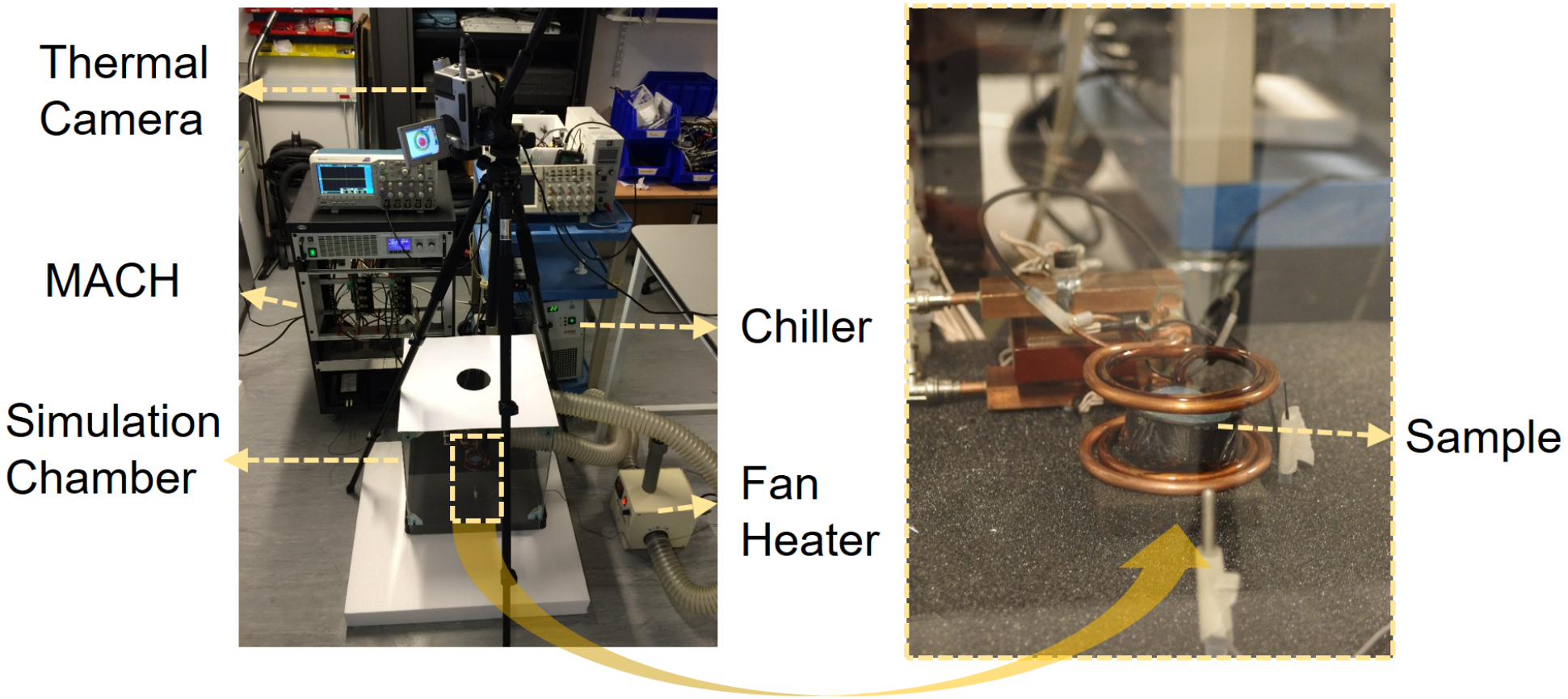

Figure 3.7: The setup for *in-vitro* experiments. This experimental setup includes a infra-red thermal camera, a field generator, i.e., MACH and a bespoke-built simulation chamber. Additionally, a chiller is used to prevent the coil from being overheated, and a fan heater is used to maintain the temperature within the simulation chamber to be at the biological temperature, i.e., 37 °C. The MACH pre-clinical coil is used in this experiment, the field distribution and the geometry of the coil have be illustrated in Fig. 1.2.

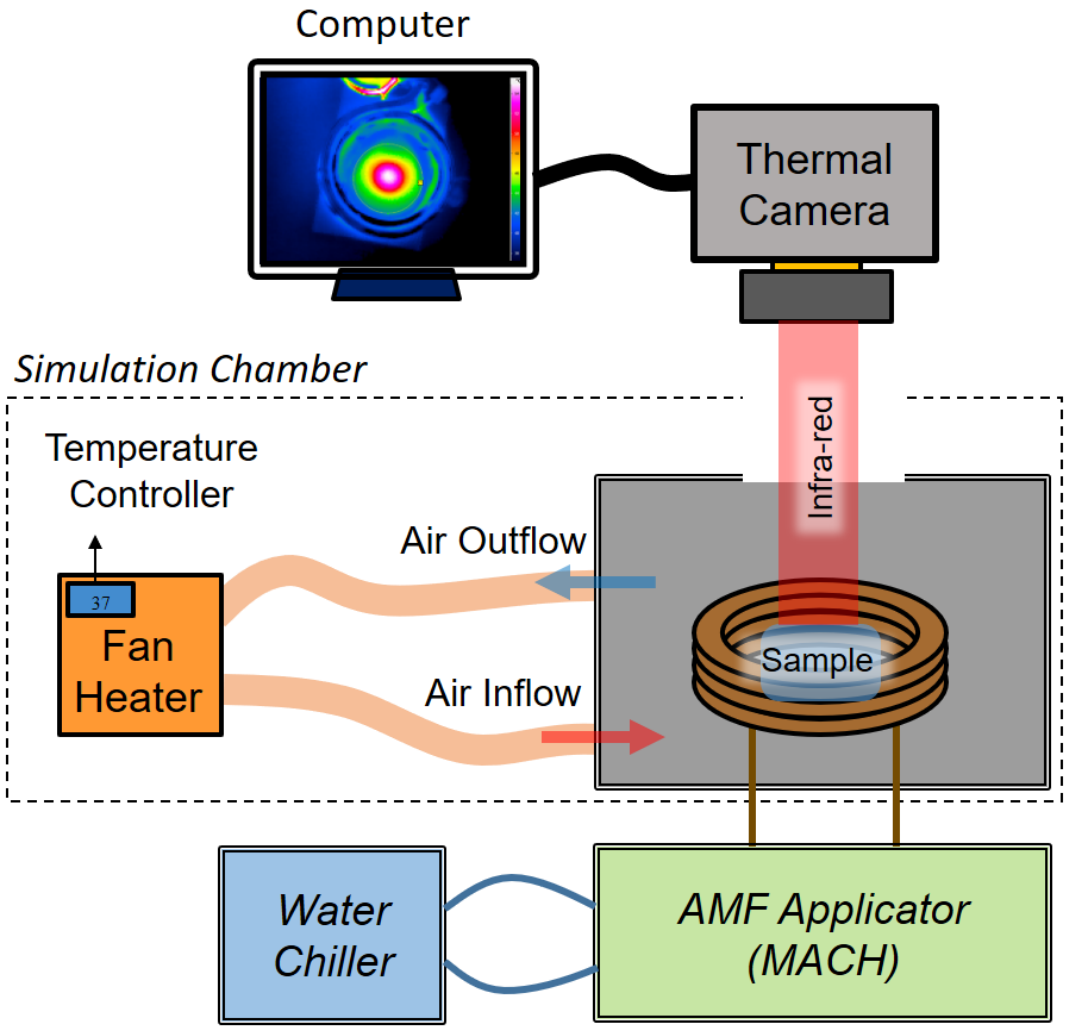

Figure 3.8: The block diagram of the setup for *in-vitro* experiments. The MACH was used to generate an AMF. The water chiller circulated cool water through the MACH pre-clinical coil to avoid overheating. The simulation chamber consists of an enclosure (grey coloured box in the figure) and a fan heater. The fan heater controlled the ambient temperature inside the enclosure to be biological temperature. An infra-red thermal camber was used to recorded the surface temperature of a phantom.

Field Generator - MACH Pre-clinical Coil

The MACH with the pre-clinical coil was used in this experiment to generate an AMF (see Section 1.2.1). The details of MACH pre-clinical coil have been illustrated in Fig. 1.2.

Thermal Imaging Camera

VarioCAM®hr from InfraTec GmbH (Dresden, Germany) was used in this study to record the surface temperature profile on phantoms. This infrared camera can measure the temperature between -40 °C and 1200 °C with the measurement accuracy of 1.5 °C. The spectrum of infra-red that can be received by the camera ranges from 7.5 μm to 14 μm. It can record up to 60 thermal images in a second, and the thermal video can be directly exported to a laptop through the FireWire (IEEE 1394) interface. The calibration of VarioCAM was done by the manufacturer when manufactured, and the maintenance of which is preformed by the manufacturer once in every two years.

Simulation Chamber and Fan Heater

In order to simulate the thermal environment inside a human body, a chamber with controlled temperature was built. A simulation chamber has been described in Section 1.2.1. The same fan heater from World Precision Instrument (Sarasota, USA) was also used in these *in-vitro* experiments, but the bespoke-built enclosure has been re-designed for the usability reason. The air temperature within the bespoke-built enclosure was heated up and held at the biological temperature, i.e., 37 °C.

Experimental Procedure

Once all the equipments were prepared, a phantom was placed in the simulation chamber. The MACH was switched on after the phantom's temperature became equivalent to the air temperature in the chamber, i.e., 37 °C, so that it simulated the thermal environment in a human body more closely.

Each phantom was magnetically heated by the AMF for 20 minutes. The surface temperature on the phantom during this 20-minute heating and an additional 10-minute cooling were monitored and recorded by the thermal imaging camera. The recording rate was set to be one frame per minute.

A thermal image contains rich information. The temperature at each point on

the thermal images is included. This rich information required to be processed for the further discussion. The handling of thermal images and the discussion of experimental results are presented in the next section.

3.3 Experimental Results

3.3.1 Handling of Thermal Images

A thermal image contains rich information. The temperature at each point on the phantom's surface was recorded by the thermal camera. As an example, the thermal image of *Phantom A* at the 10th minute of magnetic heating [1] is shown in Fig. 3.9b. A rainbow palette was used to represent the difference in temperature. The photo of *Phantom A* is presented in Fig. 3.9a.

To facilitate the discussion on experimental results, one should trim out unnecessary data and withdraw useful information from each thermal image.

The purpose of this experiment was to see the effect of particle distribution on thermal distribution. Because the geometry of an MNP gel was semi-spherical, the temperature profile of either line that crosses the centre of an MNP gel should be able to represent the overall thermal distribution. Thus, the thermal distribution was represented by plotting the temperature profile on the central line on each phantom. The central line is indicated as a red dashed line in both Fig. 3.9a and Fig. 3.9b.

The temperature profile on the red dashed line is plotted in Fig. 3.10a. This temperature profile was associated with the thermal distribution at the 10th minute of magnetic heating. If one collects all temperature profiles during the experimental period, then the phantom's thermal distribution can be visualised as Fig. 3.10b. In which, the colour indicates different temperature. In contrast to the raw data, this heat map is more informative. In the following section, the thermal images of each phantom would be re-expressed as a heat map.

[1] Overall, three phantoms were used in this chapter, the details of each phantom can be found in Fig. 3.13.

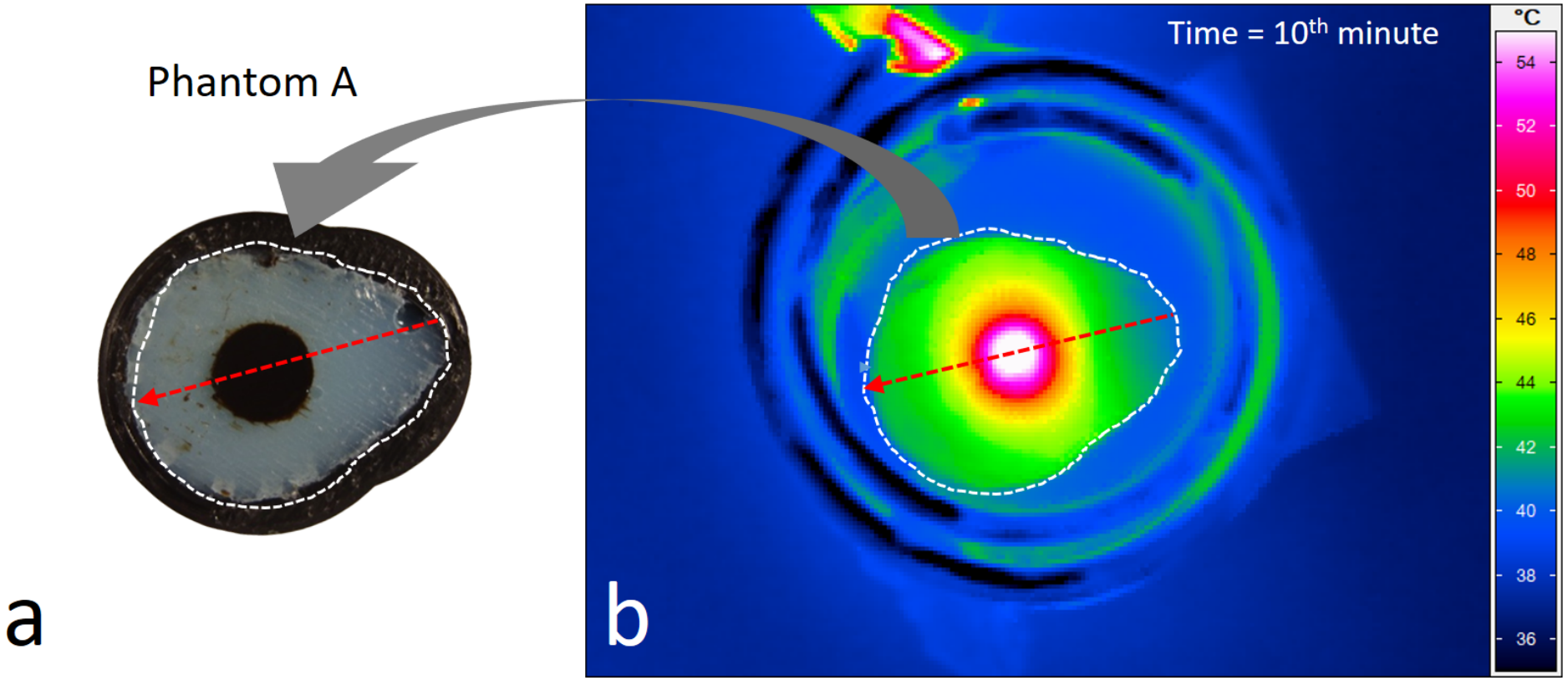

Figure 3.9: Handling of thermal images. (a) The photo of a phantom (*Phantom A*) (b) A thermal image of *Phantom A* from VarioCAM®hr at the 10th minute of magnetic heating. The temperature on central line (denoted as red dashed line) is visualised in Fig. 3.10.

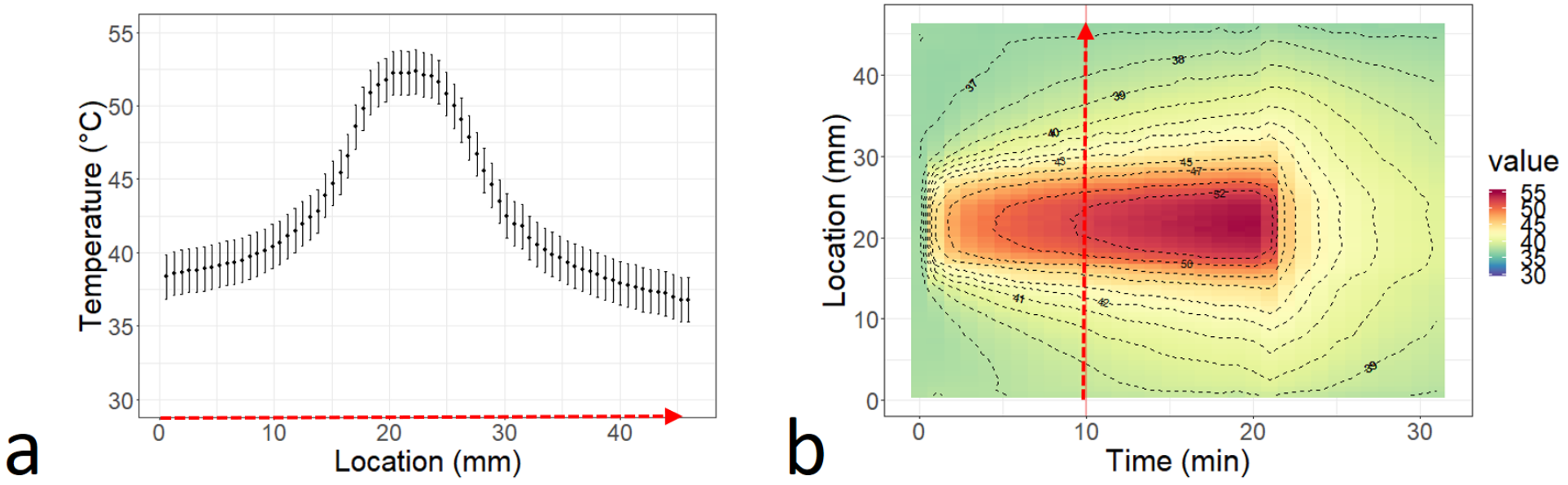

Figure 3.10: Handling of thermal images. (a) The temperature profile on the central line of *Phantom A* at the 10th minute (see the red dashed line in Fig. 3.9). Note that the measurement accuracy of inferred thermal camera is ± 1.5 °C. (b) The variation of temperature profile along with time. In the plot, the temperature is visualised in different colours. The unit of temperature value is °C.

3.3.2 Peripheral Heating

Magnetic hyperthermia aims at specifically heating target tissues. In the procedure, the MNPs are only deposited in target tissues; thus, ideally, the magnetic heating would only occur at the target. In addition to the desired magnetic heating, all other non-specific heating happen during the procedure are termed as peripheral heating.

There are two main sources of peripheral heating. Firstly, as mentioned in the Eq. 2.20, when placing a conductive object in an AMF, even if the object does not contain magnetic materials, heat would still be generated due to the induced eddy current. As tissues or the phantoms (see Table 3.1) are conductive, the induced eddy current in them contributes to the peripheral heating.

Secondly, when MACH is on, an electrical current running through the coil, part of energy would dissipate as heat. Even though a chiller is used to remove the redundant heat from the coil, an increase in coil temperature is still evident. In the presented experiments, after MACH was switched on for 1 minute, the coil temperature rose from 37 °C to 41 °C. Since the 2nd minute, the coil temperate remained at 42 °C.

Because the phantom and the coil were close to each other in the experimental configuration, the temperature of phantom could be affected by the coil temperature. In order to understand, to what extent, the peripheral heating affected the phantom temperature, a phantom without MNPs was exposed to an AMF for for 20 minutes. The field intensity was 3.97 ± 0.02 kA/m and the field frequency was 917531 ± 24 Hz.

The heat map of the controlled phantom is presented in Fig. 3.11a (note that the MACH was only on for the first 20 minutes). The surface temperature of this phantom increased from 37 °C to 42 °C. While there was no MNPs being deposited in the phantom, this temperature increase should be contributed by the peripheral heating. In addition, after 20 minutes, the phantom's temperature became to be identical to the coil's temperature, i.e., 42 °C.

Now, if we average the temperature on the central line, and plot the average temperature against the time, we would attain Fig. 3.11b. In this figure, the boundaries of error bars indicate the maximum and minimum temperature on the central line at each time step.

This heating curve is useful. To focus on the discussion of the heating caused by MNPs, we would like to remove the effect of peripheral heating. This heating curve provides us with a chance to remove the peripheral heating.

The heating curve was fitted with the Box-Lucas equation[2]. The Box-Lucas equation is written as: $T_{start} + A(1 - e^{(-Bt)})$. In which, T_{start} is the starting temperature. The parameters A and B are respectively related to the heating power and the heat loss rate. For the first 20 minutes, the fitted Box-Lucas equation is: $35.7+9.7(1-e^{(-0.05t)})$. For the last 10 minute, when the MACH was turned off, the temperature of this phantom started to decrease with the rate of 0.004 °C per minute.

Taking the fitted Box-Lucas equation and the heat loss rate of 0.004 °C/min in into consideration, the peripheral heating can be removed or corrected from Fig. 3.11. As a result, the average temperature of central line along with time is plotted in Fig. 3.12b. The heat map of which is presented in Fig. 3.12a. Both graphs suggest that after the removal of peripheral heating, the temperature variation across the experimental duration became much smaller. While the average temperature variation in Fig. 3.11b ranged from 36 °C to 42 °C, the average temperature in Fig. 3.12b remained at 36 °C throughout the whole 30 minutes.

This correction method allows the author to focus only on the temperature variation caused by MNPs. **The heat maps presented in the following sections are all corrected heat maps.** That is, the temperature variation associated with the peripheral heating has been removed.

[2]The Box-Lucas equation is widely used to fit the heating curve of an object [102]

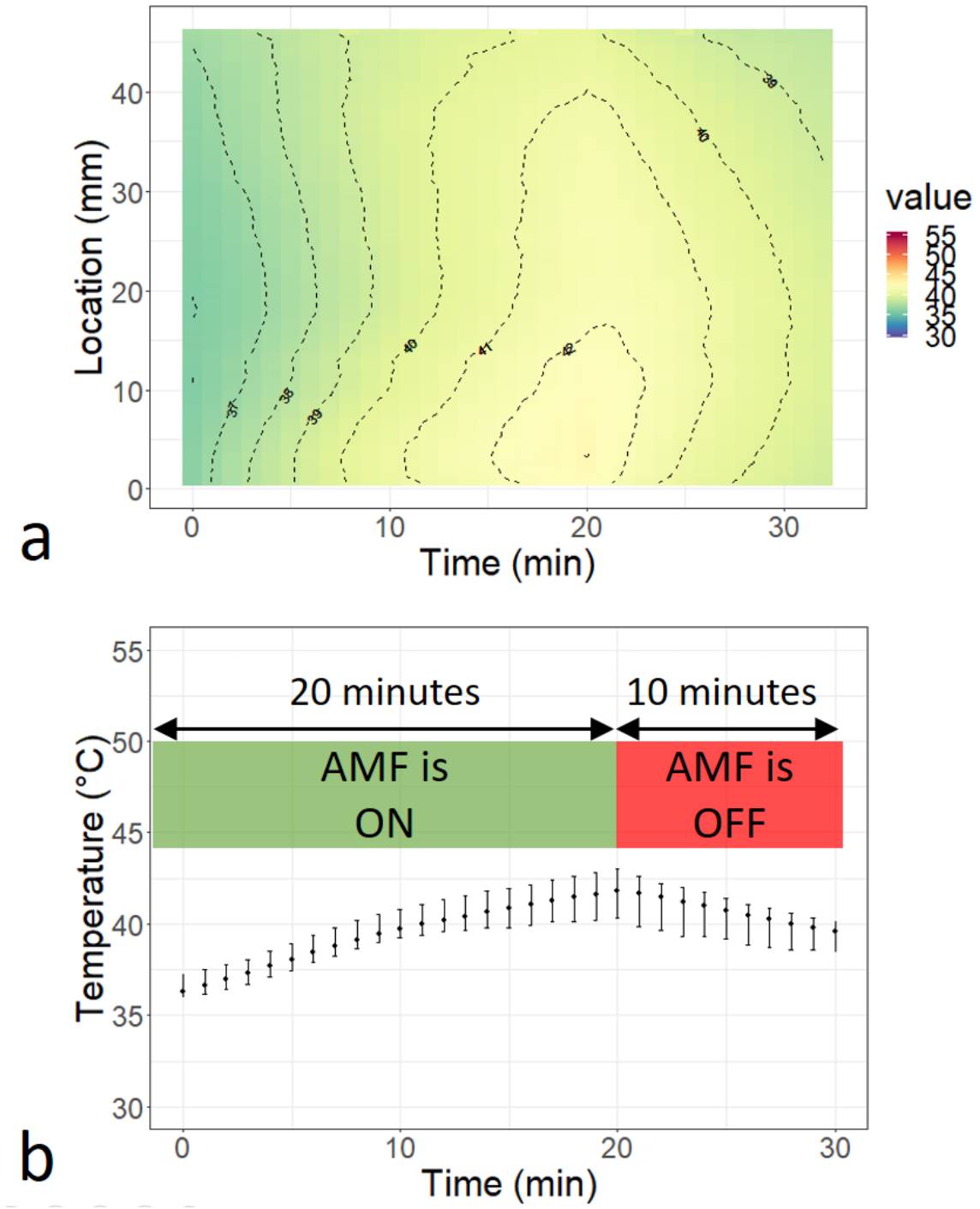

Figure 3.11: The temperature increase caused by the peripheral heating, when a phantom without MNPs is exposing to an AMF for 20 minutes. The MACH was then turned off for the last 10 minutes. (a) The heat map of the phantom. The temperature level is visualised with different colours. (b) The heating curve of the phantom. The black dot represents the average of temperature on the phantom's central line. The upper and lower limits of error bars at each time step represent the maximum and minimum temperature on the central line.

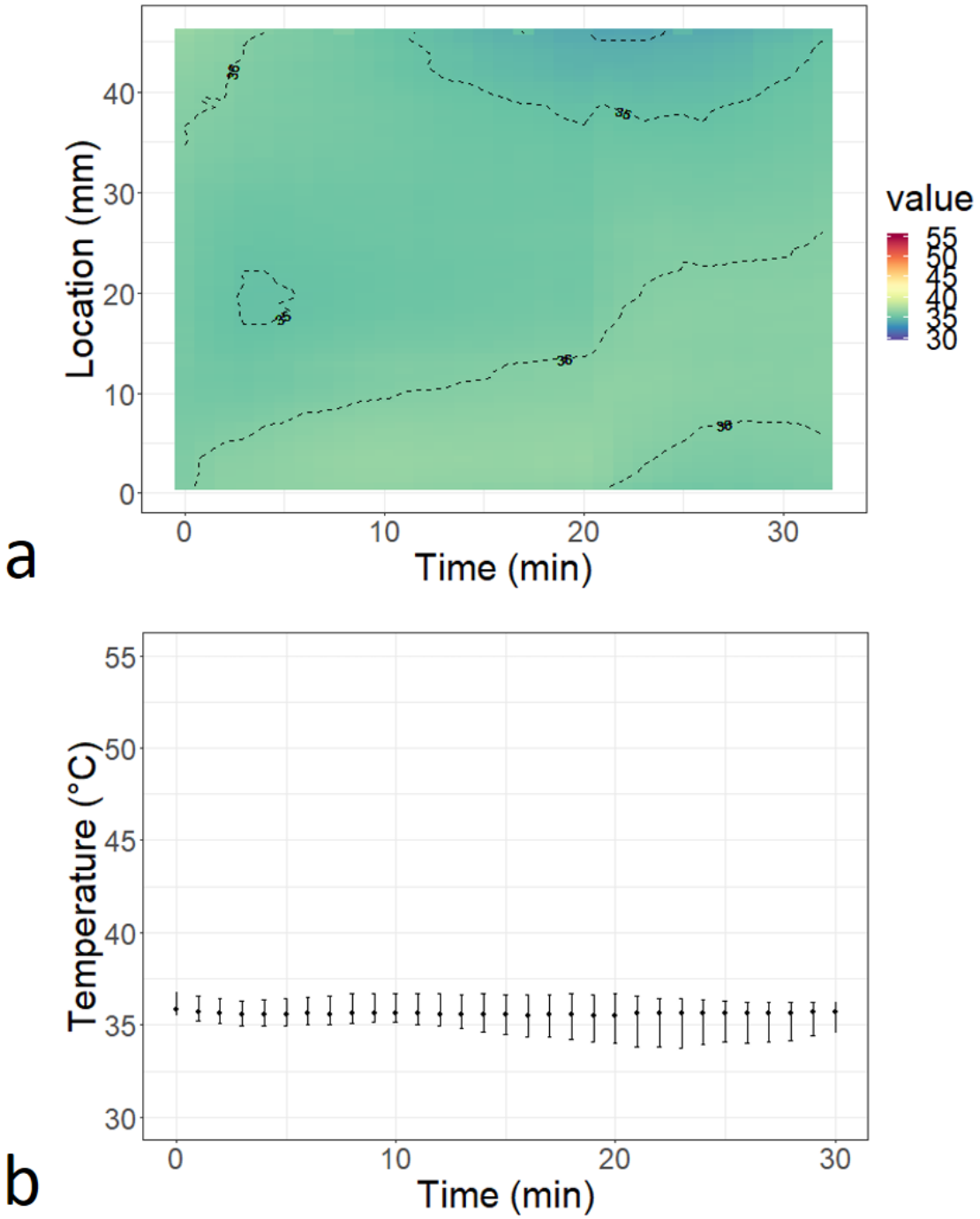

Figure 3.12: The corrected temperature distribution on the phantom without MNPs. (a) The heat map of the phantom. (b) The heating curve of the phantom. The black dot represents the average of temperature on the phantom's central line. The upper and lower limits of error bars at each time step represent the maximum and minimum temperature on the central line.

3.3.3 The effect of particle distribution on thermal distribution

One of the key issues in magnetic hyperthermia is the distribution of MNPs. Once the MNP suspension is injected into a target, MNPs would not just stay where they are; they distribute or spread to its surroundings. That is, even if the applied AMF is the same, the thermal distribution within the target would be different when the distribution of MNPs changes. The experiment presented in this chapter simulated the MNP diffusion inside a tissue by 3 phantoms.

These 3 phantoms were denoted as *Phantom A*, *Phantom B* and *Phantom C*. Each phantom had a cavity at the centre. The cavities were reserved for being filled with an MNP gel. the quantity of MNPs in each phantom was controlled to be similar, if not identical.

The *Phantom A* represented the initial status of the particle diffusion, so the volume of its MNPs gel was the smallest among the 3 phantoms. The *Phantom C* represented its final status after the particle is distributed, so the volume of its MNP gel was the largest among all the phantoms, and the MNP concentration was the lowest. The *Phantom B* simulated the transition status from *Phantom A* to *Phantom C*.

The photo of each phantom is shown at the top of Fig. 3.13. The concentration and volume of the MNP gel in each phantoms are also presented in the same figure.

The neat concentration of Perimag® is 20 mg_{Fe}/ml (see Table C.1). Perimag® was diluted with distilled water to be 10.6 mg_{Fe}/ml, 5.9 mg_{Fe}/ml and 5.4 mg_{Fe}/ml before the fabrication of MNP gels.

As to the volume of each MNP gel, it was estimated based on its weight. The weight of agarose phantom without an MNP gel was measured first, then after the MNP solution was poured into the cavity on the agarose phantom and formed a gel, its weight was measured again. By comparing the difference in weights, the weight of an MNP gel was obtained. Based on which, the volume of an MNP gel was estimated (see the discussion in Appendix F).

The mass of MNPs in each phantom was then calculated based on the concentration and volume of its MNP gel. The masses of MNPs are presented in Fig. 3.13, the values of which were at a similar level, ranged from 3.7 mg to 4.2 mg.

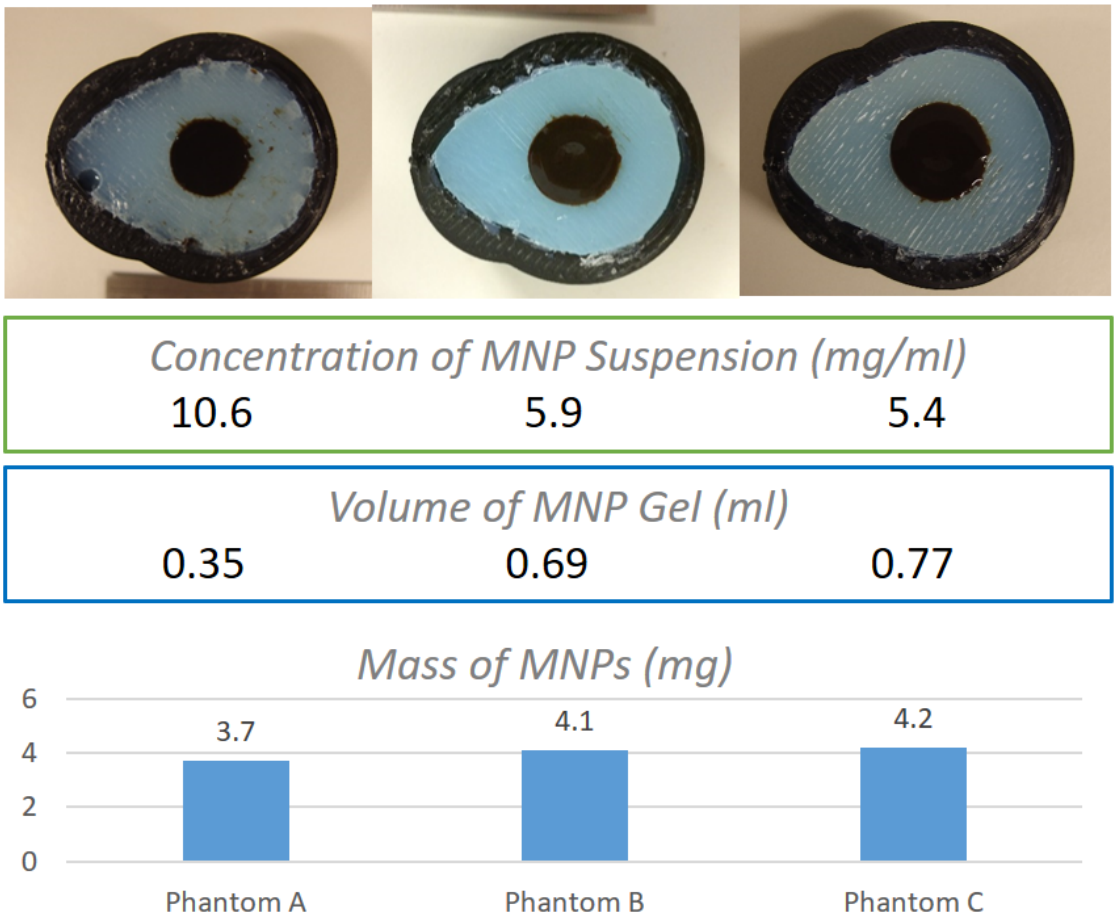

Figure 3.13: The three phantoms used for simulating the particle distribution inside a tissue. The concentrations of MNP suspensions, the volumes of MNP gels and the quantities of MNPs are presented. The volume of MNP gel was estimated based on its weight (see Appendix F).

Each phantom was exposed to the AMF (3.97 ± 0.02 kA/m; 917531 ± 24 Hz.) for 20 minutes. After the MACH was turned off, each phantom's temperature decrease in an additional 10 minute was also recorded. The heat map of each phantom was derived based on the method described in Section 3.3.1 for handling thermal images. As a result, the heat map of *Phantom A*, *Phantom B* and *Phantom C* are respectively shown in Fig. 3.14a - c. In each plot, the boundaries of an MNP gel are indicated with two horizontal lines.

The experimental results indicate that the effect of particle distribution on thermal distribution is evident. When MNPs were concentrated, i.e., *Phantom A*, the rate of temperature increase was high. The temperature at the centre of the MNP gel rose from 37 °C to 52 °C within 10 minutes.

When MNPs were more dispersed, the temperature increase rate was relatively

low. For instance, the temperature at the centre of *Phantom B* and *Phantom C* only increased to 47 °C and 46 °C at the 10th minute. This increase was 5 °C lower in comparison to the increase observed in *Phantom A*. Depending on the scenario, this 5 - 6 °C difference can lead to a difference between a treated outcome and an under-treated outcome.

In addition to the effect on the rate of temperature rise, another associated effect of the particle distribution was on the temperature gradient. Once again, let us take the temperature profile at the 10th minute as an example. The temperature difference between the centre of phantom and the edge of the MNP gel can be estimated from heat maps in Fig. 3.14a - c. The temperature difference in *Phantom A*, *Phantom B* and *Phantom C* were 5 °C, 3 °C and 2.5 °C respectively, and radii of associated MNP gels were 7.23 mm, 8.76 mm and 8.78 mm. Based on this, one can derive the temperature gradient in the MNP gel in each case. The temperature gradient at the 10th minute in each case varied from 0.28 °C/mm (*Phantom C*) to 0.69 °C/mm (*Phantom A*). That is, for an MNP-concentrated sample, i.e., *Phantom A*, a misplacement of thermometer, say 5 mm from the target, can result in an inaccuracy of 3.5 °C.

The results presented in Fig. 3.14 was reasonable and expected. Because the quantity of MNPs in each case was controlled to be similar if not identical, the heating power (denoted as P in the figure) would then be at the same level in each case, as long as the applied AMF was also the same.

However, apart from the heating power, the temperature distribution was also determined by the power density. The power density inside an MNP gel (denoted as P/V in the figure) would depend on both the heating P and the overall volume of the MNPs V. That is, how the MNPs were distributed in a tissue could fundamentally affect the power density and thus alter the thermal distribution.

While some treatments aim at heating target tissues with extremely high temperature, e.g. above 55 °C, others tend to heat up a relatively large area, e.g. the whole gland of the prostate, but with a milder temperature elevation. In some literature, the former and the latter refer to thermal ablation and hyperthermia respectively.

What the author would like to emphasise here is that even if the quantity of MNPs and the applied AMF were controlled to be identical, the thermal conditions of the target was still very much dependent on the particle distribution. For instance, the treatment can be shifted from an ablation to a hyperthermia, if the particles disperse unexpectedly much.

The discussion so far focuses on the phantom's temperature. Certainly, the temperature is an important information to know and it has a direct effect on the treatment, but the temperature itself is not an informative indicator, because the influence of heating time is not included in this indicator. To better inform clinicians on the treating condition of a target, there is a need for adapting new indicators. Apart from those two indicators, i.e., CEM43 and HSP70, described in Section 2.1, the following section proposed an indicator that associates the heating duration with the treated area. The indicator is called **activation time**.

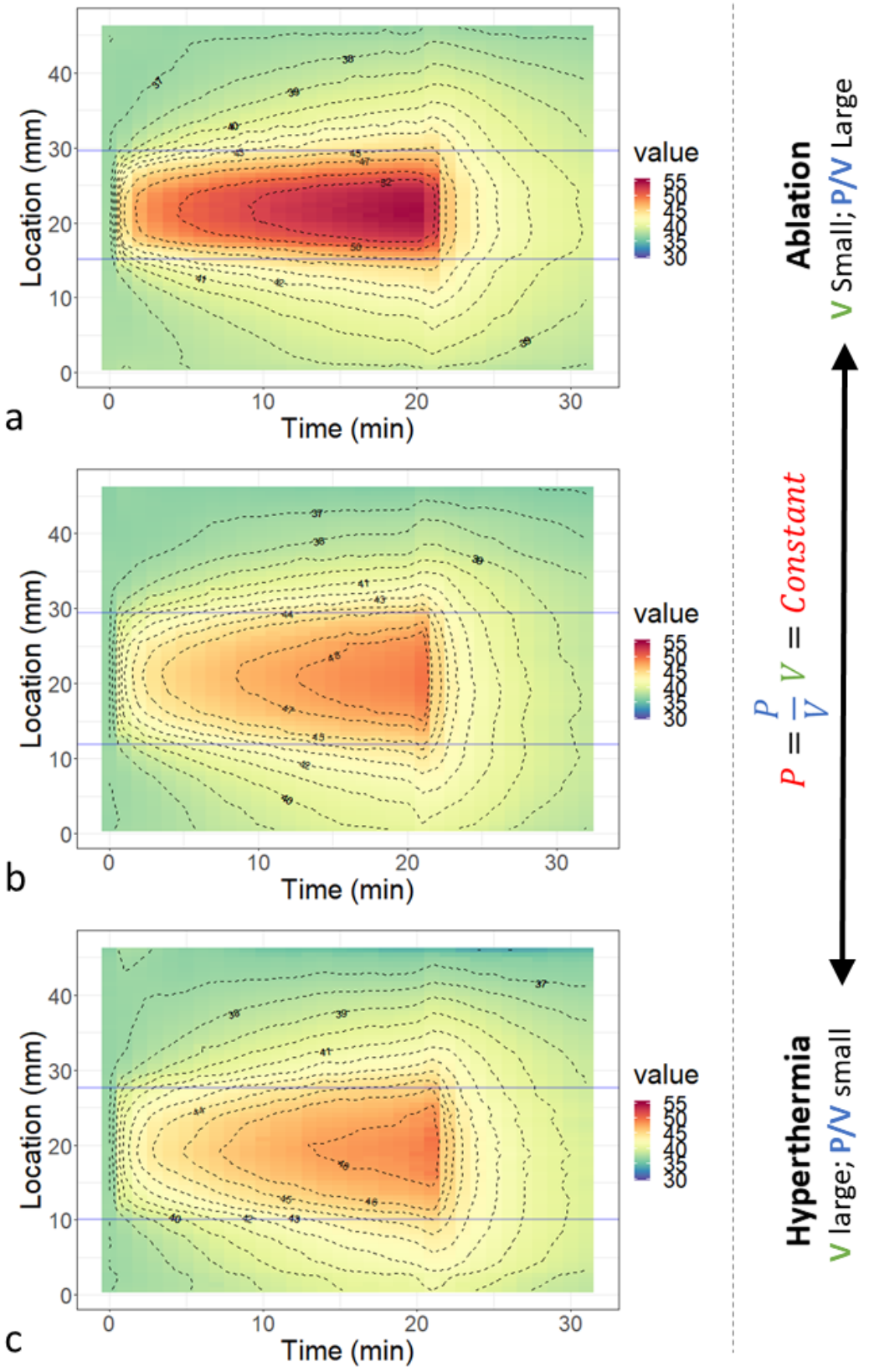

Figure 3.14: The heat maps of (a) *Phantom A*, (b) *Phantom B* and (c) *Phantom C*. The two horizontal blue lines in each graph represents the boundaries of an MNP gel. The P, P/V and V respectively represent the heating power of MNPs, the power density of and the volume of MNP gel. These graphs indicate that despite the similar MNP quantities in each phantom, the particle distribution affects the thermal distribution.

An indicator of treated area - activation time

The temperature distribution in a magnetic hyperthermia is time dependent. The longer the heating time, the larger the treated area.

Before we jump into the introduction of the new indicator **activation time**, let us clarify the terminology first. The treated area is defined here to refer to an area in which the temperature is all above 43 °C. And we say that those cells with temperature higher than 43 °C are activated. The rationale behind the term of **activation** is based on the fact that the thermal damage to tissues begins to be more rapidly activated when the temperature starts to exceed 43 °C (see Section 2.1).

The heat maps presented in Fig. 3.14 are informative, but we cannot always cut the target in half and monitor its surface temperature variation with a thermal camera. Say if we can only measure the maximum temperature of the target, can we still estimate the treated area of the target during a hyperthermia?

Take *Phantom C* as an example. By taking a closer look at Fig. 3.14c, one can find the isotherm of 43 °C. Let us define the distance between the 43 °C isotherm and the centre of the phantom to be R_{43C}. The R_{43C} along with time is re-plotted and presented in Fig. 3.15a. Then, the treated area (denoted as $Area_{43C}$) can be obtained by the calculation of πR_{43C}^2. The correlation of $Area_{43C}$ and time is plotted in Fig. 3.15b. A good linearity has been found in this correlation ($R^2 = 0.96$).

This linear correlation suggests that the longer the accumulated heating time, the larger the treated area. Thus, this accumulated heating time is defined to be an indicator, known as activation time. To be more specific, the **activation time** is defined to be the period, during which the temperature of the target exceeds 43 °C.

Using the activation time as an indicator of magnetic hyperthermia cab be particular useful when it comes to the discussion of HSP70 level, because HSP70 level is measured from slices of histological samples. In principle, the larger the treated area, the higher the HSP70 level. More details of the discussion are presented in Section 4.4.3.

The next section discusses on another essential indicator for evaluating hyperthermia, which is the thermal dose CEM43.

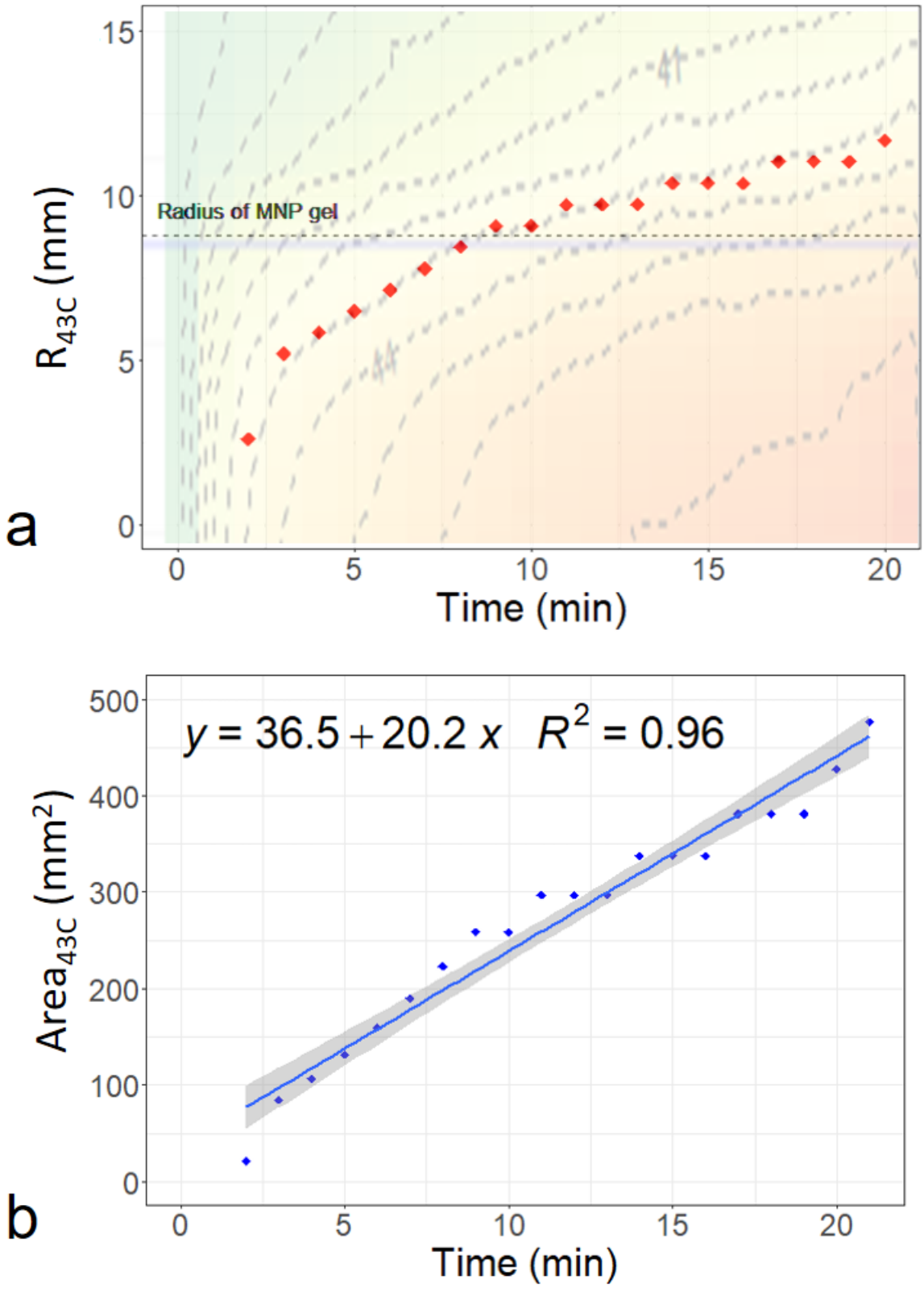

Figure 3.15: The activation time of *Phantom C*. (a) The radius of treated area, i.e., the area with the temperature higher than 43 °C. The radius is denoted as R_{43C}. (b) The treated area as a function of the heating time. The linearity of their correlation is reasonably good, $R^2 = 0.96$.

3.3.4 The Distribution of CEM43

As mentioned previously, not only the intensity but also the duration of heating would affect the level of cell death. In contrast to the thermal distribution of a target, a better way to evaluate the intensity of hyperthermia may be expressing the experimental result in the form of thermal doses.

Through the Eq. 2.2, the heat maps of temperature in Fig. 3.14 can be converted into the distribution of thermal doses, i.e. CEM43. The CEM43 distribution of each phantom is presented in Fig. 3.16.

While the heat map demonstrates the temperature distribution at each single time step, the CEM43 distribution predicts the accumulated thermal damage over a period of time. As a result, when the AMF was turned off after 20 minutes of magnetic heating, even if the temperature started to drop, the CEM43 did not decrease. Once the thermal damage has been caused, cells would not easily recover even though the temperature drops back to its biological temperature.

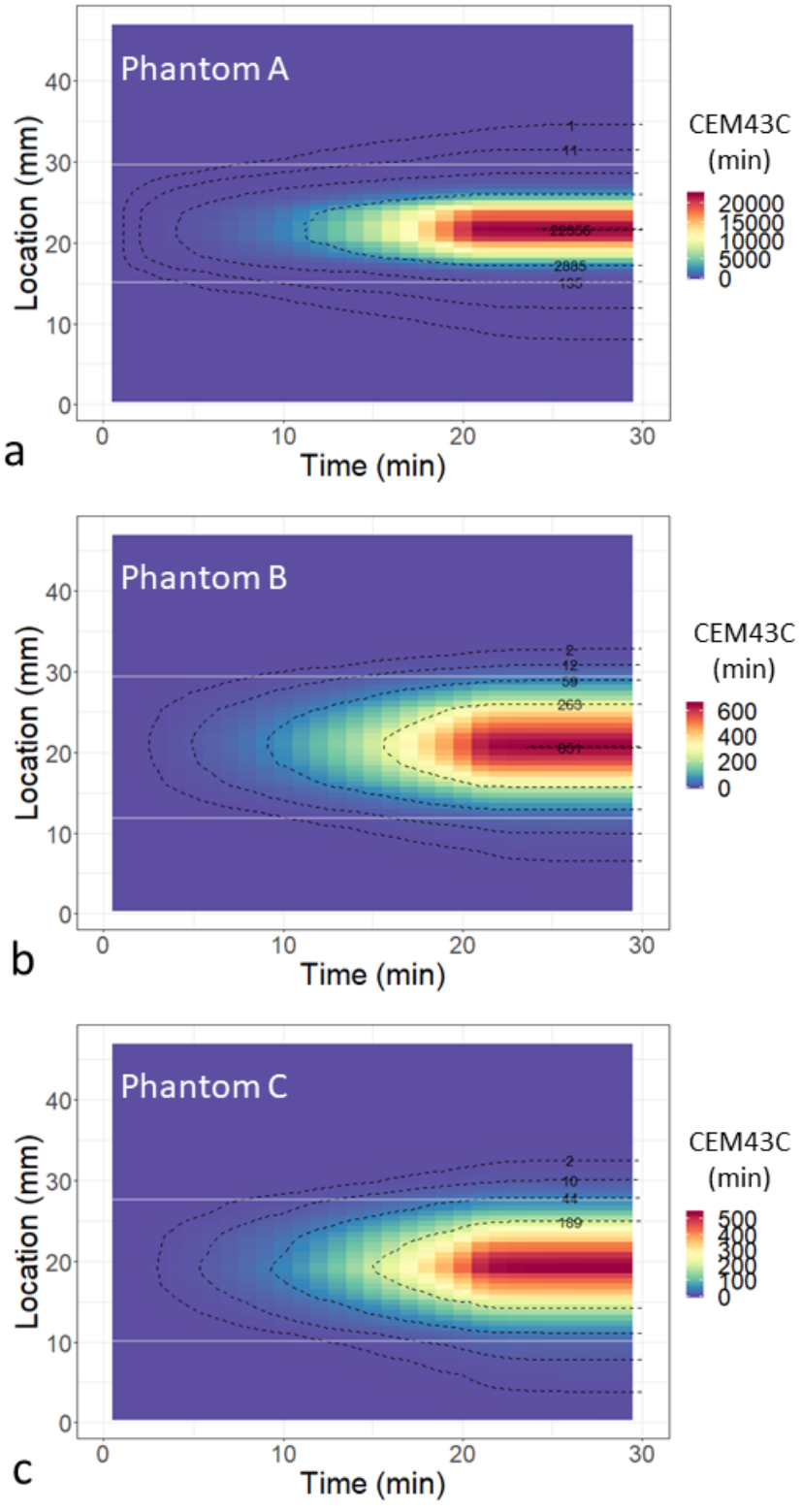

Figure 3.16: The CEM43 distribution of (a) *Phantom A*, (b) *Phantom B* and (c) *Phantom C*. The two horizontal white lines in each graph represents the boundaries of an MNP gel.

Although the CEM43 calculation provides us with a better way to express the intensity of hyperthermia, due to the exponential term in Eq. 2.1, the CEM43 can be extremely large if the average temperature in an interval is much higher than 43 °C.

For example, when the average temperature is 55°C during an interval of 1 minute, the CEM43 would be 4096 minutes. This extremely high CEM43 does not suggest a more severe damage to the target, because the target tissues may already be destroyed at a much lower CEM43, e.g., 200 minutes.

After all, what really interests us is the level of cell death rather than the exact value of CEM43. Thus, to make the result more comprehensible, one can covert the CEM43 distributions to a scale that indicates the cell death severity.

The scale for converting CEM43 to cell damages of different types of tissue has been suggested in the study by Yarmolenko et al. [26]. This report suggests that no damage was found on prostates when the applied thermal dose is lower than 50 minutes of CEM43, while a complete coagulation was observed at 240 minutes of CEM43.

To be more clear, Table 3.2 describes damage conditions of cells related to 3 ranges of thermal dose. Based on the ranges, the author converted CEM43 to the severity of cell damage in a range of 0% and 100%. The 0% and 100% severity of cell damage respectively represent the conditions of *Not obvious* and *Complete coagulation*. The cell damage severity from 1% to 99% refers to the thermal dose from 51 CEM43 to 240 CEM43.

CEM43	0-50 min.	51-240 min.	>240 min.
Damage Conditions [26]	*Not obvious*	*Minor and significant*	*Complete coagulation*
Severity of Cell Damage (%)	0	1-99	100

Table 3.2: The upper bound and lower bound thresholds of thermal dose that associated with the status of damage on prostate tissues.

Based on this table, the Fig. 3.16 was converted to Fig. 3.17. The latter indicates the distribution of the accumulated damage to cells in theory at each time step. Unlike temperature profiles in Fig. 3.14, which do not have obvious clinical meanings, the Fig. 3.17 more clearly expresses the intensity of hyperthermia on each point on a phantom at different durations of time.

The Fig. 3.17 indicates that the predicted cell damage on *Phantom A*, *Phantom B* and *Phantom C* started to appear at different time steps, which were respectively

at the 3rd, the 8th and the 9th minute. These were directly related to their heating performances.

For the well-heated *Phantom A*, the thermal dose accumulated more quickly than others. Because of the strong heating, the margin between 0 % and 100 % cell damage was smaller than others. The estimated severity of cell damage at centre of *Phantom A* rose from 0 % and 100 % within only 3 minutes, while those of the rest two cases took around 7 minutes.

This conversion described above is straightforward yet important. While the cell damage is the main purposed of hyperthermia, the temperature is just a way to achieve it. Overall, the effect of particle diffusion on temperature distribution or on CEM43 has been investigated. The following section will then validate these experimental results with FEA.

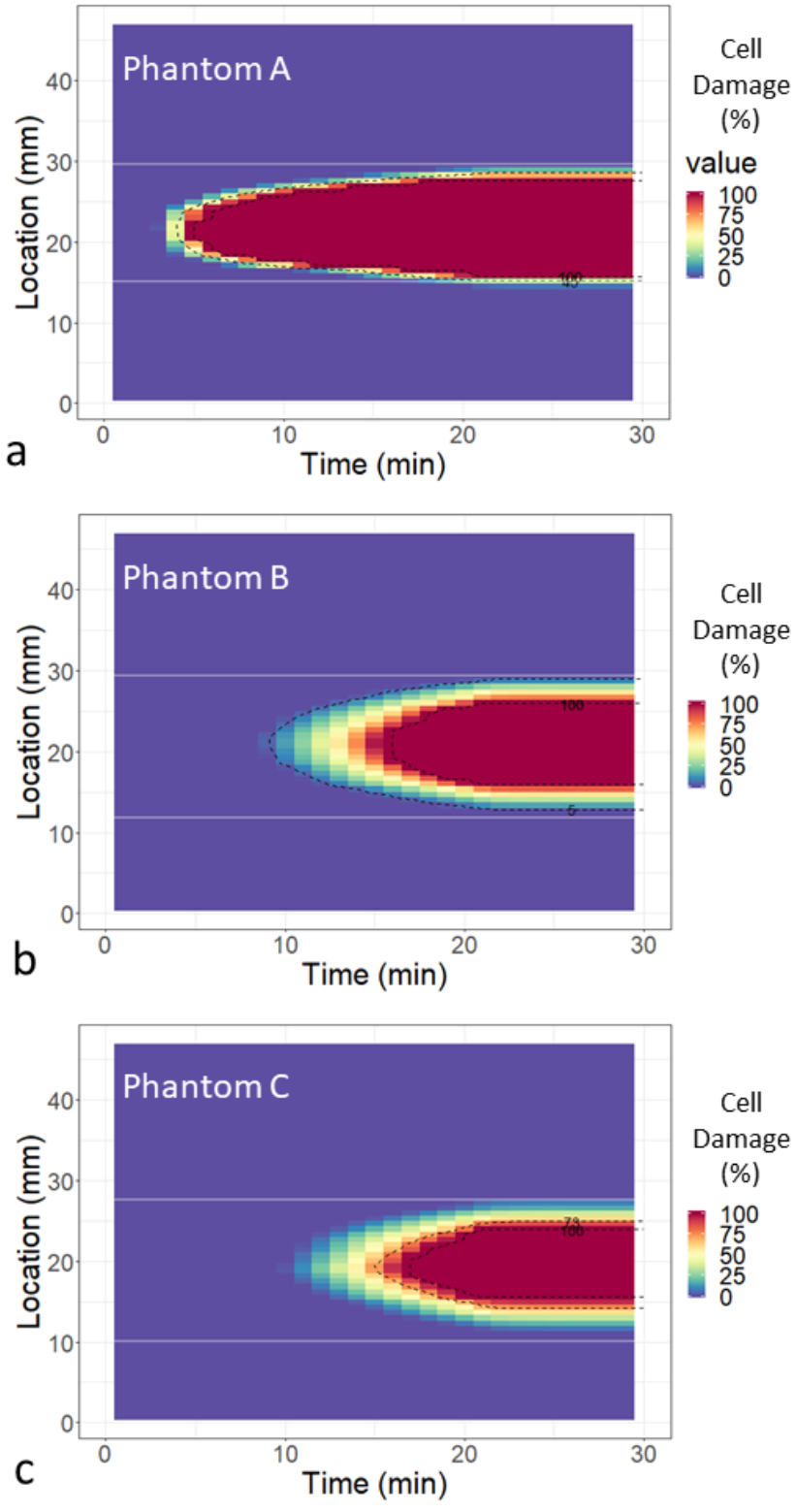

Figure 3.17: The predicted severity of cell damage versus time in (a) *Phantom A*, (b) *Phantom B* and (c) *Phantom C*. The two horizontal white lines in each graph represents the boundaries of an MNP gel.

3.4 Validating Results with Simulations

To validate the experimental results, simulations have been performed. Phantoms in this study were designed in the CAD environment (Autodesk Inventor Professional 2015), which has an FEA package for analysing transient heat transfer. The general heat transfer equation adapted by Autodesk is written as:

$$K\vec{T} + C\dot{\vec{T}} = R \tag{3.1}$$

In which,

- K is the conductive matrix.
- C is the capacitance matrix.
- $\vec{T}$ is the temperature vector.
- $\dot{\vec{T}}$ is the time derivative of $\vec{T}$.
- R is the thermal load vector.

The FEA is a computational technique that divides a large problem into smaller elements. Once the solutions of elements are found, they would be assembled to represent the solution of the large problem.

To apply the FEA to simulate the phantom heating experiment, parameters needed to be determined. The parameters include material properties (mainly associated with thermal properties), initial values, the boundary condition and heat sources. The material properties are listed in Table 3.3.

The initial values are initial temperatures of the phantom and the environment, which are both 37 °C. The boundary condition is the thermal exchange through the convection between the phantom and the environment. As to the heating sources, there were two heating sources, which were magnetic heating and peripheral heating. Based on the experimental result in Section 3.3.2, it is possible to derive both the peripheral heating power and the convection coefficient.

The peripheral heating power can be derived based on the initial slope of its heating curve (see Fig. 3.11b). The initial slope of the heating curve was 0.5 °C/min [3].

[3]The initial slope of heating curve can also be derived from the fitted Box-Lucas equation, i.e., $T_{start} + A(1 - e^{(-Bt)})$. The product of parameters A and B is equivalent to the initial slope. In this case, the initial slope was $9.7 \times 0.05 \approx 0.5$. The details of the derivation can be found in [102].

Once the peripheral heating power is known, we can then find an appropriate convection coefficient to make the simulated heating curve fit the experimental data, of which the details have been listed in Table 3.4.

With regards to the power of magnetic heating, it could be easily calculated based on the mass and ILP of MNPs, the frequency and intensity of the applied magnetic field, which are described in Table 3.5. The duration of heat was set to be the same as experiments, i.e. 20 minutes.

The results of a simulation are like thermal images obtained from experiments (see Fig. 3.18 (a)). Similarly, the temperature distribution on the central line was withdrawn to represent the whole (see Fig. 3.18 (b)). To validate the experimental results, Fig. 3.19 compares the simulated results with experimental results at three time steps, the 10th minute, the 20th minute and the 30th minute. The simulated results and experimental results are respectively indicated by solid lines and coloured circles in the graphs.

For the peripheral heating, *Phantom B* and *Phantom C*, the results of their simulation and experiments were similar. The maximum temperature rises were almost the same, but the rises at edges in experiments were stronger than those in simulation. In relation to *Phantom A*, the experimental temperature rise was about 3 °C higher than the simulated one. The result might imply that the actual amount of MNPs in experiment was higher than what we measured, which led to a 3 °C difference in the maximal temperature rises between the simulation and the experiment.

Parameters	Phantom
Specific Heat Capacity, $C_s(J/kg \cdot K)$	4181
Thermal Conductivity, $\delta_T(W/m \cdot^\circ C)$	0.6
Density, $D(kg/m^3)$	1070
Initial Temperature of Phantom, $T_{initial}^{Phantom}(^\circ C)$	37
Initial Temperature of Environment, $T_{initial}^{Environment}(^\circ C)$	37

Table 3.3: The material properties (see Section 3.1.1) and initial temperatures of both phantom and environment, i.e., 37 °C.

Parameters	
Initial Slope, $\frac{\Delta T_{initial}}{\Delta t_{initial}}$ $(^{\circ}C/min)$	0.5
Heat Energy per Unit Mass, $E = C_s \cdot \frac{\Delta T_{initial}}{\Delta t_{initial}} (W/kg)$	35.5
Peripheral Heating Power per Volume, $\frac{P_{Peripheral}}{V} = E \cdot D(kW/m^3)$	**380.3**
Convection Coefficient, K_c $(W/m^2 \cdot K)$	12.8

Table 3.4: The peripheral heating power per unit volume derived from the initial slope of the heating curve. The convection coefficient estimated from the heating curve.

Parameters	Phantom A	Phantom B	Phantom C
Mass of MNPs, M_{Fe} (mg)	3.7	4	4.2
Volume of MNP gel, V_{MNP} (ml)	0.35	0.69	0.77
ILP (nHm^2kg^{-1})	5.5	5.5	5.5
Field Frequency, f (kHz)		918	
Field Intensity, H (kA/m)		4	
Magnetic Heating Power, $P_{magnetic} = ILP \cdot M_{Fe} \cdot H^2 \cdot f(W)$	0.30	0.32	0.34
Magnetic Heating Power per Volume, $\frac{P_{magnetic}}{V_{MNP}}$ (kW/m^3)	**861.3**	**471.8**	**440.6**

Table 3.5: The magnetic heating power per unit volume in each phantom, which is derived based on the mass and ILP of MNPs, the volume of MNP gel and the features of applied magnetic field.

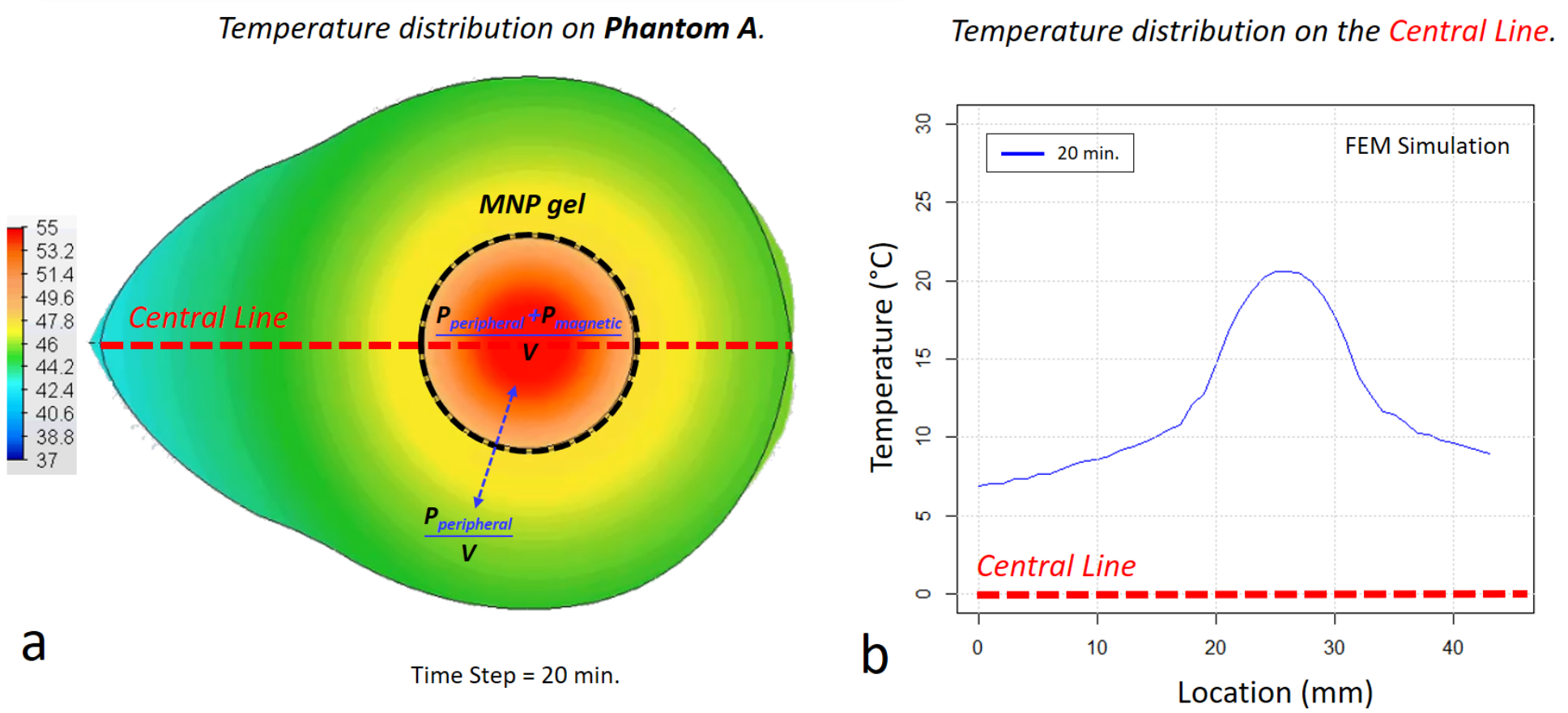

Figure 3.18: (a) The thermal distribution on a phantom obtained from the simulation at 20 minutes. The simulation of *Phantom A* is presented as an example. (b) The distribution of temperature rise on the central line of the phantom.

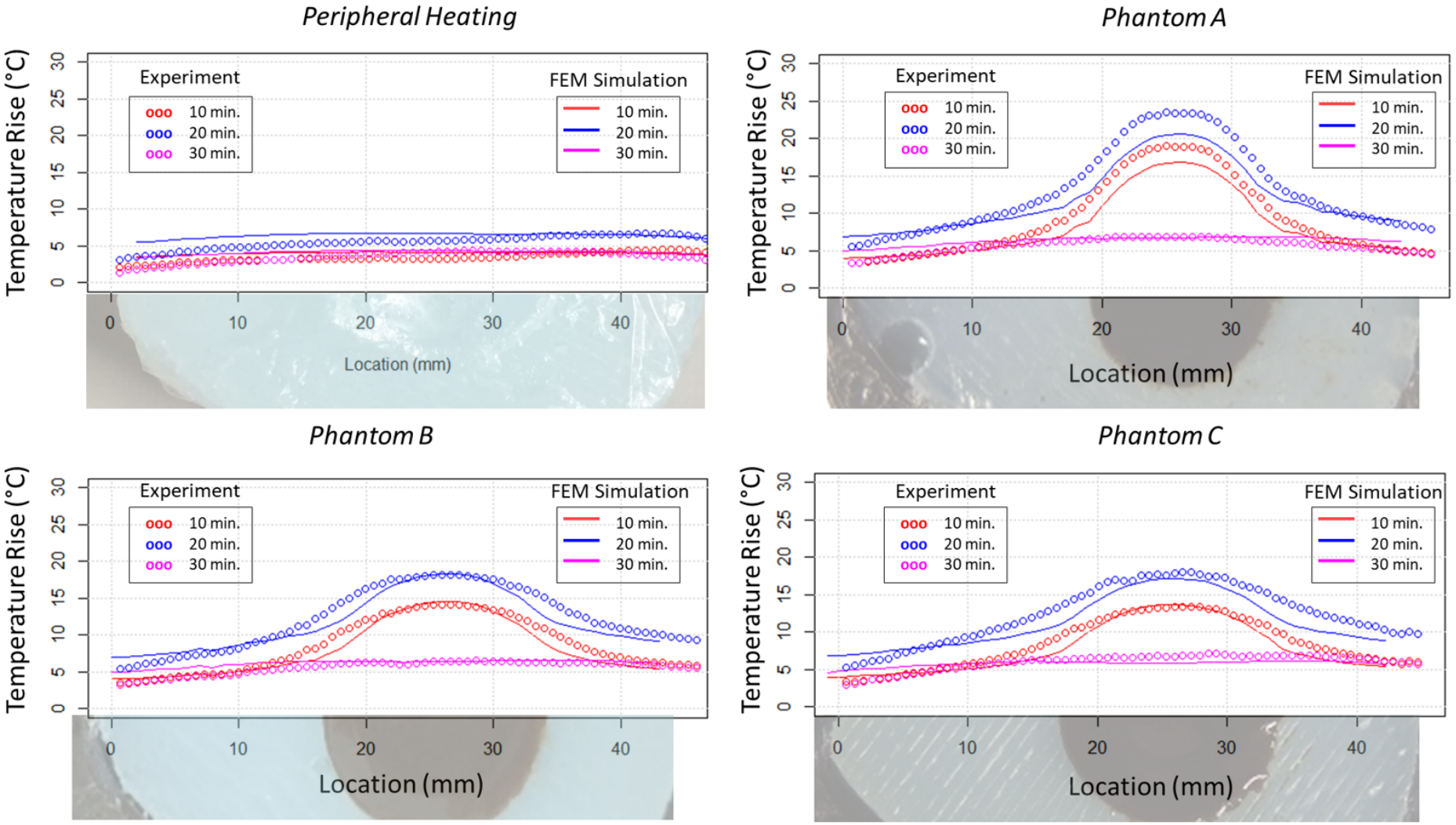

Figure 3.19: The distribution of temperature rise at time steps of 10 minutes, 20 minutes and 30 minutes on the phantom without MNPs, *Phantom A*, *Phantom B* and *Phantom C*. While the coloured circles represent the results of experiments, the solid lines indicate the simulated results.

3.5 Discussion

In this chapter, the discussion started from the construction of tissue-mimicking phantom. Although the phantom was made to be like a prostate in this study, the process of phantom construction allows us to build any sort of phantoms by simply modifying the mould design in CAD environment. Afterwards, the temperature distribution on phantoms when exposing to an AMF had been studied. The thermal distribution was then converted to CEM43 distribution and the distribution of *severity of cell damage* for the convenience of predicting the efficacy of hyperthermia. During the discussion, a new indicator called activation time was proposed. The activation time will also be used for the discussion of HSP70 level in *in-vivo* experiments (see Section 4.4.3).

The experimental results was later compared with simulations. The comparison implied that the mass of MNPs in *Phantom A* might be underestimated, but the simulated results generally fit the experimental ones.

In conclusion, the phantom heating experiments performed in this study have provided a platform to study the temperature distribution on a target which can potentially benefit the research of magnetic hyperthermia in two perspectives.

Firstly, it can calibrate an AMF generator. Some field generators produce an inhomogeneous AMF. That is, when placing a target in different locations inside the field, the target would be exposed to a different intensity of the field. The phantom heating experiments can help to point out that situation. Secondly, this method can help to reduce the need for animal experiments. For instance, the use of doses of MNPs can be simulated in phantoms. Even though it is difficult to predict the temperature distribution in an animal accurately, a safe range of MNP doses associated with temperature rises may still be defined through these *in-vitro* experiments.

In addition, the *in-vitro* experiments demonstrated in this chapter have also validated the infra-red thermography. This infra-red thermography made it possible to monitor the temperature profiles and thus helped the author to investigate the effect of particle diffusion on the temperature variation. Since we have been familiar with the data analysis of thermography, we will move on and have a discussion on the usage of the infra-red thermometry in *in-vivo* studies in the next chapter.

Chapter 4

In-vivo Temperature Sensing with Infra-red Thermography

4.1 Introduction

The preceding chapter has illustrated an *in-vitro* experiment on magnetic hyperthermia. The primary advantage of the *in-vitro* experiment is that the conditions are able to be controlled. Based on this advantage, the experiment presented in the previous chapter has investigated the individual effect of particle distribution on the temperature distribution. This investigation was possible because the infra-red thermometry allowed the author to perform a multipoint measurement of temperatures. The infra-red thermography is preferable over the conventional single point measurement, e.g., optic fibre thermometer, as the accuracy of the latter depends on not only the clinician's experience on probe placement but also the particle distribution during and after the injection. And we have little ability to precisely control the diffusion of particle due to the complexity in biology.

Although the *in-vitro* experiment allows the author to study an individual effect in hyperthermia, the *in-vivo* environment is, after all, different from the controllable environment in phantoms. Accordingly, this study has also made an attempt to understand the magnetic hyperthermia in a more realistic scenario. In collaboration with the Cancer Institute, University College London, four experiments have been performed on pre-clinical models.

The first two experiments were designed to evaluate the experimental procedure itself. Based on the results of which, the dose of the MNP and field parameters were

adjusted. With these adjusted parameters, the 3rd experiment was conducted to examine the biological response of pre-clinical models to heat. The amount of HSP70 in each tumour was quantified based on histological studies after magnetic heating[1]. When the aforementioned CEM43 is regarded as an indicator of the *severity of cell damage*, the quantity of HSP70 may be helpful in assessing this indicator, as the HSP70 is an actual biological response. Additionally, the 4th experiment was performed to investigate the *in-vivo* distribution of MNPs and its effect on temperature variation. The distribution of particles was imaged with a micro-CT [2]. The apparatus and setup used in these experiments are presented in the next section. The experimental procedures and the results of each experiment will be specified in the following sections. Lastly, a conclusion will be drawn at the end of this chapter.

4.2 Setup, Apparatus and Materials

4.2.1 Setup for *In-vivo* Experiment

The experimental setup in all four experiments were identical. The experiment setup consists of a field generator, an infrared thermal camera, and an anaesthesia machine. This setup is illustrated in Fig. 4.1a. The photo of a mouse model is shown in Fig. 4.1b. The thermal image of the mouse's tumour is presented in Fig. 4.1c. Apparatuses and materials are described in following sections.

[1]The author thanks Dr Thomas Carter from the Cancer Institute, University College London, for his assistance with the presented pre-clinical study. The reading of HSP70 were kindly provided by Dr Carter and his colleagues.

[2]The author thanks Dr May Zaw Thin from the Centre for Advanced Biomedical Imaging, University College London, for her help in acquiring CT images of pre-clinical models.

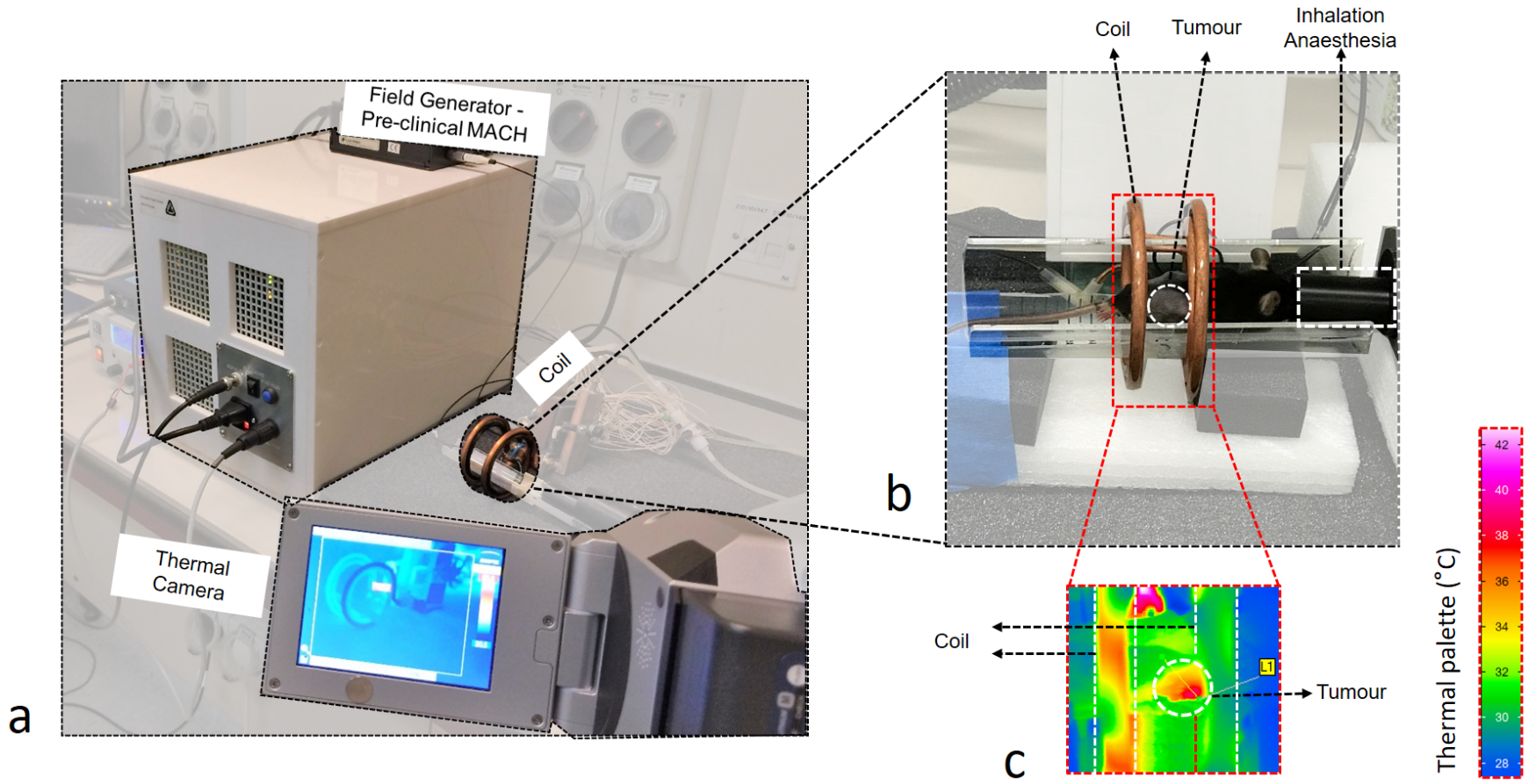

Figure 4.1: (a) The experimental setup for *in-vivo* experiments, which consists of a field generator, an infrared thermal camera and an anaesthesia machine. (b) The photo of a mouse model. The white dashed circle indicates the tumour on the mouse. The white dashed rectangular indicates the device for inhalation anaesthesia. (c) A thermal image that contains a mouse's tumour and the coil.

4.2.2 Apparatus

Field Generator - MACH Pre-clinical Coil

The pre-clinical coil was also used in these *in-vivo* experiment, the description of which can be seen in Section 1.2.1. As to the driving signal of MACH, another version was used in these experiment. The frequency of the new version of MACH was 690 kHz[3]; the field intensity ranged from 2 kA/m to 6 kA/m.

Thermal Imaging Camera

The thermal imaging camera used here was the same as the one used in the *in-vitro* experiment. Its description has been stated in Section 3.2

Anaesthesia Machine

The anaesthesia machine is a pneumatic device that deliveries gas mixture to the breathing system of a subject, i.e., a mouse model in this study. This inhalation anaesthesia leads to the general anaesthesia of a subject. The gas mixture used for anaesthesia was 2 % isoflurane in oxygen 1.5 - 2 L/min.

4.2.3 Materials

Magnetic Nanoparticles

The MNP suspension used in *in-vivo* experiments was Perimag®-COOH. The core of this MNP is Perimag® (see Section 3.1.2), but a layer of carboxylic acid (COOH) is combined on top of Perimag® to make it become Perimag®-COOH. The Perimag®-COOH was also provided by micromod (see Table C.1). It has slightly stronger heating ability than Perimag®. The ILP of Perimag®-COOH is $5.78 \pm 0.3 \mathrm{nHm^2kg^{-1}}$.

Pre-clinical Model

Mouse model (C57BL/6) was applied in this pre-clinical study. All mice were approved by University College London Biological Services Ethical Review Committee and licensed under the UK Home Office regulations and the Guidance for the Operation of Animals (Scientific Procedures) Act 1986 (Home Office, London, United

[3]The operation frequency of the MACH used in Chapter 3 was 918 kHz.

Kingdom). The mice were classified as non-obese diabetic/severe combined immunodeficiency/gamma mice, which were female and 6-8 week old. The weight of mice was 21.7 ± 2.5g.

Tumour Model

In the four experiments presented in this chapter, the immunocompetent Glioma 261 (GL 261) model was used. Using GL261 together with C57BL/6 is a murine glioma (a type of brain tumour) model that is commonly used in pre-clinical studies for developing novel therapies. GL261 can introduced through a subcutaneous injection, which is ideal for the hyperthermia experiment, because the tumour temperature can be easily monitored by a thermal camera. GL261 tumours are invasive but are not metastatic. Unlike other tumour cell line, the spontaneous regression of GL261 tumours is rare [103]. These suggest that the growth of the tumour is stable and it would not easily spread and affect other organs of the murine model. In the experiments GL 261 was grown in the flanks of mice through subcutaneous injection. The injection was done by following the protocol suggested in [104].

The tumour volumes were estimated by measuring the width (w), length (l) and height (h) with a caliper, and using the ellipsoid volume equation, i.e., $\frac{4\pi}{3}(w \times l \times h)$.

4.3 Preliminary Study on Experimental Protocol

The experimental setup, apparatus and materials have been described. This section will further introduce the experimental procedures.

As shown in Fig. 1.9, the two factors need to be determined before the action of injection are (1) the dose of MNPs and (2) the parameters of applied AMF. In this section, two protocol-determining experiments have been conducted to help us to determine these two parameters.

Once these two parameters have been determined, an experimental protocol was developed based on these results. The protocol provided us with a guideline when conducting the third and forth experiment (see Section 4.4 & 4.5).

4.3.1 Dose Determination

As to the dose of MNPs, the higher the dose, the more thermal energy it would be produced at the target site. There is a limit in dosage, as discussed in Section 2.3.2.

In which section, an equation, i.e., Eq. 2.21, has been described for estimating the dose limitation. Key factors in the equation are the systematic dose factor F and the retention rate R.

Although the retention rate R was not examined in this thesis, the author would like to cite the result of another work given by Dr Carter. In which, the retention rate of particles has found to be diverse from case to case. Dr Carter examined 9 samples, which were the same murine model applied in this thesis. Radio-labelled Perimag®-COOH suspension[4] was injected in each sample. Then, the bio-distribution of labelled MNPs was visualised by PET/CT scanning.

His study pointed out that ca. 49% of MNPs on average remained at the injection site. The retention rate of the 9 cases ranged from 30% to 80%. Part of the work was disclosed in a meeting in [105]. More details of the work will be further published by Dr Carter in the future.

According to the finding by Dr Carter, the R was presumed to be 0.5 in the presented experiments. In relation to another factor F, the author assumed that the murine model has a good tolerability to Perimag®-COOH, and presumed the F to be 0.8. With these parameters, i.e., F = 0.8 and R = 0.5, the intratumoural dose limit for a 20 g mice can be derived from the Eq. 2.21. The derived result suggests that the dose of MNPs in this murine model should not exceed 3.35 mg_{Fe}.

On the basis of this derived theoretical limit, the practical concentration could then be considered. Here, the author made another assumption to presume that the dispersion rate was 3. This assumption was based on the the suggestion in [59]. After reviewing the clinical report in [23], Southern and Pankhurst later concluded that the average dispersion rate was 2.4 for the highly concentrated MNP suspension (Nanotherm® - 112 mg_{Fe}/ml) used in Wust et. al.'s study. Considering the relatively low concentration (the neat concentration of Perimag ®-COOH was 50 mg_{Fe}/ml) deployed in this thesis, Dr Carter and the author inferred that the dispersion rate of 3 would be closer to our experimental situation.

It would be an ideal situation if the MNPs evenly disperse to the whole tumour. In this case, the particle density across the tumour would be the same, which would then

[4]The MNPs were labelled with ^{89}Zr.

make the power density be constant in all cases if field parameters remains the same[5]. To achieve this, we injected one-third of the tumour volume of MNP suspension into each murine model. Assuming that the tumour volume is 250 mm^3, then the maximum injection concentration of Perimag®-COOH would be around 40 mg_{Fe}/ml. Because, after the dispersion, the particle density within each tumour would be 40/3 = 13.33 mg_{Fe}/cc_{tissue} or 0.0133 mg_{Fe}/mm^3_{tissue}, for a 250 mm^3 tumour, the overall amount of injected particles would be 3.33 mg_{Fe}, which is just below the theoretical limit 3.35 mg_{Fe}.

From the above discussion, the concentration of Perimag®-COOH suspension had been selected to be 40 mg_{Fe}/ml. The initial experiment presented here was for assessing the dose of MNPs. The injection protocol was as described below: the Perimag®-COOH was diluted from the neat concentration to 40 mg_{Fe}/ml with distilled water. Then, the subcutaneous tumour on each mouse was injected with the diluted MNP suspension. The injection volume was controlled to be 1/3 of the tumour volume.

[5]Note that this does not guarantee the same amount of temperature rise. However, to avoid inconsistency in experimental conditions, the author chose to maintain both the MNP concentration and the field intensity throughout the experiments.

Samples for the 1st experiment

The quantity of particles in each murine model was dependent on the tumour volume. In this experiment, there were seven mice included. The tumour volume and injection volume of each mouse are presented in Table 4.1.

Label	Tumour Volume (mm^3)	Injection Volume (ml)	Particle Mass (mg_{Fe})
A1	138	0.047	1.88
A2	95	0.032	1.29
A3	177	0.060	2.41
A4	74	0.025	1.01
A5	280	0.095	3.81
A6	267	0.091	3.63
A7	271	0.092	3.69
Concentration of Perimag®-COOH is 40 mg_{Fe}/ml			

Table 4.1: The parameters of the experiment for assessing the MNP concentration. The Perimag®-COOH of 40 mg_{Fe}/ml was injected into murine models. Note that the theoretical limit derived from above discussion is 3.35 mg_{Fe}.

Results

Four mice (A3, A5, A6 and A7) developed illness after the injection of 40 mg_{Fe}/ml Perimag®-COOH. Two reasons might cause this illness. The first was that some of the tumours were larger than we expected. For instance, because of the large tumour, the iron amount in A5, A6 and A7 exceeded the limit 3.35 mg_{Fe}. The second potential reason might be that the assumption on systemic dose tolerance ($F = 0.8$) was too optimistic. For either reason, the concentration of Perimag®-COOH suspension needed to be decreased. Thus, the suspension was diluted to 20 mg_{Fe}/ml for the second experiment (see Section 4.3.2).

For the third and forth experiments (see Section 4.4 & 4.5), the dose limit was lowered to be 2 mg_{Fe} from 3.35 mg_{Fe}. The dose limit was decreased because it was later found that the Perimag®-COOH suspension was not specifically sterilised for the *in-vivo* study[6]. Non-sterilised suspension might contain bacteria. The existence

[6]Even so, with the control of dosage, Perimag can still be a good material for research purpose. Studies have applied the same type of material in their pre-clinical experiments [106] [107].

of bacteria could lead to endotoxicosis or endotoxic shock, which was likely to be the main cause of the illness of mice in the first experiment.

Based on this fact, the systemic dose tolerance F was presumed to be 0.5 instead of 0.8, which made the dose limit of Perimag®-COOH for a 20 g mouse to be 2.09 mg_{Fe} (see Eq. 2.21). For the convenience of implementation, **the injected iron amount in Section 4.4 & 4.5 was controlled to be lower than 2 $\mathbf{mg_{Fe}}$.**

4.3.2 Field Determination

The aim of the second experiment presented here was for determining an adequate field intensity for later experiments. The apparatus, materials and experimental setup of this experiment were the same as described in Section 4.2.2.

Samples for the 2nd experiment

Overall, there were 12 mice included in this experiment. Six of them were treated with magnetic hyperthermia and the other 6 were regarded as control samples. The experimental parameters in both groups are respectively listed in Table 4.2 and Table 4.3.

Label	Tumour Volume (mm^3)	Injection Volume (ml)	Particle Mass (mg_{Fe})	Field Intensity (kA/m)
B1*	692	0.200	4.00	4.5/4.0 changed at 240 sec
B2	195	0.066	1.33	4.0/4.5 changed at 600 sec
B3	92	0.031	0.63	4.5
B4	83	0.028	0.56	4.5
B5	133	0.045	0.90	5.0
B6	205	0.068	1.39	4.5
Concentration of Perimag®-COOH is 20 mg_{Fe}/ml				

Table 4.2: The parameters of the treat group in the second experiment. The Perimag®-COOH of 20 mg_{Fe}/ml was injected into each mouse (*The tumour of Sample B1 grew unexpectedly large. With the subsequently refined injection protocol, the amount of iron injected exceeded the dose limit. However, no evident illness was observed in this model after the injection. The experiment continued.)

Label	Tumour Volume (mm^3)	Field Intensity (kA/m)
B7	159	4
B8	438	4
B9	243	4.5
B10	76	4.5
B11	557	4.5
B12	88	4.5

Table 4.3: The parameters of the second experiment. No MNPs were deposited in the mice.

Data Handling of Thermal Images

The processing of thermal image is as shown in Fig. 4.2. The maximum temperature at the target tumour, i.e., the area within the measurement circle in the figure, was seen as the temperature that represented each case. Heating curves of tumours on treated mice (see Table 4.2) are presented in Fig. 4.3.

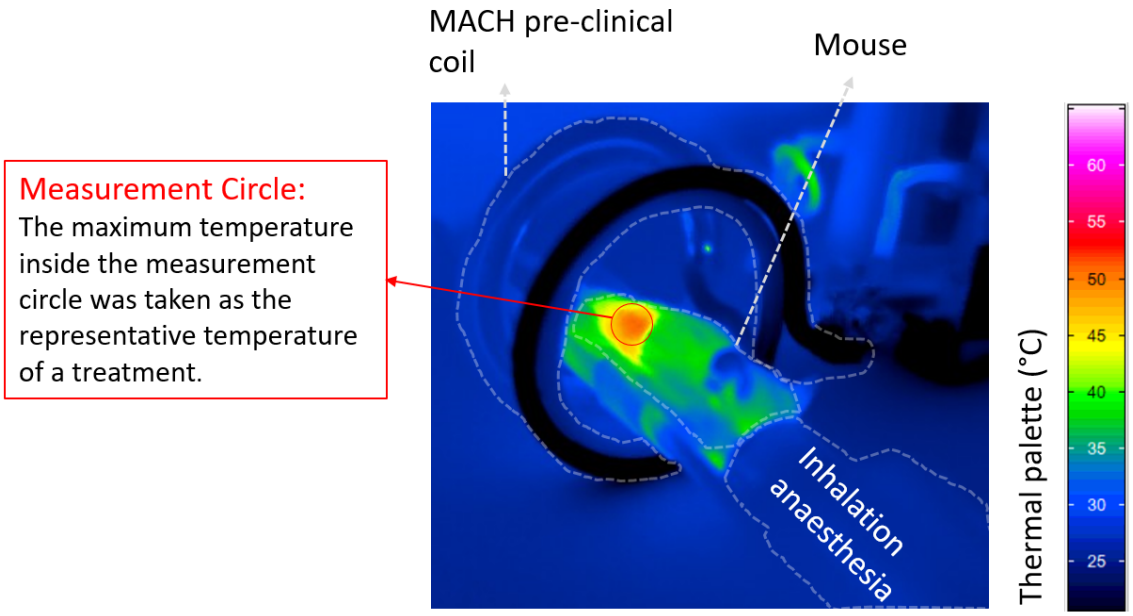

Figure 4.2: Handling of thermal images in the 2nd *in-vivo* experiment. The maximum temperature inside the measurement circle was regarded as the representative temperature of each case.

Field Adjustment

Each mouse was exposed to an AMF generated by MACH. The heating curves in treated mice are shown in Fig. 4.3. The intensity of 4.5 kA/m was first applied to Mouse B1. However, the temperature rose too fast at the beginning (the maximum surface temperature reached 40 °C within 60 seconds), so the field intensity was tuned to be 4 kA/m at the 240th second for the safety of the mouse. For Mouse B2, because of the small temperature rise, the field intensity was enhanced to be 4.5 kA/m again at the 600th second. The intensity was kept to be 4.5 kA/m when heating Mouse B3 and Mouse B4. However, no evident temperature elevation was observed, so the field intensity was further raised to be 5 kA/m for the case of Mouse B5, of which the surface temperature reached nearly 40 °C and then dropped.

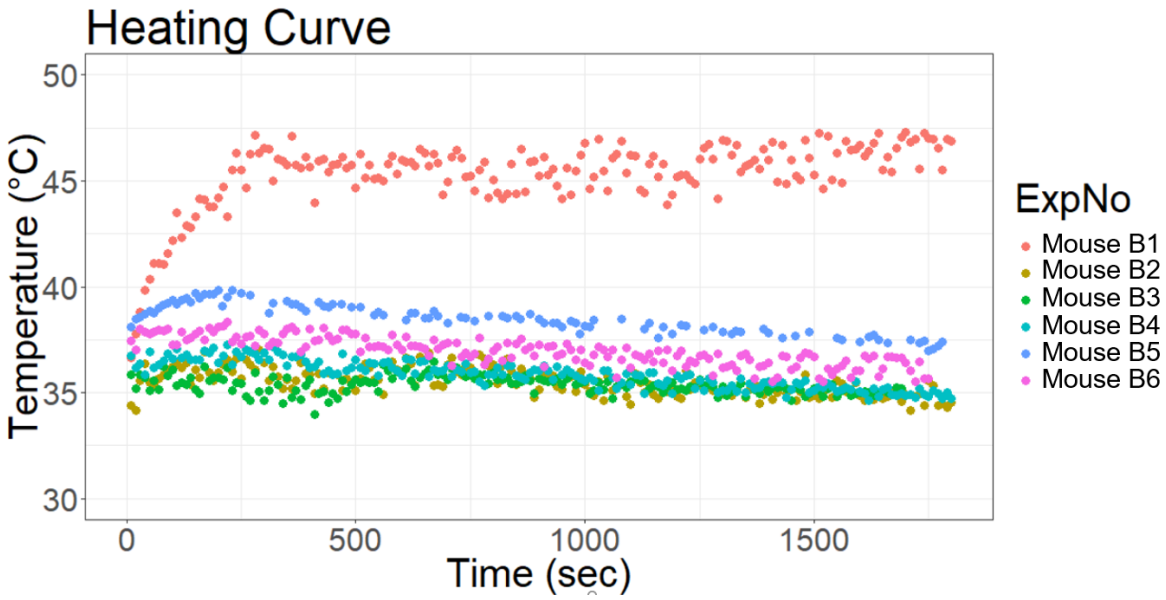

Figure 4.3: The maximum surface temperature of mice in the treated group.

Here, Dr Carter and the author had a debate: to what extent, the detected surface temperature represented the intratumoural temperature? On the one hand, if the intratumoural temperature was a few degrees higher than the surface temperature, then we might have over-heated the Sample B1. On the other hand, the mice were under-treated if the difference was negligible. Clearly, it is best to avoid both over-treating and under-treating.

Although this debate can potentially be settled by measuring the intratumoural temperature with a thermal probe, due to the restriction of the license, we were not allowed to insert a thermal probe into the tumour in the experiments presented in this thesis.

However, one can theoretically estimate the intratumoural temperature based on the surface temperature measured by the infra-red thermometry. The temperature estimation in a biological environment is a complex topic. The temperature can be affected by many factors such as the time, metabolic heating, blood flow and the body's thermoregulation. Studies, such as [63] [108] and [109], have made efforts to explore the effects of those factors on the temperature estimation.

Nevertheless, the accurate estimation of temperature was not the main purpose of the discussion here. The presented discussion aims to understand the temperature difference between the skin and the tumour. It would be especially essential when comparing the HSP70 level with the calculated thermal dose (see Section 4.4).

A simplified estimation of temperature has been proposed by Andra et al. [110]. The proposed model estimate the spatial temperature distribution within a spherical region and its surroundings after prolonged time of heating. The estimation equations are described as:

$$\Delta T(r) = \frac{P_d R^2}{6k_1}[1 - \frac{r^2}{R^2} + 2\frac{k_1}{k_2}] \text{ for } r < R \tag{4.1}$$

$$\Delta T(r) = \frac{P_d R^2}{3k_2}\frac{R}{r} \text{ for } r \geq R \tag{4.2}$$

In which, R is the radius of the sphere where has MNPs deposited and P_d is the power density; k_1 and k_2 are the thermal conductivities of the medium within and beyond the sphere (the thermal conductivities of tissues is 0.52 W/Km). The temperature variation ΔT is dependent on its distance r from the centre of the sphere. Despite of the simplicity of this estimation method, it has been found that the estimated result is reasonably good to approximate the actual temperature variation [59].

The equation suggests that, for a 300 mm^3 tumour, provided that the difference between k_1 and k_2 is negligible, then the temperature at the tumour centre would be ca. 3 ° C higher than the skin temperature (note that the dispersion rate is assumed to be 3, the concentration to be 20 mg_{Fe}/ml and the injection volume is assumed to be 100 mm^3).

Applying this to the data in Fig. 4.3, we saw that for Mouse B1 (which had a larger tumour) the centre temperature was ca. 49 °C at H = 4.0 k/Am, while the rest of the mice had centre temperature at ca. 38-40 °C at H = 4.5 or 5.0 k/Am. After discussion, we decided to use H = 4.5 k/Am in the 3rd and 4th experiments, and

for large tumour to monitor the skin temperature and be ready to reduce the field to avoid overtreatment.

Elements of Temperature Variation

This subsection discusses on 3 elements that affect the temperature variation in preclinical experiment. The first element is the magnetic heating, which was the main function of MNPs. When those region with MNPs were exposing to an AMF, heat was generated. Evident temperature rises were shown in both cases of Mouse B1 and B2.

The second element is the starting temperature. A mouse has a stable body temperature because of thermal homeostasis. It is reasonable that the body temperature of each mouse varies a bit from each other, as it is rarely to find two biologically identical organisms. For studies in the heating ability of MNPs, this element was sometimes ignored. In such studies, the temperature increase associated with magnetic heating is of their interests. However, it is an important factor in *in-vivo* experiments. The difference in starting temperature can significantly affect the intensity of hyperthermia, i.e., thermal dose.

As to the third element, it is interesting to notice the decrease in temperature in Mouse B5. Its temperature only increased in the first 300 seconds, then it constantly dropped over time. The similar tendency in temperature drop was also observed in cases of Mouse B3-B6. This drop in temperature should be the result of anaesthesia. When mice fall asleep, their body temperature decreased. This effect was clearly observed in the control group. As shown in Fig. 4.4c, the temperature of all the mice in the control group (see Table 4.3) decreased over time[7]. Most cases had approximately 3 °C temperature drop after 30 minutes, apart from the cases of Mouse B9 and B12. Their temperature drops were around 1 °C and 5 °C respectively.

The author regards this as a result of biological differences in each mouse. Each mouse reacted to the anaesthesia differently. To gain an equation that is representative enough to describe this cooling effect, the author considered all control cases together and applied a polynomial regression to fit all the cooling curves.

Consequently, a representative equation of temperature cooling,
i.e., $\Delta T = 8.04 \times 10^{-7} t^2 - 2.76 \times 10^{-3} t$,

[7]Two different field intensities were applied in control group. This change in field intensity, i.e., from 4 kA/m (see Fig. 4.4a) to 4.5 kA/m (see Fig. 4.4b), did not to affect the cooling much.

was obtained, in which the ΔT and t represent the temperature difference and the time respectively (see Fig. 4.4c). This fitted equation could then be seen as the temperature baseline for the mice in treated group.

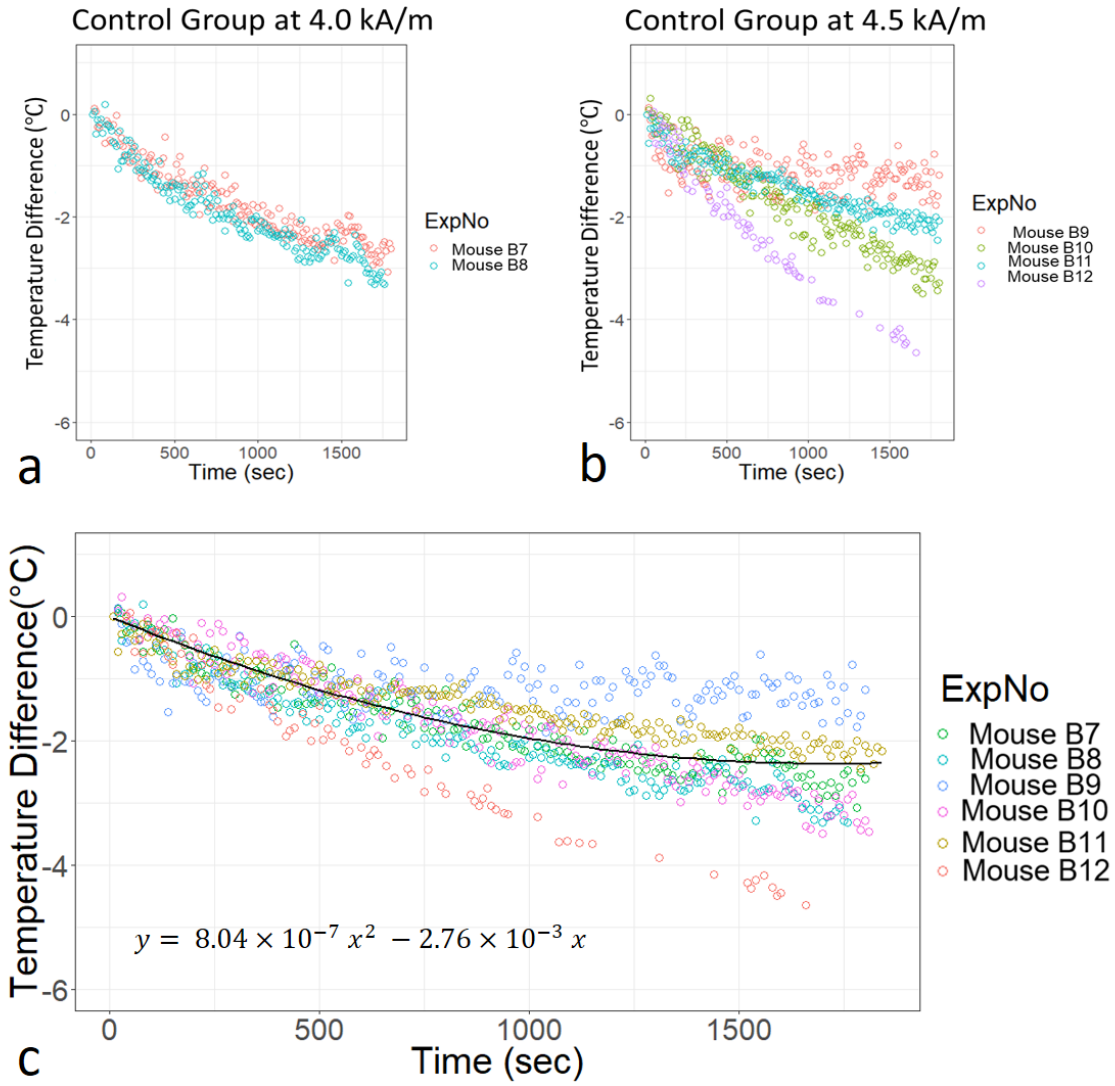

Figure 4.4: The temperature variation of mice in the control group. Two mice were applied with 4 kA/m (figure a), and other four were exposed to 4.5 kA/m field (figure b). All cooling curves were used for in poly regression analysis. The fitted equation of which was regarded as the baseline, which was used for correcting the heating curve in the treat group of every case in this preliminary study.

The Fig. 4.5 more clearly illustrates the effect of each element discussed above. Undoubtedly, the overall effect is of the utmost importance in magnetic hyperthermia because the overall temperature and duration of heating determine the severity of cellular damage; nevertheless, it is still beneficial to consider each phenomenon separately. By doing so, researchers will be able to adjust the experimental parameters accordingly.

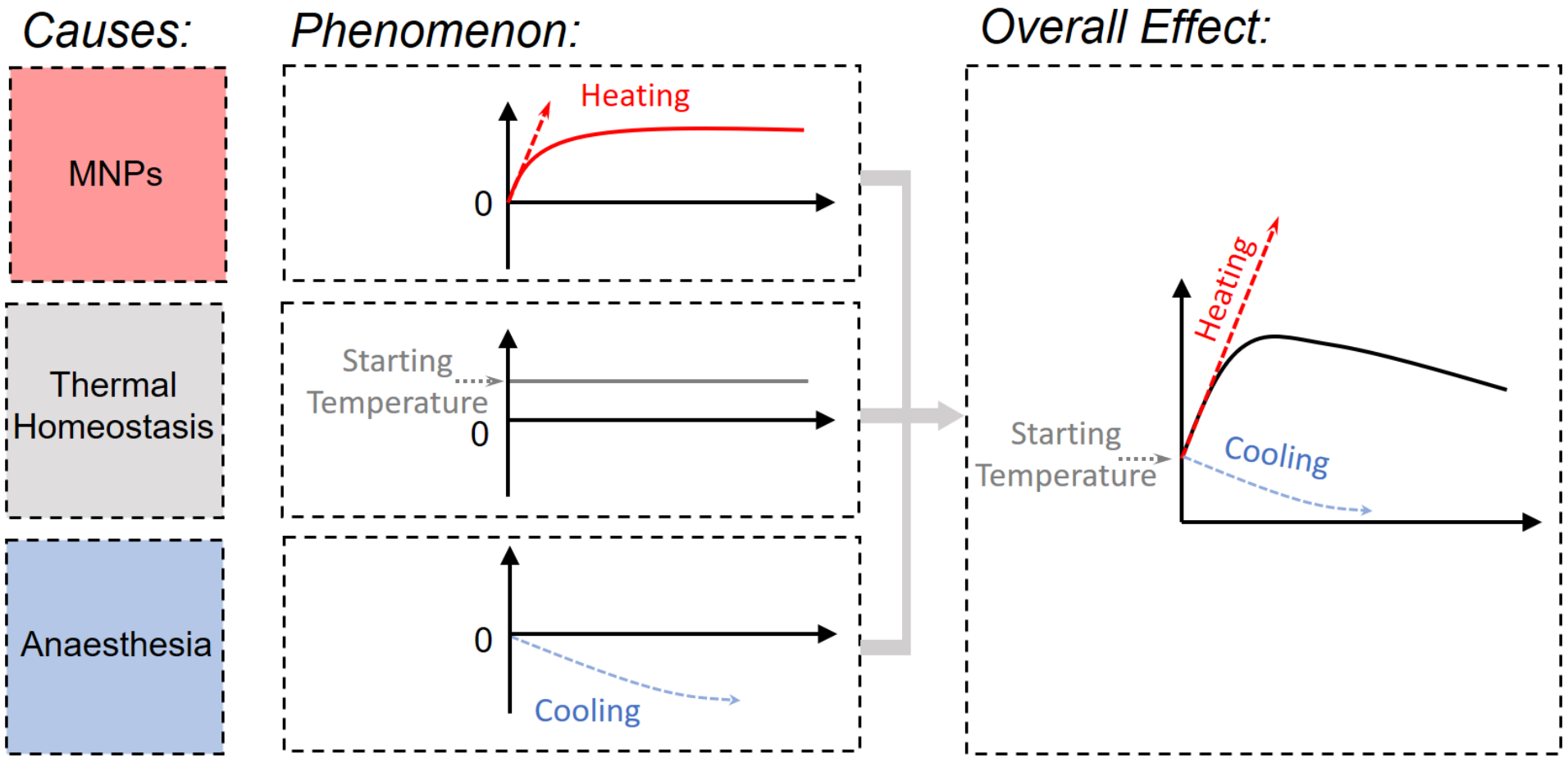

Figure 4.5: The overall effect of the three elements of temperature variation, which includes (1) the heating induced in MNPs, (2) the starting temperature associated with the thermal homeostasis of mice, and (3) the cooling due to anaesthesia.

For instance, if one wants to understand the magnetic heating caused by MNPs and ignore the cooling caused by anaesthesia, one can correct heating curves in Fig. 4.3 by subtracting them with the baseline temperature (the value at each time point was calculated from the fitted equation in Fig. 4.4c). The corrected heating curves are termed magnetic heating curves (see Fig. 4.6).

Apart from attaining the baseline temperature from the control group, an alternative method for removing the cooling effect is to measure the baseline temperature from another region of the same mouse. However, because the tumour's vessel structure tends to be different from the normal tissue, the blood perfusion rate in a tumour can be different from a normal tissue. As a result, the surface temperature of a tumour can be different from a normal tissue. In fact, some study suggests to use a infra-red thermal imaging to diagnose cancer [111]. Thus, to mitigate this issue, one can probably grow two tumours in a murine model, While one is treated with magnetic hyperthermia, the other can be seen as a control. This method has been used in the 4th experiment in this chapter.

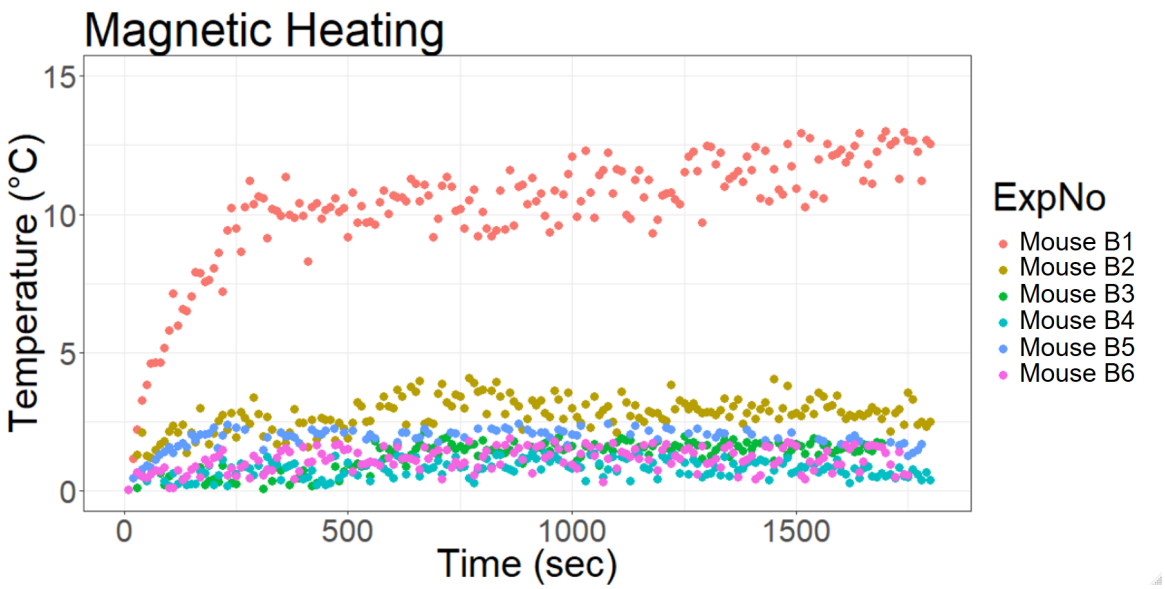

Figure 4.6: The corrected heating curve is called magnetic heating, i.e., the temperature variation associated with magnetic heating.

The understanding of temperature variation elements is helpful for later experiments. On the one hand, the next section describes the third experiment that examined the effect of thermal dose on the biological reaction, i.e. HSP70 induction. What has been measured by the thermal camera was the skin temperature of a tumour, which might be different from the intra-tumoural temperature. To consider each temperature variation element in the discussion of the experiment would be helpful.

On the other hand, the fourth experiment investigated in the effect of particle distribution. In which, both the starting temperature and the cooling effect would not be essential as they would not be affected by the particle distribution much. Mainly the magnetic heating curves (like those in Fig. 4.6) would be affected and thus will be specifically focused in Section 4.5.

4.3.3 Experimental Protocol

Based on the results of the two preliminary experiments, the experimental protocol was determined. The protocol is as below. The flow chart of the protocol is shown in Fig. 4.7.

Protocol: (1) Before the intratumoural injection, the tumour volume was measured. (2) one-third tumour volume of Perimag®-COOH suspension would be deposited into a tumour. The concentration of the suspension was 20 mg_{Fe}/ml. Because the particles may continue to disperse shortly after injection, each mouse was treated with a magnetic field 24 hours after the injection up to maximum dose at 2.0 mg_{Fe}. (3) The intensity and the frequency of the field were adjusted to be 4.5 kA/m and 690 kHz. The treatment lasted for 30 minutes.

This protocol was used in following experiments. Note that a fixed field intensity was used in this protocol. Consequently, if both the dispersion rate and the retention rate were constant in all the cases, then the temperature elevation would only depend on the amount of MNP injected. Because the injected MNP quantity depended on the tumour volume, the larger the tumour, the higher the temperature rise would be expected. Different temperature elevations lead to a wider range of thermal dose. It is beneficial when examining the correlation between the thermal dose and the induction of HSP70.

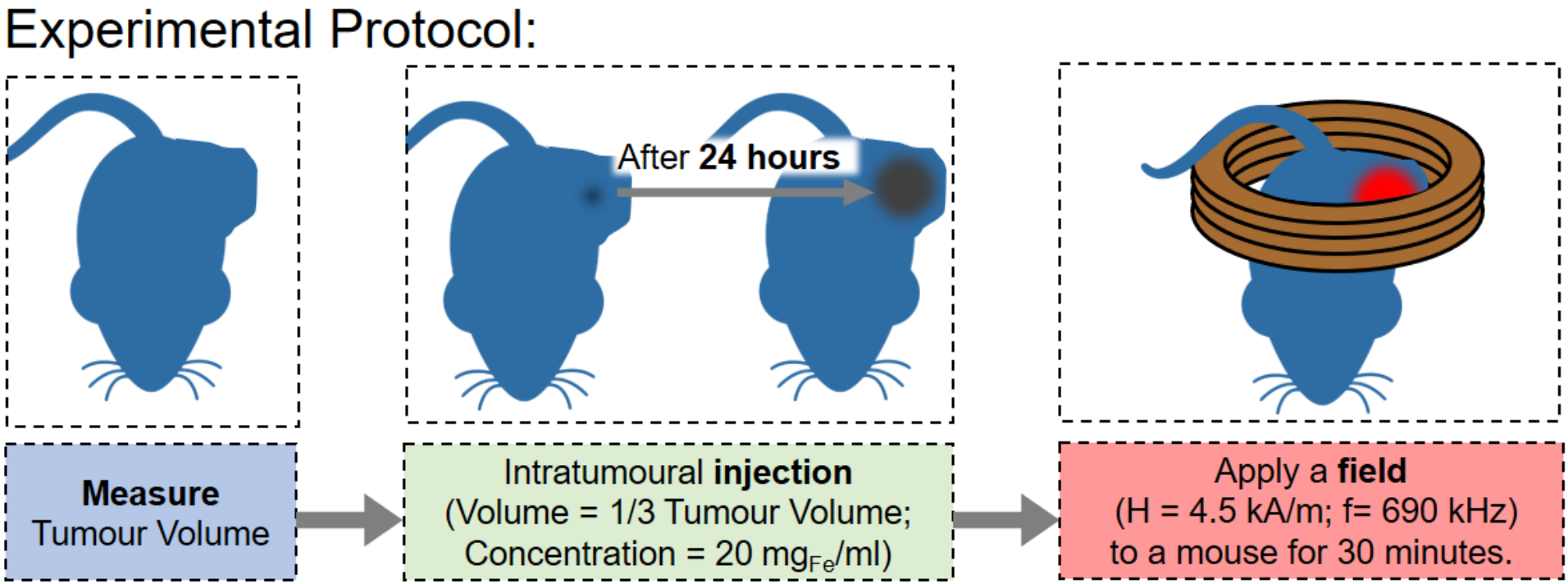

Figure 4.7: The experimental protocol. There are overall three steps: (1) tumour volume measurement, (2) intratumoural injection and waiting for 24 hours until the particle distribution was stable, and (3) applying an AMF.

4.4 Evaluation of Thermal Dose

The biological effect of heat has been reviewed in Section 2.1. In the section, two indicators for cellular damage have been introduced. The thermal dose, i.e., CEM43, is a temperature-based indicator that predicts the severity of cellular damage, while another indicator, HSP70, directly reflects the biological response of cells to the environmental stress, e.g., heat. With the aforementioned experimental setup and protocol, an experiment has been conducted to compare these two indicators. In theory, the predicative indicator, CEM43, should be correlated with the HSP70 level.

The materials and the experimental procedure are described in the following subsection. Then, the experimental results are presented and discussed afterwards.

4.4.1 Materials and Preparation

The experimental setup, the apparatus, the MNP material and the mouse model were described in Section 4.2. The injection volume of each sample is listed in Table 4.4.

Samples for the 3rd experiment

There were 11 mice in this experiment. Among them, 3 mice were in the control group and 8 of them were in the treated group. Those parameters, e.g., the volume of tumour, the injection volume of MNP suspension and the applied field, in treated group and in control group are presented in Table 4.4 and Table 4.5, respectively.

Label	Tumour Volume (mm^3)	Injection Volume (ml)	Particle Mass (mg_{Fe})	Field Intensity (kA/m)
C1	154	0.052	1.05	4.5
C2	337	0.100*	2.00	4.5
C3	90	0.031	0.61	4.5
C4	156	0.053	1.06	4.5
C5	59	0.020	0.40	4.5
C6	1052	0.100*	2.00	4.5
C7	281	0.096	1.91	4.5
C8	729	0.100*	2.00	4.5
Concentration of Perimag®-COOH is 20 mg_{Fe}/ml				

Table 4.4: The parameters of the **treat group** in the third experiment. The Perimag®-COOH of 20 mg_{Fe}/ml was injected into each mouse (*The maximum iron dose was limited to be 2 mg_{Fe}.)

Label	Tumour Volume (mm^3)	Field Intensity (kA/m)
C9	626	4.5
C10	51	4.5
C11	65	4.5

Table 4.5: The parameters of the **control group** in the third experiment. No MNP was deposited.

4.4.2 Experimental Procedure

The experimental procedure was as shown in Fig. 4.7. After the magnetic heating, the tumour of each mouse was dissected and kept for histological examination. The measurement result of HSP70 level from each tumour was kindly provided by Dr Thomas Carter.

4.4.3 Results and Discussion

The CEM43 and the HSP70 level in each mouse were measured and calculated. The following sections first describe the temperature variation in each case. Then, the

tumour temperature is later converted to CEM43. At the end of this subsection, a table compares the CEM43 with HSP70 level.

Temperature Variation

As indicated in Section 4.3.2, there are 3 temperature variation elements, which are (1) the magnetic heating, (2) the starting temperature and (3) the cooling effect.

The cooling effect can be estimated from those mice in the control group. The tumour temperatures of Mouse C09-C11 were fitted with a regression line (see Fig. 4.8). The fitted result is: $\Delta T = 3.20 \times 10^{-7} t^2 - 2.18 \times 10^{-3} t$. The equation represents the temperature change (ΔT) over time (t) caused by the anaesthesia.

The tumour temperature in the treated group are shown in Fig. 4.9a. After removing the variation caused by the cooling effect, the magnetic heating curve of each case is as presented in Fig. 4.9b.

There are two things worth mentioning. One is that the starting temperature of Mouse C06 was 37.5°C, which was approximately 2°C higher than others. Another is that the temperature increase in Mouse C02 was the strongest. The increase in Mouse C02 was 6°C, while temperature increases in others were below 3.75°C, i.e., the increase in Mouse C06.

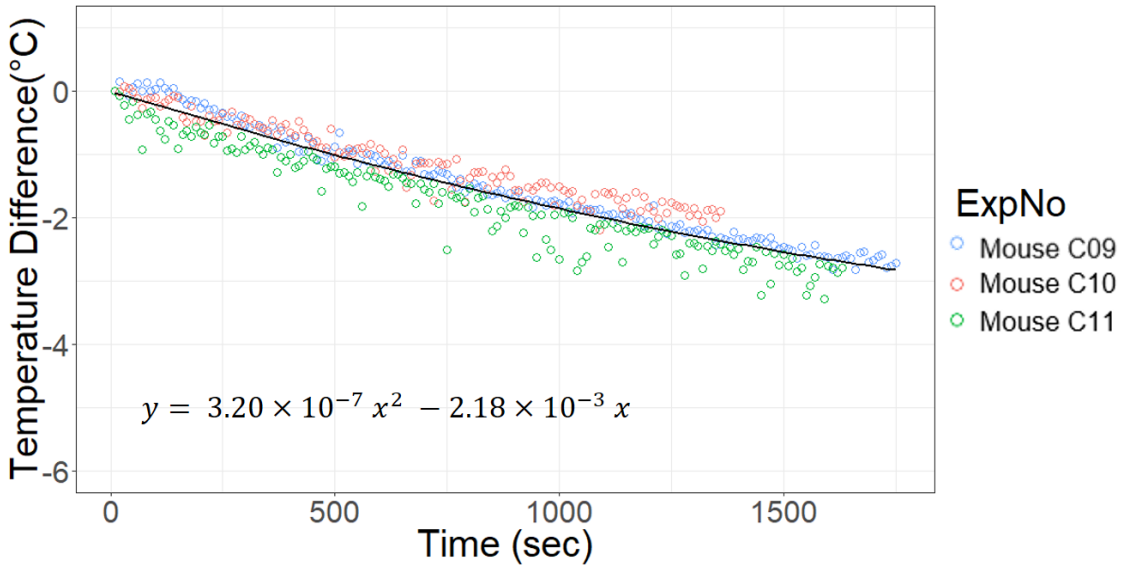

Figure 4.8: The temperature variation of Mouse C09-C11. The temperature curves was fitted with a regression line.

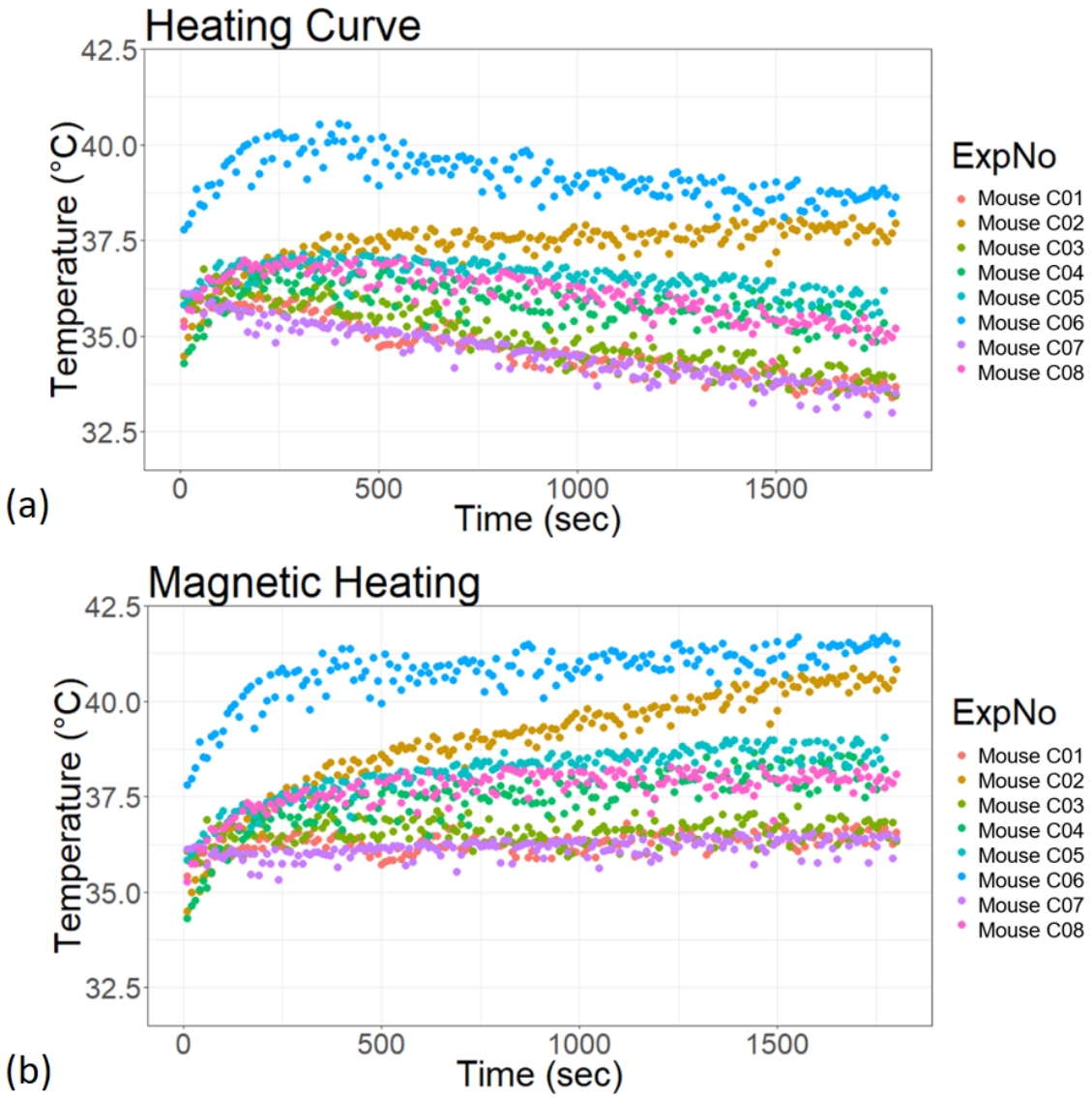

Figure 4.9: The maximum surface temperature of mice in the treated group, of which each figure represents (a) the heating curve, i.e., the absolute temperature over time, (b) the magnetic heating curves, i.e., the temperature variation in which was only associated with magnetic heating.

CEM43 at Skin

Based on Eq.2.2, the heating curves and the magnetic heating curves in Fig. 4.9 were converted to CEM43 and corrected-CEM43, respectively. The values of both the CEM43 and corrected-CEM43 of each case are presented in Table 4.6.

The thermal doses in all cases were low. The maximum thermal dose was only 1.9 minutes among them. At a glance, these thermal doses might be too low to induce HSP70 formation. But one should not ignore the exponential relationship between the thermal dose and the temperature (see Eq.2.2). As previously mentioned, the intratumoural temperature can be a few degrees higher than the skin temperature. This could lead to a huge difference in CEM43 between the tumour centre and the skin of a mouse. As shown in the FEA simulation in Chapter 3 (see Fig 3.16), while the CEM43 at the edge of MNP gel, i.e., at the edge of dispersion sphere, was as low as 20 minutes, the thermal dose at the centre could be above 600 minutes. Therefore, to see if the CEM43 is a good indicator to predict the HSP70 induction, it is important to estimate the intratumoural thermal doses of each case.

Label	CEM43 at the 30th minute	Corrected CEM43 at the 30th minute
	Treated Group	
C1	< 0.01	< 0.01
C2	0.02	0.35
C3	< 0.01	< 0.01
C4	< 0.01	0.02
C5	< 0.01	0.05
C6	0.20	1.90
C7	< 0.01	< 0.01
C8	< 0.01	0.02

Table 4.6: The thermal doses at the end of each experiment (at the 30th minute), which includes the CEM43 derived from the heating curve and the corrected-CEM43 derived from magnetic heating.

Intratumoural Thermal Dose

To attain the intratumoural thermal doses, Eq. 4.1 and Eq. 4.2 were deployed to estimate the intratumoural temperature. To better understand the estimation model, a schematic diagram is presented in Fig. 4.10. In this study, the skin thickness was assumed to be 1.5 mm. Other parameters such as the tumour volume and the injection volume listed in Table 4.4 were also used in the calculation. Note that the dispersion rate was assumed to be 3. That is, the dispersion volume is 3 times of the injection volume (the dispersion sphere radius can then be calculated). Based on these parameters together with the skin temperatures in Fig. 4.9b, the intratumoural temperatures at different r were derived.

Afterwards, the concept of CEM43-Tx mentioned in Section 2.1.2 was used to evaluate the heating condition. As discussed earlier, instead of the thermal dose of a single point, a regional thermal dose like CEM43-T90 is more commonly used in the literature to represent the heating condition of a subject. The accumulated CEM43-T90 of each mouse was derived and listed in Table 4.7.

Label	Accumulated CEM43-T90 (minutes)	Accumulated Activation Time (minutes)
C1	0.01	0.00
C2	12.15	22.17
C3	0.01	0.00
C4	0.23	2.67
C5	0.81	7.17
C6	68.09	29.00
C7	0.00	0.00
C8	0.46	1.67

Table 4.7: The accumulated CEM43-T90 and the activation time at the end of each experiment (at the 30th minute)

Activation Time

In addition to CEM43-T90, another indicator Activation Time was considered here. The activation time (see Section 3.3.3) represented how long the duration was when any part of the tumour had the temperature above 43°C.

Both the CEM43-T90 and the activation time are indicators derived from the heating curve of the target, and they are both design to indicate the intensity of hyperthermia. While the equation of the CEM43-T90 is derived from the empirical study of cell death, the activation time is proposed to indicate the increasing treated area along with time.

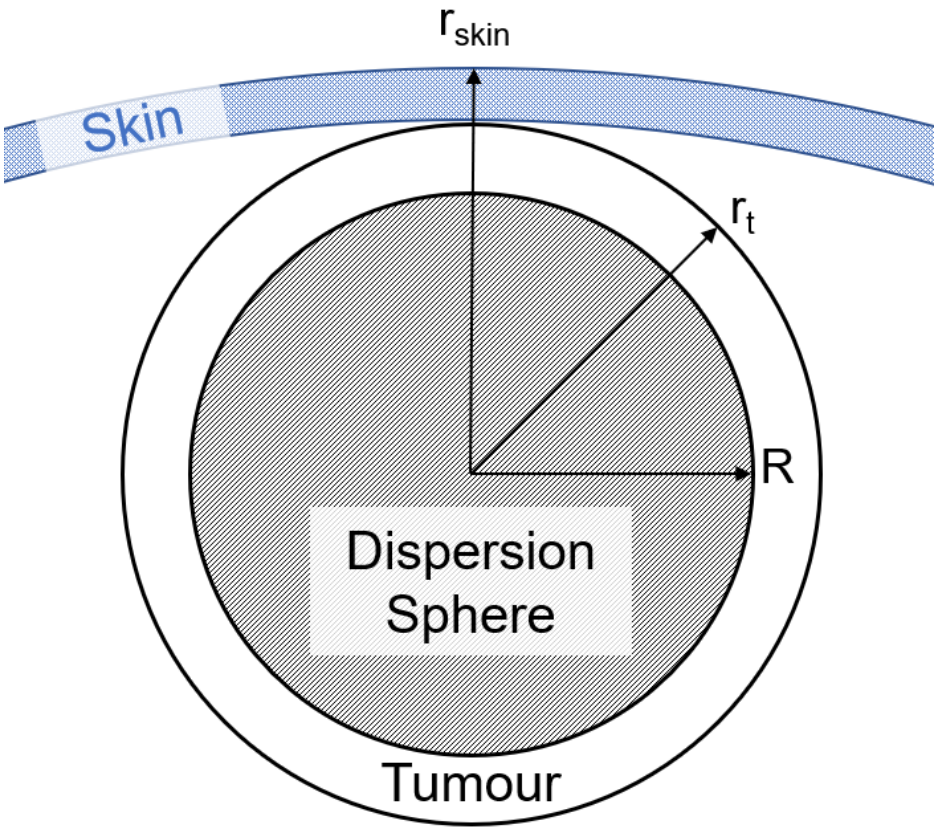

Figure 4.10: The schematic diagram of a subcutaneous tumour. The parameters r_{skin} and r_t represent the distances from the centre to the skin and the edge of tumour respectively. The parameter R is radius of dispersion sphere. The skin thickness was assumed to be 1.5 mm in all cases, i.e., $r_{skin} - r_t = 1.5$ mm.

HSP70 Level

After each hyperthermia experiment, the tumour of each mouse was dissected. The separated tumour was then placed in 10 % PBS (phosphate-buffered saline) based formalin solution. After 24 hours the samples were placed in paraffin blocks, which were later handed to UCL Institute of Neurology IQPath. With the help from Angela Richar-Londt, these samples were sliced and stained in IQPath.

There were 3 stains being applied: (1) H&E (hematoxylin and eosin stain) stain, (2) Prussian blue stain and (3) IHC (immunohistochemistry) stain. The H&S, Prussian blue and IHC were used to respectively visualise cell nuclei, MNPs and HSP70.

These stained samples were analysed via digital image analysis of whole slide images (WSI). The amount of cell nuclei in each sample was first counted. This was regarded as the background. Then, the HSP70 was counted. The examined result was expressed as the HSP70 level. The HSP70 level in each case was quantified based on the percentage of the number of HSP70 and the number of cells of the histological sample. The HSP70 level relative to the slice area in each case is presented in Table 4.8.

Note that HSP70 existed in cells even if there was no stimulus. The background HSP70 level was shown in untreated mice, i.e., Mouse C09-C11. The background level of HSP70 could be as high as 1.1%.

By comparing the background HSP70 level to those HSP70 levels in treated mice, one could notice that HSP70 levels in Mouse C01 and C07 were lower than the background level, i.e., 1.1%. Slightly higher HSP70 levels were found in Mouse C03, C04, C05 and C08. The values were between 1.1% and 1.6%. The rest two mice, i.e., Mouse C02 and C06, had particularly high HSP70 levels, which were 7.1% and 5.1 % respectively.

If the sample was treated with whole body hyperthermia, the HSP70 relative to slice area could be representative. However, in the case of this experiment, the injection volume is similar to or smaller than the tumour volume. If one wants to examine the thermally induced HSP70 level, one needs to convert this HSP70 level to **HSP70 level relative to dispersion level**. This could be simply done by multiplying **the HSP70 level relative to the area of whole slice** with **the ratio** r_t^2/R^2. These parameters are listed in Table 4.8. For the discussion in the later sections, the **HSP70 level** would all refer to **the HSP70 level relative to dispersion area**.

Label	The HSP70 Level relative to slice area (%)	r_t (mm)	R (mm)	The HSP70 Level relative to dispersion area (%)
	Treated Group			
C1	0.5	3.83	3.35	0.7
C2	7.1	4.82	4.15	9.6
C3	1.3	3.28	2.80	1.8
C4	1.1	3.84	3.36	1.4
C5	1.6	2.92	2.43	2.3
C6	5.1	6.81	4.15	13.7
C7	0.2	4.56	4.09	0.2
C8	1.5	6.08	4.15	3.2
	Control Group			
C9	0.1			
C10	0.1			
C11	1.1			

Table 4.8: The HSP70 level relative to slice area of each case was converted to the HSP70 level relative to slice area based on the ratio of r_t^2/R^2

Comparison among Intratumoural Thermal Dose, Activation Time and HSP70 Level

Based on Table 4.7 and Table 4.8, the CEM43-T90 of each case was compared with HSP70 level. The comparison is presented in Fig. 4.11a. In the figure, a clear correlation has been found between these two parameter. This correlation suggests that the predictive indicator CEMT43-T90 was able to estimate the HSP70 level. Approximately, the CEM43-T90 increased exponentially with HSP70 level. This exponential correlation might be because that CEM43-T90 was sensitive to temperature, while HSP70 formation responses more mildly to the change in temperature.

In addition, it is also interesting to compare the HSP70 level with the Activation Time (see Table 4.7). The comparison is illustrated in Fig. 4.11b. A linear correlation has been found between them. This linear relationship may be because that both parameters are related to the treated area.

On the one hand, the Fig. 3.15b shows that the Activation Time can be used to approximate the increase in treated area. On the other hand, the examination of HSP70 level was based on slices of tumours. Supposedly, the larger the treated area, the more the HSP70 would be induced. Thus, apart from CEM43-T90, the Activation Time can also be an indicator for evaluating hyperthermia treatment.

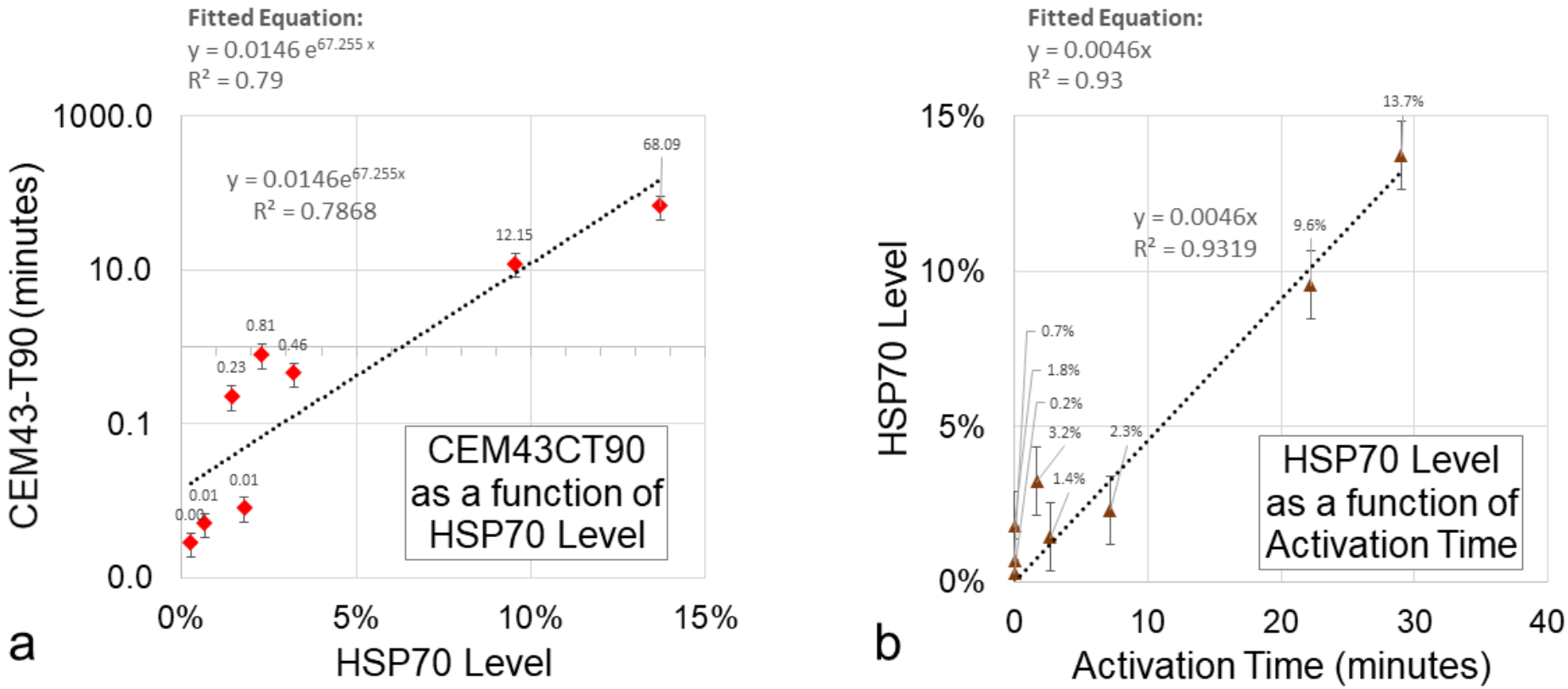

Figure 4.11: (a) The correlation of the predicative CEM43-T90 and the measured HSP70 level. (b) The correlation of HSP70 level and the activation time.

4.5 The Effect of Particle Distribution on Temperature

In the previous section, the particle distribution of MNPs was assumed to be identical in all cases. Nonetheless, when exposing to a same magnetic field, different temperature increases were found in cases deposited with the same amount of MNPs. The difference in temperature increase might be caused by the difference in particle distribution. As indicated in the Chapter 3, the particle distribution has an evident effect on the temperature distribution in the phantom.

An attempt had been made in this chapter to examine the *in-vivo* particle distribution. The particle distribution was visualised by a CT scanner. Then, the particle distribution of each case was compared with the temperature distribution that measured by thermal camera.

4.5.1 Materials and Preparation

Samples for the 4th experiment

There were 5 mice in this experiments, i.e., the fourth experiment. In terms of the experimental materials and preparation, two things were different from the third experiment.

Firstly, to be more cost effective, two tumours were grown on each mouse. One of the tumours was seen as the control, while the other tumour was treated. Secondly, because most the temperature elevations in the previous experiment were not evident, the concentration of Perimag®-COOH was increased from 20 mg_{Fe}/ml to 40 mg_{Fe}/ml in order to acquire a more observable temperature variation. For the safety of mice, the dose limit of MNPs was set to be 2 mg_{Fe}, i.e., the maximum injection volume was 0.05 ml. These parameters are listed in the table below.

Label	Injection Volume (ml)	Particle Mass (mg_{Fe})	Field Intensity (kA/m)
D1	0.020	0.8	4.5
D2	0.050	2.0	4.5
D3	0.035	1.4	4.5
D4	0.050	2.0	4.5
D5	0.040	1.6	4.5
Concentration of Perimag® COOH is 40 mg_{Fe}/ml			

Table 4.9: The injection volume of the treated tumours and the applied field in each case in the fourth experiment. The Perimag® COOH of 40 mg_{Fe}/ml was injected and the dose limit was 2 mg.

CT Scanner

The CT scanning was acquired by nanoScan PET/CT from Mediso Limited. (Budapest, Hungary). The photo of the scanner is shown in Fig. 4.12. Each mouse was scanned using a 50 kVp and 300 ms exposure time in 720 projections. The acquisition time of each case was 8 minutes. The voxel size was 112 x 112 x 112 μm.

Data Handling of CT Images

The CT image was reconstructed with Nucline software (Mediso Limited.). Three-dimensional (3D) visualization were performed by using VivoQuant from Invicro LLC. (Boston, USA). Image analysis and quantification of MNPs were completed with Mango - v4.0.1 (Research Imaging Institute, The university of Texas Health Science Centre).

Figure 4.12: The photo of nanoScan PET/CT scanner and the anaesthesia machine used during the scanning process.

4.5.2 Experimental Procedure

The experimental setup was as described in Fig. 4.1. The experimental protocol was similar to that described in Fig. 4.7, but with two differences. The first difference was the concentration of MNP suspension. The concentration in this experiment was 40 mg_{Fe}/ml instead of 20 mg_{Fe}/ml. The second difference was that each mouse was imaged by a CT scanner just before the magnetic heating.

4.5.3 Results and Discussion

The temperature distribution and particle distribution were respectively measured by the thermal camera and the CT scanner. Experimental results are presented into three 3 individual subsections, which are related to (1) thermal and CT images, (2) the temperature variation, and (3) the quantification of MNPs in each case. Discussions on experimental results are presented at the end.

Thermal and CT images

The CT images of Mouse D1-D5 are individually illustrated in Fig. 4.13b - Fig. 4.17b. In those figures, the locations of the MNPs are indicated with red dashed lines. The local maximum intensity of CT images, quantified by Hounsfield units (HU), is also labelled by a red cross. Overall, Mouse D1 and D2 had relatively higher values in CT number. Their maximum CT numbers were 1440 HU and 1234 HU respectively. The remaining 3 mice had local maximum CT numbers ranged from 646 HU to 675 HU. The report by Attaluri has indicated that a linear correlation exists between the MNPs concentration in tissue and the HU of CT images [10]. Based on which, one may claim that the local maximum concentration of MNPs in Mouse D1 and D2 were up to twice as high as that in Mouse D3-D5.

As to the thermal images, the thermal image (at the 17th minute) of each case is respectively presented in Fig. 4.13a - Fig. 4.17a. By applying the same visualisation technique used in Fig. 3.10, these thermal images could be converted to Fig. 4.13c - Fig. 4.17c respectively. Each figure represents the temperature profile on L1 on each mouse along with time. These figures point out that the temperature gradients of Mouse D1 and D2 were higher than that of the remaining cases. These findings agree with the readings of CT images (high local concentrations did not only result in high CT numbers, but also caused high temperature gradients).

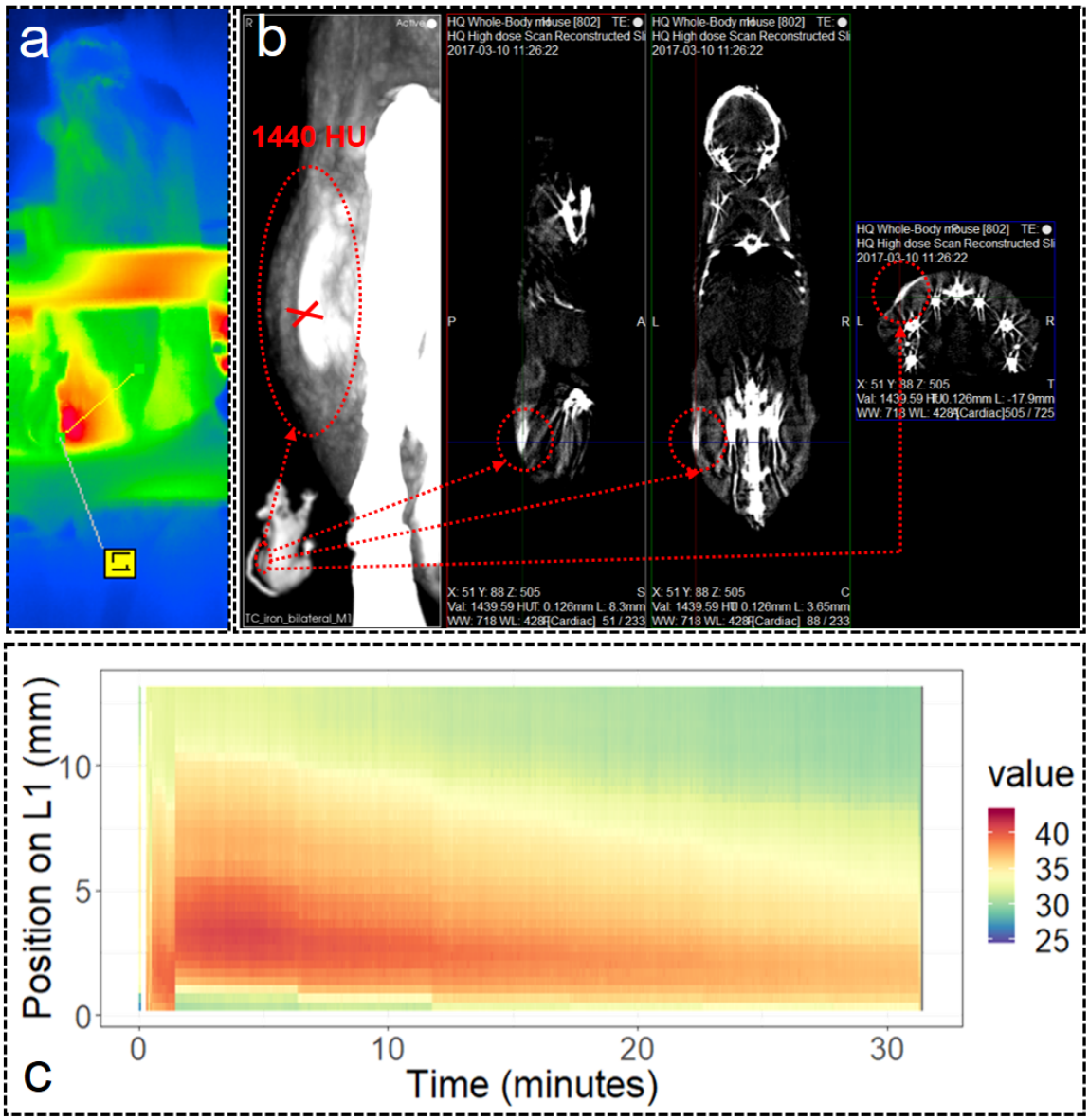

Figure 4.13: Mouse D1. (a) The thermal image at the 17th minute. (b) CT images. (c) The temperature profile on L1 along with time.

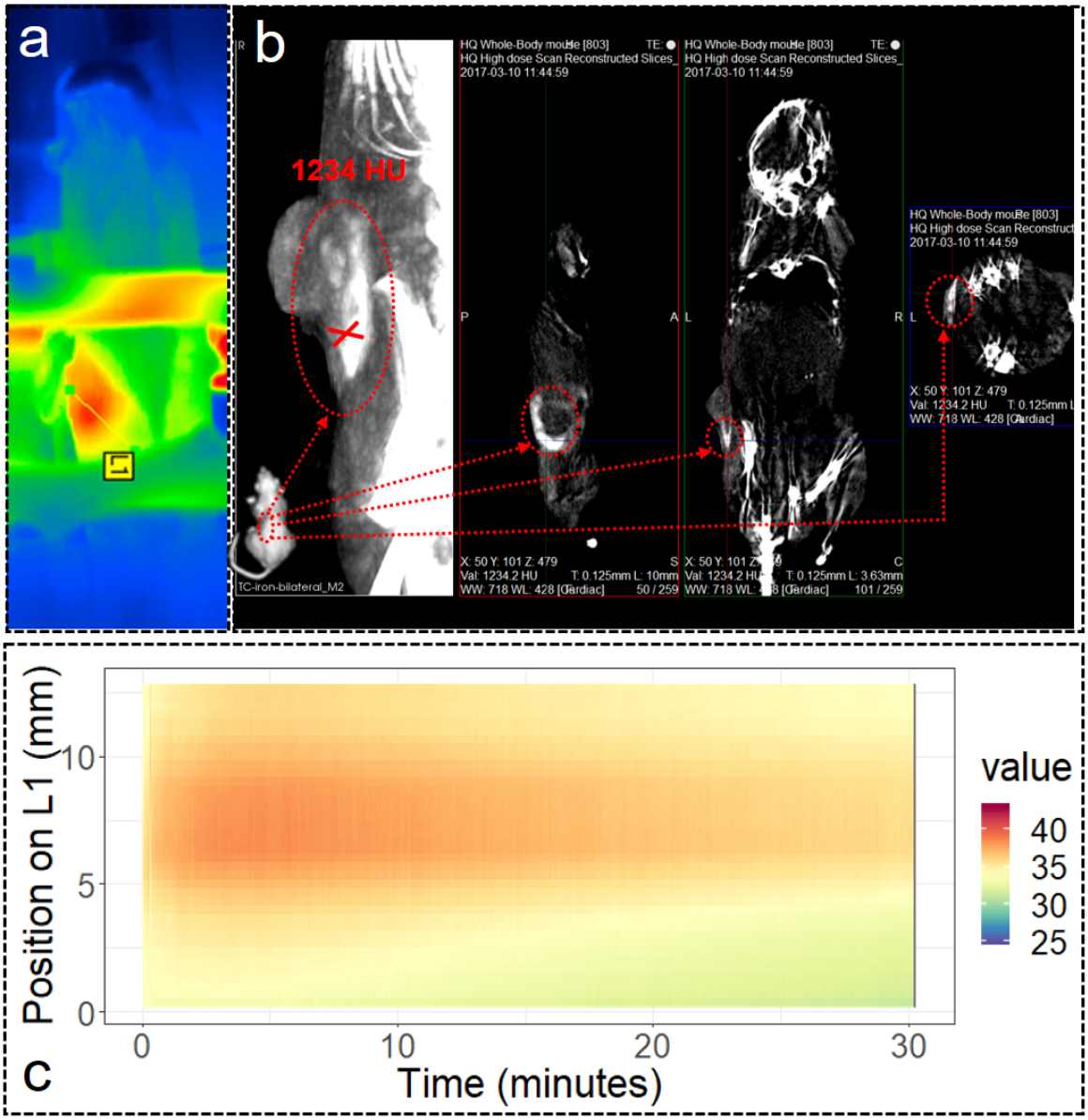

Figure 4.14: Mouse D2. (a) The thermal image at the 17th minute. (b) CT images. (c) The temperature profile on L1 along with time.

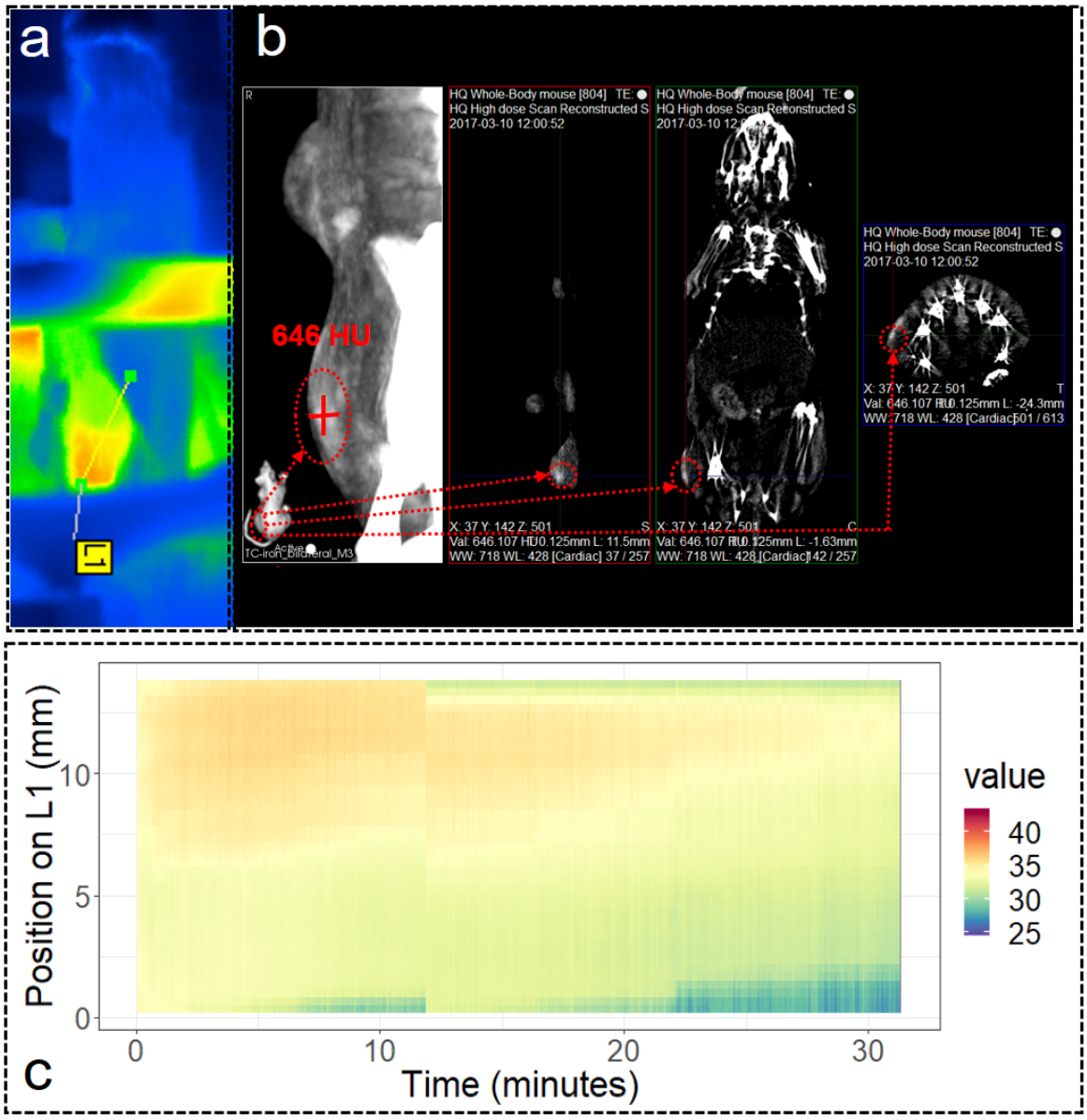

Figure 4.15: Mouse D3. (a) The thermal image at the 17th minute. (b) CT images. (c) The temperature profile on L1 along with time.

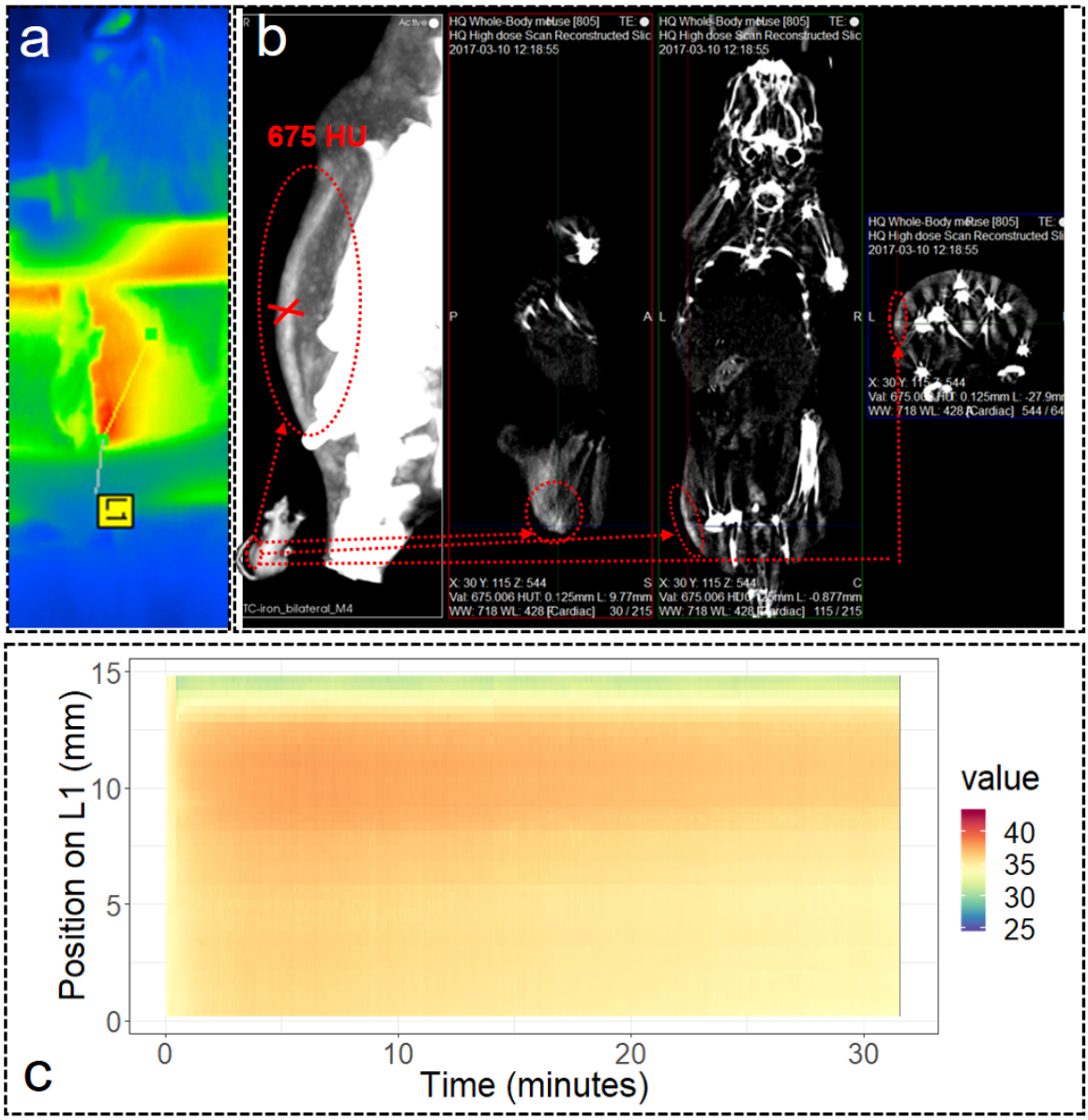

Figure 4.16: Mouse D4. (a) The thermal image at the 17th minute. (b) CT images. (c) The temperature profile on L1 along with time.

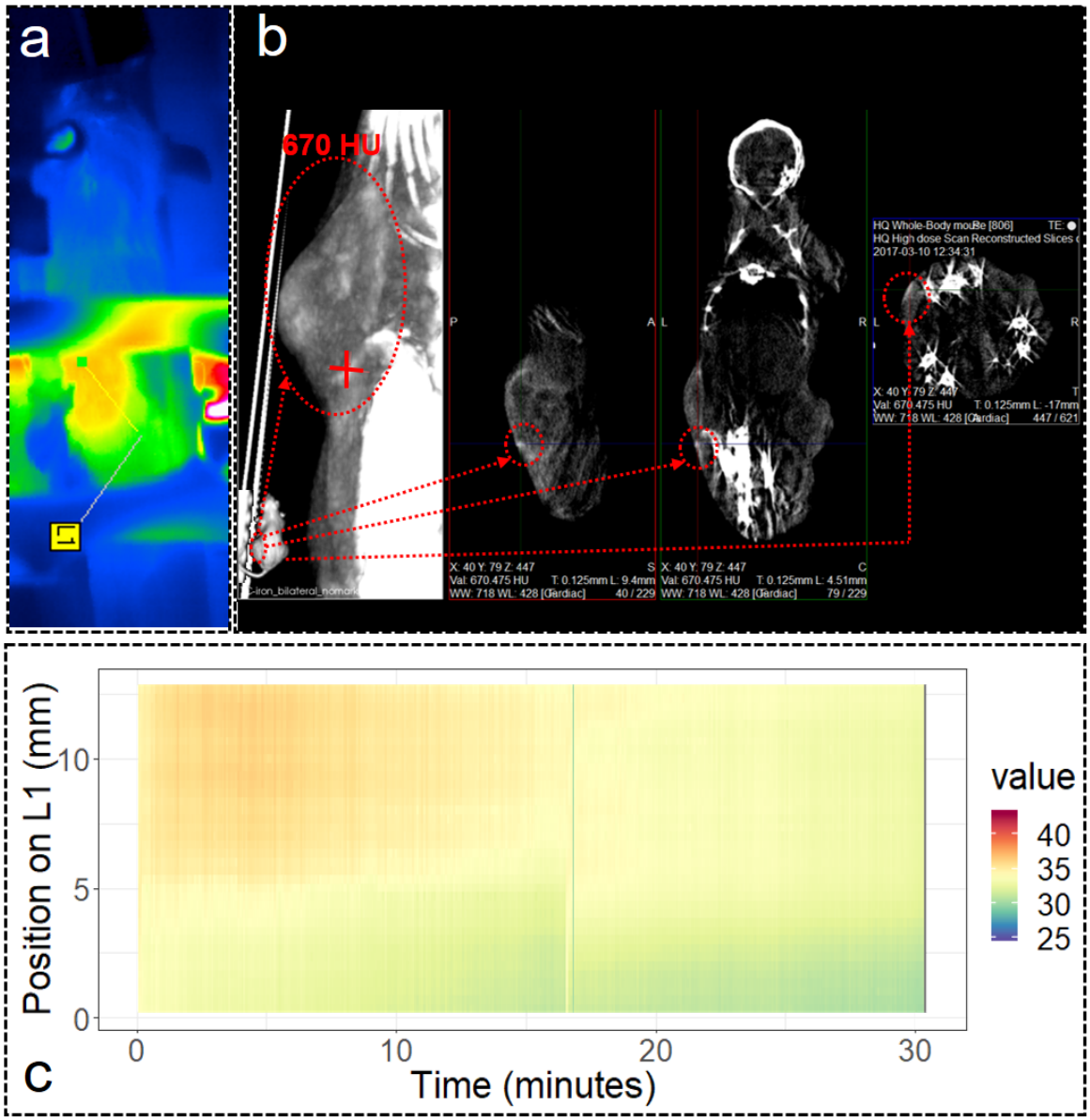

Figure 4.17: Mouse D5. (a) The thermal image at the 17th minute. (b) CT images. (c) The temperature profile on L1 along with time.

Temperature Variation

The data handling of thermal images was the same as described previously (see Section 3.3.1). The maximum surface temperature over time was seen as the heating curve of each case. On the one hand, the heating curve of the untreated tumour (see Fig. 4.18) was regarded as the baseline. On the other hand, the heating curve of the treated tumour (see Fig. 4.19a) consisted of three elements, i.e., magnetic heating, starting temperature and cooling effect. By subtracting the baseline from the heating curve, one would obtain a temperature difference that was only associated with the magnetic heating. The temperature difference was then depicted in Fig. 4.19b.

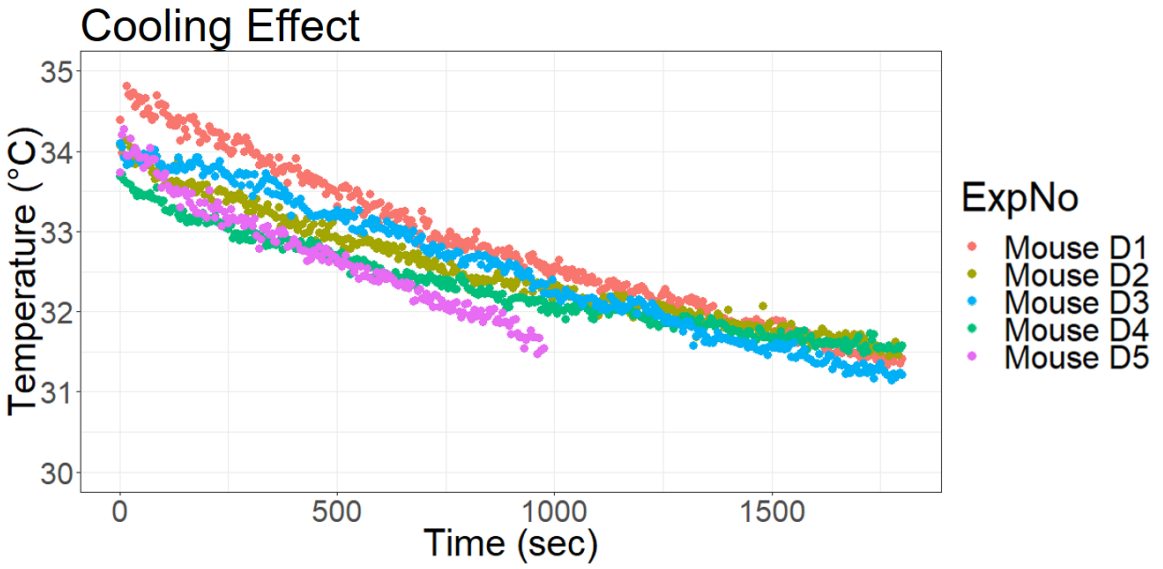

Figure 4.18: The temperature variation of the **untreated tumour** in each mouse in the fourth experiment. Note that a part of the temperature of Mouse D5 was missing due to the movement of the mouse during the experiment. The temperature of its untreated tumour failed to be detected by the thermal camera after the movement.

It is worth pointing out a phenomena in the temperature variation. The temperature increase in Mouse D1 was unexpectedly high. While the iron amount in Mouse D1 (0.8 mg_{Fe}) was the lowest, its heating performance was the strongest. The increase in Mouse D1 quickly reached 6.5 °C after 250 seconds, while no increase in other cases exceeded 5 °C over the whole treatment. That is, the high injection volume of MNP suspension did not guarantee high heating performance. This phenomenon was most likely caused by the particle distribution. A further discussion on this would be given in the following section.

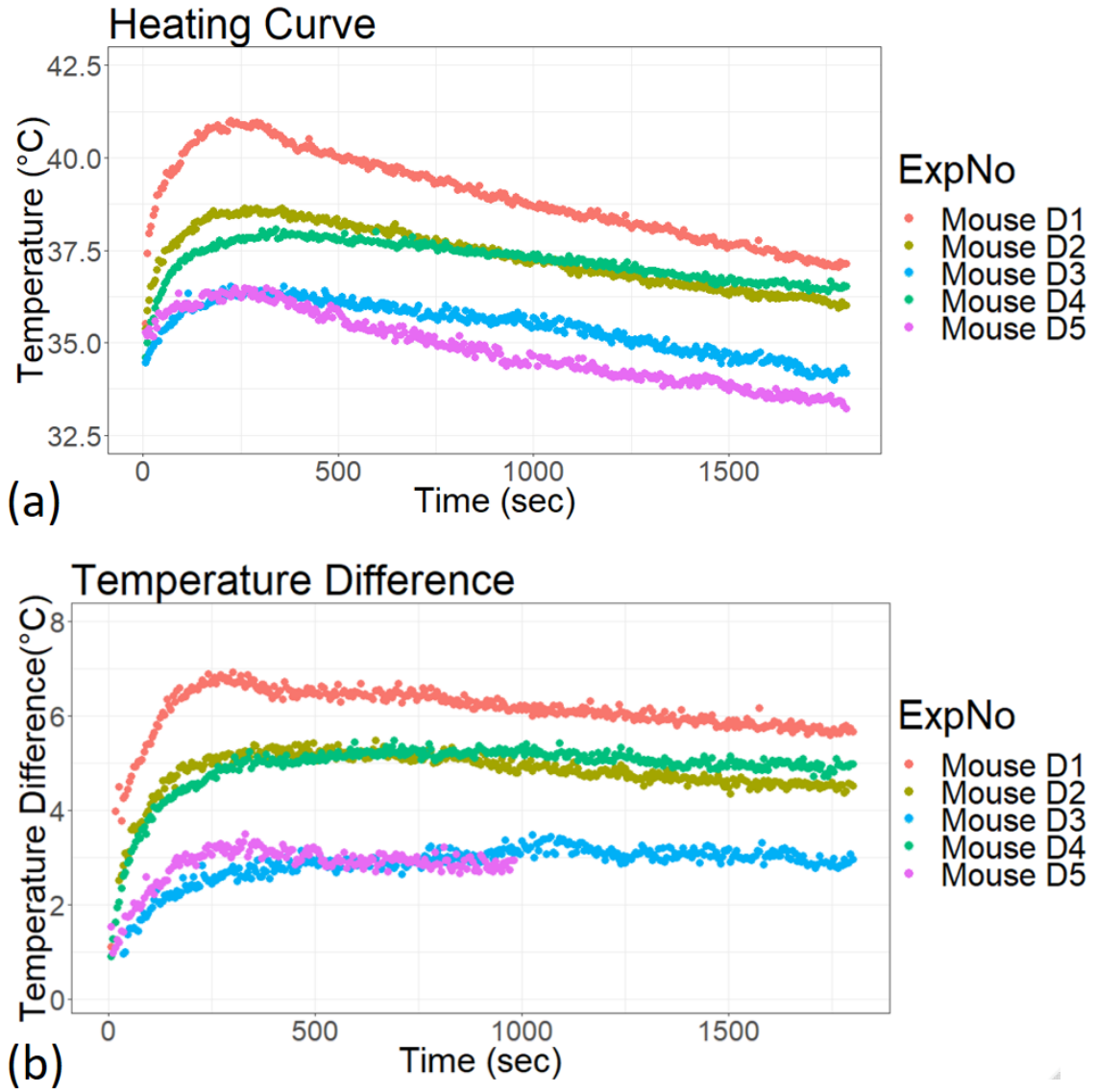

Figure 4.19: The temperature variation of treated tumour on each mouse. (a) The heating curves of treated tumours. (b) The temperature increase in treated tumours caused by magnetic heating, i.e., the temperature variation that associated with magnetic heating. Note that a part of untreated tumour temperature of Mouse D5 was missing, because of the movement of Mouse D5 during the experiment. The temperature difference of which was only calculated for the first 1000 seconds.

Quantification of MNPs

The CT number of each part of a body is different. The CT number of bones can be more than a thousand HU, which is much higher than that of soft tissues like muscles, the value of which is usually just a few hundreds HU.

To quantify the MNPs, the first step is to address the question: **can we distinguish MNPs from other tissues in CT images?** To answer this, the author selected the sagittal plane presented in Fig. 4.13b as an example. This slice of CT image was selected because the CT number of MNPs on this CT image was the highest, i.e., 1440 HU, among the five cases.

The region of the tumour deposited with MNPs was labelled with a green circle, while the region of another tumour on the right hand side was labelled with a red circle (see Fig. 4.20b). As the latter did not have MNPs present, it was considered a control. The region within each circle is commonly termed as Region of Interest (ROI) in the literature. The box diagram and the histogram of the HU values in both ROIs are respectively presented in 4.20a and 4.20c.

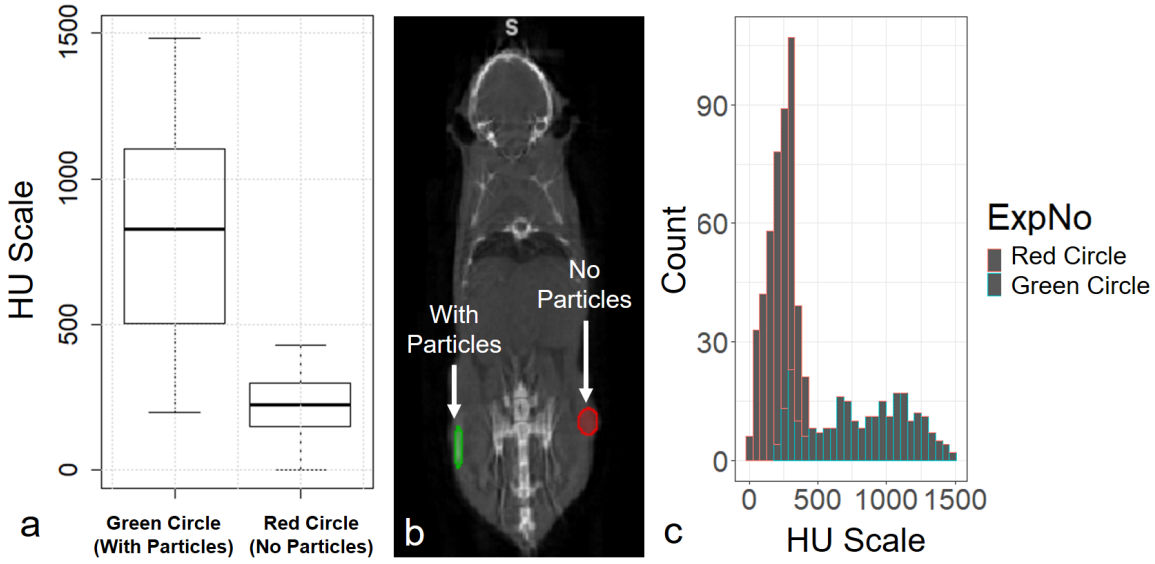

Figure 4.20: The data handling of CT number for the quantification of MNPs. The green and red circles represent the region with and without MNPs. (a) The box diagram of the HU values within green and red circles. (b) The sagittal plane of the CT scan of Mouse D1. (c) The histogram of the HU values within the green and red circles.

Let us take a look at Fig. 4.20a. The upper bound of the red ROI was 430 HU. Because the only difference between two ROIs was the presence of MNPs, one can

then be confident to claim that the CT number within the green ROI, ranged from 430 HU to 1440 HU, was associated with the presence of MNPs. Nevertheless, we could not rule out the possibility of having MNPs in those areas with the CT number less than 430 HU. To be more specific, in those areas, the MNPs might still exist but they had little influence to the CT number due to their low concentration. This made it difficult to distinguish all the signal caused by MNPs from the background signal.

From another perspective, the low concentration does not only have little effect on CT number but also have a limited heating ability. The temperature variation during the hyperthermia was dominated by concentrated MNPs. For the objective of improving thermal management, the quantification of high concentration MNPs was still valuable.

In this experiment, two parameters were required for the quantification of MNPs, which were (1) the volume of tissues deposited with MNPs, i.e., particle dispersion volume, and (2) *in-vivo* MNP concentration. Both are introduced below.

Particle Dispersion Volume To quantify the MNPs, a layer of ROI (indicated with red colour in Fig. 4.21) with the threshold of 430 HU was added to each CT model. Afterwards, other layers of ROI with the thresholds from 500 HU to 1100 HU with a step of 100 HU were respectively added to each case. The results are visualised in Fig. 4.21. The volume of ROI (where the CT number is $>$ 430 HU) of each case can be estimated according to the number of voxels, the value of which is listed below each CT model in the same figure. Each value represented the particle dispersion volume of each case.

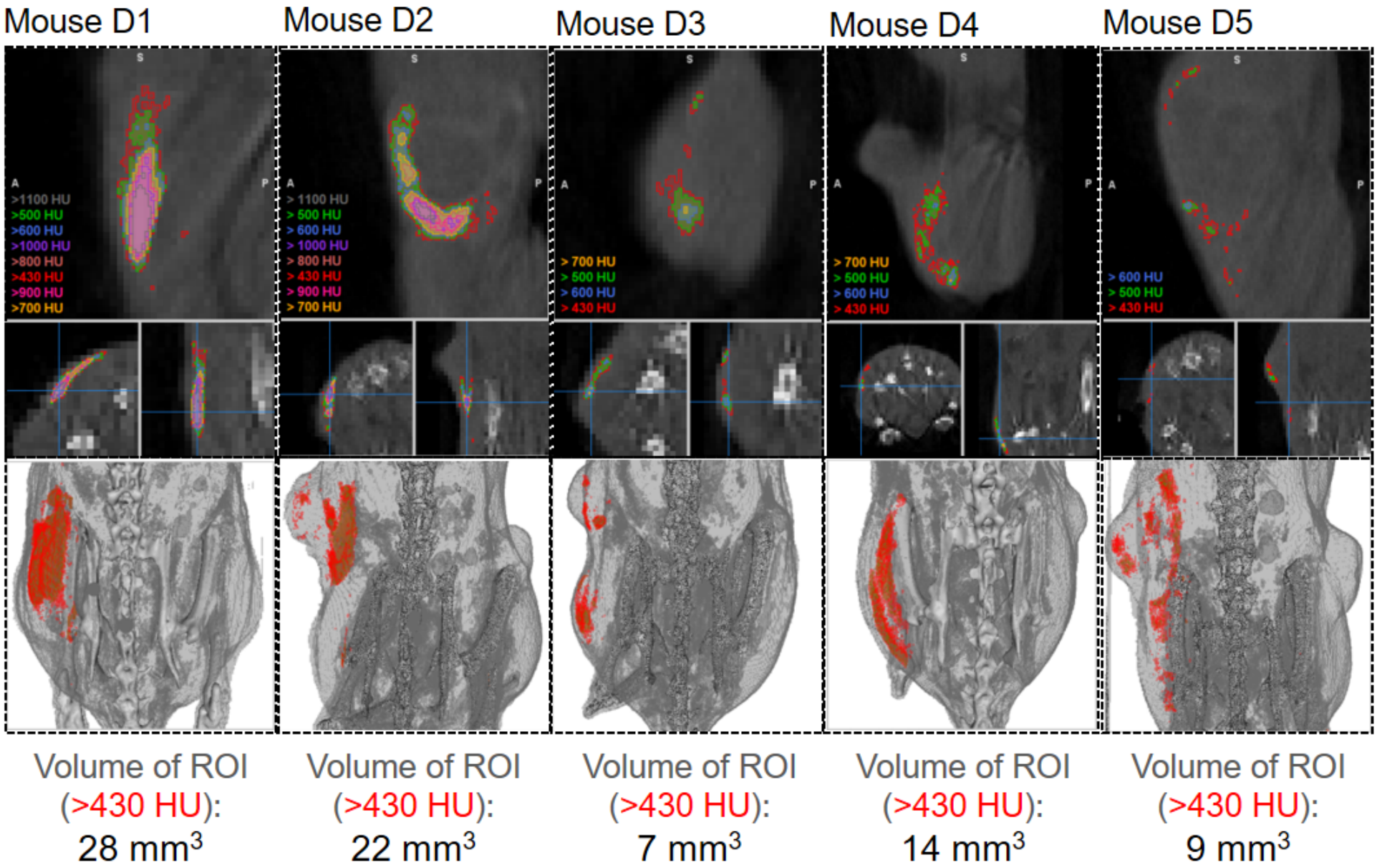

Figure 4.21: The CT image of each case added with a number of layers of ROI, and the thresholds of which ranged from 430 HU to 1100 HU.

In-vivo Concentration of MNPs To quantify MNPs, one still needs to know the *in-vivo* concentration of MNPs. Here, to demonstrate the feasibility of quantifying MNPs *in-vivo*, the author presumed that the maximum measured CT number, i.e., 1440 HU, was identical to the injection concentration, i.e., 40 mg_{Fe}/ml. The CT number of the area with no MNPs deposited was assumed to be 0 HU. As a consequence, the MNP concentration and CT number conversion would be $40/1440 = 0.028$ $mg_{Fe}/(ml_{tissue}.HU)$. Then, the CT number of 430 HU would then be referred to the MNP concentration of 12.04 mg_{Fe}/ml_{tissue}.

Following upon the analysis, the distribution of MNP concentrations of each case can be estimated. The estimation was done based on the distribution of CT number presented in the box diagram in Fig. 4.21. The CT numbers were converted to the concentration of MNPs based on the conversion ratio, i.e., 0.028 $mg_{Fe}/(ml_{tissue}.HU)$. The distribution of CT number and the associated concentration are plotted as a box diagram in Fig 4.22a.

The Estimation of MNPs based on CT Numbers The estimation of MNP mass was done based on three values, which are (1) the mean value of CT number presented in Fig 4.22a, (2) the dispersion volume of MNPs in Fig. 4.21, and (3) the conversion ratio, i.e., 0.028 $mg_{Fe}/(ml_{tissue}.HU)$. The quantity of MNPs in each case, estimated by CT numbers, can then be attained by multiplying these three values. The estimated mass of MNPs is presented in Fig. 4.22b.

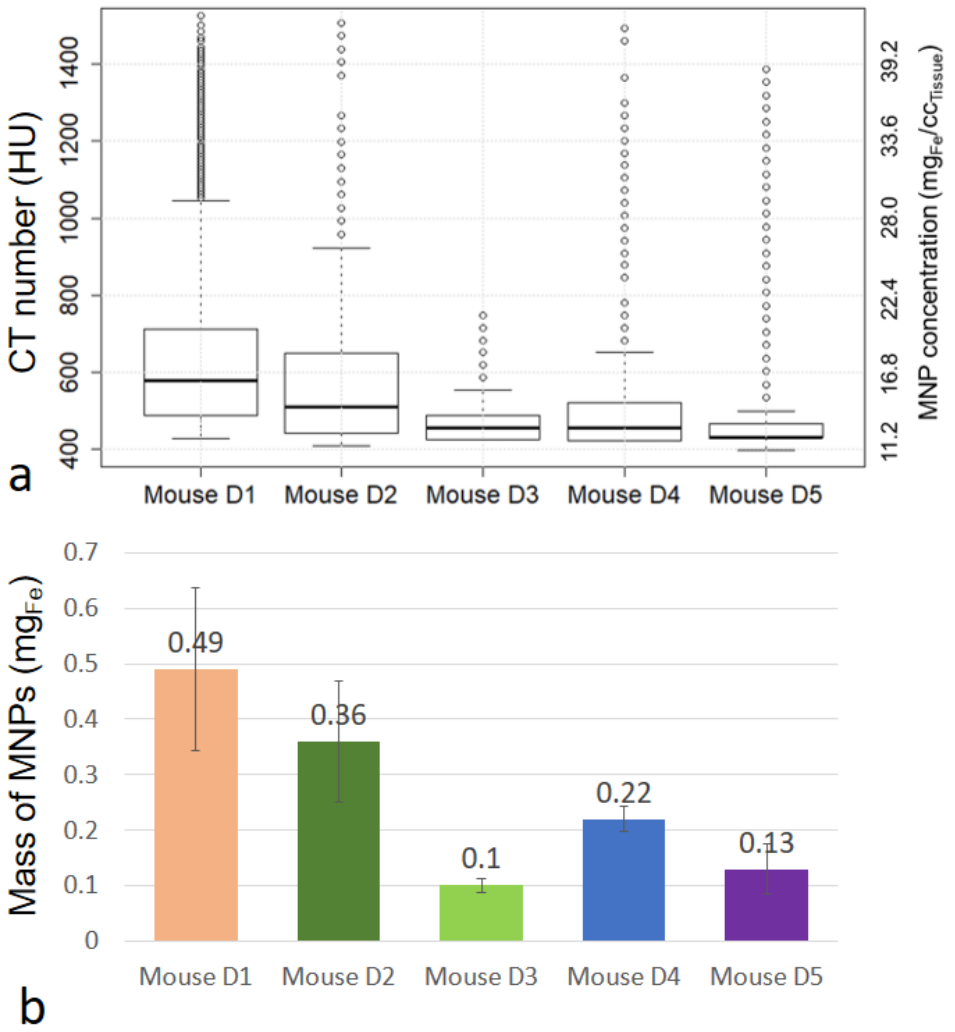

Figure 4.22: (a) The box diagram displays the distribution of CT numbers, which were also converted to the distribution of concentration based the conversion ration, i.e., 0.028 $mg_{Fe}/(ml_{tissue}.HU)$. (b) The bar chart indicates the mass of MNPs in those regions where the estimated MNP concentration was above 12.04 mg_{Fe}/ml_{tissue} (i.e. 430 HU) in each case.

Discussions

The CT image was helpful to explain the temperature distribution. For instance, the CT image suggested that the Mouse D1 possessed the largest amount of MNPs, i.e., 0.49 mg_{Fe} among the all. This was in correlation with the temperature variation. The heating performance in the case of Mouse D1 was also the highest ($\Delta T = 6.5°C$). Oppositely, the CT images indicated that Mouse D3 and D5 had the iron content less than 0.15 mg_{Fe}. Accordingly, the magnetic heating in them ($\Delta T = 3°C$) was relatively mild.

As for Mouse D2 and D4, they both had an increase of 5.2 °C in their temperature. However, the Mouse D2 had 1.7 times more MNPs than the Mouse D4. This was because the MNPs in Mouse D4 just located underneath the skin, while the MNPs in Mouse D2 was deposited deeper inside the skin. That is, the depth of MNPs could largely affect the observation in temperature variation. Overall, both the quantity and the location of MNPs would affect the temperature variation in magnetic hyperthermia.

Moreover, another thing should be mentioned was the injected quantity of MNPs. In principle, the more the injected MNPs, the better the heating performance. Nonetheless, the biological complexity makes it difficult to estimate the particle distribution. Thus, it becomes difficult to predict the temperature variation based on the injected quantity of MNPs. As shown in Fig. 4.23a, the injected quantities of MNPs had a weak correlation with the maximal temperature increases of tumours.

This emphasises the importance of *in-vivo* quantification of MNPs. As presented in Fig. 4.23b, a much better correlation had been found between the CT estimated quantities of MNPs and the the maximal temperature increases of tumours.

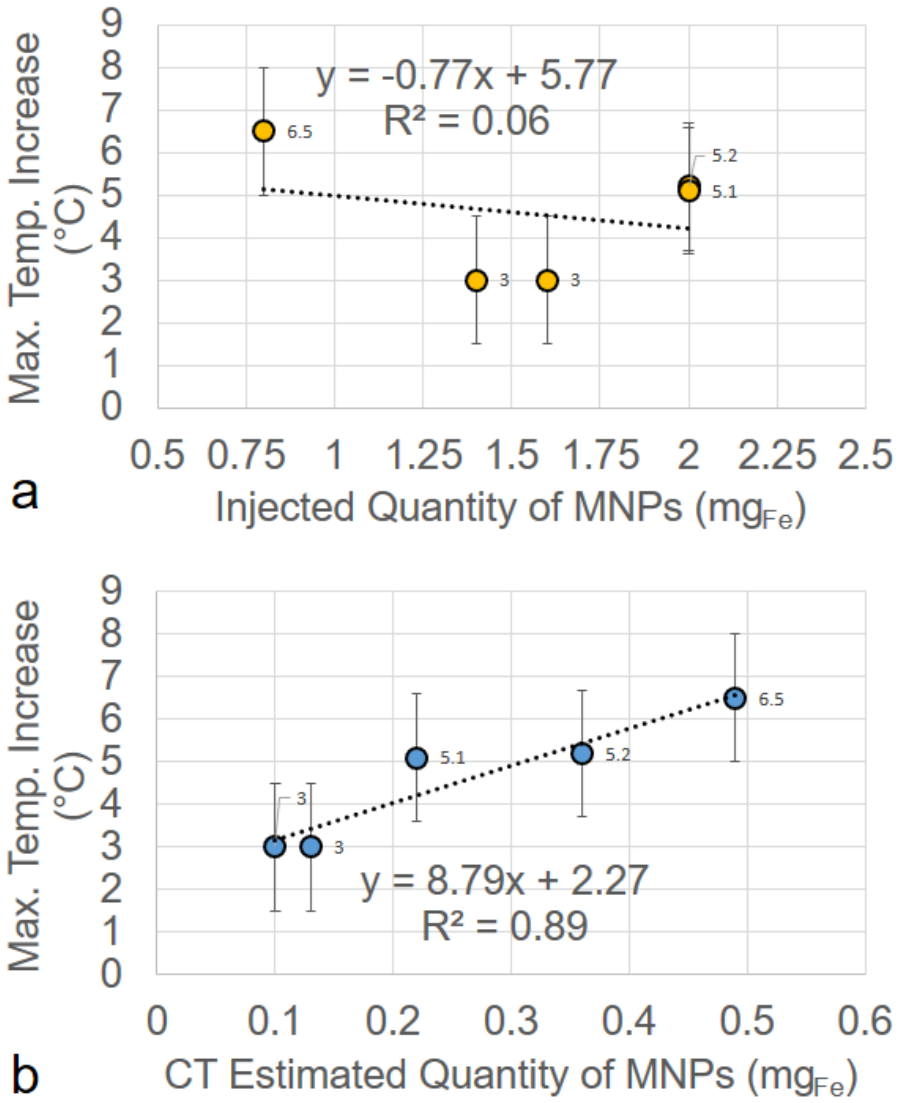

Figure 4.23: (a) The correlation between the injected quantities of MNPs and the maximal temperature increases in tumours. (b) The correlation between the CT estimated quantities of MNPs and the maximal temperature increases in tumours.

4.6 Conclusion

Magnetic hyperthermia is a straightforward idea, but the technique it requires is complex. This treatment can be discussed from a variety of aspects. To facilitate the discussion, a framework of magnetic hyperthermia has been proposed in Section 1.3. In the framework, the magnetic hyperthermia was divided into three actions and five elements (see Fig. 1.9). This framework was proposed for a clinical scenario. In such a scenario, the parameters like the dose limit, the retention and the dispersion rates of MNPs should have been studied. Nevertheless, these properties are normally unknown at the research stage. These parameters need to be determined before the actual treatment. To determine these parameters, only certain elements of the framework would be taken into consideration.

As illustrated in Fig. 4.24, Experiment A and Experiment B were conducted for determining the MNP concentration and the field intensity respectively. In the Experiment A, samples were not heated, as the aim of the experiment was to find the safe dose of MNPs.

In the Experiment B, 3 actions of magnetic hyperthermia were all performed, but only the last element, i.e, thermometry, was specifically focused. The temperature measured by the infra-red thermometry provided the feedback for the field adjustment.

After these two experiments, both the concentration of MNP suspension and the field parameter were determined, another experiment (the Experiment C) was conducted to evaluate the predictive indicator for cell damage, i.e., CEM43. The preliminary result showed that the corrected-CEM43 was in correlation with the HSP70 level.

Although the infra-red thermometry provided us with insight into hyperthermia, to have the whole picture of magnetic hyperthermia, it is still essential to know the particle distribution. With the assistant of CT imaging, the particle distributions of all five cases in Experiment D were visualised.

In literature, particle distributions are often presumed to be homogenous. However, those CT images have indicated the heterogeneousness of particle dispersion. Therefore, to well manage the temperature variation during magnetic hyperthermia, it is required to perform the *in-vivo* imaging.

Overall, both the *in-vivo* imaging and the thermometry are crucial to the thermal management of magnetic hyperthermia. The above discussion showed that the CT

imaging together with the infra-red thermometry could provide sufficient information for understanding the heating performance of a sample.

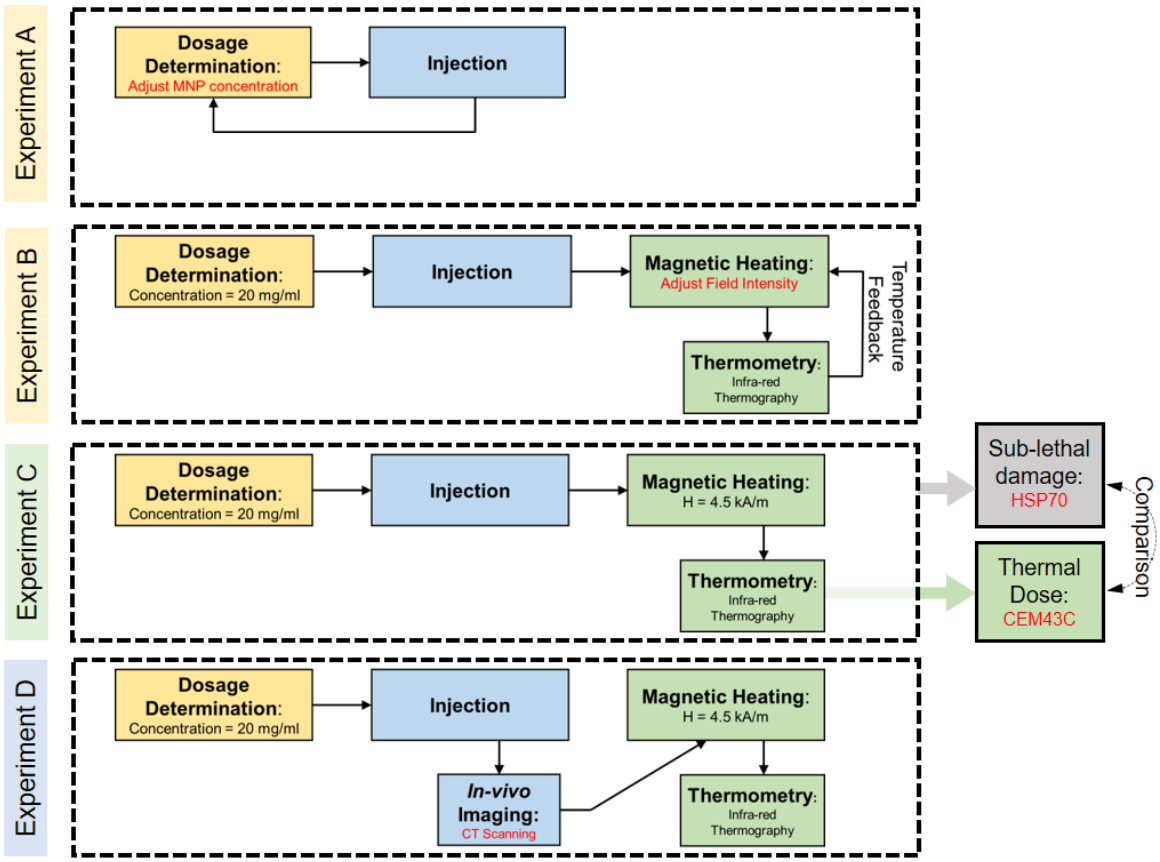

Figure 4.24: The framework of four experiments presented in this chapter.

Limitations

Both CT imaging and the infra-red thermometry have intrinsic limitations. On the one hand, the limitation of the CT imaging lies in the properties of the surrounding tissues. If the surrounding tissues, e.g., bones, have CT numbers similar to that of MNPs, the detection of particle would then be difficult. On the other hand, the infra-red thermometry can only detect the surface temperature. That is, when treating deep-seated tumours, e.g. prostate tumour, it would be difficult to withdraw meaningful temperature from the signal measured by the infra-red thermometry.

In short, both the CT imaging and infra-red thermometry are suitable for magnetic hyperthermia for subcutaneous tumours, but may not be suitable for the hyperthermia for deep-seated tumours. However, the advantage of magnetic hyperthermia is more evident when treating deep-seated tumours. Subcutaneous tumours can be well treated by the conventional surgical operation. Even so, the use of CT imaging and infra-red thermometry for pre-clinical studies are still attractive, because both are

commonly accessible and easily affordable.

A potential alternative for *in-vivo* imaging is the aforementioned MPI, which is expected to have quality imaging resolution and good contrast from the background. But before MPI becomes widely accessible, the presented experimental method is beneficial for pre-clinical studies in magnetic hyperthermia.

Findings of Four Pre-clinical Studies

Based on the above discussion, finding of these pre-clinical experiments are summarised as below.

1. The Effectiveness of Dose Limit Calculation

   The presented empirical studies have shown that Eq. 2.21 could be a good guidance for dosage determination, as long as both the retention rate and the systematic dose factor are carefully considered.

2. The Effect of Anaesthesia on Temperature

   The Experiment B showed that there was an approximate 3 °C decrease in the surface temperature of the tumour over 30 minutes. This cooling was believed to be caused by the anaesthesia. It was found that the cooling effect was less evident in areas deep in side the body.

3. The Effect of Starting Temperature on Thermal Dose

   Not only the temperature increase caused by the magnetic heating but also the starting temperature could both largely affect the thermal dose.

4. The CEM43-T90 and HSP70 level

   The preliminary results presented in this study imply the positive correlation between CEM43 and HSP70 level.

5. The Activation Time and HSP70 level

   The Activation Time proposed in this study has shown a linear correlation with the HSP70 level.

6. Quantification of MNPs based on CT images.

   The quantification was found to be possible. Furthermore, compared with the injected MNP quantities, the CT estimated quantities of MNPs had a better correlation with the temperature variations in tumours.

The experiments presented in both Chapter 3 and Chapter 4 have shown the advantages of one of the remote sensing techniques, i.e., the infra-red thermometry. This thermometry is useful for *in-vitro* and pre-clinical experiments, but as stated earlier, because of its intrinsic limitation, it is not suitable for detecting the temperature of deep-seated tumours, even though the deep-seated tumours are most likely to benefit from the magnetic hyperthermia. Therefore, another thermometry for sensing deep-seated target is still required. To address this issue, this study presents another remote sensing technique, i.e., a novel MPT, the details of which will be illustrated in the following chapter.

Chapter 5

Novel Magnetic Particle Thermometry

The effectiveness and safety of hyperthermia rely on the accurate control of temperature distribution. The current method of temperature monitoring in clinical scenarios is to insert thermometers into a tumour, which is invasive and spot measurement only [112] [113] [58]. Sensing the temperature of wrong spots can lead to treatment failure and complications.

To address these issues, three approaches have been suggested. The most common method is preoperative estimation [114]. Although these prediction models are beneficial for optimising MNP dosimetry, it is risky to merely rely on it due to the complexity of biology. Therefore, another approach aims at limiting the maximal temperature that MNPs can heat, to avoid the hazard of overheating. Because MNPs lose the heating ability when the temperature is above their Curie point, the maximal therapeutic temperature becomes controllable by tuning the Curie temperature [115]. Nevertheless, the monitoring of intra-tumoural temperature is still desired in order to ensure it reaches the therapeutically effective temperature, i.e. above 42 °C. As a result, the third approach is to develop a better way of monitoring intra-tumoural temperature during hyperthermia. By coupling the temperature of MNPs into the ratio of harmonics from magnetisation, Weaver *et al.* described a technique for remote monitoring of temperature [65], which has inspired other research such as [72], [76] and [84] (more discussion on this can be found in Section 2.4.2). Nevertheless, those methods require a different coil set and drive system from that used for applying hyperthermia. In the presence of the treatment field, the signal detection could be challenging, because of the huge voltages which would tend to be induced in the coil used to record the magnetisation of MNPs.

To achieve the same goal, the author took a different route. Instead of introducing

an additional sensing device, the author investigated the device currently used in hyperthermia, i.e. the LC oscillator circuit for generating an AMF. Through analysing the variation in resonant frequency, which is an easily measured quantity, the author has attained the aim of remote detecting and monitoring of the dose and the temperature of MNPs. The simplicity of this technique makes it certainly translatable to a clinical setting. The principle and preliminary results are presented in the following sections.

5.1 The Principle of Novel Magnetic Particle Thermometry

The technique outlined here is based on an integration of three effects, which are respectively the resonant effect of LC oscillator, the magnetisation of MNPs, and the dose and temperature dependence of magnetic susceptibility. Despite the fact that each effect is well known, to the best of the author's knowledge, no one has integrated these effects for the application of remote monitoring of temperature. However, this simple technique has the potential to benefit biomedical applications, such as magnetic hyperthermia. These effects are individually briefed below.

5.1.1 Resonant effect of *LC* oscillator

The LC oscillator is an electrical system that is generally used as an amplifier. Once an electric current is injected into an LC oscillator, it oscillates between the inductor and the capacitor at a certain frequency. This frequency, known as natural frequency (denoted as f_0), is a system characteristic decided by the inductance and capacitance, which can be written as:

$$f_0 = 1/(2\pi\sqrt{LC}) \tag{5.1}$$

When the frequency of the driving current equals to the natural frequency, the oscillating current would constantly be accumulated and thus greatly amplified, of which the phenomenon is called resonant effect. In addition to the amplification of current, the induced AMF at the inductor is also amplified. Because of the energy efficiency, an LC oscillator is sometimes used as an AMF generator for hyperthermia, e.g. the MACH system used in this study. In such a system, the driving frequency can

constantly be locked in the natural (or resonant) frequency through the feedback control. Although this frequency control aims at ensuring the resonance in LC oscillator; interestingly, this also allows one to monitor the change in resonant frequency, based on which, one can deduce the change in system characteristics, e.g. the inductance and the capacitance.

5.1.2 Magnetisation of MNPs

As mentioned in Eq. 5.1, the resonant frequency of an LC oscillator can be an indicator that shows the integrated information of the capacitance and the inductance of the system. The capacitance in an AMF generator tends to remain unchanged during the hyperthermia. Nevertheless, the presence of MNPs increases the overall inductance, because the magnetisation of MNPs would alter the magnetic flux density around the coil, and thus varies the inductance of LC oscillator.

By definition, the inductance of a solenoid coil is:

$$L_0 = \frac{N\phi_0}{I} \tag{5.2}$$

where L_0 is the inductance of a coil without the presence of MNPs. N is the number of coil turns. I is the electrical current running through the coil. ϕ_0 is magnetic flux received by the coil in the absence of MNPs.

$$\phi_0 = B_0 A_{coil} \tag{5.3}$$

where B_0 is the flux density applied to the coil, and A_{coil} is the area of the coil.

To understand the effect of the presence of MNPs on the overall inductance, one can analogue the magnetisation of MNPs to a imaginary solenoid coil. The area of the imaginary coil is denoted as a_{sample} and magnetic flux induced from the magnetisation of MNPs is termed as ϕ_{sample}. Then, in the presence of MNPs, the overall inductance of the coil, i.e., L, becomes:

$$L = \frac{N(\phi_0 + \phi_{sample})}{I} \tag{5.4}$$

$$L = L_0 + \frac{N}{I}(\phi_{sample}) \tag{5.5}$$

The magnetisation of MNPs can be derived from the volumetric susceptibility χ and the applied field H_0. The magnetisation M_{sample} is a product of the volumetric

concentration ξ and bulk magnetisation M_0 (see Eq. 2.23). The former and the latter can be expressed by $\frac{n\nu}{V}$ and χH_0, respectively. Hence, the M_{sample} can be written as:

$$M_{sample} = \frac{n\nu}{V}\chi H_0 \tag{5.6}$$

$$\phi_{sample} = \frac{n\nu}{V}\chi\mu_0 H_0 a_{sample} \tag{5.7}$$

where n is the number of MNP particles. ν is the volume of each particle. V is the volume of the sample. a_{sample} is the area of the sample (the direction of the area is aligned with coil area). μ_0 is the permeability of free space.

The coil configuration is illustrated in Fig. 5.1, in which the diameters of coil and sample are indicated.

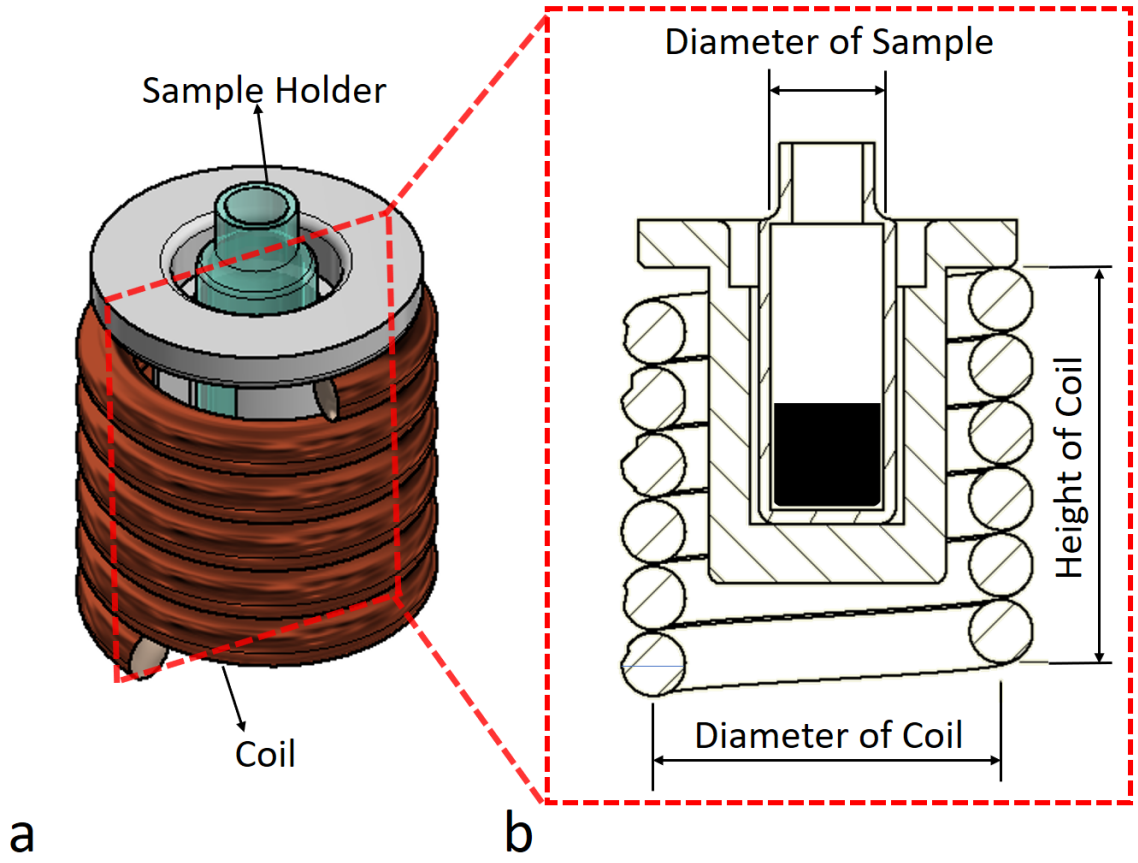

Figure 5.1: The schematic figure of the measurement configuration. (a) the dimension of coil. (b) the diameters of sample and coil. The value of sample area a_{sample} and coil area A_{coil1} were derived based on these two diameters.

Substituting Eq. 5.7 into Eq. 5.5, the equation becomes:

$$L = L_0 + \frac{n\nu}{V}\chi\frac{N\mu_0 H_0 A_{coil}}{I}\frac{a_{sample}}{A_{coil}} \tag{5.8}$$

Because $L_0 = \frac{N\phi_0}{I} = \frac{NB_0A_{coil}}{I} = \frac{N(\mu_0H_0A_{coil})}{I}$, the Eq. 5.8 becomes:

$$L = L_0 + \frac{a_{sample}n\nu}{A_{coil}V}\chi L_0 \tag{5.9}$$

The term $\frac{a_{sample}n\nu}{A_{coil}V}$ in Eq. 5.9 is dependent on the quantity of MNPs, the area of MNPs, the volumetric concentration and the coil area. To be more specific, the more the MNPs, the stronger the signal. The signal is also stronger when the coil area is small. Thus, the term $\frac{a_{sample}n\nu}{A_{coil}}$ is defined to be the filling factor ϵ, in which the a_{sample} is an empirical factor. The Eq. 5.9 can then be written as:

$$L = (1 + \epsilon\chi)L_0 \tag{5.10}$$

By substituting Eq. 5.10 into Eq. 5.1, one attains an equation (see Eq. 5.11) that describes the relationship between the resonant frequency and the susceptibility. The symbol $f(\epsilon, \chi)$ indicates that the frequency f is a function of ϵ and χ.

Because the $f(\epsilon, \chi)$ in Eq. 5.11 has a continuous derivative, and χ is usually far less than 1, i.e. similar to 0, one can approximate the $f(\epsilon, \chi)$ by the first two Taylor series expansion of Eq. 5.11 at $\chi = 0$, as shown in Eq. 5.12. By subtracting f_0 in both sides of Eq. 5.12, one can then obtain Eq. 5.13, which implies that the change in frequency $\Delta f(\epsilon, \chi)$ is linear with χ, if both ϵ and f_0 are constant during the procedure of magnetic hyperthermia.

$$f(\epsilon, \chi) = \frac{1}{2\pi\sqrt{L_0C(1 + \epsilon\chi)}} \tag{5.11}$$

$$f(\epsilon, \chi) = f_0 - \frac{1}{2}\epsilon f_0\chi \tag{5.12}$$

$$\Delta f(\epsilon, \chi) = -\frac{1}{2}\epsilon f_0\chi \tag{5.13}$$

5.1.3 Dose and Temperature Dependence

The dose dependence of $\Delta f(\chi)$ is related to the filling factor ϵ, which equals to $\frac{a_{sample}n\nu}{A_{coil}V}$. Because n and ν are not quantities can be easily measured, for the convenience of characterisation, one can convert the filling factor to be: $\epsilon = \frac{a_{sample}m_{MNP}}{\rho A_{coil}V}$, of which the m_{MNP} and ρ are the mass of MNPs and the density of a single MNP.

Let us now draw the attention to another effect, the temperature dependence of $\Delta f(\chi)$. It is associated with the temperature dependence of susceptibility, which can

be broken down into three effects. The first effect is the Hopkinson effect, which describes the phenomenon that the susceptibility peaks just before the Curie temperature [116]. The explanation of Hopkinson effect is that the environmental thermal energy facilitates the rotation of domain walls. In other words, Hopkinson is an effect that would be observed in multi-domain magnetic materials. For the single-domain magnetic material, Radhakrishnamurty & Likhite discovered a similar increase in susceptibility along with the growth in temperature [117]. However, the susceptibility of single-domain material peaks at blocking temperature instead of Curie temperature. This effect is associated with the transition from a single-domain ferromagnet to a superparamagnet. The third effect is a mixture of both effects mentioned above. The cause of the third effect is the change in grain size during the heating and does not apply to nanoparticulate system. For instance, if the heat makes a single-domain material become a multi-domain material, then the second effect would be dominant during the heating; after the heating, when the material starts to cool down, the Hopkinson effect becomes dominant. All these three effects are indicated in the Fig. 5.2.

MNPs used in magnetic hyperthermia are often single-domain material; hence, MNPs are normally associated with the second effect, in which the susceptibility of some magnetic materials is proportional to the temperature at the range for hyperthermia, i.e., between 35 °C and 55 °C. Considering both the dose dependence of ϵ and temperature dependence of χ, the Eq. 5.13 can be re-expressed as:

$$\Delta f(m_{MNP}, T_{MNP}) = -\frac{1}{2} \cdot \frac{a_{sample} m_{MNP}}{\rho A_{coil} V} \cdot f_0 \cdot \chi(T_{MNP}) \tag{5.14}$$

In which T_{MNP} represent the temperature of MNPs. The term $\chi(T_{MNP})$ emphasises that the temperature dependence of χ. Similarly, the $\Delta f(\epsilon, \chi)$ in Eq. 5.13 is written as a function of m_{MNP} and T_{MNP} in the equation above.

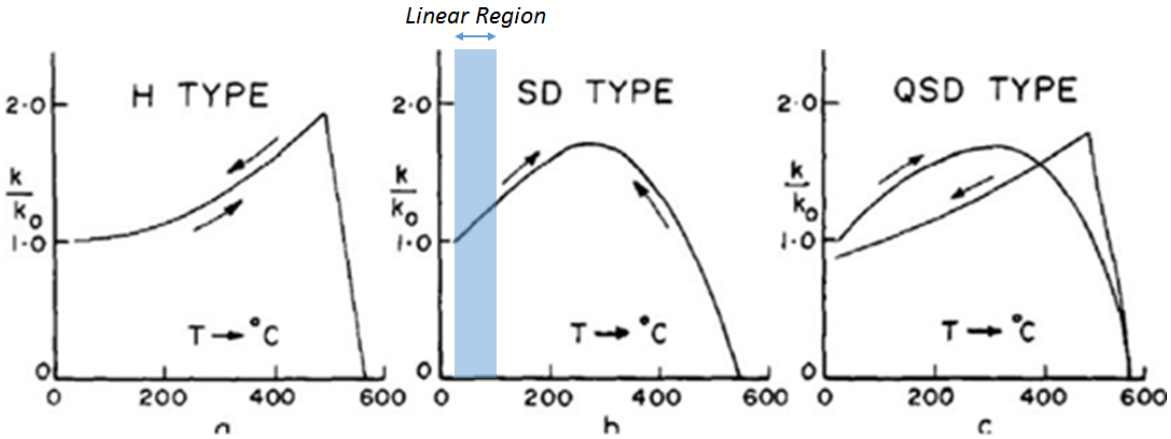

Figure 5.2: Three categories of thermal change in susceptibility: (a) Hopkinson effect. (b) Variation in a single-domain material. (c) Quasi-single domain type (the k in the graphs indicates susceptibility). This figure is adapted from [117].

5.2 Experimental Setup and Handling of Data

The Eq. 5.14 correlates the change in resonant frequency with the dose of MNPs and the temperature-dependent susceptibility, which is the basis of MPT proposed in this study. A proof of concept study has been performed and will be presented later. The experimental setup will be first described in the following subsection. Afterwards, other sections will respectively elaborate the method for characterising MNPs and potential applications of this proposed technique.

5.2.1 Experimental setup

The experimental setup is shown in Fig. 5.3. Every sample, i.e., MNP suspension, was stored in a glass vial before being placed in MACH *in-vitro* coil (see Fig. 5.4). The temperature of MNP suspension was measured by a fiber-optic thermometer (LumaSense Technologies, CA, USA). Both the frequency and amplitude of the field were derived based on the current waveform detected by CWT Rogowski probe (Power Electronic Measurements Limited, Nottingham, UK). While the measured temperature was exported to a computer through the USB connection, the field parameters were recorded through a digital oscilloscope, Picoscope 4227 (Pico Technology, Cambridgeshire, UK). The data was then processed by Labview 2015 (National Instruments Corporation, Austin, US).

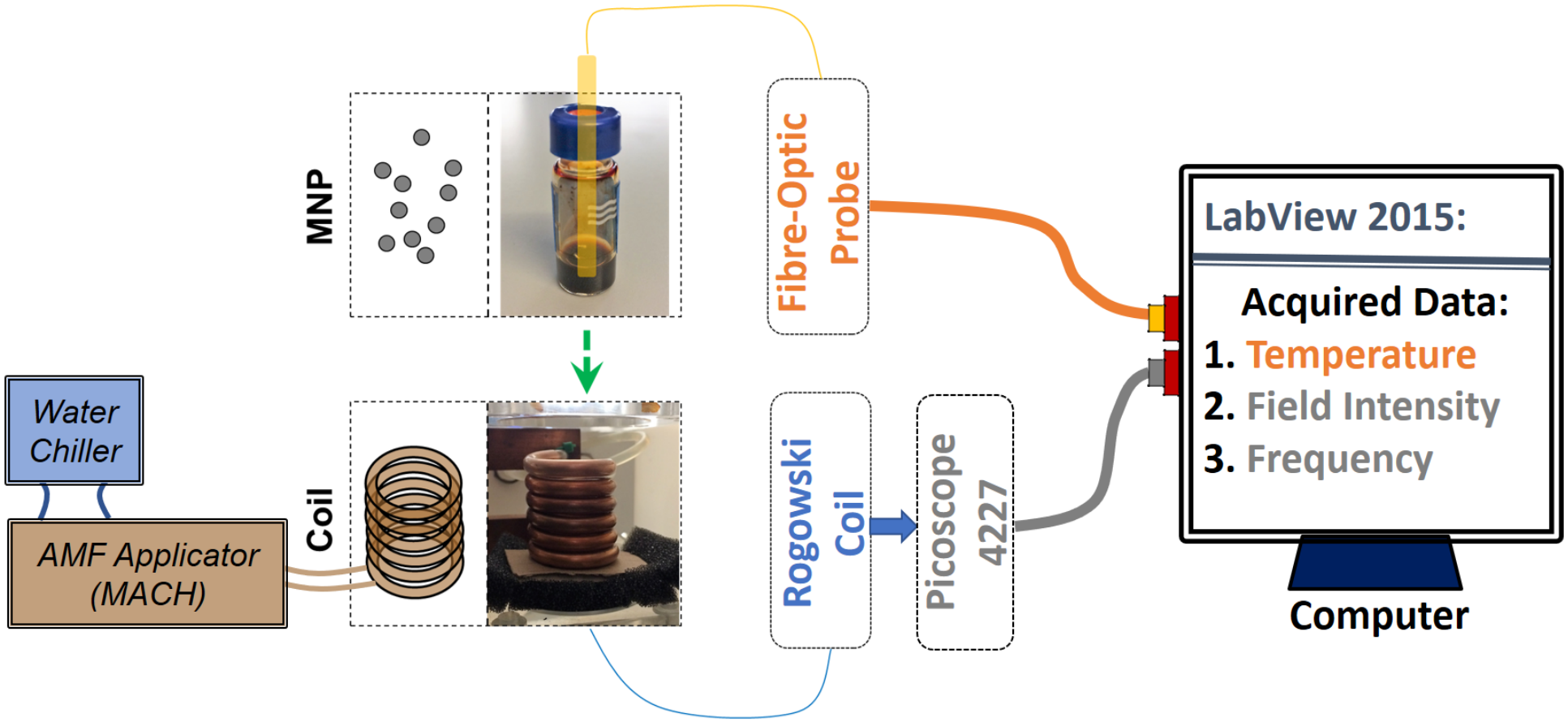

Figure 5.3: The experimental setup for demonstrating the novel MPT (magnetic particle thermometry).

The dimension and field distribution of MACH *in-vitro* coil

The MACH *in-vitro* coil and the sample holder are illustrated in detail in another figure, Fig. 5.4A. The cross-section of the coil is depicted as shown in Fig. 5.4B. The coil diameter and height are 29 mm and 33 mm. The field distribution of MACH *in-vitro* coil is calculated based on the script in Appendix A. When the coil current is 37 A, the field intensity at the centre of coil would be 5 kA/m.

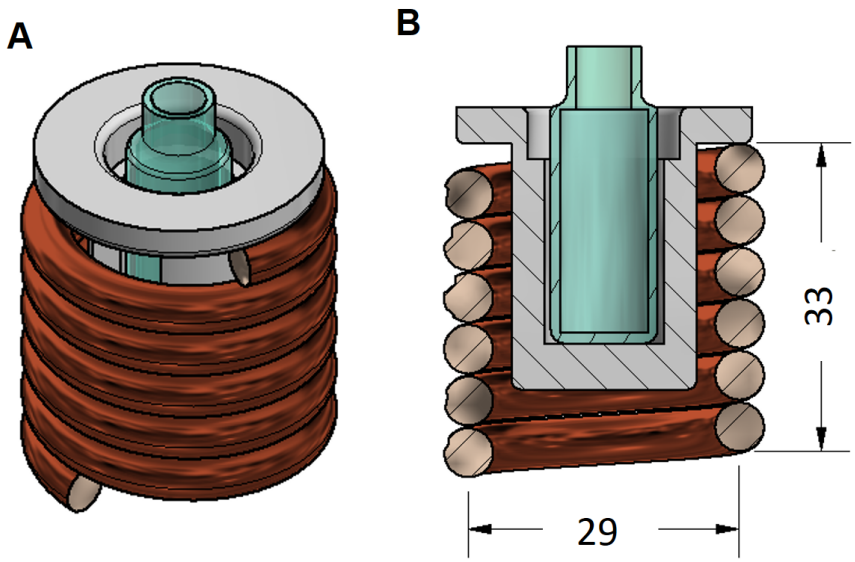

Figure 5.4: The mechanical configuration of resonant coil, which was regarded as the excitation coil during the measurement of susceptibility. (A) The illustration of the coil, sample holder and the glass vial. (B) The cross-section of the diagram in A.

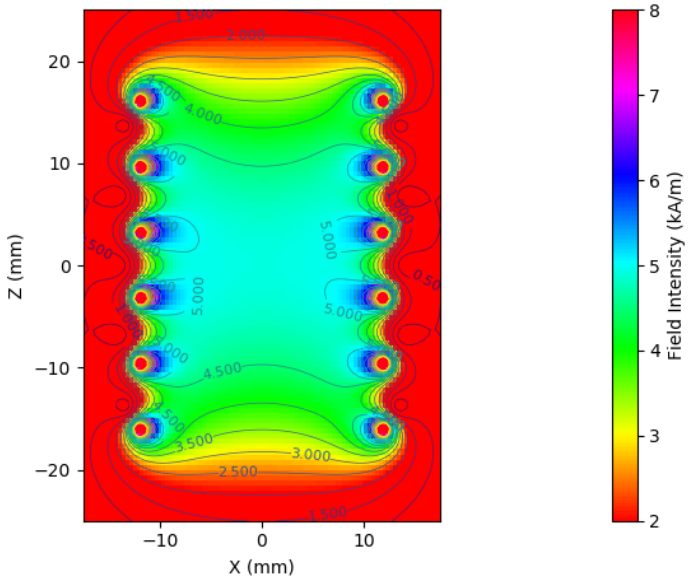

Figure 5.5: The field distribution of MACH *in-vitro* coil. When the coil current is 37 A, the field intensity at the centre of coil is 5 kA/m (see the script in Appendix A).

5.2.2 Handling of Data

With the experimental configuration in Fig. 5.3, the temperature of MNP suspension and the resonant frequency of the AMF applicator were measured simultaneously. An example of the collected experimental result is illustrated in Fig. 5.6a, in which the volume and the concentration of the MNP suspension were 0.4 ml and 11.25 mg_{Fe}/ml. The sample deployed here was RCL-01, provided by Resonant Circuits Limited. By observing the figure, one can see that when a sample was placed in the coil, the frequency immediately dropped. Assuming that the elevation in the temperature of the MNP suspension was not too rapid so that the T_{MNP} in Eq. 5.14 remained unchanged when the initial frequency drop was just observed, then if one knows the initial T_{MNP}, one can derive the m_{MNP} from the Eq. 5.14 as long as the characterisation is completed.

For instance, say T_{MNP} equals 20 °C before being placed in, the frequency variation in the Eq. 5.14 could be seen as a function of m_{MNP} only. Let the coil area of MACH to be A_{coil1}, the equation becomes:

$$\Delta f(m_{MNP}, T_{MNP} = 20°C) = -\frac{1}{2} \cdot \frac{a_{sample} m_{MNP}}{\rho A_{coil1} V} \cdot f_0 \cdot \chi(T_{MNP} = 20°C) \tag{5.15}$$

Through the characterisation of MNPs, it is possible to know that a milligram of a specific MNP, e.g., 1 mg of RCL-01 in this study, at 20 °C would account for how much drop in the resonant frequency. In other words, $\Delta f(m_{MNP} = 1mg, T_{MNP} = 20°C)$ can be easily attained before the actual measurement. In the actual measurement, once the $\Delta f(m_{MNP}, T_{MNP} = 20°C)$ is measured, one can then obtain the value of m_{MNP} in the unit of milligram by dividing $\Delta f(m_{MNP}, T_{MNP} = 20°C)$ by the characterised term $\Delta f(m_{MNP} = 1mg, T_{MNP} = 20°C)$, as long as both $\frac{a_{sample}}{\rho A_{coil1} V}$ and f_0 remain constant during the measurement.

The scenario above does not only demonstrate the possibility of deploying Eq. 5.14 for iron quantification but also illustrate the first step of MNP characterisation for the proposed MPT. The first step of MNP characterisation is to divide both sides of Eq. 5.14 by m_{MNP}, which leads the equation to become:

$$\Delta f_u(T_{MNP}) = -\frac{a_{sample} f_0}{2\rho A_{coil1} V} \cdot \chi(T_{MNP}) \tag{5.16}$$

In which, $\Delta f_u(T_{MNP})$ represents Δf per unit mass, and it is a function of T_{MNP} only, as long as both $\frac{a_{sample}}{\rho A_{coil1} V}$ and f_0 are assumed to be constant. Unlike the correla-

tion between the Δf and m_{MNP}, which is linear by definition, the correlation between the Δf and T_{MNP} is based on the temperature dependence of χ. The temperature dependence of χ may not always be linear, but it is approximately linear when the range of the temperature of our interest is narrow. The temperature of the target tissues during hyperthermia normally ranges between 37 °C and 55 °C, even for thermal ablation, where clinicians may further push the target temperature to be above 60 °C, even up to 90 °C, within the range of 50 °C difference, the temperature dependence of χ is still likely to be linear.

Let us look again at the empirical data presented in Fig. 5.6. Once the RCL-01 suspension was placed in the coil, there was an initial frequency drop. Then, the frequency constantly decreases when the suspension was magnetically heated. At the end of the experiment, when the suspension was taken out from the coil, the frequency returned to its original level f_0. For the convenience of observation, the correlation between the temperature and the frequency during the magnetic heating is plotted in Fig. 5.6b, which, fortunately, was a linear relationship for this particular MNP suspension. Consequently, the Δf in Eq. 5.14 during the time that the sample was in the coil can be expressed by a linear function of T_{MNP}; thus, it becomes:

$$\Delta f(m_{MNP}, T_{MNP}) = S(m_{MNP})T_{MNP} + C(m_{MNP}) \tag{5.17}$$

The slope $S(m_{MNP})$ can be attained through the linear regression of the plot in Fig. 5.6b. Once the $S(m_{MNP})$ is known, the intercept $C(m_{MNP})$ can be calculated as both the initial T_{MNP} and Δf are measurable. Then, similar to what has been done earlier, the mass normalisation is performed by dividing both sides of the Eq. 5.17 by m_{MNP}; hence, the frequency variation per unit mass $\Delta f_u(T_{MNP})$ is expressed by the slope per unit mass S_u and the intercept per unit mass C_u, as below:

$$\Delta f_u(T_{MNP}) = S_u T_{MNP} + C_u \tag{5.18}$$

This equation is regarded as the characteristic equation of the MNPs for the proposed MPT [1]. This simple equation provides us with a powerful tool for two applications, which are (1) quantifying the amount MNP, and (2) remotely monitoring the temperature. Both scenarios will be elaborated in the subsections below.

[1]Note that both $\frac{1}{\rho Vol_1}$ and f_0 are assumed to be constant during the measurement.

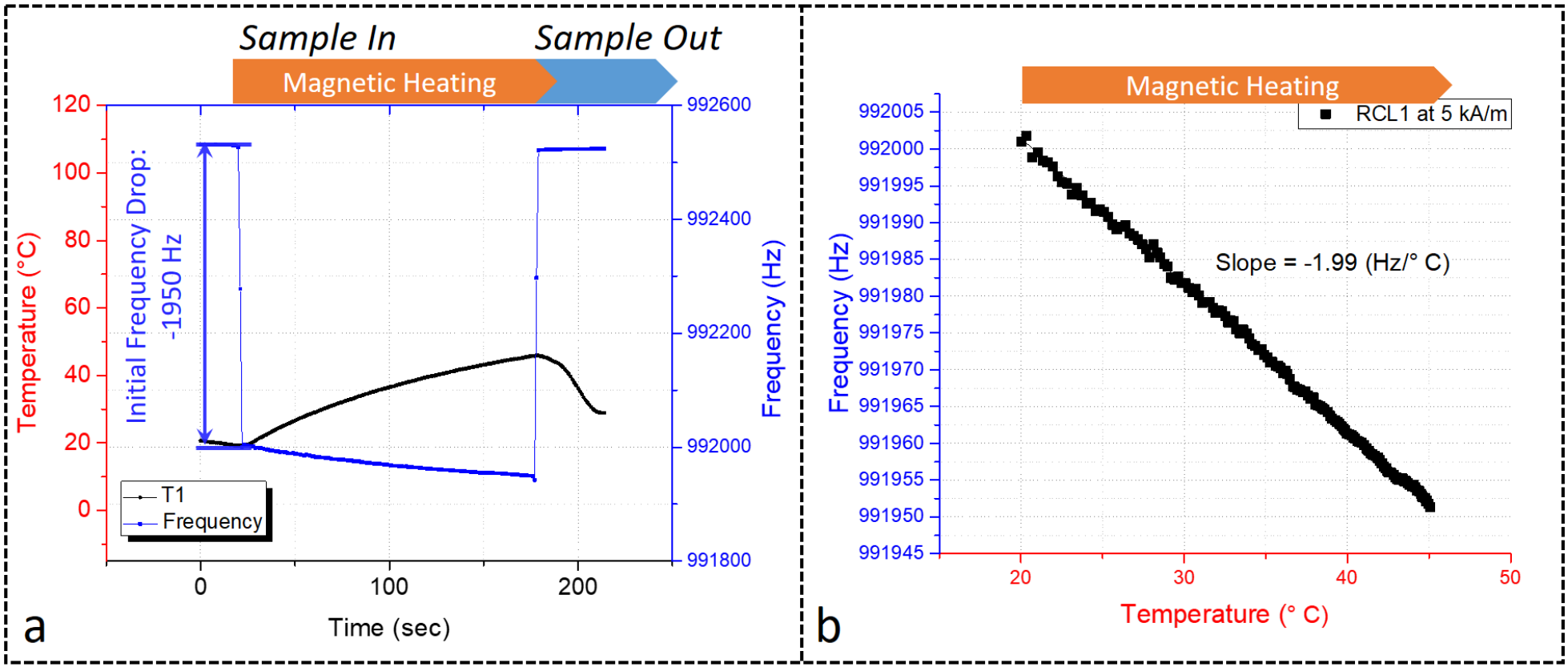

Figure 5.6: (a) An experimental result shows both the resonant frequency of the system and the temperature of Sample B0 (i.e., a 0.4 ml water-based suspension of RCL-01 with the concentration of 11.25 mg_{Fe}/ml)). This sample was measured at 5.0 kA/m and 992533 Hz. (b) The linear correlation between the frequency and the temperature of the sample.

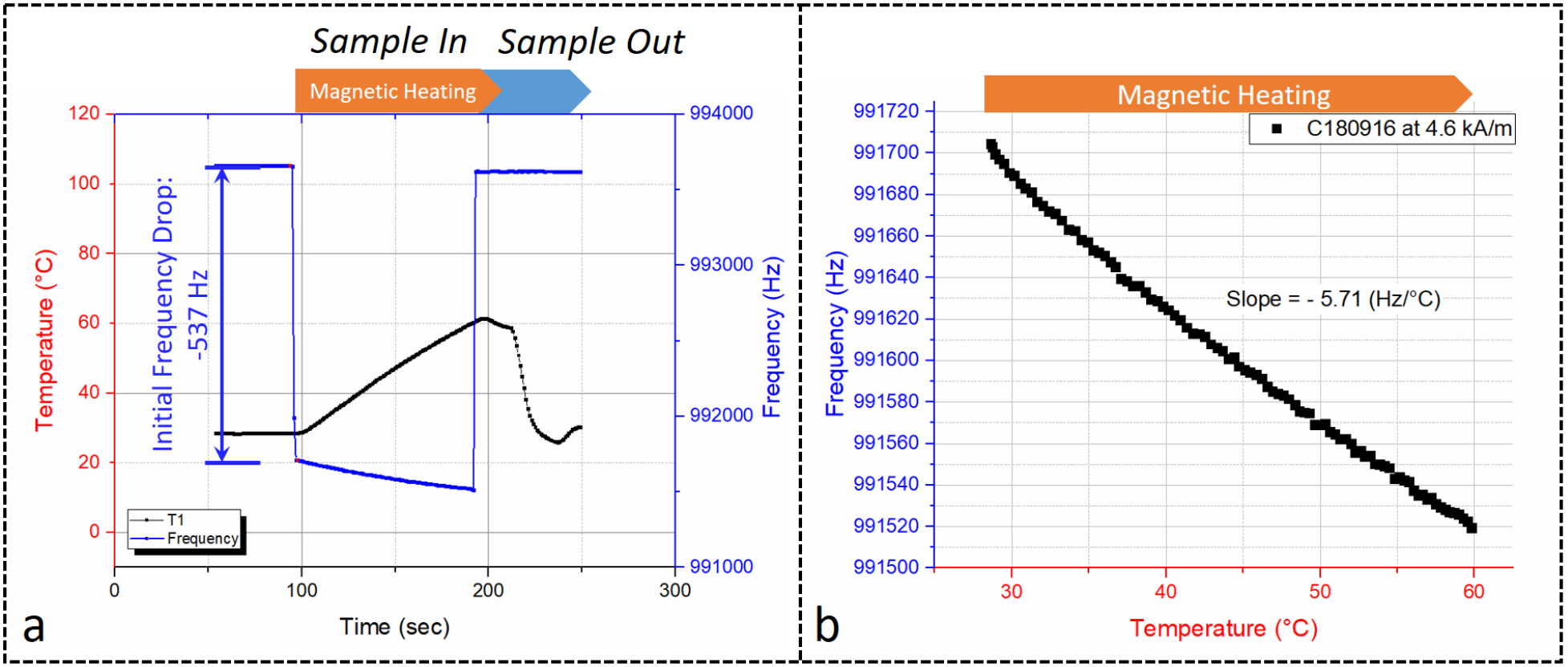

Figure 5.7: (a) An experimental result shows both the resonant frequency of the system and the temperature of Sample A0 (i.e., a 0.5 ml water-based suspension of C180916 with the concentration of 60.00 mg_{Fe}/ml)). This sample was measured at 4.6 kA/m and 991704 Hz. (b) The linear correlation between the frequency and the temperature of the sample.

5.3 Results and Discussions

Experiments have been conducted in order to investigate in the possibility of (1) quantifying MNPs and (2) remotely monitoring the temperature through the proposed technique.

5.3.1 Characterisation of MNPs

Two samples have been used in this study. One was the aforementioned RCL-01, and the other was C180916 provided by Chemicell GmbH (Berlin, Germany). The slope of Δf versus T_{MNP}, the initial Δf and initial T_{MNP} of each sample was recorded and listed in the table below. Besides, the parameters of samples, i.e. concentrations and volumes of MNP suspensions, are also listed, based on which the m_{MNP} of Sample A0 (C180916) and B0 (RCL-01) was 31.6 mg and 4.5 mg respectively.

Label	A0	B0
Sample	C180916	RCL-01
Concentration (mg/ml)	60.00	11.26
Volume (ml)	0.53	0.40
m_{MNP} (mg)	**31.6**	**4.5**
Initial Frequency Drop (Hz)	-1950	-537
Initial T_{MNP} (°C)	28.5	22.6
Slope (Hz/°C)	-5.7	-2.0

Table 5.1: The initial Δf, initial T_{MNP}, the slope of Δf versus T_{MNP} and parameters of RCL-01 and C180916. Samples were measured at 993 kHz with the field intensity of 5 kA/m.

Based on Table 5.1, the characteristic equations of both samples (see Eq. 5.18) were calculated:

$$\Delta f_u^{C180916}(T_{MNP}) = -0.18\ T_{MNP} - 57 \quad (unit: Hz/mg) \tag{5.19}$$

$$\Delta f_u^{RCL-01}(T_{MNP}) = -0.44\ T_{MNP} - 109 \quad (unit: Hz/mg) \tag{5.20}$$

With these characteristic equations, one can apply them to two scenarios, i.e., quantifying MNPs and remotely sensing the temperature. Both scenarios will be described in the following subsections.

5.3.2 Scenario I: Quantifying MNPs

To evaluate the possibility of quantifying MNPs based on the initial frequency drop of a sample, the C180916 suspension was diluted from 60 mg_{Fe}/ml to 33 mg_{Fe}/ml and 18 mg_{Fe}/ml. In addition, another batch of RCL-01 with a concentration of 10 mg_{Fe}/ml and an MNP suspension named Perimag® with a concentration of 20.2 mg_{Fe}/ml were used in this experiment. The parameters of each sample are listed in Table 5.2.

Label	A1	A2	B1	B2
Sample	C180916	C180916	Perimag	RCL-01
Concentration (mg/ml)	33	18	20.2	10
Volume (ml)	0.47	0.43	0.47	0.32
m_{MNP} (mg)	**15.5**	**7.7**	**9.5**	**3.2**

Table 5.2: The parameters of samples used to evaluate the possibility of quantifying MNPs.

According to the characteristic equations, i.e., Eq. 5.19 and Eq. 5.20, if the T_{MNP} of a sample is known, then the frequency drop caused by per milligram of MNPs, i.e., $\Delta f_u^{C180916}$ and Δf_u^{RCL-01}, at that particular temperature can be calculated. Hence, the quantity of MNPs can be estimated by comparing its associated frequency drop with the calculated Δf_u, the result of which is shown in Table 5.3. The error between the estimated quantity of MNPs and the values listed in Table 5.2 lies in $\pm$ 6 %. These results demonstrate the opportunity of using this simple technique to quickly quantity MNPs.

Label	A1	A2	B1	B2
Sample	C180916	C180916	Perimag	RCL-01
T_{MNP} (°C)	29.39	29.35	27.44	25.89
Measured Frequency Drop (Hz)	-992.00	-487.50	-1129.90	-363.90
Δf_u (Hz/mg)	-62.28	-62.29	-121.07	-120.39
Estimated m_{MNP} (mg)	**15.93**	**7.83**	**9.33**	**3.02**
Error	-2.68 %	-1.62 %	-1.76 %	5.88 %

Table 5.3: The estimated quantity of MNPs in each sample based on Δf_u, measured frequency and its temperature. Samples were measured at 4 kA/m and 993 kHz

5.3.3 Scenario II: Remotely Sensing the Temperature

If the m_{MNP} of a sample is known, then its temperature can be attained based on the shift in resonant frequency. Take the Sample B0 as an example, if one multiplies the characteristic equation Eq. 5.20 with its mass of MNPs, i.e., 4.5 mg, and moves the T_{MNP} to the left-hand side and other terms to the right-hand side of the equation, then one would obtain the Eq. 5.21:

$$T_{MNP} = -0.505\ \Delta f_{4.5mg}^{RCL-01} - 247.725 \tag{5.21}$$

This equation allows us to convert the frequency variation caused by 4.5 mg of RCL-01 into the temperature of RCL-01. To evaluate this method, the author repeated the measurement of sample B0 for four times. The estimated temperature of each sample was compared with its temperature measured by an optic thermometer. The comparisons presented in Fig. 5.8 show an adequate accuracy of estimated temperature, of which the root-mean-square error (RMSE) was less than 1.40 °C.

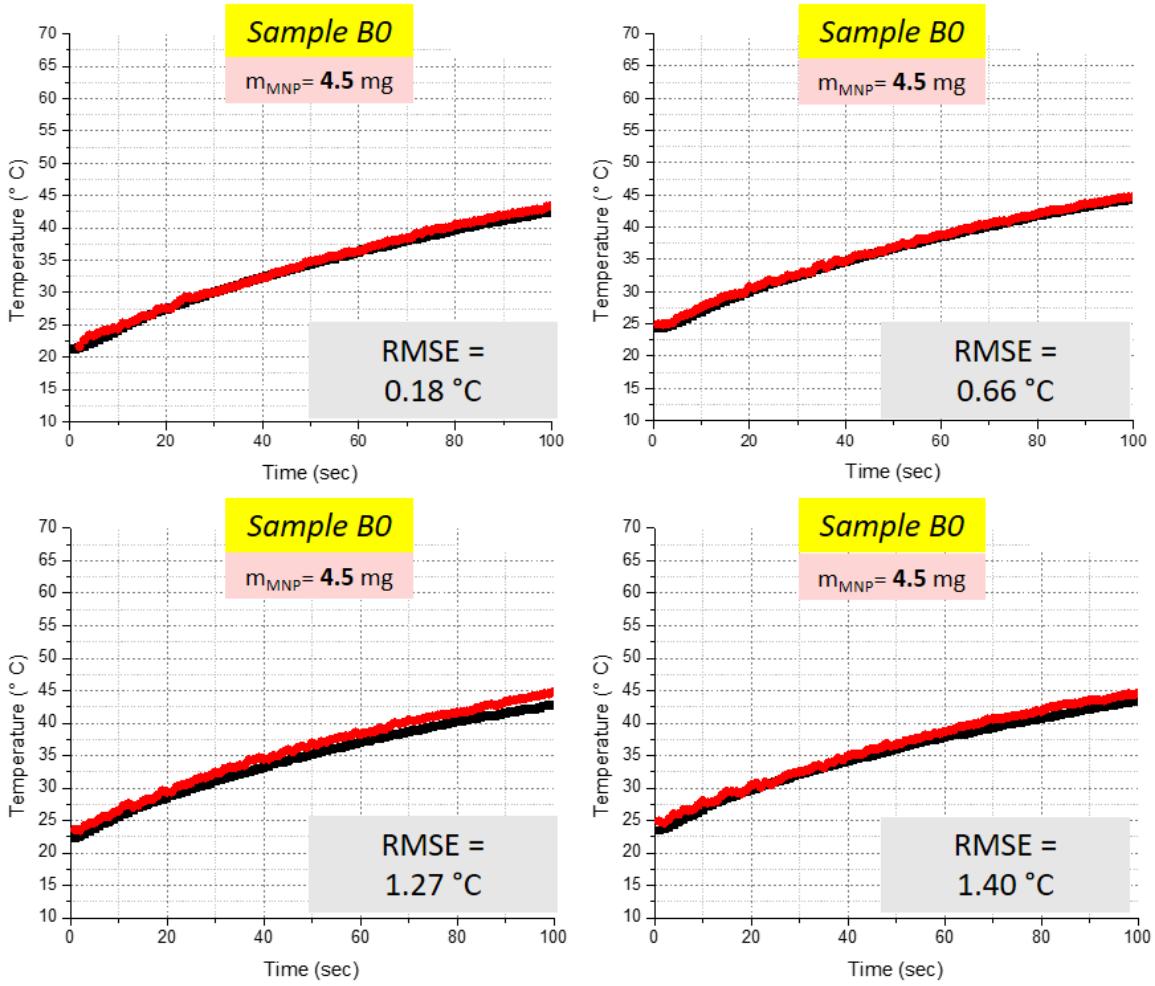

Figure 5.8: Repeated temperature measurement of *Sample B0*. The black square symbolises the temperature measured by a thermometer, while the solid red circle represents the estimated temperature based on the frequency variation. The sample was measured at 5 kA/m and 993 kHz.

The Sample B0 was selected to be an example for a reason. Because of the characteristic equation Eq. 5.20 was derived based on the measurement result of Sample B0, the m_{MNP} of 4.5 mg of Sample B0 was seen as a truth. So the author could investigate the linearity of T_{MNP} and Δf and its repeatability without worrying the uncertainty in m_{MNP}.

The next thing the author would like to examine was the effect of m_{MNP} on temperature sensing. The same method was used for estimating the temperatures of Sample A1, Sample A2, Sample B1 and Sample B2 respectively. The m_{MNP} of each sample listed in Table 5.2 was used in these temperature estimation. The estimated temperature of each sample was then compared with its measured temperature, the values of both are shown in Fig. 5.9. One would notice that even though the estimated temperature followed the trend of the measured temperature, the RMSE of estimated

values range from 5.42 °C to 15.69 °C, of which the inaccuracies were unacceptable.

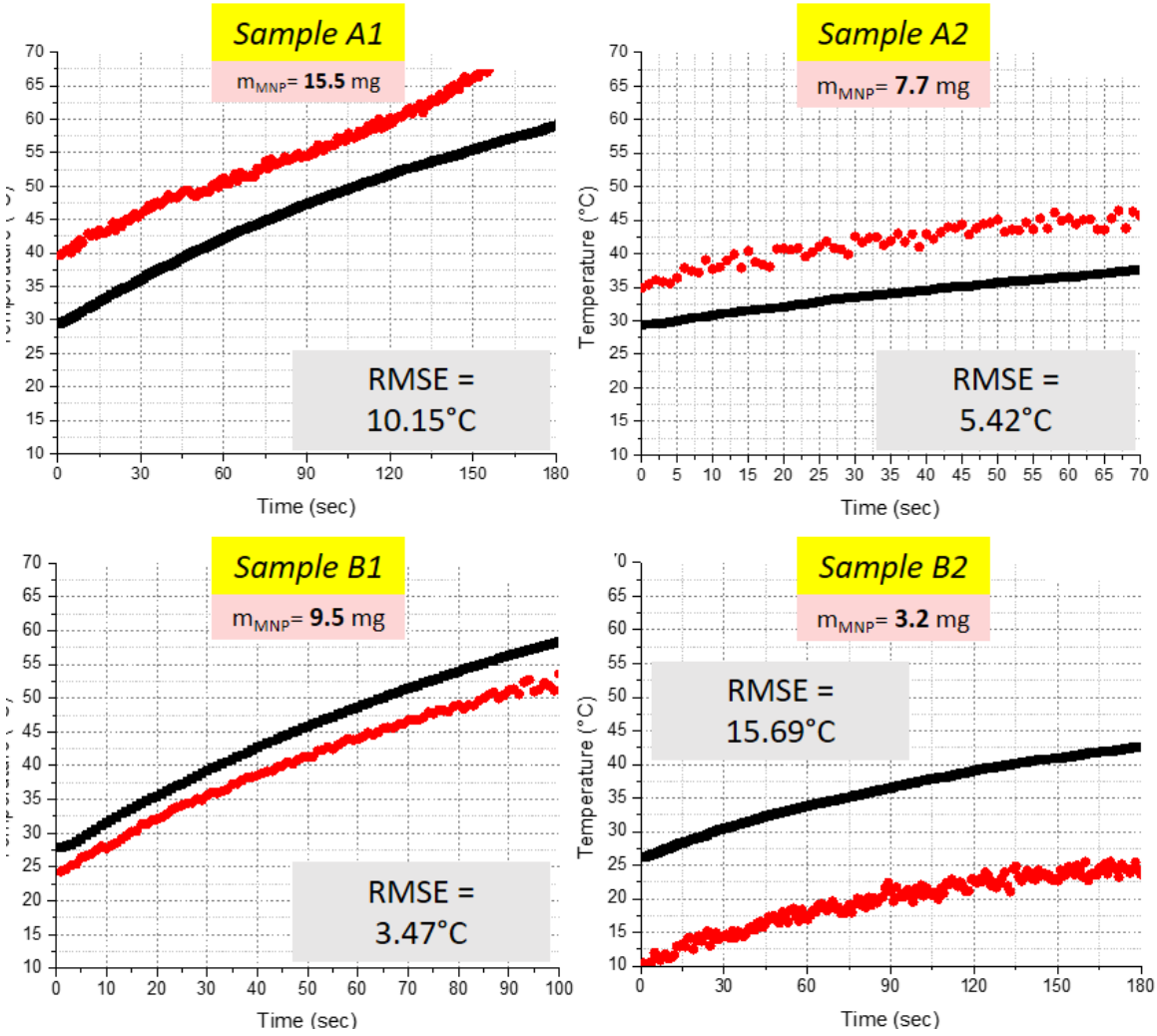

Figure 5.9: Temperature sensing of Sample A1, Sample A2, Sample B1 and Sample B2, based on the m_{MNP} in Table 5.2. The black square symbolises the temperature measured by a thermometer, while the solid red circle represents the estimated temperature based on the frequency variation. The sample was measured at 5 kA/m and 993 kHz.

This inaccurate estimation of temperature should be the combination of marginal error during dilution and the volume loss of the sample during the temperature measurement. On the one hand, the marginal error during dilution can affect the calculation of m_{MNP} in diluted samples. On the other hand, the volume of sample would also decrease each time when its temperature was invasively measured by an optic thermometer. Both reasons could lead to an uncertainty in m_{MNP} of diluted samples that presented in Table 5.2.

Fortunately, the method described in section 5.3.2 allowed one to estimate the m_{MNP} in a sample. By using the *Estimated* m_{MNP} in Table 5.3, one would obtain the

results as shown in Fig. 5.10. The RMSE between the estimated and the measured temperature significantly reduced to a range between 0.28 °C and 1.54 °C.

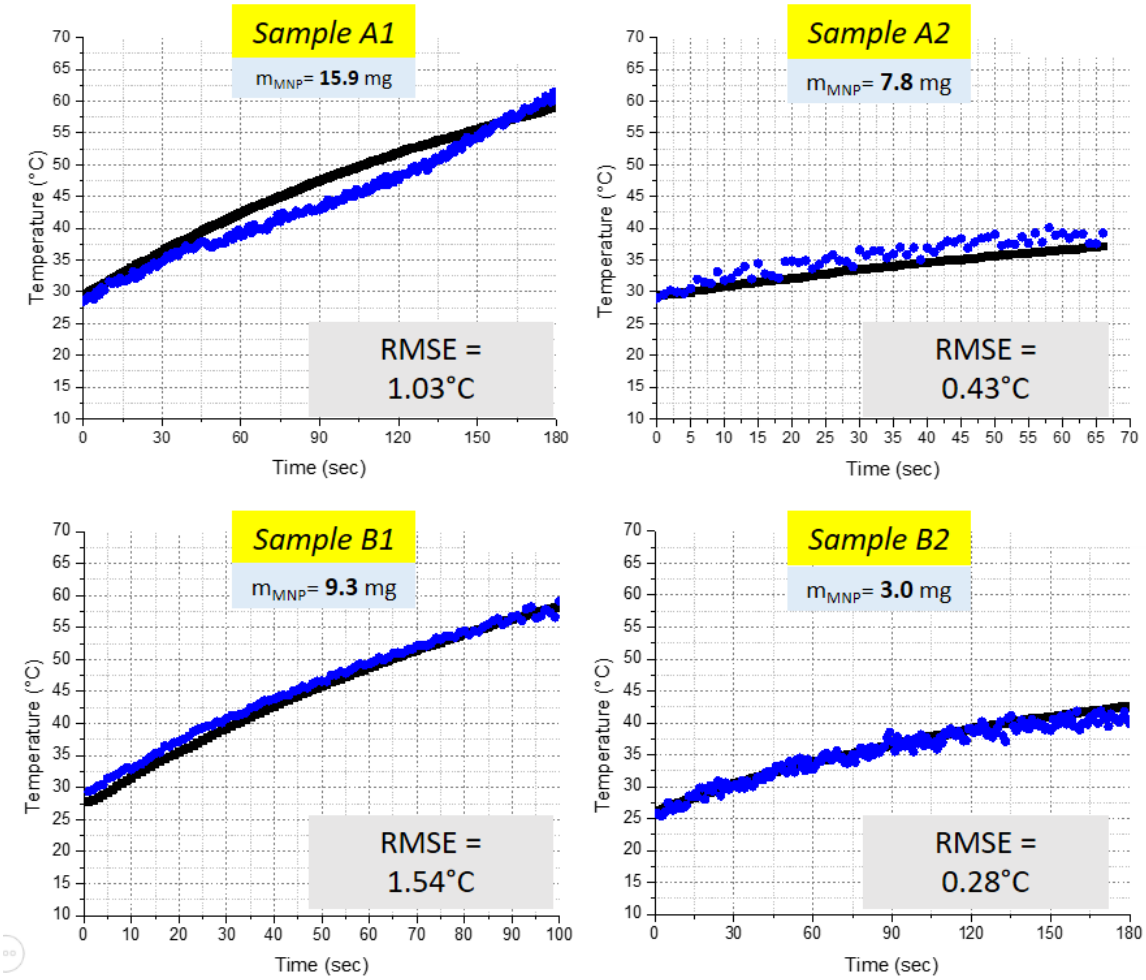

Figure 5.10: Temperature sensing of Sample A1, Sample A2, Sample B1 and Sample B2, based on the m_{MNP} in Table 5.10. The black square symbolises the temperature measured by a thermometer, while the solid blue circle represents the estimated temperature based on the frequency variation. The sample was measured at 5 kA/m and 993 kHz.

5.3.4 Scenario III: *In-vivo* Detection of Dose and Temperature

The assumptions of the first and second scenarios were that (1) the initial T_{MNP} and (2) m_{MNP} were known, which respectively led to the possibility of detecting the (1) m_{MNP} and (2) T_{MNP}.

The two scenarios above reflect the fact that the proposed technique is based on the phenomenon that the variation in the resonant frequency contains two pieces of information; while one is the quantity of MNPs m_{MNP} and the other is the temperature of MNPs T_{MNP}. Once the characteristic equation of the MNP is determined, knowing

the value of one allows us to deduce the value of the other.

For magnetic hyperthermia, it would be ideal to understand both *in-vivo* m_{MNP} and T_{MNP} during the procedure. To achieve this, the author proposes a suggestion here. This suggestion is based on that the initial T_{MNP} is presumed to be the same as the temperature of the target tumour. This assumption is reasonable, because the deposited MNPs would stay at the target site for more than 24 hours after the injection. After 24 hours, the MNPs should have achieved the thermal balance with its surroundings.

Provided that this assumption is true, then there are two ways to find out the initial T_{MNP}. The first is to assume that the initial T_{MNP} is identical to the core temperature of the subject, e.g., 37 °C. The second is to more precisely measure the temperature at the target site by invasively inserting a thermometer. As no heating was involved at the beginning of the procedure, the temperature should be homogeneous across the whole target. Thus, the initial T_{MNP} should be identical to the measured temperature.

Once the initial T_{MNP} is attained, the *in-vivo* m_{MNP} can be derived with the procedure described in Scenario I. Then, to obtain the relation between the T_{MNP} and Δf, one multiplies this derived m_{MNP} with the characteristic equation of the specific MNP, as the procedure elaborated in Scenario II. Consequently, *in-vivo* monitoring of temperature could be achieved.

5.3.5 Discussion

These preliminary results indicate not only the feasibility of this technique being used to remotely detect temperature, but also validate the possibility of the proposed method being used for measuring m_{MNP}. The author believes this non-invasive detecting method has a significant potential to benefit the thermal management of magnetic hyperthermia as well as other biomedical applications.

However, one feature of this technique should be emphasised here. Because the proposed MPT measures only the average T_{MNP} at the target region, it is required to have the *in-vivo* imaging of particle distribution in order to better understand the thermal condition during the treatment.

In addition, the discussion at the end of Scenario II implies that quantifying MNPs using the proposed method is more reliable than the MNPs calculated based on the concentration and volume of the suspension. The ability to quantify the MNPs provides a chance to more precisely control the concentration of a diluted MNP suspen-

sion. This is essential for hyperthermia studies.

At the present, researchers rely on an inductively coupled plasma mass spectrometry (ICP-MS) to measure the quantity of MNPs in a suspension. The ICP-MS is able to accurately detect the quantity of MNPs, but the device itself is expensive and thus not easily accessible. While MNP manufacturers have the access to ICP-MS, the end-users often rely on the information provided by manufacturers.

Depending on the research purpose, the neat suspension is often required to be further diluted to a specific concentration. In this case, the end-users only rely on the accuracy of pipette. If the suspension volume the end-user is dealing with is small, say 0.1 ml, an accurate dilution would be difficult to be achieved. A small marginal error during the dilution can result in a concentration that is very different from the expectation.

The proposed method provides an quick and reliable way to confirm the relative concentration of the diluted MNP suspension. More importantly, this technique is cost effective. The cost of a technique is very often overlooked in an academic research; nevertheless, cost-effectiveness is one of the main drivers of technology diffusion. Similarly, as a thermometry, this proposed technique shares the same advantage of cost-effectiveness. Although there were a number of positive results reported in the literature on deploying MRI or MPI to sense the *in-vivo* temperature during the hyperthermia, the cost of these techniques are expensive. And their compatibility with the procedure of magnetic hyperthermia has yet to be resolved. For the sake of these reasons, the author believes the MPT proposed here is a more easily accessible alternative.

In this chapter, the variation in resonant frequency was theoretically correlated with the temperature dependence of magnetic susceptibility. However, no empirical study has been done to prove this relation. Although a linear correlation has found between the Δf and the T_{MNP} for both RCL-01 and C180916, there is still no answer whether this correlation is the result of the temperature dependence of susceptibility. In the following chapter, a simplified AC susceptometer will be introduced, which was used for validating the fundamental assumption of the proposed MPT. To be more specific, the simplified AC susceptometer allowed the author to simultaneously perform the MPT and the susceptometer. Thus, the MPT signal, i.e., the variation in resonant frequency, and the susceptibility of MNPs can be measured under the same field condition.

Chapter 6

Validation of Magnetic Particle Thermometry

The description of the MPT in the previous chapter was engineering-orientated. The description of which focused on the linear correlation between Δf and T_{MNP} as well as the method for characterising MNPs. Although an explanation for this correlation has been given at the beginning of the previous chapter, no empirical evidence was presented to validate this deduced explanation.

The fundamental assumption of the explanation is that the Δf is a function of the χ (see Eq. 5.13). The linear temperature dependence of Δf is believed to be a result of the linear temperature dependence of χ.

To prove this assumption, a simplified AC susceptometer has been built and embedded in the field applicator used in MPT, the configuration of which was able to measure both Δf and χ at the same time and in the identical conditions.

The following section will first illustrate the mechanism of the simplified AC susceptometer. The handling of data will also be included. In another section, the experimental results will be presented and discussed. Once the χ of MNPs was attained, the measured χ could then be compared with the Δf obtained from the field applicator MACH. According to Eq. 5.13, a linear correlation between them was expected, of which the empirical results will be presented in Section 6.2.3.

6.1 The Design of Simplified AC Susceptometer

6.1.1 Why a Bespoke Susceptometer?

There are commercial AC susceptometers, one can probably measure the temperature dependence of χ of a type of MNP; then, followed by a separate measurement of Δf by using the resonant field applicator MACH. Once both χ and Δf are measured under the same conditions and the comparison of them shows a linear correlation, the Eq. 5.13 would be validated.

However, it is not straightforward to measure both values under the same conditions. The χ of MNPs does not only depend on the temperature but also on both the field intensity and frequency. To be more specific, the linear temperature dependence of χ depends on factors such as the temperature, the field intensity and the field frequency.

The practical issue here is that to tune the field parameters of a commercial AC susceptometer to be the same as that in MACH might not be easily achievable, because their adjustable ranges of the field might be different. After all, they were designed for different purposes.

Therefore, in the author's perspective, the best way to validate the proposed technique is to directly integrate an AC susceptometer within the MACH. In this case, one would obtain χ and Δf at the same time and, more importantly, under the same conditions.

The mechanical configuration of simplified AC susceptometer will be first depicted in the next subsection. Then, handling of data will be described in another subsection. A discussion on the limitation of this simplified susceptometer will then be presented.

6.1.2 The Mechanical Configuration of Susceptometer

The principle of an AC susceptometer has been stated in Section 2.4.2. In the previous section, the device was termed as magnetometer, which was essentially identical to a susceptometer. If the magnetisation is measured under a known field intensity, then the susceptibility of a material can be calculated through dividing the measured magnetisation by the applied field. Thus, the mechanical configuration of a susceptometer was the same as that depicted in Fig. 2.6.

The excitation coil provided an AMF during the measurement. Because the pick-

up coil and the cancellation coil were identical but oppositely wounded, on the one hand, when no sample was present, the induced voltage in the pick-up coil would be evened by the voltage induced in the cancellation coil; that is, the overall voltage would be zero; on the other hand, when a sample was present in the pick-up coil, a part of the induced voltage in the pick-up coil was caused by the magnetisation of sample. Thus, this induced voltage would not be zeroed by the voltage induced in the cancellation coil, which resulted in a situation that the residual voltage was only associated with the magnetisation of sample. Consequently, with this mechanical configuration, the magnetisation of a sample could be measured. As the excitation field was known, the magnetic susceptibility of the sample can then be calculated.

Take the field applicator MACH as an example. In this study, there is already a coil that generates an AMF. This makes the coil act as an excitation coil. In principle, as long as a pair of oppositely wounded coils are placed in this excitation coil, the configuration would allow one to measure the magnetic susceptibility of a sample.

Let us look again at the coil of MACH in Fig. 5.3. Considering this configuration, the easiest way to build up a susceptometer is to insert a pair of balancing coils into the excitation coil in Fig. 5.4. As a result, the cross-section of the configuration would be like that presented in Fig. 6.1A. The pair of the balancing coils consist of a pick-up coil and a cancellation coil. The former and latter are represented with green and red circle, respectively.

One may notice that the number of turns the cancellation coil has is higher than that of the pick-up coil. This is because of the inhomogeneous field distribution. The field tends to be stronger at the centre than it at the edge. To balance the induced voltage in absence of a sample, the number of turns the balancing coils have needs to be adjusted accordingly.

However, in practice, it was difficult to balance the induced voltages by adjusting the coil position and/or the number of turns. At least, in the author's attempt, even in the absence of a sample, a none-zero signal always existed when an AMF was applied; hence, a calibration is necessary. The calibration process and the handling of data will be described in the following section.

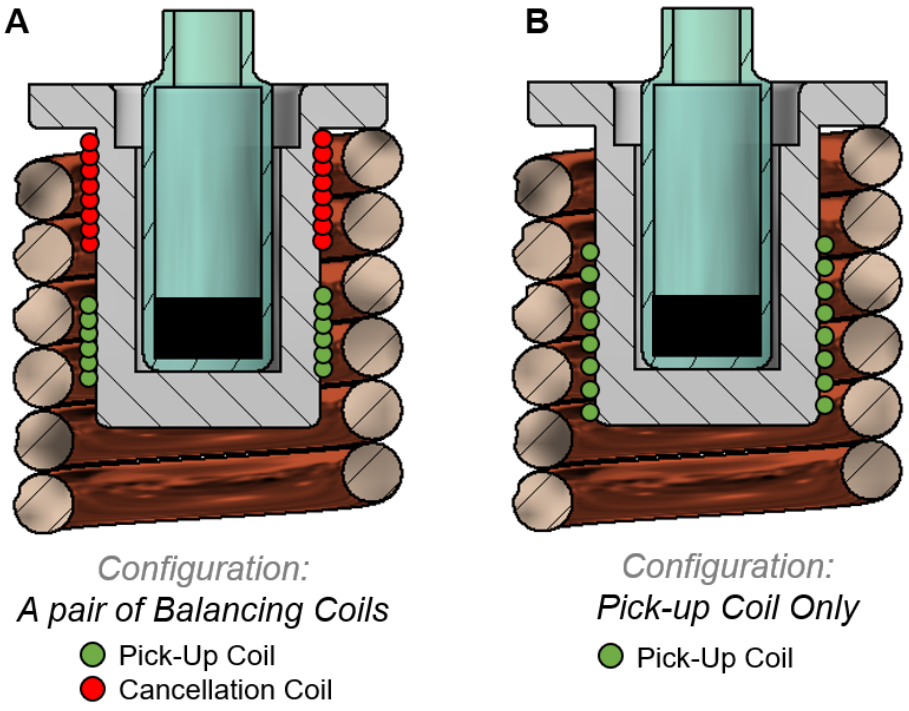

Figure 6.1: The configurations of detection coil. (A) The configuration of a pair of balancing coils. (B) The configuration of a pick-up coil only.

6.1.3 Handling of Data

The coil configuration illustrated in the previous section has been commonly used for detecting the magnetisation in the literature [80] [72] [74]. But it was practically difficult to zero the offset signal by adjusting the number of turns or the relative positions of pick-up and cancellation coils. To achieve this, a delicate mechanism would be required for finely adjusting relative positions of coils.

Nonetheless, the author would like to emphasise that the goal of this experiment was not to build up a quality susceptometer with high accuracy; instead, the susceptometer described here was for us to measure the susceptibility under the same condition of proposed MPT, so that its assumption could be examined. For this purpose, the author avoided using a complicated circuit design or a delicate mechanical configuration in the susceptometer. This was the why this measurement setup was described as a simplified susceptometer.

The measurement setup of this susceptometer is illustrated in Fig. 6.2. The key signals of a susceptometer are the excitation field and the magnetisation of a sample. To acquire these two signals, firstly, the resonant voltage that oscillated between the excitation coil and the capacitor was measured by the aforementioned Rogowski coil (see Section 5.2.1). Based on this detected periodic voltage, the intensity and the

frequency of excitation field could both be derived. Secondly, the voltage induced in the detection coil was recorded and converted to the magnetisation of a sample. The induced voltage was directly measured by an oscilloscope.

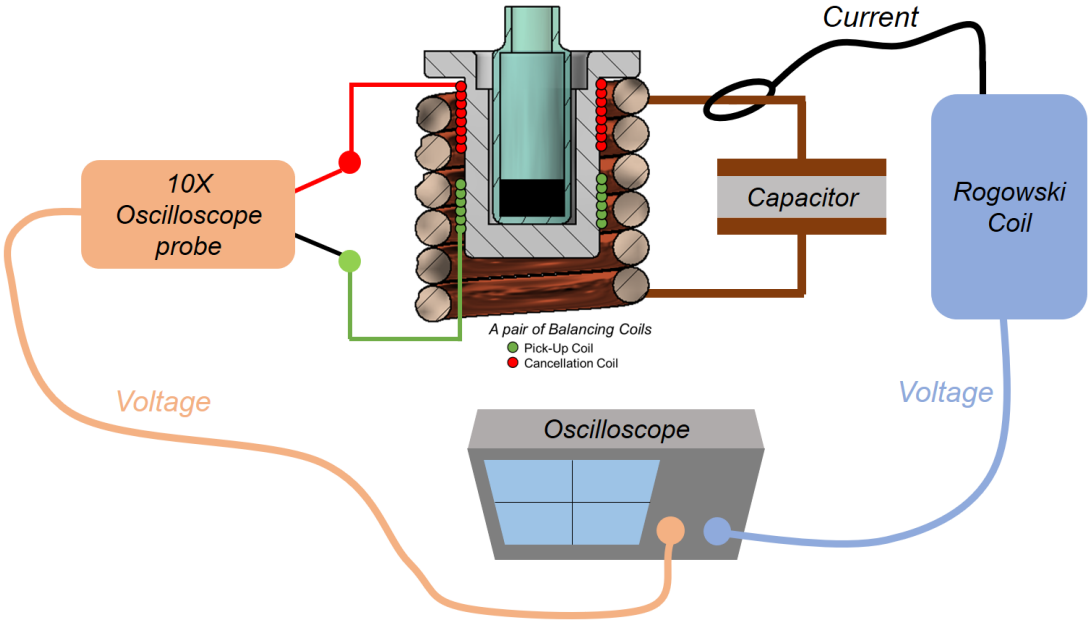

Figure 6.2: The measurement setup of susceptometer. While the current oscillating between the capacitor and excitation coil was measured by a Rogowski coil, the induced voltage was directly measured by a 10x oscilloscope probe.

This measurement setup was straightforward. In principle, both the excitation field and the magnetisation of a sample could be derived from the measured signals. But, in practice, additional steps were required, of which the steps were respectively associated with **(a) the calculation of magnetisation**, **(b) the phase shift caused by the Rogowski coil**, **(c) converting periodic signals to phasors** and **(d) the calculation of susceptibility**. Each step will be further elaborated in the following subsections.

a. The Calculation of Magnetisation

According to both Faraday's Law and Lenz's Law, the relationship between electromotive force (abbreviated as emf) and the magnetic flux ϕ can be expressed as the equation below:

$$emf = -\frac{d\phi}{dt} \tag{6.1}$$

The concept of flux density B has been introduced in Section 2.2.1. By definition,

the ϕ can be expressed as $\phi = BA_{coil}$. It is necessary to consider the filling factor (see Eq. 5.9) when calculating the magnetisation. Previously, the filling factor was described as: $\epsilon = \frac{n\nu a_{sample}}{VA_{coil1}}$, in which A_{coil1} is the area of the MACH coil. To avoid the confusion, the filling factor of susceptometer is set to be α. The α is described as: $\alpha = \frac{n\nu a_{sample}}{VA_{coil2}}$, in which A_{coil2} is the coil area of the susceptometer.

As a result, the emf induced by the time-varying magnetisation of a material can be described as:

$$emf = -\alpha \frac{d\phi}{dt} \tag{6.2}$$

Which can also be expressed as:

$$emf = -\alpha \frac{d(BA_{coil2})}{dt} \tag{6.3}$$

In the scenario of AC susceptibility measurement, it is reasonable to assume that the flux density caused by the magnetisation of MNPs (denoted as B^{MNP}) is a periodic signal. Provided that its angular frequency is identical to that of the excitation field, denoted as ω, and the amplitude of B^{MNP} peaks at B_0^{MNP}, then B^{MNP} can be expressed by $B_0^{MNP}cos(\omega t)$. Consequently, the emf associated with material's magnetisation, denoted as emf^{MNP}, equals:

$$emf^{MNP} = -\alpha \frac{d(B_0^{MNP}A_{coil2}cos(\omega t))}{dt} \tag{6.4}$$

For the convenience of calculation, $B_0^{MNP}cos(\omega t)$ can be seen as a phasor. The exponential form of this phasor is $\mathrm{Re}\{B_0^{MNP}e^{i\omega t}\}$. Then, after differentiation, the above equation becomes:

$$emf^{MNP} = \mathrm{Re}\{-\alpha B_0^{MNP}A_{coil2}(i\omega)e^{i\omega t}\} \tag{6.5}$$

Which further becomes:

$$emf^{MNP} = \mathrm{Re}\{\alpha B_0^{MNP}A_{coil2}\omega e^{i(\omega t - \frac{\pi}{2})}\} \tag{6.6}$$

This equation states the relationship between emf^{MNP} and B^{MNP}. It suggests that the induced emf^{MNP} always lags B^{MNP} by 90°, and the ratio of $|B^{MNP}|/|emf^{MNP}|$ is $1/(\alpha A_{coil2}\omega)$. With this relationship in mind, the emf^{MNP} measured by the oscilloscope probe in Fig. 6.2 can be converted to B^{MNP}. Assume that $emf^{MNP} = V_0cos(\omega t)$, then B^{MNP} can be derived through the equation below:

$$B^{MNP} = \mathrm{Re}\{\frac{V_0}{\alpha A_{coil2}\omega} e^{i(\omega t + \frac{\pi}{2})}\} \tag{6.7}$$

Or

$$B^{MNP} = \frac{V_0}{\alpha A_{coil2}\omega} cos(\omega t + \frac{\pi}{2}) \tag{6.8}$$

According to Eq. 2.6 and Eq. 2.7, the flux density B^{MNP} can be converted to the magnetisation of sample M through $B^{MNP} = \mu_0 M$. Based on this relation and Eq. 6.8, the M of sample can be derived from measured signal, i.e., $V_0 cos(\omega t)$ through:

$$M = \frac{V_0}{\mu_0 \alpha A_{coil2}\omega} cos(\omega t + \frac{\pi}{2}) \tag{6.9}$$

b. The phase shift caused by Rogowski coil

The magnetisation of a material was attained through Eq. 6.9. Theoretically, if one divides the magnetisation of a material by the excitation field, one would obtain the susceptibility of the material. Nevertheless, in practice, the Rogowski coil used for monitoring current (see Fig. 6.2) would introduce a phase shift during the measurement.

It was caused by the embedded circuit that designed for converting the detected current to a voltage. The current was converted because most oscilloscopes only read voltage signals. The phase difference between the magnetisation and excitation field can affect the calculation of AC susceptibility. To attain the AC susceptibility of a material, it was necessary to remove or correct the phase shift that was not caused by the magnetisation.

A potential method for addressing this issue is measuring the phase shift and taking it into consideration when calculating the susceptibility. Unfortunately, the phase shift was not a constant value. It tended to shift over time. Hence, the attention should now be drawn to methods for **(1) measuring** and **(2) correcting** the **undesired phase shift**.

To measure the undesired phase shift, the pair of balancing coils in Fig. 6.2 had been replaced by an 8-turn pick-up coil, as shown in Fig. 6.1B, for the later measurements (see the detailed discussion in Appendix G). The photo of 8-turn pick-up coil applied in this study can be seen in Fig. 6.3. As to the correction of phase shift, it will be discussed in the section of *The Calculation of Susceptibility*.

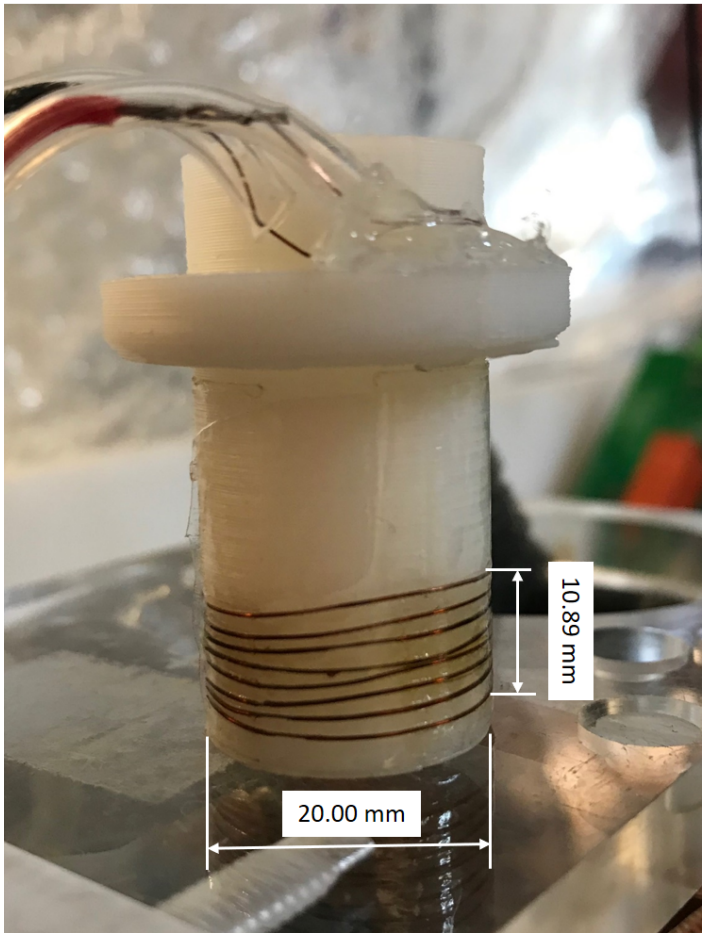

Figure 6.3: The picture of 8-turn pickup coil used in the simplified susceptometer.

c. Converting Periodic Signals to Phasors

The previous two subsections have introduced (1) how to derive the magnetisation from the detected voltage and (2) using the pick-up coil to generate a reference signal for correcting the unwanted phase shift in measured excitation field cause by Rogowski coil. Nevertheless, both descriptions were theoretical.

To practically attain the susceptibility, an additional step for converting the detected signals to phasors would be helpful (see more discussions in Appendix H.1). Once the phasors of detected signals were obtained, both the calculation of magnetisation and the phase correction of shifted excitation field could be easily achieved.

d. The Calculation of Susceptibility

Measurement Procedure At first, we need to clarify the procedure of measurement. The susceptibility measurement could be divided into two stages. **At the first stage**, the pick-up coil was in absence of a sample. The $H_{shifted}$ was recorded. The induced voltage was also recorded and at this stage the induced voltage was denoted as $V_{baseline}$.

Then, **at the second stage**, a sample was placed in the pick-up coil and the induced voltage was denoted as V_{pickup}. The excitation field at the second stage remained the same as that at the first stage. Both V_{pickup} and $H_{shifted}$ were recorded.

The handling of data at each stage are individually introduced in the following paragraphs.

The First Stage - Baseline Signal To facilitate the calculation, the first step of data handling at each stage was to convert the detected signals to complex numbers (the mathematics of the conversion can be seen in Appendix H.5). Thus, the $V_{baseline}$ and $H_{shifted}$ were expressed as $\mathbb{V}_{baseline}$ and $\mathbb{H}_{shifted}$.

According to Eq. 6.9, the induced magnetic field at the pick-up coil is described as below:

$$\mathbb{M}_{baseline} = \frac{\mathbb{V}_{baseline}}{\mu_0 \alpha A \omega}(cos(\frac{\pi}{2}) + isin(\frac{\pi}{2})) \tag{6.10}$$

Here, the induced magnetic field was termed as $\mathbb{M}_{baseline}$. The Eq. 6.9 indicates that there was a phase difference of $\frac{\pi}{2}$ between $\mathbb{M}_{baseline}$ and $\mathbb{V}_{baseline}$; thus, to fulfil the condition, a phasor, i.e., $cos(\frac{\pi}{2}) + isin(\frac{\pi}{2})$, was placed in the equation as above. In addition, no sample is place in the coil, the Then the Eq. 6.10 could be simplified to be:

$$\mathbb{M}_{baseline} = i\frac{\mathbb{V}_{baseline}}{\mu_0 \alpha A \omega} \tag{6.11}$$

Then, for the purpose of calibration, a pseudo susceptibility $\mathbb{X}_{baseline,shifted}$ was derived through[1]:

$$\mathbb{X}_{baseline,shifted} = \frac{\mathbb{M}_{baseline}}{\mathbb{H}_{shifted}} \tag{6.12}$$

Because the $\mathbb{M}_{baseline}$ was theoretically in phase with the excitation field $\mathbb{H}$, the phase difference between $\mathbb{H}_{shifted}$ and $\mathbb{M}_{baseline}$ represents the undesired phase shift.

As $\angle\mathbb{X}_{baseline,shifted} = \angle\mathbb{M}_{baseline} - \angle\mathbb{H}_{shifted}$, the phase of pseudo susceptibility actually represented the phase shift caused by Rogowski coil $\theta_{shiftedH}$.

[1]This was termed as pseudo susceptibility because the value of which was not an actual susceptibility of any material. Here, the induced magnetic at the pick-up coil $\mathbb{M}_{baselnie}$ was regarded as the magnetisation of a reference material. Thus, through division, a pseudo susceptibility was obtained, which was a useful baseline information for calibrating the system.

Since $\theta_{shiftedH}$ was attained, one could then create a signal, termed as $\mathbb{U}_{PhaseCorrection}$, of which the amplitude was 1 and the phase equalled to $\angle\mathbb{X}_{baseline,shifted}$. By dividing Eq. 6.12 with $\mathbb{U}_{PhaseCorrection}$, another pseudo susceptibility $\mathbb{X}_{baseline}$ would be:

$$\mathbb{X}_{baseline} = \frac{\mathbb{M}_{baseline}}{\mathbb{H}_{shifted}/\mathbb{U}_{PhaseCorrection}} = \frac{\mathbb{M}_{baseline}}{\mathbb{H}} \tag{6.13}$$

Of which $\angle\mathbb{X}_{baseline}$ equalled to 0.

The Second Stage - Signal of Sample At the first stage, both $\mathbb{X}_{baseline}$ and $\mathbb{U}_{PhaseCorrection}$ were attained and saved for the later use. At the second stage, a sample was placed in the coil and another set of data, i.e., V_{pickup} and $H_{shifted}$ were monitored and both were expressed with complex numbers. The results of which were $\mathbb{V}_{pickup}$ and $\mathbb{H}_{shifted}$.

Referring to Eq. 6.11 and Eq. 6.13, the induced magnetic field at the pickup coil $\mathbb{M}_{pickup}$ and the pseudo susceptibility $\mathbb{X}_{pickup}$ were:

$$\mathbb{M}_{pickup} = i\frac{\mathbb{V}_{pickup}}{K\omega} \tag{6.14}$$

$$\mathbb{X}_{pickup} = \frac{\mathbb{M}_{pickup}}{\mathbb{H}_{shifted}/\mathbb{U}_{PhaseCorrection}} = \frac{\mathbb{M}_{pickup}}{\mathbb{H}} \tag{6.15}$$

Additionally, because the signal $\mathbb{V}_{pickup}$ could be decomposed into $\mathbb{V}_{sample}+\mathbb{V}_{baseline}$, the Eq. 6.15 could be broken down and became:

$$\mathbb{X}_{pickup} = \frac{\mathbb{M}_{sample} + \mathbb{M}_{baseline}}{\mathbb{H}} = \mathbb{X}_{sample} + \mathbb{X}_{baseline} \tag{6.16}$$

According to the above equation, the susceptibility of a sample, $\mathbb{X}_{sample}$ can be attained by subtracting the pseudo susceptibility obtained at the second stage, i.e., $\mathbb{X}_{pickup}$ with the one measured at the first stage, i.e., $\mathbb{X}_{baseline}$, as stated below:

$$\mathbb{X}_{sample} = \mathbb{X}_{pickup} - \mathbb{X}_{baseline} \tag{6.17}$$

Discussions on the detailed features of the simplified susceptometer is presented in Appendix K

6.1.4 Calculation of MNP Induced Voltage

Eq. 6.6 could estimate either $\mathbb{V}_{sample}$ or $\mathbb{V}_{sample}$ for a single-turn pick-up coil. Nevertheless, the pick-up coil applied in the experiment presented in this chapter was 8

turns, so a factor of 8 needs to be added in the Eq. 6.6, which leads to:

$$|emf| = 8\alpha B_0^{MNP} A_{coil2}\omega \tag{6.18}$$

As described in Section 6.1.3, there were two measurement stages. We can consider the $|emf|$ at each stage separately. **At the first stage**, the parameters of B_0, A_{coil2} and ω were either known or measurable. Assume that an excitation field of 5 kA/m and 963 kHz was applied during the measurement; after unit conversion, the parameters of B_0 and ω would be 6.27×10^{-3} T and 6050707 rad $\cdot$ s^{-1}. As to the area of coil A_{coil2}, because the diameter of pick-up coil was 20 mm (see Fig. 6.3), the A_{coil2} would be 0.314×10^{-3} m^2. In relation to α, as the whole pick-up was immersed in the excitation field, its α could be regarded as 1. Hence, according to these information, a $|\mathbb{V}_{baseline}|$ of 95.300 V was expected to be induced in the pick-up coil at the first measurement stage.

At the second stage of the measurement, in the presence of a sample, the calculation would be slightly more complicated. Although the values of A and ω remained the same as those at the first stage, both the values of α and B_0 at this stage were sample-specific values.

Taking the **Sample A1** in Table 5.2 as an example, the α of which could be decomposed into $\alpha = a_{sample} m_{MNP}/\rho A_{coil2} V$ (see Section 5.1.3). The m_{MNP} in **Sample A1** was 15.5 mg, and the density ρ of which[2] was 5.18 g_{Fe}/cm^3. The A_{coil2} could be easily attained based on the dimensions in Fig. 6.3. The A_{coil2} is 0.31×10^{-3} m^2. The a_{sample} was dependent on the 2 ml glass vial. The diameter of which is 11 mm, which led to the a_{sample} of 0.095×10^{-3} (m^2). The V of Sample A1 was 0.47 ml or 470 mm^3 (see Table 5.2.) Consequently, α at the second stage for calculating $|\mathbb{V}_{15.5mg}^{C180916}|$ was 0.0020.

Afterwards, the last value to be determined was the B_0 caused by the magnetisation of **Sample A1**. Although this was a time-varying magnetisation, one may still predict its value to some extent based on the static measurement.

The main material of C180916 (Sample A1) is magnetite. The static mass susceptibility χ_{mass} of magnetite is $11 \times 10^{-4} m^3 \cdot kg^{-1}$ [119]. By multiply χ_{mass} with its density $\rho = 5.18$ g_{Fe}/cm^3, one would attain its volumetric susceptibility χ, of which the value is

[2]The specification of C180916 did not provide the information of particle density. The density was assumed to be the same as magnetite, i.e., 5.18 g_{Fe}/cm^3. This values was also used in other study that applied similar MNPs from Chemicell [118].

5.7. This value was also used in another study, in which MNP suspension from Chemicell was used [118]. The flux density, $B_0^{C180916}$, associated with the magnetisation of **Sample A1** would then become: $B_0^{C180916} = \chi B_0 = 5.7 \times 6.27 \times 10^{-3} T = 35.74 \times 10^{-3} T$

Until this step, all the parameters required for $|\mathbb{V}_{15.5mg}^{C180916}|$ have been obtained. These parameters are listed in the table below.

10x Oscilloscope Probe

An issue should be addressed here. The estimated values of $|\mathbb{V}_{baseline}|$ was 95.30 V. The high value of which brought a practical issue during the measurement. The maximum voltage range of digital oscilloscope (Picoscope 4227) was ± 20 V, but $|\mathbb{V}_{baseline}|$ was approximately 5 times beyond the range. Thus, to properly read the value of $|\mathbb{V}_{baseline}|$, a 10x oscilloscope probe was used in the measurement setup (see Fig. 6.2). A 10x probe acts as a voltage divider, of which the measured value is one-tenth of the actual value. As a result, the measured $|\mathbb{V}_{baseline}|$ at 5 kA/m and 963 kHz was expected to be 9.53 V.

Although this step allowed us to read the baseline signal, it also led to a consequence that the measured $|\mathbb{V}_{15.5mg}^{C180916}|$ was weaken from 1.18 V to be 0.12 V.

To be more specific, the measured voltage caused by 1 mg of C180916 is: $|\mathbb{V}_{1mg}^{C180916}| = 0.12/15.5 = 0.008$V or 8 mV (at 300 K). The theoretical measurement sensitivity can be described as: $0.027\ mV \cdot^{\circ} K^{-1} \cdot mg^{-1}$.

Stage	Label	α	$B_0(T)$	$A(m^2)$	$\omega(rad/s)$	Coil Turns	est. $\lvert emf\rvert(V)$
I	$\lvert\mathbb{V}_{baseline}\rvert$	1	6.27×10^{-3}	0.31×10^{-3}	6050707	8	95.30
II	$\lvert\mathbb{V}^{C180916}_{15.5mg}\rvert$	0.0020	35.74×10^{-3}	0.31×10^{-3}	6050707	8	1.18

Table 6.1: Parameters used to theoretically estimate the induced voltage in the 8-turn pick-up coil. The $\mathbb{V}_{baseline}$ was the induced voltage at the first stage of the measurement, i.e., the coil was in absence of a sample. The $\mathbb{V}_{C180916,15.5mg}$ was the estimated voltage that induced by the magnetisation of **Sample A1** at the second stage.

6.2 Experiments

The purpose of experiments presented in this chapter was to validate the fundamental assumption of the MPT proposed in Chapter 5. To fulfil this purpose, a simplified susceptometer was devised. The details of which has been explained in previous sections. The data handling has been elaborated. Both the $|\mathbb{V}_{baseline}|$ and $|\mathbb{V}_{15.5mg}^{C180916}|$ have been theoretically derived (see Table 6.1).

To validate the MPT with susceptometer, it is necessary to validate the susceptometer first (a discuss on the measurement sensitivity of susceptometer is given in Section 6.2.1). After the validation, the susceptibility measured by susceptometer could then be compared with the frequency variation in MPT. Both the validation and the comparison will be discussed below.

6.2.1 Measurement Sensitivity and Resolution

Sensitivity of Susceptometer

To attain the noise level of susceptometer, the measured $|\mathbb{V}_{15.5mg}^{C180916}|$ versus the temperature of MNPs is plotted as shown in Fig. 6.4 (the upper figure). The amplitude of $\mathbb{V}_{C180916,15.5mg}$ is expressed as $V_{15.5mg}^{C180916}$ in the figure. A linear regression has been performed. As expected, the $V_{15.5mg}^{C180916}$ was linearly correlated with T_{MNP}. The R^2 of the correlation is 0.88. The noise level is obtained by subtracting the measured $V_{15.5mg}^{C180916}$ by those values derived from the fitted equation, i.e., $V_{15.5mg}^{C180916} = 0.23T_{MNP} + 48.6$. The result is shown at the bottom of Fig. 6.4. Thus, the temperature sensitivity per mg of C180916 would be $0.23(mV/K)/15.5(mg) = 0.015\ mV \cdot K^{-1} \cdot mg^{-1}$.

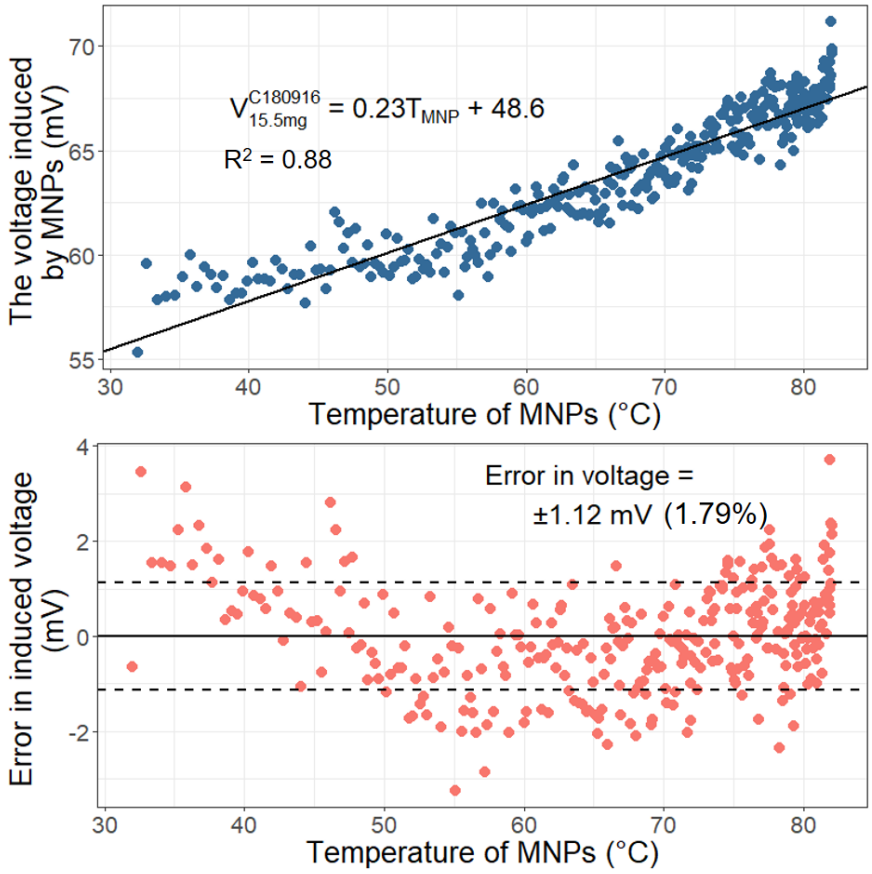

Figure 6.4: The upper figure is the relationship $V_{15.5mg}^{C180916}$ and T_{MNP}. The R^2 value of the linear regression is 0.88. The figure at the bottom is the difference between the induced voltage and the fitted line. The difference is regarded as the noise of $V_{15.5mg}^{C180916}$. The noise level of which is 1.12 mV. The noise level is attained by the standard deviation of the scattering. The noise level here represents the uncertainty of the measurement.

Sensitivity of MPT

In the same measurement, the resonant frequency was also measured. The $\Delta f_{15.5mg}^{C180916}$ was compared with T_{MNP} in Fig. 6.5. Their correlation was high ($R^2 = 0.9988$).

The detected signal in MPT, i.e., $\Delta f_{15.5mg}^{C180916}$, ranged from -931 Hz to -1053 when along with the temperature varying from 30°C to 80°C. The bottom figure (see Fig. 6.5) indicates the amplitude of noise was around 1.14 Hz (i.e. 0.11 %). As to the measurement sensitivity, based on the fitted equation in the figure above, i.e., $\Delta f_{15.5mg}^{C180916} = -2.44T_{MNP} - 858$, the measurement sensitivity of MPT was $2.44(Hz/K)/15.5(mg) = 0.157\ Hz \cdot K^{-1} \cdot mg^{-1}$.

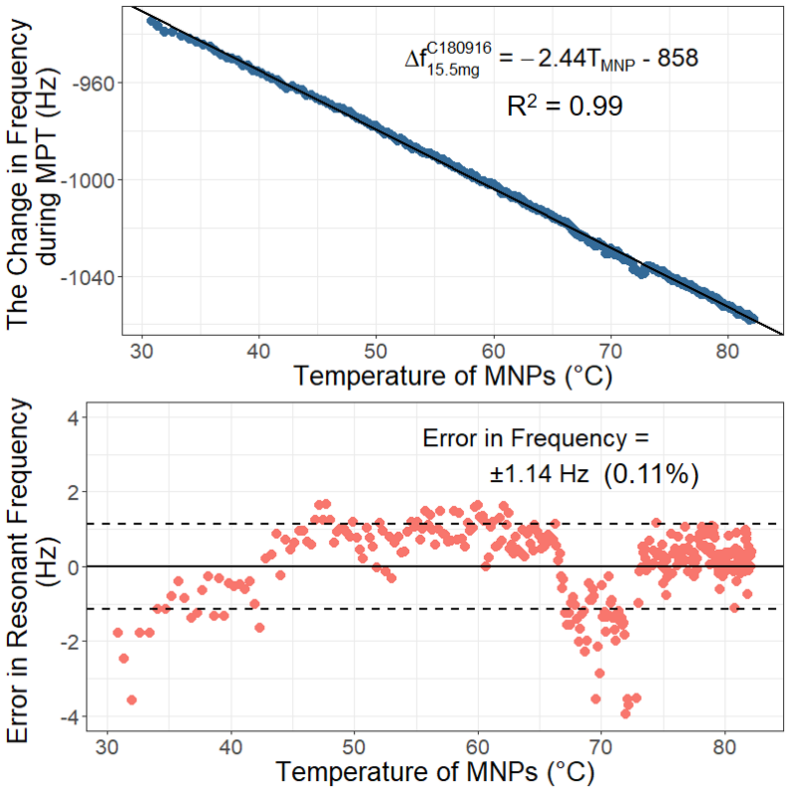

Figure 6.5: The upper figure is the relationship $\Delta f_{15.5mg}^{C180916}$ and T_{MNP}. The R^2 value of the linear regression was close to 1 (0.9988). The figure at the bottom is the noise in $\Delta f_{15.5mg}^{C180916}$.

Resolution

The noise levels of Susceptometer and MPT were 1.12 mV and 1.14 Hz respectively. Thus, their resolutions can be estimated by dividing their noise levels with their sensitivities. As a result, the resolution of susceptometer and MPT were 75 $K \cdot mg_{Fe}$ and 7 $K \cdot mg_{Fe}$. The measurement resolution of MPT was about 10 times higher than that of the susceptometer presented here.

The Table 6.2 below concludes both the sensitivities and resolutions of MPT and susceptometer.

Device	Sample	Sensitivity($\frac{mV}{K \cdot mg_{mg}}$)	Resolution ($K \cdot mg_{Fe}$)
Susceptometer	C180916	0.015	75
MPT	C180916	0.157	7

Table 6.2: The measurement resolution of MPT and simplified susceptometer.

6.2.2 Validating the Simplified Susceptometer

The focus of this section is the question: *whether the signal measured by the susceptometer is the susceptibility of a sample?* To address this, the following discussion focuses on the comparison of empirical and theoretical values of induced voltage.

Comparison of Empirical and Theoretical Voltages

In Section 6.1, the induced voltage has been theoretically estimated. The values of which are compared with the empirically measured voltages presented in Table 6.3.

Firstly, let us look at the $|\mathbb{V}_{15.5mg}^{C180916}|$. The measured value (10.01 V) was close to the estimated value (9.53 V). For the convenience of discussion, a factor termed as empirical factor γ was defined. It was defined to be the ratio of measured value to the estimated value. That is, the γ_1 at the first stage was $10.01/9.53 = 1.06$. This implies that there was a 6% difference between estimation and the actual measurement. The value attained in the actual measurement was straightforward and thus not adjustable.

As for the theoretical estimation, parameters in Eq. 6.18 include α, B_0, A_{coil2} and ω. At the first stage, both B_0 and ω were determined by the excitation field. And both values were measured by the Rogowski coil. Also, as mentioned, because the whole pickup coil was immersed in the excitation field, $\alpha = 1$ should be a reasonable assumption.

Therefore, the only factor that would cause this 6% difference would be A. If this is the case, the actual A_{coil2} should be $0.314 \times 10^3 \times \gamma_1$. This suggests that the diameter of pick-up coil may be 20.59 mm instead of 20.00 mm that described in Fig. 6.3. This little difference validated the calculation used for estimating the baseline signal.

Stage	Label	$est.\frac{\lvert emf\rvert}{10}(V)$	measured $\frac{\lvert emf\rvert}{10}(V)$	$\gamma = \frac{measured\lvert emf\rvert}{est.\lvert emf\rvert}$
I	$\lvert\mathbb{V}_{baseline}\rvert$	9.53	10.01	1.06
II	$\lvert\mathbb{V}_{15.5mg}^{C180916}\rvert$	0.12	0.05	0.42

Table 6.3: Theoretically estimated value and empirical value of $\mathbb{V}_{baseline}$ and $\mathbb{V}_{C180916,15.5mg}$. An empirical parameter γ is attained by dividing the empirical value with the theoretical value.

Secondly, the γ_2 at the second stage was 0.42, which indicates the fact that the empirical data was 58% lower than the estimated one. Because the A_{coil2} was the

same at both stages, the γ_1 should have the same effect at Stage II. In addition, the ω was measured and used in the theoretical estimation; that is, ω itself was an empirical value and would not affect γ_2.

The rest two parameters that could affect γ_2 were α and $B_0^{C180916}$. In relation to α, although error might be introduced during the calculation, it was unlikely that the error was as large as 58%. Hence, one can confidently say that the main cause of this low empirical factor was related to $B_0^{C180916}$.

To be more specific, the difference in $B_0^{C180916}$ between estimation and the actual value should be the main cause that resulted in the difference of $\gamma_2/\gamma_1 = 42\%$. That is, in the actual measurement, the $B_0^{C180916}$ could be only 42% of the estimated value.

The Frequency Dependence of Susceptibility

The 58% difference in $B_0^{C180916}$ might be associated with the frequency dependence of χ. The frequency dependence has been mathematically described in Eq. 9a and Eq. 9b in [48]. Based on these equations, a simulated frequency dependence of susceptibility is plotted in the figure below. Parameters' details and the simulation's script can be found in Appendix L.

In the figure, the black line indicates the amplitude of susceptibility. The green and red respectively represent the real and imaginary susceptibility. Overall, as the applied frequency was as high as 963 kHz, the decrease in susceptibility could be evident. According to the demonstrative simulation, the AC susceptibility became 42 % of the static value was possible.

To briefly conclude, the empirical data did either fit the theoretical predications or could be theoretically explained. Based on which, the author believes that the presented susceptometer and the data handling method were both validated.

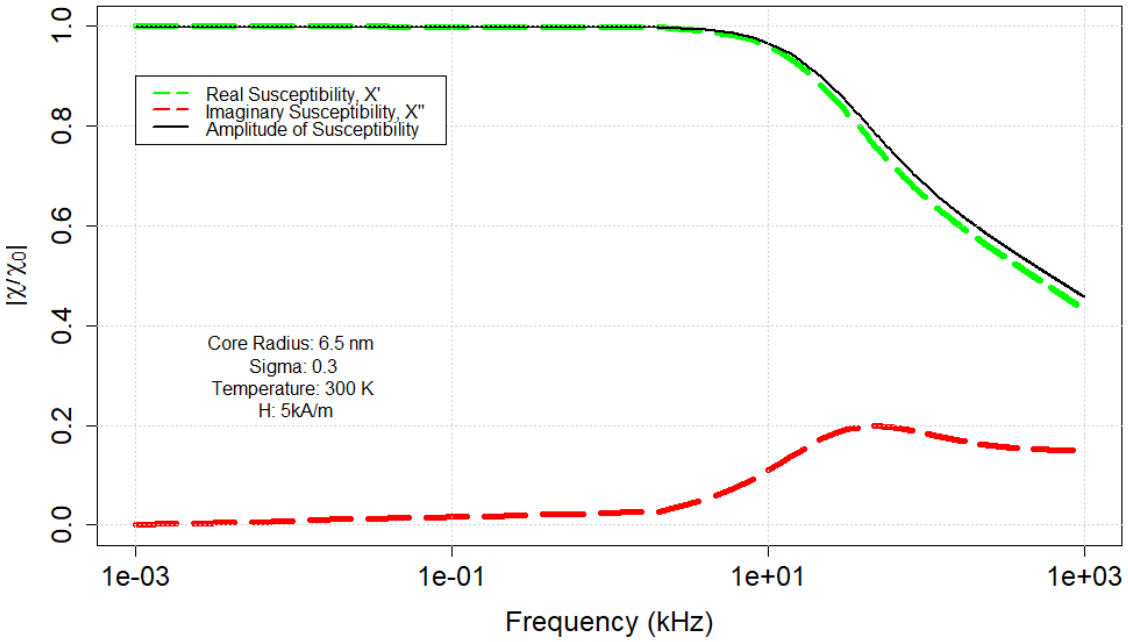

Figure 6.6: The decrease in dynamic susceptibility as a function of applied frequency relative to its static value. The simulation is based on [48]. The *Sigma* is the standard deviation of normal distribution of particle size. The value of which was assumed to be 0.3. The core radius of an MNP was assumed to be 6.5 nm. The field intensity and temperature were relatively assumed as 5 kA/m and 300 K (Note that the simulated result here aims at demonstrating the frequency dependence of the amplitude of susceptibility. The parameters used in the simulation were not necessarily the same as those in the experiment presented in this section. The detail of which can be found in Appendix L).

Convert the Measured Voltage in Susceptometer to χ

Since the susceptometer was validated, we can now covert the measured voltage to the form that we are actually interested in, i.e., the susceptibility. The conversion could be done by rearranging Eq. 6.18 to make it become:

$$B_0^{C180916} = \frac{V_{15.5mg}^{C180916}}{8\alpha A\omega} \tag{6.19}$$

Then, the unit conversion is shown as below:

$$M^{C180916} = \frac{V_{15.5mg}^{C180916}}{8\mu_0\alpha A_{coil2}\omega}(unit : A/m) \tag{6.20}$$

By dividing the $M^{C180916}$ with H (in the unit of A/m), one obtains the $\chi^{C180916}$:

$$\chi^{C180916} = \frac{M^{C180916}}{H}(unit : dimensionless) \tag{6.21}$$

To validate the assumption used in MPT, this susceptibility measured by the susceptometer $\chi^{C180916}$ was then compared with the susceptibility derived from the frequency variation in MACH. The detail of which is described below.

6.2.3 Validating the Magnetic Particle Thermometry

The experiment presented here aimed at measuring the same parameter with two different devices. The parameter was the magnetic susceptibility of a material. To avoid confusion, the author would like to emphasise that, although previous discussions focused much on temperature and quantity measurements, the key function of both devices is to obtain the susceptibility of sample.

And it is because of the quantity dependence of filling factor, e.g., α or ϵ, as well as the temperature dependence of susceptibility that made those measurements possible. Since signals measured by both devices were associated with the same parameter, no matter what the material is, the measured results from them should be equivalent.

Thus, the next section will focus on the discussion of this equivalence. This will be followed by another section that describes an experiment conducted for validating the concept of filling factor.

Comparison between Susceptibility and Resonant Frequency Variation

As mentioned, the signals of both MPT and susceptometer are determined by the susceptibility of a material. The χ derived from Eq. 5.13 would be the same as that derived from Eq. 6.20 and Eq. 6.21. The derivations of both are described as below:

$$\chi \text{ derived from MPT: } \chi_{mpt} = -\frac{2}{\epsilon}\frac{\Delta f}{f_0}(unit : dimensionless); \tag{6.22}$$

$$\chi \text{ derived from Susceptometer: } \chi_{sus} = \frac{V_{Sample}}{8\mu_0\alpha A\omega H}(unit : dimensionless) \tag{6.23}$$

The chief purpose of the following experiment was to examine the equivalence of χ_{mpt} and χ_{sus}. Once the equivalence is proved, the fundamental assumption of MPT

is validated. For better visualisation of experimental, the above two equations are re-expressed as below:

$$-\frac{\Delta f}{f_0} = \frac{1}{2}\epsilon\chi_{sus} \tag{6.24}$$

The above equation implies that the slope of $-\frac{\Delta f}{f_0}$ and χ_{sus} equals to $\frac{1}{2}\epsilon$. The filling factor ϵ can be attained through: $\frac{a_{sample}m_{MNP}}{A_{coil1}\rho V}$. According to the dimension mentioned in Fig. 5.4, A_{coil1} is $0.68 \times 10^{-3}m^2$. Because the ϵ is dependent on m_{MNP}, the slope should increase along with m_{MNP}. To demonstrate the effect, three sample applied in Chapter 5 were used again in this experiment. They were **Sample A0**, **Sample A1** and **Sample A2**. The three samples contained the same MNP, i.e., C180916, but its m_{MNP} ranged from 7.7 mg to 31.6 mg.

On the one hand, the ρ of C180916 is known to be 5.18 g/cm^3, so the theoretical slope of each measurement can be calculated. They were respectively 2.1×10^{-4}, 4.2×10^{-4} and 8.6×10^{-4}. On the other hand, the empirical slope of each measurement can be attained through comparing the measured susceptibility χ_{sus} and the measured frequency variation $\frac{\Delta f}{f_0}$, as illustrated in the upper picture in Fig. 6.7.

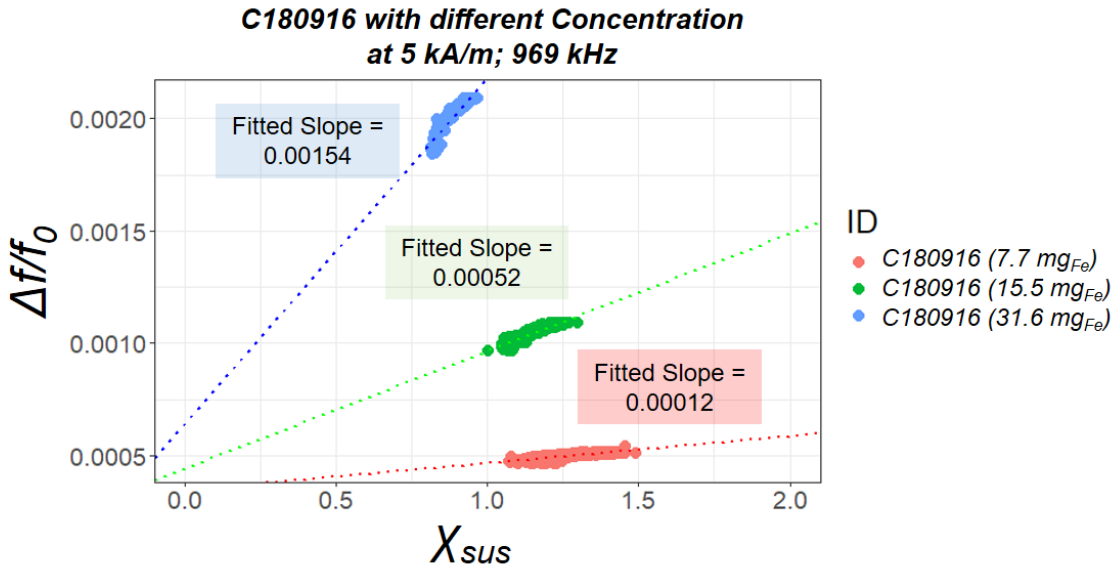

Figure 6.7: Measurement results of C180916 at 5 kA/m and 969 kHz. The quantity of them were at three different levels, i.e., 7.7 mg, 15.5 mg, 31.6 mg.

Sample	m_{MNP} (mg)	Theoretical Slope	Empirical Slope	Error
C180916	7.7	2.1×10^{-4}	1.2×10^{-4}	-43%
C180916	15.5	4.2×10^{-4}	5.2×10^{-4}	26 %
C180916	31.6	8.6×10^{-4}	15.4×10^{-4}	80 %

Table 6.4: The empirical and theoretical slopes of $\Delta f/f_0$ versus χ for measurement of C180916 at three difference quantities.

Both the theoretical and empirical slopes are listed in Table 6.4. These two sets of values were not consistent. The errors of them was up to 80%. A possible reason behind this inconsistency is the low measurement resolution of susceptometer.

As discussed in Table 6.2, the susceptometer's resolution for measuring C180916 was 75 ($K \cdot mg_{Fe}$). That is, for 7.7 mg_{Fe}, 15.5 mg_{Fe} and 31.6 mg_{Fe} of C180916, the detectable temperature variations were 9.7 K, 4.8 K and 2.4 K, respectively. The temperature elevations in MNPs were ca. 50 K. Therefore, some temperature variations were not detectable by the susceptometer. This might be the main reason that the empirical slopes were different from the theoretical ones.

A Larger Range of χ_{sus} If the signal generated by the temperature change in a sample was not reliable enough, one could probably **enlarge the range of signal through varying** m_{MNP} or **using different types of MNPs**. To achieve this, the author included a variety of MNPs in the another measurement presented below.

The various types of samples ensured a large range of χ. Overall, 27 MNP suspensions and 2 powder samples were included; measurements were performed 119 times at a variety of field strengths, the field strengths, frequencies and the sample details of each measurement are listed in Appendix M.

Unlike the previous experiment described in Fig. 6.7, the diversity of samples in this experiment ensured a large range of χ_{sus}; nevertheless, there was an issue when calculating χ_{sus}. To attain χ_{sus}, it was necessary to know the sample-specific parameter ρ for attaining α, but not all suppliers provided this information. In order to bypass this uncertain parameter, the Eq. 6.24 is re-expressed as below:

$$-\frac{\Delta f}{f_0} = \frac{1}{2}\frac{\epsilon}{\alpha}\alpha\chi_{sus} \tag{6.25}$$

In which, the m_{MNP}/ρ in both ϵ and α was cancelled through the division ϵ/α.

This ratio equals to A_{coil2}/A_{coil1}. Thus, in theory, the slope of $-\frac{\Delta f}{f_0}$ and $\alpha\chi_{sus}$ would be a constant, i.e., $\frac{1}{2}0.46 = 0.23$. Besides, considering the fact that $\alpha\chi_{sus}$ equals to $\frac{V_{sample}}{8\mu_0 A_{coil2}\omega H}$, the parameters in which were all measurable and there was no need for considering the sample-specific filling factor α. As a result, the correlation of susceptibility and frequency variation is as shown in Fig. 6.8.

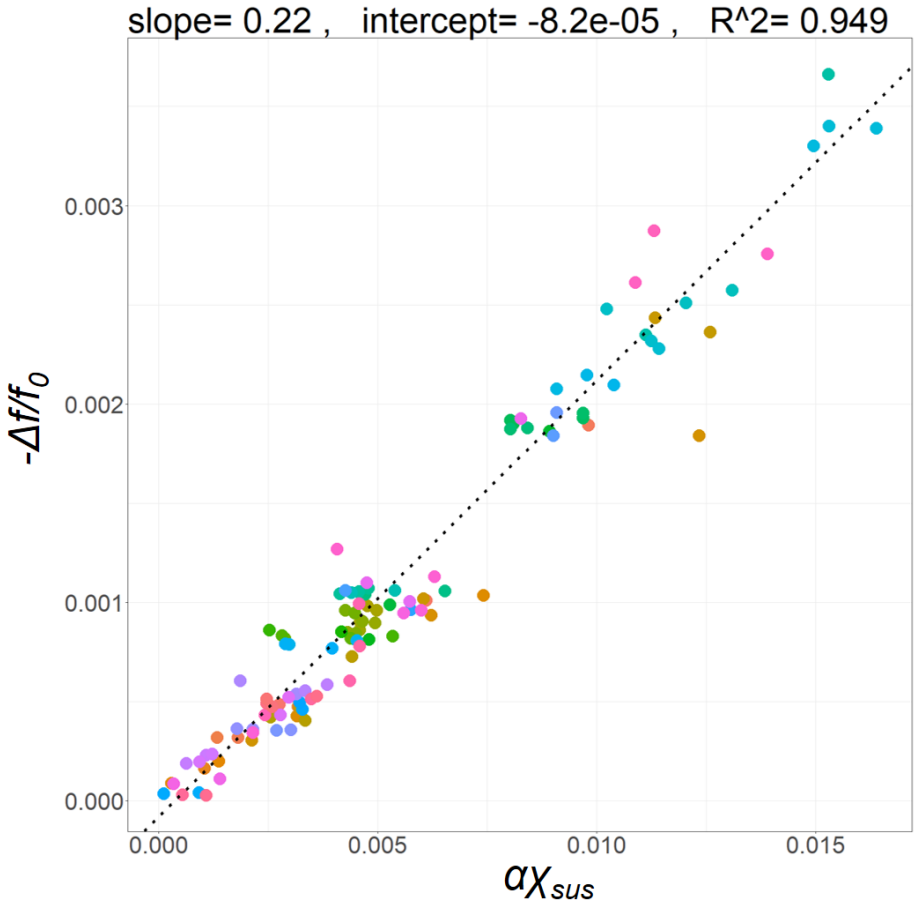

Figure 6.8: The correlation of susceptibility and frequency variation. The sample details are stated in Appendix M.

The figure shows a clear linearity between $-\frac{\Delta f}{f_0}$ and $\alpha\chi$. The R^2 of the linear regression was as high as 0.949. This linear correlation well supports the Eq. 6.25. The empirical slope of their correlation (0.22) was less than 5 % different from the estimated slope (0.23).

Apart from the linear correlation, it is worth describing the experimental data in Fig. 6.8 from another perspective. By dividing both sides of the Eq. 6.24 by m_{MNP}, one obtains the equation below:

$$-\frac{\Delta f}{f_0 m_{MNP}} = \frac{1}{2}\frac{a_{sample}}{\rho A_{coil1} V}\chi \tag{6.26}$$

In this equation, the parameters on the right hand side are sample-specific. In

other words, if the equation is correct, the $-\frac{\Delta f}{f_0 m_{MNP}}$ would be a sample-specific value. This effect is shown in Fig. 6.9. In this figure, four types of MNP suspensions from Fig. 6.8 were selected. Each type possessed different particle diameters. Every type had more than one sample be measured. Each sample either had different m_{MNP} or it was produced in different batches.

The figure shows that the correlation of susceptibility and frequency variation was, as described, linear. Its slope was identical to the previous value 0.22. Interestingly, once the y axis $-\frac{\Delta f}{f_0}$ was divided by the m_{MNP}, the result $-\frac{\Delta f}{f_0 m_{MNP}}$ could be classified into 4 levels as expected.

Each level should represent the value of $\frac{a_{sample}\chi}{2\rho A_{coil1} V}$. Because the coil and the sample were not changed during the measurement, A_{coil1}, a_{sample} and V was a constant. As to $\frac{\chi}{\rho}$, this was the characteristics of each type of MNP. This empirical result met the prediction of Eq. 6.24 and hence it could also be regarded as an evidence of the MPT theory.

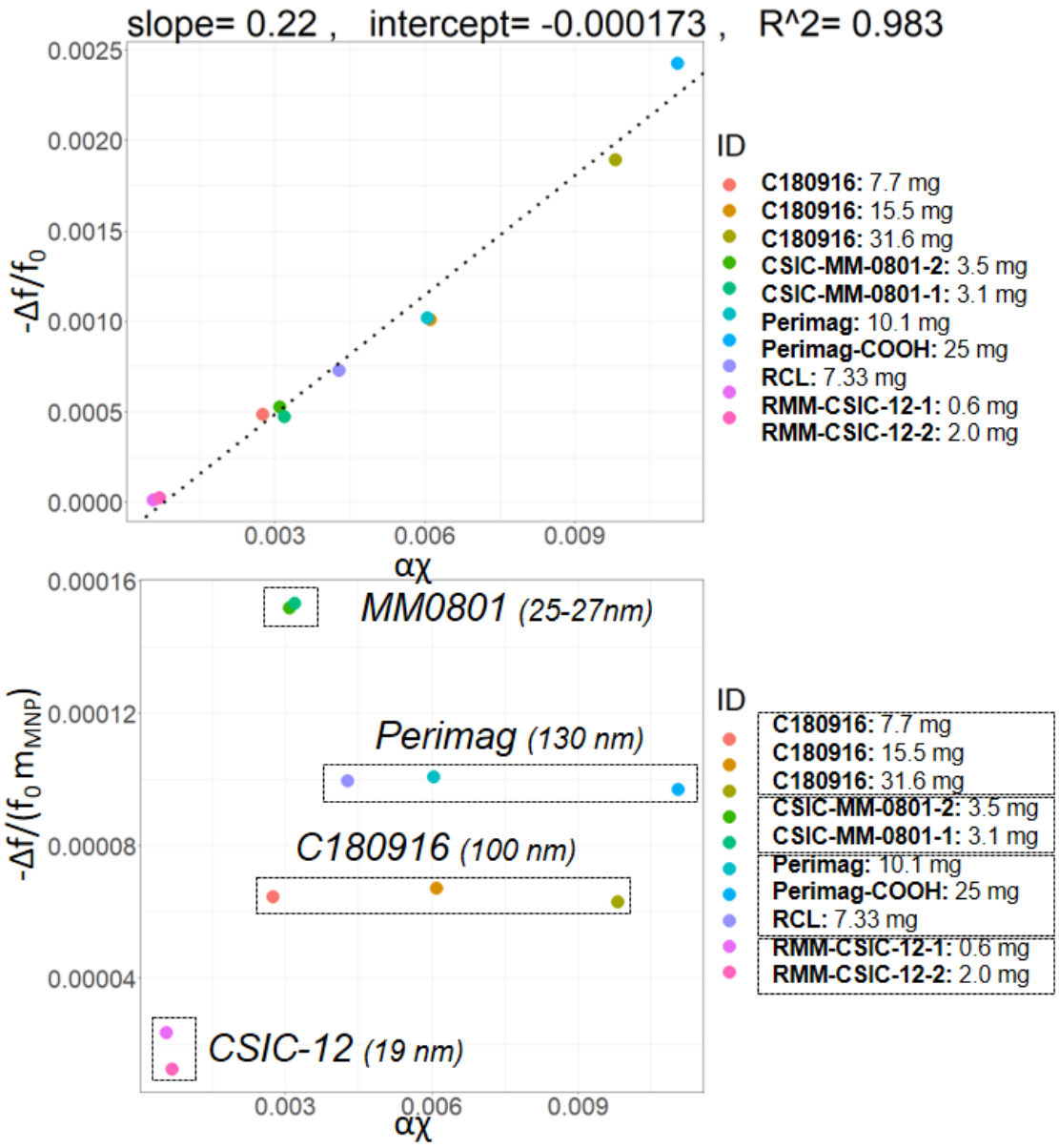

Figure 6.9: The upper graph is the correlation of susceptibility and frequency variation for four types of samples when exposing to a 10 kA/m and 970 kHz field. The bottom graph shows the fact that each type of sample has a specific value of $-\Delta f/f_0 m_{MNP}$. The particle diameter of each type of MNP is also stated.

High Filling Coil

The smaller the coil, the higher the filling factor. To further confirm the theory, a coil with higher filling factor was built. Another MPT measurement was performed based on this high filling coil. Say the filling factor of this new coil was termed as β, and the area of this coil was termed as A_{coil3}. The aim of this experiment was to see if α/β equalled to A_{coil_3}/A_{coil1}.

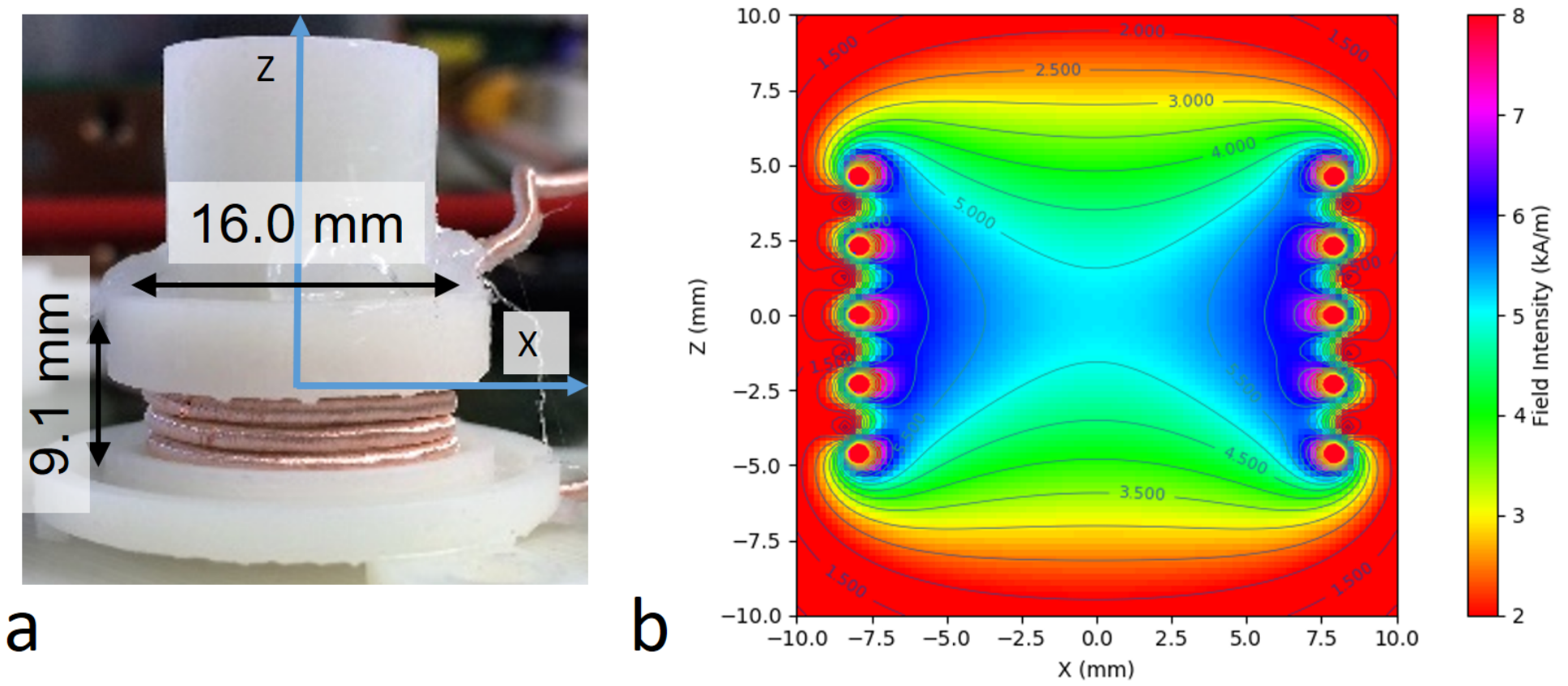

Figure 6.10: (a) A higher filling factor. The diameter and the height of the coil are 16.0 mm and 9.1 mm. The volume of coil is denoted as A_{coil3}, of which the value is $0.2 \times 10^{-3} m^2$. (B) The calculated field distribution of this high filling coil, the field intensity at the centre is 5 kA/m when the coil current is 20 A (see the script in Appendix A).

The configuration of the high filling coil and its field distribution are presented in Fig. 6.10a. Based on the geometry of the high filling coil and Biot-Savart Law, the field distribution is calculated. If the resonant current was 20 A, then the field strength at the centre is 5 kA/m, as shown in Fig. 6.10b.

The MPT measurement of **Sample A0**, **Sample A1** and **Sample A2** were performed. The experimental result were then compared with the aforementioned results measured by MACH coil. The comparison is presented in Fig. 6.11. In which, the experimental results are displayed with the term of $-\frac{\Delta f}{f_0 m_{MNP}}$ (see Eq. 6.26).

The advantage of expressing the results with this form was that $-\frac{\Delta f}{f_0 m_{MNP}}$ depends only on the characteristics of MNP, i.e., $\frac{a_{sample}}{\rho V}$, and the geometrical feature of the coil, i.e., $\frac{1}{A_{coil3}}$.

Since the same sample was applied in both measurement, the value of $\frac{a_{sample}}{\rho V}$ should remain the same in measurements of both MPT coils. Thus, the ratio of $-\frac{\Delta f}{f_0 m_{MNP}}$ obtained in MACH coil and that attained in high filling coil would only be associated with A_{coil13}/A_{coil1}. That is, theoretically, the ratio α/β would be $0.2/0.68 = \mathbf{0.29}$.

As indicated in Fig. 6.11, the value of $-\frac{\Delta f}{f_0 m_{MNP}}$ of C180916 suspensions measured in MACH coil was 0.000066. Its counterpart measured in high filling coil was 0.000222. As a result, the empirical ratio of filling faction α/β was **0.30**.

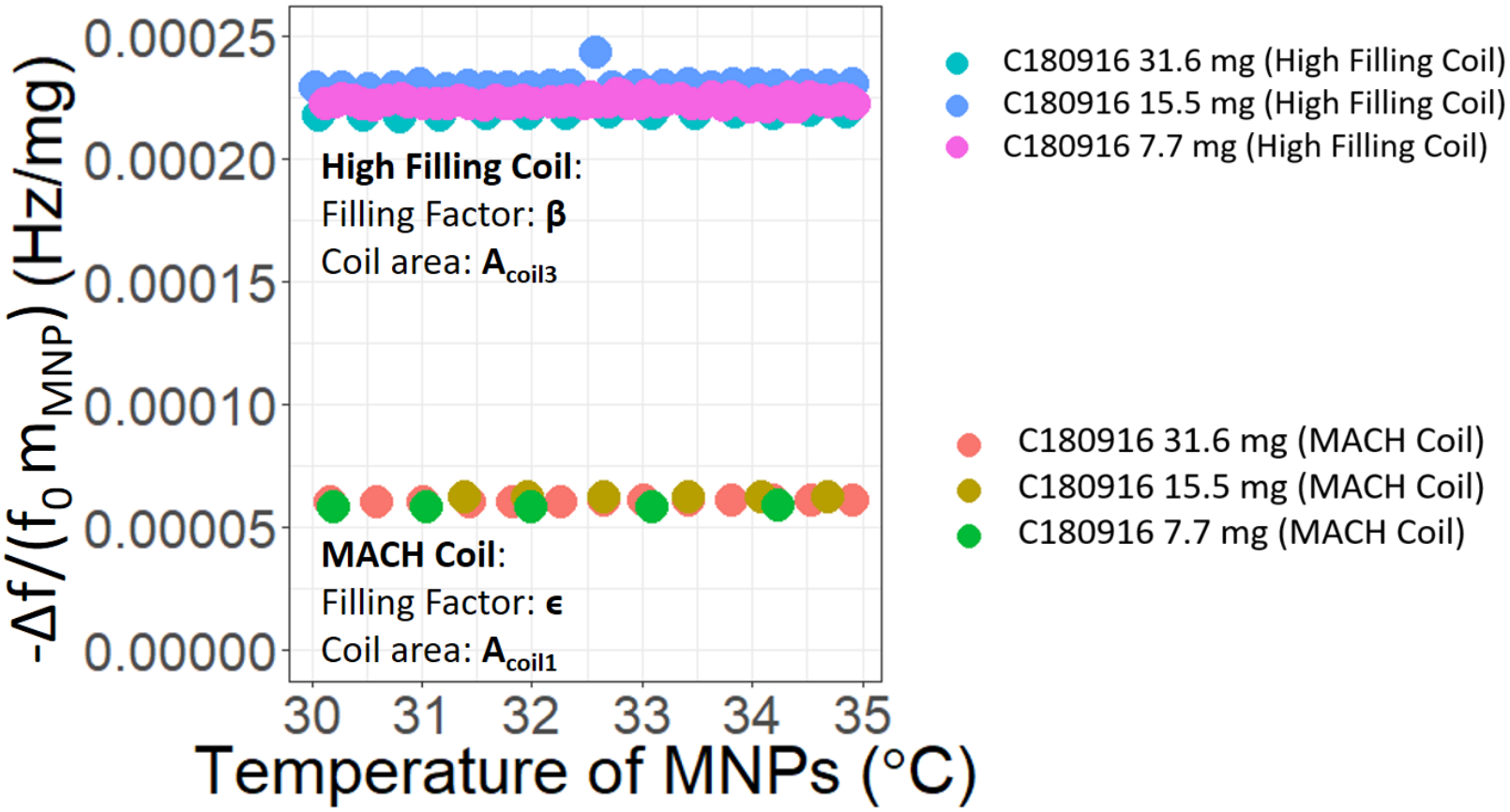

Figure 6.11: The values of the term $-\Delta f/f_0 m_{MNP}$ that respectively measured in MACH coil and high filling coil. Three samples, i.e., Sample A0, Sample A1 and Sample A2, were applied in both coils. The main difference in both measurements was the filling factor. This difference resulted in two levels of $-\Delta f/f_0 m_{MNP}$. And the ratio of ϵ/β was 0.30.

Coil	Filling Factor Symbol	Coil Area (m^2)
MACH	ϵ	0.68×10^{-3}
Susceptometer	α	0.31×10^{-3}
High Filling	β	0.20×10^{-3}

Table 6.5: The filling factors, coil volume and coil area of each device.

Theoretical Ratio	Empirical Ratio	Error
$\epsilon/\alpha = 0.46$	$\epsilon/\alpha = 0.44$	4%
$\epsilon/\beta = 0.29$	$\epsilon/\beta = 0.30$	3%

Table 6.6: Ratios of filling factor and the ratio of coil area.

To have a more clear picture of filling factor, Table 6.5 and Table 6.6 summarise the coil areas and the ratio of filling factors. The results indicate that the difference between the empirical and theoretical values was lower than 5%. This is strong evidence that **the fundamental assumption of MPT**, i.e., the change in resonant frequency is caused by the variation in χ, **is correct**.

6.3 Discussion

The main purpose of above discussions is to validate the proposed MPT. In Chapter 5, the linear correlation between the change in resonant frequency Δf and the temperature of MNPs T_{MNP} has been clearly stated. For an engineering-oriented study, the linear correlation itself would probably be enough. The correlation allows one to easily convert Δf to T_{MNP} through characterisation. As a result, monitoring the temperature at a distance becomes possible. This may be the completion phase of an engineering task, but this could be a new chapter of a science-related task. The former tends to apply, while the latter tends to explain. Hence, unlike the discussion in the previous chapter, which focused on the possible applications of MPT, this chapter made efforts to explain and validate the causal relationship of parameters in MPT

To achieve this, a simplified susceptometer has been built and embedded in the field applicator of MPT. This configuration allows one to measure the same parameter

χ with two devices, i.e., MPT and susceptometer. The first section described the principle of the susceptometer. The measurement sensitivity of which were theoretically discussed. Then, the following section, compared the empirical data collected by the susceptometer with the deduced values. By doing so, the susceptometer was validated.

Afterwards, the data measured by both MPT and susceptometer were compared. A strong linear correlation has been found between them, the slope of the correlation was closed to the theoretical value. Another coil with high filling factor was built for further confirming the correctness of the finding.

Overall, the fundamental assumption of MPT has been validated through a series of empirical studies presented in this chapter. This MPT is proposed as a way to improve the thermal management in magnetic hyperthermia, also with the potential to benefit other applications.

Chapter 7

Conclusion

A simple yet influential idea - magnetic hyperthermia. Since the idea was proposed six decades ago, the key idea of magnetic hyperthermia does not vary much. Researchers are still trying to cure cancer by heating, a strategy that dates back more than two thousand years. While some utilises the heat as a monotherapy, others rely on it to enhance the performance of alternatives, e.g., chemo-therapy and radio-therapy.

Although the key idea remains unchanged, our knowledge of magnetic hyperthermia has been much improved in different aspects. Biologists have gained more insight into the thermal response of cells. Quantitative metrics such as thermal dose has been proposed based on empirical *in-vivo* studies. Biological studies on bio-distribution of MNPs have provided valuable information for researches in this field. Engineers have built more energy efficient field applicator. Field applicators have been shrunk from devices occupying the entire operating room to desktop-sized devices. Physicists have theorised the mechanism of magnetic heating. The quantification of magnetic heating provides key metrics for chemists to evaluate those MNPs they designed and manufactured. When it comes to chemists, it has to mention the nanotechnology boom that began at the start of this century. The emerging researches in nanotechnology has fuelled researches in magnetic hyperthermia. As indicated in Fig. 7.1, the number of associated papers published in the first decade of this century was about 25 times of that in the previous decade. Advances in nanotechnology have greatly enhanced the heating ability and stability of MNPs. Improvements in different aspects have made this 60-year-old idea popular again. Until 2019, there have been more than 10 thousands reports on magnetic hyperthermia being published in the past decade.

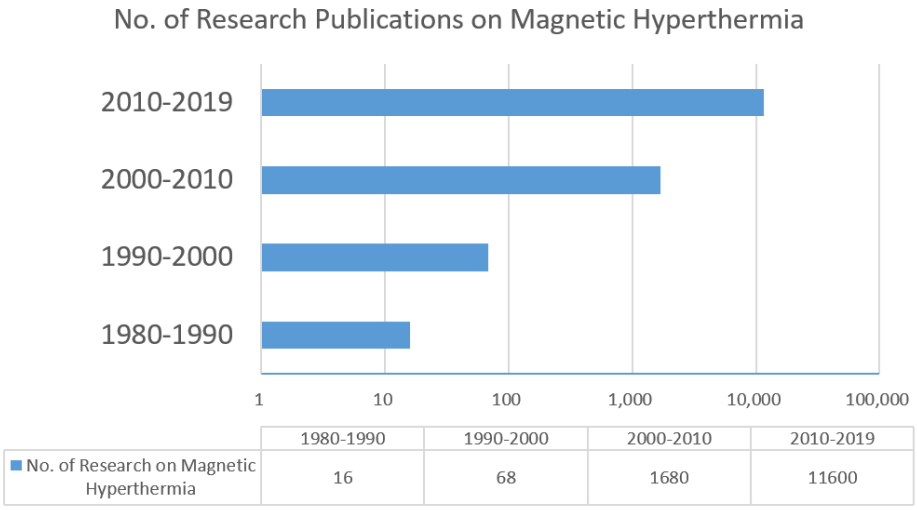

Figure 7.1: The number of research publications published in each decade between 1980 and 2019. The number of papers is attained through the search of *magnetic hyperthermia* in Google Scholar

Practical Challenge. Despite of much effort made by outstanding researchers, magnetic hyperthermia is still a step away from clinical use. To understanding the difficulties, the author immersed himself in the scenario of performing magnetic hyperthermia and gained first-hand experience through an *ex-vivo* study of porcine prostate tissues (see Chapter 1). Based on which as well as related literatures, the author summarised magnetic hyperthermia with a framework. The procedures of magnetic hyperthermia are categorised into three actions. Each action has its own associated elements. The framework of three actions and five elements was illustrated in Fig. 1.9. A framework is particularly important to a multidisciplinary subject like magnetic hyperthermia. As indicated earlier, biologists, engineers, physicists and chemists are contributing to this field in their own perspectives. A framework or a map to visualise positions of our researches is beneficial. It is beneficial either for the purpose of cross-disciplinary collaboration or simply for conveying our own findings to the public.

The *ex-vivo* study illustrated a practical challenge associated with the last element in the framework, i.e., thermometry. The current gold standard of temperature sensing is to place thermal probes in the target. However, tissues are deformable; thus, accurate placement is challenging. Inadvertent misplacement of probes can lead to treatment failure or even serious complications. In this case, false information is worse than no information. Follow up on this discussion, the study aimed at improving the thermal management of magnetic hyperthermia. This topic is still very board. The

thermal management can be related to the control or imaging of particles, the heating performance of particles. Some achieve the thermal management through limiting the its heating ability the target temperature. Moreover, some focus on seeking for alternative methods for sensing temperature. This study is particularly interested in the latter, especially in remote sensing techniques. Rather than spot measurement, remote sensing techniques tend to have ability to either perform multipoint measurement or attain a representative temperature across the whole treated region. In this thesis, the remote sensing of the temperature during magnetic hyperthermia has been carefully discussed in this context, with the discussion based on both theoretical derivation and empirical experiments.

The discussion could be broadly divided into two themes. One was an investigation in a currently available thermometry, while another was an attempt to go beyond the knowledge base and seek for an alternative. To be more specific, the former is related to infra-red thermography and the latter is in relation to a novel magnetic particle thermometry.

Giants Sir Isaac Newton (1642 - 1726) once said that one sees further by standing upon the shoulders of giants. Everything comes from something. The same is true of a research. The fundamental concepts of magnetic hyperthermia has been reviewed in Chapter 2. It includes topics of biological effects of heat, mechanisms of magnetic heating, concerns of safety and a review of current methods for remote monitoring temperature. The discussions of these topics formed the theoretical lens of the study. Those theories were main tools that the author used to explore and interpret the empirical results of this study.

For instance, the concepts of CEM43 and ILP have been utilised in Chapter 3. The dose limitation descried in the section of Safety Concerns has been considered at the beginning of Chapter 4. In which chapter, the biological effect of heat was regarded as an indicator of hyperthermia. Furthermore, the review of magnetism in Section 2.2 did not only facilitate the theory derivation in Chapter 5 but also provide the author with a way to explain the difference between theoretical and empirical values (see Table 6.5).

Infra-red thermometry. A thermometry is one of the five elements of the magnetic hyperthermia framework (see Fig. 1.9). Discussion on the widely used infra-red ther-

mography without considering other elements would not be as interesting. The utilisation of infra-red thermography would be better evaluated in the context of magnetic hyperthermia. Thus, Chapter 3 and Chapter 4 individually described *in-vitro* and *in-vivo* hyperthermia experiments, in which temperatures of targets were monitored by infra-red thermography. While experimental conditions in *in-vitro* experiments were controllable, conditions in *in-vivo* environment were specific to each murine model. On the one hand, the controllable conditions in the former provided a chance to evaluate the experimental setup. On the other hand, the experiments in the latter demonstrated the practical issues in the *in-vivo* environment during the procedure of magnetic hyperthermia. More detailed conclusion are individually described as below.

In-vitro magnetic hyperthermia on phantoms. The procedure of making a phantom has been proposed in Chapter 3. Taking the advantage of controllability of phantom, the effect of particle distribution on the temperature distribution was studied. It was demonstrated that not only the dose of MNPs but also the pattern of particle distribution would affect the temperature variation during the hyperthermia. This result emphasises the importance of an element in the hyperthermia framework, i.e., the *in-vivo* imaging of particle distribution.

Although prostate phantoms were built in this study, the procedure of phantom construction allows one to easily create phantoms with other anatomical shapes. Phantom studies can benefit the magnetic hyperthermia research in some ways. One of those is that it is able to evaluate the experimental setup. As the heating ability of MNPs is often known from the manufacturers, when exposing to a known field, the temperature variation can be predicted or simulated. By comparing the simulated temperature variation with the measured one, the experiment setup can be validated.

Despite of the simplicity of simulating method presented in this study, measured empirical temperature distributions were similar to those estimated through simulation (see Fig. 3.19). In other words, if one can attain the particle distribution through the third element, i.e., *in-vivo* imaging, then it is possible to simulate the three dimensional temperature distribution in the context of clinical scenario. Afterwards, the temperature distribution can be converted to the distribution of CEM43. The latter is regarded as a predictive indicator of hyperthermia. To be more specific, CEM43 is a parameter derived from the average temperature and heating duration, and the value of which can predict the severity of cell damage. Visualisation of CEM43 distribution

(see Fig. 3.17) can potentially facilitate the process of determining the intensity of hyperthermia.

Generally speaking, *in-vitro* experiments described in Chapter 3 was related to the last action in the hyperthermia framework. Two elements were covered, which were the temperature distribution prediction and the thermometry. The infra-red thermography has been validated through *in-vitro* studies. The same thermometry was then applied in the *in-vivo* studies.

In-vivo magnetic hyperthermia on murine models The framework illustrated in Fig. 1.9 is for the treatment of hyperthermia. However, at the pre-clinical stage, it is unlikely that every information is known. For instance, the first two elements, i.e., the dosage determination and field adjustment, would depend on the characteristics of MNP suspension. Thus, these two elements need to be evaluated before the actual treatment. At the research stage, the framework of an experiment should be adjusted according to its purpose.

Overall, there were four *in-vivo* experiments presented in Chapter 4. The framework of each experiment is as shown in Fig. 4.24. Each experiment had its own purpose. Experiments A and B aimed at determining the injection protocol and the applied field intensity respectively. For the dosage determination, the experiment indicated that Eq. 2.21 provided a good guidance. On the other hand, Experiment C aimed at validating the thermal dose CEM43 with the empirical indicator of cell damage HSP70 level. A trend of correlation between CEM43 and HSP70 level was observed. Nevertheless, to make this statement more solid, it requires more empirical evidences. As to the Experiment D, CT images were used to interpret the unexpected temperature distribution. Due to the difference in retention rate of MNPs in each murine model, injecting high dose did not guarantee a high dose of MNPs deposited in the target. Consequently, the *in-vivo* imaging of particle distribution plays a crucial role in magnetic hyperthermia. The author took a step forward, quantified the deposited MNPs within target tumours with CT numbers of each scan. The experiment indicated that, for subcutaneous tumours, the quantification of MNPs based CT images is possible.

In conclusion, both the CT imaging and the infra-red thermography are good tools for assessing pre-clinical magnetic hyperthermia, of which the targets are subcutaneous tumours. However, for deep-seated tumours, because the CT number of bones is at the

similar level as that of MNPs, the quantification in which is less likely to succeed. In addition, the infra-red thermography would also not be able to sense the temperature of a deep-seated target. Therefore, an alternative thermometry is required for clinical scenarios.

Novel magnetic particle thermometry. A novel MPT based on the resonant effect of an LC oscillator has been proposed in Chapter 5. The theoretical basis is that the resonant frequency is a function of magnetic susceptibility. Because of the temperature dependence of susceptibility, the frequency also depends on the temperature of MNPs. Thus, theoretically speaking, the shift in frequency would be related to the average temperature of MNPs. The linear correlation of the variation in frequency and the temperature of MNPs has been illustrated in Fig. 5.6. A method for characterising MNPs was stated and discussed in the same chapter. Moreover, depending on the scenario, the MPT can be either performed as a temperature measurement or quantity measurement of MNPs. The empirical estimations of both temperature and quantity of MNPs were presented in Fig. 5.8 and Table 5.3. Both estimation showed a good fit with measured values. It is worth noting that the temperature estimation is sensitive to the quantity of MNPs. Hence, the temperature estimations in Fig. 5.8 were different from the values measured by the optic fibre thermal probe. This inconsistency was not caused by the principle of MPT but by the inaccurate dilution. Because the quantity of MNPs in those samples applied in this study was small, it was difficult to perform accurate dilution. Furthermore, the temperature measurement of optic fibre was invasive, it could result in decreases in quantities of MNPs. Fortunately, as long as the initial temperature of an MNP suspension is known and the MNP has been properly characterised, then the estimated quantity can be attained based on the initial drop in the resonant frequency. By modifying the quantity to the estimated quantity, the temperature estimation showed a good fit with the values of the thermal probe.

While Chapter 5 focused on the application, Chapter 6 aimed at interpreting and validating the principle of MPT. To achieve this, a simplified susceptometer has been built and embedded in the device of MPT. As a result, it was possible to measure the susceptibility and the frequency shift at the same time. Through a series of experiments, the theory of MPT has been validated. In which, an additional experiment was performed to support the theoretical interpretation. Overall, the theory of the

proposed MPT has been validated.

In summary, with the aim of improving the thermal management of magnetic hyperthermia, this study has assessed two temperature sensing techniques in the context of magnetic hyperthermia. While one was the widely used infra-red thermography, the other was the MPT newly proposed by this study. The assessment indicated that both technique are useful for magnetic hyperthermia researches. For pre-clinical studies, the multipoint measurement of infra-red thermography showed its advantages. The MPT, on the other hand, has the potential to be used in a clinical scenario because of its simplicity.

To translate the proposed MPT to a clinical setting, more future work is still required. One of the foreseen difficulties lies in the sensitivity of the MPT measurement. As discussed in Chapter 6, the sensitivity of presented MPT very much depends on the ratio of sample area and coil area (see Eq.6.26). It suggests that the larger the coil, the lower the sensitivity. An intuitive way to mitigate this issue is to increase the amount of MNP being injected into the target; this however may increase the concern of toxicity. Therefore, how to scale up the coil but at the same time to keep the measurement being acceptable will be of the most importance for the future work. There is one more thing, the author would like to add here. Although the magnetic materials used in this study were MNP suspensions, the application of the proposed MPT should not be constrained. An investigation in using MPT with other magnetic materials will be another interesting field to explore.

Bibliography

[1] W. Busch, "Uber den Einfluss, welchen heftigere Erysipelin zuweilig auf organisierte Neubildungen ausuben," in *Uber den Einfluss, welchen heftigere Erysipelin zuweilig auf organisierte Neubildungen ausuben*, p. 23:28.

[2] R. K. Gilchrist, R. Medal, W. D. Shorey, R. C. Hanselman, J. C. Parrott, and C. B. Taylor, "Selective inductive heating of lymph nodes," *Annals of Surgery*, vol. 146, no. 4, 1957.

[3] Q. A. Pankhurst, N. T. K. Thanh, S. K. Jones, and J. Dobson, "Progress in applications of magnetic nanoparticles in biomedicine," *Journal of Physics D: Applied Physics*, vol. 42, no. 22, p. 224001, 2009.

[4] K. Nishimoto, S. Ota, G. Shi, R. Takeda, S. B. Trisnanto, T. Yamada, and Y. Takemura, "High intrinsic loss power of multicore magnetic nanoparticles with blood-pooling property for hyperthermia," *AIP Advances*, vol. 9, p. 035347, mar 2019.

[5] S. Dutz and R. Hergt, "Magnetic nanoparticle heating and heat transfer on a microscale: Basic principles, realities and physical limitations of hyperthermia for tumour therapy," *International Journal of Hyperthermia*, vol. 29, no. 8, pp. 790–800, 2013.

[6] M. Ortner, "magpylib PyPI https://pypi.org/project/magpylib/#description," 2019.

[7] J. S. Hutchison, R. E. Ward, J. Lacroix, P. C. Hébert, M. A. Barnes, D. J. Bohn, P. B. Dirks, S. Doucette, D. Fergusson, R. Gottesman, A. R. Joffe, H. M. Kirpalani, P. G. Meyer, K. P. Morris, D. Moher, R. N. Singh, and P. W. Skippen, "Hypothermia therapy after traumatic brain injury in children," *New England Journal of Medicine*, vol. 358, pp. 2447–2456, jun 2008.

[8] J. M. Kijowski and M. G. Mast, "Thermal properties of proteins in chicken broiler tissues," *Journal of Food Science*, vol. 53, pp. 363–366, mar 1988.

[9] A. Attaluri, R. Ma, Y. Qiu, W. Li, and L. Zhu, "Nanoparticle distribution and temperature elevations in prostatic tumours in mice during magnetic nanoparticle hyperthermia," *International Journal of Hyperthermia*, vol. 27, no. 5, pp. 491–502, 2011.

[10] A. Attaluri, R. Ma, and L. Zhu, "Using MicroCT Imaging Technique to Quantify Heat Generation Distribution Induced by Magnetic Nanoparticles for Cancer Treatments," *Journal of Heat Transfer*, vol. 133, no. 1, p. 011003, 2011.

[11] H. Dähring, J. Grandke, U. Teichgräber, and I. Hilger, "Improved hyperthermia treatment of tumors under consideration of magnetic nanoparticle distribution using Micro-CT imaging," *Molecular Imaging and Biology*, vol. 17, no. 6, pp. 763–769, 2015.

[12] A. LeBrun, T. Joglekar, C. Bieberich, R. Ma, and L. Zhu, "Treatment efficacy for validating microCT-based theoretical simulation approach in magnetic nanoparticle hyperthermia for cancer treatment," *Journal of Heat Transfer*, vol. 139, no. 5, p. 051101, 2017.

[13] A. LeBrun, R. Ma, and L. Zhu, "MicroCT image based simulation to design heating protocols in magnetic nanoparticle hyperthermia for cancer treatment," *Journal of Thermal Biology*, vol. 62, pp. 129–137, 2016.

[14] H. F. Rodrigues, F. M. Mello, L. C. Branquinho, N. Zufelato, E. P. Silveira-Lacerda, and A. F. Bakuzis, "Real-time infrared thermography detection of magnetic nanoparticle hyperthermia in a murine model under a non-uniform field configuration," *International Journal of Hyperthermia*, vol. 29, pp. 752–767, dec 2013.

[15] G. L. DeNardo and S. J. DeNardo, "Update: Turning the heat on cancer," *Cancer biotherapy and radiopharmaceuticals*, vol. 23, no. 6, pp. 671–680, 2008.

[16] S. C. Cotran, C. Kumar, T. Collins, and W. B. Robbins, "Pathologic basis of disease," *Philadelphia: Saunders Co*, p. 18, 1999.

[17] A. S. Song, A. M. Najjar, and K. R. Diller, "Thermally Induced Apoptosis, Necrosis, and Heat Shock Protein Expression in 3D Culture," *Journal of Biomechanical Engineering*, vol. 136, p. 071006, may 2014.

[18] S. A. Sapareto and W. C. Dewey, "Thermal dose determination in cancer therapy," *International Journal of Radiation Oncology* Biology* Physics*, vol. 10, no. 6, pp. 787–800, 1984.

[19] M. Johannsen, U. Gneveckow, K. Taymoorian, B. Thiesen, N. Waldofner, R. Scholz, K. Jung, A. Jordan, P. Wust, and S. A. Loening, "Morbidity and quality of life during thermotherapy using magnetic nanoparticles in locally recurrent prostate cancer: results of a prospective phase I trial," *Int J Hyperthermia*, vol. 23, no. 3, pp. 315–323, 2007.

[20] S. Dutz and R. Hergt, "Magnetic particle hyperthermia–a promising tumour therapy?," *Nanotechnology*, vol. 25, no. 45, p. 452001, 2014.

[21] M. W. Dewhirst, B. L. Viglianti, M. Lora-Michiels, M. Hanson, and P. J. Hoopes, "Basic principles of thermal dosimetry and thermal thresholds for tissue damage from hyperthermia," *International Journal of Hyperthermia*, vol. 19, no. 3, pp. 267–294, 2003.

[22] W. C. Dewey, "Arrhenius relationships from the molecule and cell to the clinic," *International Journal of Hyperthermia*, vol. 25, pp. 3–20, jan 2009.

[23] P. Wust, U. Gneveckow, M. Johannsen, D. Böhmer, T. Henkel, F. Kahmann, J. Sehouli, R. Felix, J. Ricke, and A. Jordan, "Magnetic nanoparticles for interstitial thermotherapy - Feasibility, tolerance and achieved temperatures," *International Journal of Hyperthermia*, vol. 22, pp. 673–685, dec 2006.

[24] T. Ohguri, Y. Harima, H. Imada, H. Sakurai, T. Ohno, Y. Hiraki, K. Tuji, M. Tanaka, and H. Terashima, "Relationships between thermal dose parameters and the efficacy of definitive chemoradiotherapy plus regional hyperthermia in the treatment of locally advanced cervical cancer: data from a multicentre randomised clinical trial," *International Journal of Hyperthermia*, vol. 34, pp. 461–468, may 2018.

[25] M. Kroesen, H. T. Mulder, J. M. van Holthe, A. A. Aangeenbrug, J. W. M. Mens, H. C. van Doorn, M. M. Paulides, E. Oomen-de Hoop, R. M. Vernhout, L. C.

Lutgens, G. C. van Rhoon, and M. Franckena, "Confirmation of thermal dose as a predictor of local control in cervical carcinoma patients treated with state-of-the-art radiation therapy and hyperthermia," *Radiotherapy and Oncology*, vol. 140, pp. 150–158, jul 2019.

[26] P. S. Yarmolenko, E. J. Moon, C. Landon, A. Manzoor, D. W. Hochman, B. L. Viglianti, and M. W. Dewhirst, "Thresholds for thermal damage to normal tissues: an update," *International Journal of Hyperthermia*, vol. 27, no. 4, pp. 320–343, 2011.

[27] F. Ritossa, "A new puffing pattern induced by temperature shock and DNP in drosophila," *Experientia*, vol. 18, pp. 571–573, dec 1962.

[28] A. Tissiéres, H. K. Mitchell, and U. M. Tracy, "Protein synthesis in salivary glands of Drosophila melanogaster: Relation to chromosome puffs," *Journal of Molecular Biology*, vol. 84, pp. 389–398, apr 1974.

[29] J. G. Kiang and G. C. Tsokos, "Heat shock protein 70 kDa: Molecular biology, biochemistry, and physiology," nov 1998.

[30] R. A. Laskey, B. M. Honda, A. D. Mills, and J. T. Finch, "Nucleosomes are assembled by an acidic protein which binds histones and transfers them to DNA," *Nature*, vol. 275, pp. 416–420, oct 1978.

[31] R. J. Ellis and S. M. van der Vies, "Molecular Chaperones," *Annual Review of Biochemistry*, vol. 60, pp. 321–347, jun 1991.

[32] J. P. Hendrick and F.-U. Hartl, "Molecular chaperone functions of heat-shock proteins," *Annual Review of Biochemistry*, vol. 62, pp. 349–384, jun 1993.

[33] G. Fischer and F. X. Schmid, "The mechanism of protein folding. Implications of in vitro refolding models for de novo protein folding and translocation in the Cell," *Biochemistry*, vol. 29, pp. 2205–2212, mar 1990.

[34] M. J. Gething and J. Sambrook, "Protein folding in the cell," jan 1992.

[35] W. J. Chirico, M. G. Waters, and G. Blobel, "70K heat shock related proteins stimulate protein translocation into microsomes," *Nature*, vol. 332, pp. 805–810, apr 1988.

[36] T. Langer, C. Lu, H. Echols, J. Flanagan, M. K. Hayer, and F. U. Hartl, "Successive action of DnaK, DnaJ and GroEL along the pathway of chaperone-mediated protein folding," *Nature*, vol. 356, pp. 683–689, apr 1992.

[37] B. J. Didomenico, G. E. Bugaisky, and S. Lindquist, "The heat shock response is self-regulated at both the transcriptional and posttranscriptional levels," *Cell*, vol. 31, pp. 593–603, dec 1982.

[38] J. P. Morris, S. Thatje, and C. Hauton, "The use of stress-70 proteins in physiology: A re-appraisal," mar 2013.

[39] E. A. Craig and C. A. Gross, "Is hsp70 the cellular thermometer?," *Trends in Biochemical Sciences*, vol. 16, pp. 135–140, apr 1991.

[40] L. Tomanek and G. N. Somero, "Interspecific- and acclimation-induced variation in levels of heat-shock proteins 70 (hsp70) and 90 (hsp90) and heat-shock transcription factor-1 (HSF1) in congeneric marine snails (genus Tegula): implications for regulation of hsp gene expression.," *The Journal of experimental biology*, vol. 205, pp. 677–685, mar 2002.

[41] M. Moussa, S. N. Goldberg, G. Kumar, T. Levchenko, V. Torchilin, and M. Ahmed, "Effect of thermal dose on heat shock protein expression after radiofrequency ablation with and without adjuvant nanoparticle chemotherapies," *International Journal of Hyperthermia*, vol. 32, pp. 829–841, nov 2016.

[42] Z. Tanel and M. Erol, "Students' difficulties in understanding the concepts of magnetic field strength, magnetic flux density and magnetization," *Latin-American Journal of Physics Education*, vol. 2, no. 3, p. 4, 2008.

[43] J. J. Roche, "B and H, the intensity vectors of magnetism: A new approach to resolving a century-old controversy," *American Journal of Physics*, vol. 68, no. 5, pp. 438–449, 2000.

[44] Q. A. Pankhurst, J. Connolly, S. K. Jones, and J. Dobson, "Applications of magnetic nanoparticles in biomedicine," *Journal of Physics D: Applied Physics*, vol. 36, no. R, pp. R167–R181, 2003.

[45] B. M. Moskowitz, "Hitchhiker's guide to magnetism," in *Environmental Magnetism Workshop (IRM)*, vol. 279, p. 48.

[46] L. Néel, "Influence des fluctuations thermiques sur laimantation de grains ferromagnetiques tres fins," *Comptes Rendus Hebdomadaires Des Seances De L Academie Des Sciences*, vol. 228, no. 8, pp. 664–666, 1949.

[47] D. J. Dunlop, "The rock magnetism of fine particles," *Physics of the Earth and Planetary Interiors*, vol. 26, no. 1, pp. 1–26, 1981.

[48] R. E. Rosensweig, "Heating magnetic fluid with alternating magnetic field," *Journal of magnetism and magnetic materials*, vol. 252, pp. 370–374, 2002.

[49] W. F. Brown Jr, "Thermal fluctuations of a single domain particle," *Journal of Applied Physics*, vol. 34, no. 4, pp. 1319–1320, 1963.

[50] M. Kallumadil, M. Tada, T. Nakagawa, M. Abe, P. Southern, and Q. A. Pankhurst, "Suitability of commercial colloids for magnetic hyperthermia," *Journal of Magnetism and Magnetic Materials*, vol. 321, no. 10, pp. 1509–1513, 2009.

[51] R. R. Wildeboer, "Towards standardized and reliable heating ability measurements of magnetic nanoparticles for hyperthermia applications in a non-adiabatic setup," report, Resonant Circuits Limited, 2014.

[52] R. C. Ltd., "ILP and SAR calculator for Excel and MATLAB," 2014.

[53] J. P. Reilly, "Principles of nerve and heart excitation by time-varying magnetic fields," *Annals of the New York Academy of Sciences*, vol. 649, no. 1, pp. 96–117, 1992.

[54] W. J. Atkinson, I. A. Brezovich, and D. P. Chakraborty, "Usable frequencies in hyperthermia with thermal seeds," *IEEE Transactions on Biomedical Engineering*, vol. 31, no. 1, pp. 70–75, 1984.

[55] I. A. Brezovich, "Low Frequency Hyperthermia: Capacitive and Ferromagnetic Thermoseed Methods.," *Medical Physics Monograph No 16: Biological, physical, and clinical aspects of hyperthermia:*, pp. 82–110, 1988.

[56] K. Maier Hauff, R. Rothe, R. Scholz, U. Gneveckow, P. Wust, B. Thiesen, A. Feussner, A. von Deimling, N. Waldoefner, R. Felix, and A. Jordan, "Intracranial thermotherapy using magnetic nanoparticles combined with external

beam radiotherapy: results of a feasibility study on patients with glioblastoma multiforme," *J Neurooncol*, vol. 81, no. 1, pp. 53–60, 2007.

[57] M. Johannsen, U. Gneveckow, B. Thiesen, K. Taymoorian, C. H. Cho, N. Waldofner, R. Scholz, A. Jordan, S. A. Loening, and P. Wust, "Thermotherapy of prostate cancer using magnetic nanoparticles: feasibility, imaging, and three-dimensional temperature distribution," *Eur Urol*, vol. 52, no. 6, pp. 1653–1661, 2007.

[58] A. Matsumine, K. Takegami, K. Asanuma, T. Matsubara, T. Nakamura, A. Uchida, and A. Sudo, "A novel hyperthermia treatment for bone metastases using magnetic materials," *Int J Clin Oncol*, vol. 16, no. 2, pp. 101–108, 2011.

[59] P. Southern and Q. A. Pankhurst, "Commentary on the clinical and preclinical dosage limits of interstitially administered magnetic fluids for therapeutic hyperthermia based on current practice and efficacy models," oct 2017.

[60] M. A. Holliday, D. Potter, A. Jarrah, and S. Bearg, "The relation of metabolic rate to body weight and organ size," *Pediatric Research*, vol. 1, no. 3, pp. 185–195, 1967.

[61] T. A. Henderson and L. D. Morries, "Near-infrared photonic energy penetration: Can infrared phototherapy effectively reach the human brain?," *Neuropsychiatric Disease and Treatment*, vol. 11, pp. 2191–2208, aug 2015.

[62] F. Vatansever and M. R. Hamblin, "Far infrared radiation (FIR): Its biological effects and medical applications," *Photonics and Lasers in Medicine*, vol. 1, no. 4, pp. 255–266, 2012.

[63] H. F. Rodrigues, G. Capistrano, F. M. Mello, N. Zufelato, E. Silveira-Lacerda, and A. F. Bakuzis, "Precise determination of the heat delivery during in vivo magnetic nanoparticle hyperthermia with infrared thermography," *Physics in Medicine and Biology*, vol. 62, pp. 4062–4082, may 2017.

[64] D. Padilla-Valverde, S. Sanchez-Garcia, E. García-Santos, C. Marcote-Ibañez, M. Molina-Robles, J. Martín-Fernández, and P. Villarejo-Campos, "Usefulness of thermographic analysis to control temperature homogeneity in the development

and implementation of a closed recirculating CO2 chemohyperthermia model," *International Journal of Hyperthermia*, vol. 33, pp. 220–226, feb 2017.

[65] J. Weaver, A. Rauwerdink, and E. Hansen, "Magnetic nanoparticle temperature estimation," *Medical Physics*, vol. 36, no. 5, pp. 1822–1829, 2009.

[66] A. M. Rauwerdink and J. B. Weaver, "Harmonic phase angle as a concentration-independent measure of nanoparticle dynamics," *Medical Physics*, vol. 37, no. 6, pp. 2587–2592, 2010.

[67] J. B. Weaver, "The use of magnetic nanoparticles in thermal therapy monitoring and screening: Localization and imaging (invited)," in *Journal of Applied Physics*, 2012.

[68] D. B. Reeves and J. B. Weaver, "Simulations of magnetic nanoparticle Brownian motion," *Journal of Applied Physics*, 2012.

[69] J. B. Weaver, "MSB estimation of bound fraction: bias from binding energy uncertainty," vol. 8317, p. 83170P, 2012.

[70] J. B. Weaver, K. M. Rauwerdink, A. M. Rauwerdink, and I. M. Perreard, "Magnetic spectroscopy of nanoparticle Brownian motion measurement of microenvironment matrix rigidity," *Biomedizinische Technik*, vol. 58, no. 6, pp. 547–550, 2013.

[71] I. M. Perreard, D. B. Reeves, X. Zhang, and J. B. Weaver, "Magnetic nanoparticles temperature measurements," in *2013 International Workshop on Magnetic Particle Imaging, IWMPI 2013*, 2013.

[72] D. B. Reeves and J. B. Weaver, "Magnetic nanoparticle sensing: decoupling the magnetization from the excitation field," *Journal of physics D: Applied physics*, vol. 47, no. 4, p. 45002, 2013.

[73] I. M. Perreard, D. B. Reeves, X. Zhang, E. Kuehlert, E. R. Forauer, and J. B. Weaver, "Temperature of the magnetic nanoparticle microenvironment: estimation from relaxation times.," *Physics in medicine and biology*, vol. 59, no. 5, pp. 1109–19, 2014.

[74] J. Zhong, W. Liu, Z. Du, d. M. P. César, Q. Xiang, and Q. Xie, "A noninvasive, remote and precise method for temperature and concentration estimation using magnetic nanoparticles," *Nanotechnology*, vol. 23, no. 7, p. 75703, 2012.

[75] J. Zhong, W. Liu, L. Jiang, M. Yang, and P. C. Morais, "Real-time magnetic nanothermometry: The use of magnetization of magnetic nanoparticles assessed under low frequency triangle-wave magnetic fields," *Review of Scientific Instruments*, vol. 85, p. 094905, sep 2014.

[76] J. Zhong, J. Dieckhoff, M. Schilling, and F. Ludwig, "Influence of static magnetic field strength on the temperature resolution of a magnetic nanoparticle thermometer," *Journal of Applied Physics*, vol. 120, p. 143902, oct 2016.

[77] S. Pi, J. Zhong, K. Wei, and W. Liu, "Optimal anti-noise ability and high sensitivity in magnetic nanothermometry," *IEEE Transactions on Nanotechnology*, vol. 15, pp. 409–415, may 2016.

[78] S. Pi, W. Liu, K. Wei, and E. Mosiniewicz-Szablewska, "AC magnetic nanothermometry: an investigation of the influence of size distribution of magnetic nanoparticles," *IEEE TRANSACTIONS ON MAGNETICS*, vol. 53, no. 3, 2017.

[79] E. Garaio, J.-M. Collantes, J. A. Garcia, F. Plazaola, and O. Sandre, "Harmonic phases of the nanoparticle magnetization: An intrinsic temperature probe," *Applied Physics Letters*, vol. 107, no. 12, p. 123103, 2015.

[80] E. Garaio, J. M. Collantes, J. A. Garcia, F. Plazaola, S. Mornet, F. Couillaud, and O. Sandre, "A wide-frequency range AC magnetometer to measure the specific absorption rate in nanoparticles for magnetic hyperthermia," *Journal of Magnetism and Magnetic Materials*, 2014.

[81] B. Gleich and J. Weizenecker, "Tomographic imaging using the nonlinear response of magnetic particles," *Nature*, vol. 435, no. 7046, pp. 1214–1217, 2005.

[82] E. Y. Yu, M. Bishop, B. Zheng, R. M. Ferguson, A. P. Khandhar, S. J. Kemp, K. M. Krishnan, P. W. Goodwill, and S. M. Conolly, "Magnetic Particle Imaging: A Novel in Vivo Imaging Platform for Cancer Detection," *Nano Letters*, vol. 17, no. 3, pp. 1648–1654, 2017.

[83] J. B. Weaver, A. M. Rauwerdink, C. R. Sullivan, and I. Baker, "Frequency distribution of the nanoparticle magnetization in the presence of a static as well as a harmonic magnetic field.," *Medical physics*, vol. 35, no. 5, pp. 1988–1994, 2008.

[84] E. Garaio, O. Sandre, J.-M. Collantes, J. A. Garcia, S. Mornet, and F. Plazaola, "Specific absorption rate dependence on temperature in magnetic field hyperthermia measured by dynamic hysteresis losses (ac magnetometry).," *Nanotechnology*, vol. 26, no. 1, p. 015704, 2015.

[85] M. Beković, M. Trlep, M. Jesenik, V. Goričan, and A. Hamler, "An experimental study of magnetic-field and temperature dependence on magnetic fluid's heating power," *Journal of Magnetism and Magnetic Materials*, 2013.

[86] R. Regmi, A. Naik, J. S. Thakur, P. P. Vaishnava, and G. Lawes, "Temperature dependent dissipation in magnetic nanoparticles," *Journal of Applied Physics*, 2014.

[87] T. Funami, M. Hiroe, S. Noda, I. Asai, S. Ikeda, and K. Nishinari, "Influence of molecular structure imaged with atomic force microscopy on the rheological behavior of carrageenan aqueous systems in the presence or absence of cations," *Food Hydrocolloids*, vol. 21, no. 4, pp. 617–629, 2007.

[88] M. D. Mitchell, H. L. Kundel, L. Axel, and P. M. Joseph, "Agarose as a tissue equivalent phantom material for NMR imaging," *Magnetic Resonance Imaging*, vol. 4, no. 3, pp. 263–266, 1986.

[89] K. A. Ross, L. J. Pyrak-Nolte, and O. H. Campanella, "The effect of mixing conditions on the material properties of an agar gel - Microstructural and macrostructural considerations," *Food Hydrocolloids*, vol. 20, no. 1, pp. 79–87, 2006.

[90] Z. J. Chen, W. C. Broaddus, R. R. Viswanathan, R. Raghavan, and G. T. Gillies, "Intraparenchymal drug delivery via positive-pressure infusion: Experimental and modeling studies of poroelasticity in brain phantom gels," *IEEE Transactions on Biomedical Engineering*, vol. 49, no. 2, pp. 85–96, 2002.

[91] M. Salloum, R. H. Ma, D. Weeks, and L. Zhu, "Controlling nanoparticle delivery in magnetic nanoparticle hyperthermia for cancer treatment: Experimental

study in agarose gel," *International Journal of Hyperthermia*, vol. 24, no. 4, pp. 337–345, 2008.

[92] E. M. Shapiro, A. Borthakur, and R. Reddy, "MR imaging of RF heating using a paramagnetic doped agarose phantom," *Magnetic Resonance Materials in Physics, Biology and Medicine*, vol. 10, no. 2, pp. 114–121, 2000.

[93] A. M. Elliott, R. J. Stafford, J. Schwartz, J. Wang, A. M. Shetty, C. Bourgoyne, P. O'Neal, and J. D. Hazle, "Laser-induced thermal response and characterization of nanoparticles for cancer treatment using magnetic resonance thermal imaging," *Medical Physics*, vol. 34, no. 7, pp. 3102–3108, 2007.

[94] R. Xu, Y. Zhang, M. Ma, J. Xia, J. Liu, Q. Guo, and N. Gu, "Measurement of specific absorption rate and thermal simulation for arterial embolization hyperthermia in the maghemite-gelled model," *IEEE Transactions on Magnetics*, vol. 43, no. 3, pp. 1078–1085, 2007.

[95] S. M. Lobo, K. S. Afzal, M. Ahmed, J. B. Kruskal, R. E. Lenkinski, and S. N. Goldberg, "Radiofrequency ablation: modeling the enhanced temperature response to adjuvant NaCl pretreatment," *Radiology*, vol. 230, no. 1, pp. 175–182, 2004.

[96] M. L. Ramires, C. A. Nieto Castro, Y. Nagasaka, A. Nagashima, M. J. Assael, and W. A. Wakeham, "Standard Reference Data for the Thermal Conductivity of Water," *Journal of Physical and Chemical Reference Data*, vol. 24, pp. 1377–1381, may 1995.

[97] S. A. BARRINGER, E. A. DAVIS, J. GORDON, K. G. AYAPPA, and H. T. DAVIS, "Microwave-Heating Temperature Profiles for Thin Slabs Compared to Maxwell and Lambert Law Predictions," *Journal of Food Science*, vol. 60, pp. 1137–1142, sep 1995.

[98] T. Laas, "Agar derivatives for chromatography electrophoresis and gel bound enzymes," *Journal of Chromatography A*, vol. 66, no. 2, p. 347*355, 1975.

[99] U. Gneveckow, A. Jordan, R. Scholz, V. Brub, N. Waldofner, J. Ricke, A. Feussner, B. Hildebrandt, B. Rau, and P. Wust, "Description and characterization of the novel hyperthermia and thermoablation-system MFH 300F for clinical magnetic fluid hyperthermia," *Medical Physics*, vol. 31, no. 6, p. 1444, 2004.

[100] S. Oh, C. A. Roopnariane, M. R. Tofighi, and C. M. Collins, "MRI-based temperature and SAR mapping with a new dual-coil solenoid/birdcage heating/measurement system," *2010 IEEE Radio and Wireless Symposium, RWW 2010 - Paper Digest*, pp. 520–522, 2010.

[101] S.-J. Zhang, H.-N. Qian, Y. Zhao, K. Sun, H.-Q. Wang, G.-Q. Liang, F.-H. Li, and Z. Li, "Relationship between age and prostate size," *Asian Journal of Andrology*, vol. 15, pp. 116–120, 2013.

[102] G. T. Landi, "Simple models for the heating curve in magnetic hyperthermia experiments," *Journal of Magnetism and Magnetic Materials*, vol. 326, pp. 14–21, 2013.

[103] T. Oh, S. Fakurnejad, E. T. Sayegh, A. J. Clark, M. E. Ivan, M. Z. Sun, M. Safaee, O. Bloch, C. D. James, and A. T. Parsa, "Immunocompetent murine models for the study of glioblastoma immunotherapy," apr 2014.

[104] A. J. Giustini, R. Ivkov, and P. J. Hoopes, "Magnetic nanoparticle biodistribution following intratumoral administration," *Nanotechnology*, vol. 22, no. 34, 2011.

[105] T. Carter, G. Agliardi, M. Ellis, F.-Y. Lin, C. Jones, M. Robson, A. Richard-Londt, P. Southern, Q. Pankhurst, R. T. M. de Rosales, C. Gruettner, R. B. Pedley, T. Kalber, S. Brandner, P. Mulholland, and K. Chester, "TMIC-33Potential of magnetic hyperthermia to stimulate an immune response in glioblastoma," *Neuro-Oncology*, vol. 19, pp. vi250–vi250, nov 2017.

[106] X. Y. Zhou, K. E. Jeffris, E. Y. Yu, B. Zheng, P. W. Goodwill, P. Nahid, and S. M. Conolly, "First in vivo magnetic particle imaging of lung perfusion in rats," *Physics in Medicine and Biology*, vol. 62, pp. 3510–3522, may 2017.

[107] Z. W. Tay, P. Chandrasekharan, X. Y. Zhou, E. Yu, B. Zheng, and S. Conolly, "In vivo tracking and quantification of inhaled aerosol using magnetic particle imaging towards inhaled therapeutic monitoring," *Theranostics*, vol. 8, no. 13, pp. 3676–3687, 2018.

[108] A. A. Golneshan and M. Lahonian, "The effect of magnetic nanoparticle dispersion on temperature distribution in a spherical tissue in magnetic fluid hyper-

thermia using the lattice Boltzmann method," *International Journal of Hyperthermia*, vol. 27, pp. 266–274, may 2011.

[109] E. Kengne and A. Lakhssassi, "Bioheat transfer problem for one-dimensional spherical biological tissues," *Mathematical Biosciences*, vol. 269, pp. 1–9, nov 2015.

[110] W. Andrä, C. G. D'Ambly, R. Hergt, I. Hilger, and W. A. Kaiser, "Temperature distribution as function of time around a small spherical heat source of local magnetic hyperthermia," *Journal of Magnetism and Magnetic Materials*, vol. 194, pp. 197–203, apr 1999.

[111] N. M. Sudharsan, E. Y. Ng, and S. L. Teh, "Surface temperature distribution of a breast with and without tumour," *Computer Methods in Biomechanics and Biomedical Engineering*, vol. 2, no. 3, pp. 187–199, 1999.

[112] M. Johannsen, U. Gneveckow, L. Eckelt, A. Feussner, N. Waldofner, R. Scholz, S. Deger, P. Wust, S. A. Loening, and A. Jordan, "Clinical hyperthermia of prostate cancer using magnetic nanoparticles: Presentation of a new interstitial technique," *International Journal of Hyperthermia*, vol. 21, no. 7, pp. 637–647, 2005.

[113] B. Thiesen and A. Jordan, "Clinical applications of magnetic nanoparticles for hyperthermia," *International Journal of Hyperthermia*, vol. 24, no. 6, pp. 467–474, 2008.

[114] H. Wang, J. Wu, X. Zhang, Y. Liu, X. Zheng, Z. Zhuo, and J. Tang, "Preoperative Treatment Planning Method for Magnetically Induced Hyperthermia Using Thermoseeds," *Journal of Medical and Biological Engineering*, vol. 36, no. 5, pp. 726–732, 2016.

[115] M. Ebrahimi, "On the temperature control in self-controlling hyperthermia therapy," *Journal of Magnetism and Magnetic Materials*, vol. 416, pp. 134–140, 2016.

[116] J. Hopkinson, "Magnetic and other physical properties of iron at a high temperature," *Philosophical Transactions of the Royal Society A: Mathematical, Physical and Engineering Sciences*, vol. 180, pp. 443–465, jan 1889.

[117] C. Radhakrishnamurty and S. D. Likhite, "Hopkinson effect, blocking temperature and Curie point in basalts," *Earth and Planetary Science Letters*, vol. 7, no. 5, pp. 389–396, 1970.

[118] C. Zhou, Y. S. Choi, A. E. David, P. W. Todd, and T. R. Hanley, "Nanomaterial endocytosis: Estimation of particles per cell by magnetic measurement," *IEEE Magnetics Letters*, vol. 9, pp. 1–5, 2018.

[119] C. P. Hunt, B. M. Moskowitz, and S. K. Banerjee, "Magnetic properties of rocks and minerals," pp. 189–204, mar 1995.

[120] M. Ortner and B. Filipitsch, "Feedback of Eddy Currents in Layered Materials for Magnetic Speed Sensing," *IEEE Transactions on Magnetics*, vol. 53, aug 2017.

[121] R. R. Wildeboer, P. Southern, and Q. A. Pankhurst, "On the reliable measurement of specific absorption rates and intrinsic loss parameters in magnetic hyperthermia materials," *Journal of Physics D: Applied Physics*, vol. 47, p. 495003, 2014.

[122] J. J. Pouw, M. Ahmed, B. Anninga, K. Schuurman, S. E. Pinder, M. Van Hemelrijck, Q. A. Pankhurst, M. Douek, and B. ten Haken, "Comparison of three magnetic nanoparticle tracers for sentinel lymph node biopsy in an in vivo porcine model," *International Journal of Nanomedicine*, vol. 10, pp. 1235–1243, feb 2015.

[123] D.-X. Chen, V. Skumryev, and B. Bozzo, "Calibration of ac and dc magnetometers with a Dy 2 O 3 standard," *Review of Scientific Instruments*, vol. 82, p. 045112, apr 2011.

Appendices

Appendix A

The Simulation of Coil Field Distribution

This Python script is used to calculate the field distribution of the coils used in this thesis. The script is based on a Python package called magpylib [6]. The fundamental equations of magpylib can be found in [120].

The presented geometrical parameters in the script are associated with the MACH pre-clinical coil (Chapter 1, Chapter 3 and Chapter 4). The simulated result is presented in Fig. 1.2. This script has also been used to simulate the field distribution of the MACH *in-vitro* coil (Chapter 5 and Chapter 6) and the High filling coil (Chapter 6), and their geometrical parameters were adjusted accordingly. The simulated results of MACH *in-vitro* coil and High filling coil are presented in Fig. 5.5 and Fig. 6.10, respectively.

```
import magpylib as magpy
import numpy as np
import matplotlib.pyplot as plt
from magpylib.source.current import Circular

# windings of two parts of a coil
Current = 113 #unit: A
# The thickness of coil is 5 mm.
coil1a = [Circular(curr=Current,dim=52.0,pos=[0,0,z]) for z in np.linspace(
-17.5,17.5,2)]
coil1b = [Circular(curr=Current,dim=57.0,pos=[0,0,z]) for z in np.linspace(
-17.5,17.5,2)]

col = magpy.Collection(coil1a,coil1b)

# create positions (x-z graph for visualising the field distribution)
xs = np.linspace(-40,40,100)
zs = np.linspace(-40,40,100)
posis = [[x,0,z] for z in zs for x in xs]
print(len(posis))

# calculate field and amplitude
B = [col.getB(pos) for pos in posis]
Bs = np.array(B).reshape([100,100,3]) #reshape
Bamp = np.linalg.norm(Bs,axis=2)*0.7977 #convert the unit to be kA/m

#plot
plt.pcolor(xs,zs,Bamp,cmap='hsv',vmin = 2, vmax = 8)
plt.colorbar().set_label('Field Intensity (kA/m)')
cs=plt.contour(xs,zs, Bamp, linewidths=0.5, levels=np.linspace(0,10,21))
plt.clabel(cs, inline=True, fontsize=8)
plt.xlabel('X (mm)')
plt.ylabel('Z (mm)')
plt.axis('image')
plt.show()

print(col.getB([0,0,0])*0.7977) # the unit of B in magpy is mT.
```

Appendix B

The Measurement of ILP

The measurement of ILP can be divided into two parts. The first is to attain the heating curve of the MNP suspension when exposing to an AMF with known field intensity and frequency. The second is to derive ILP from the heating curve.

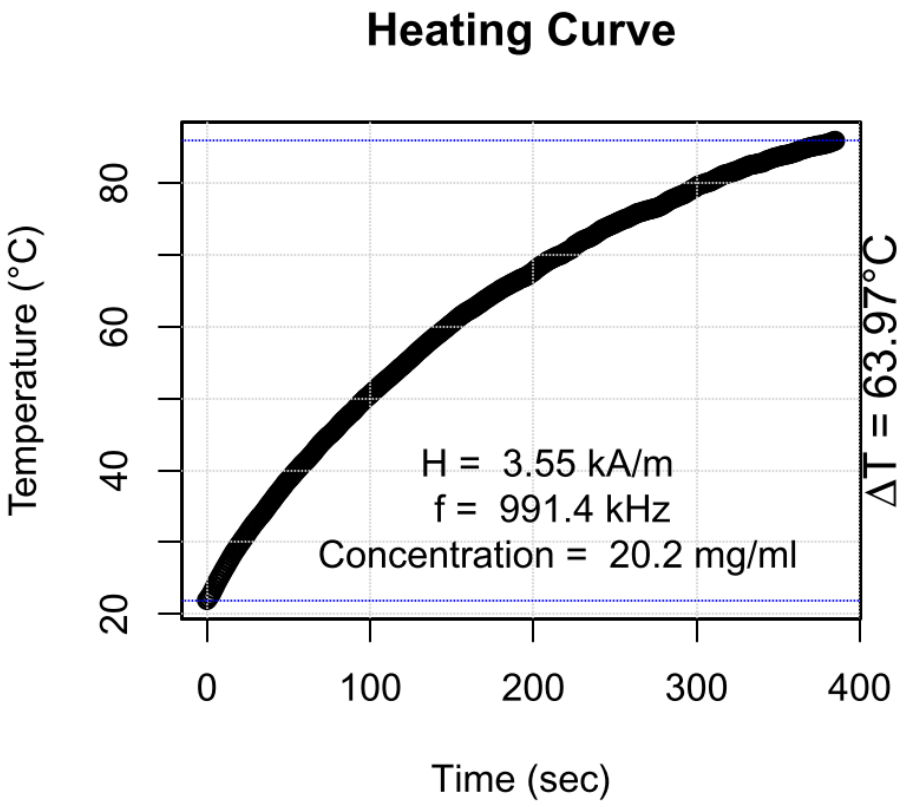

Figure B.1: The heating curve of an MNP suspension, e.g., Perimag®-COOH

Firstly, the magnetic heating curves of MNP suspensions presented in this study were all measured by the MACH *in-vitro* coil. The dimension and the field distribution of coil can respectively be found in Fig. 5.4 and Fig. 5.5. Take Perimag®-COOH as an example (see Appendix C), the concentration was diluted from 50 mg_{Fe}/ml to 20.2

mg_{Fe}/ml. The heating curve of which is presented in Fig. B.1.

Secondly, the algorithm of ILP calculation is based on the corrected slope method proposed in [121]. The corrected slope method consists of two concepts. The first concept is that the slope of heating curve indicates the heating power (the heating power is the production of (1) the initial slope of heating curve and (2) the heat capacity of the medium). The second concept is this method is related to the adjective *corrected*.

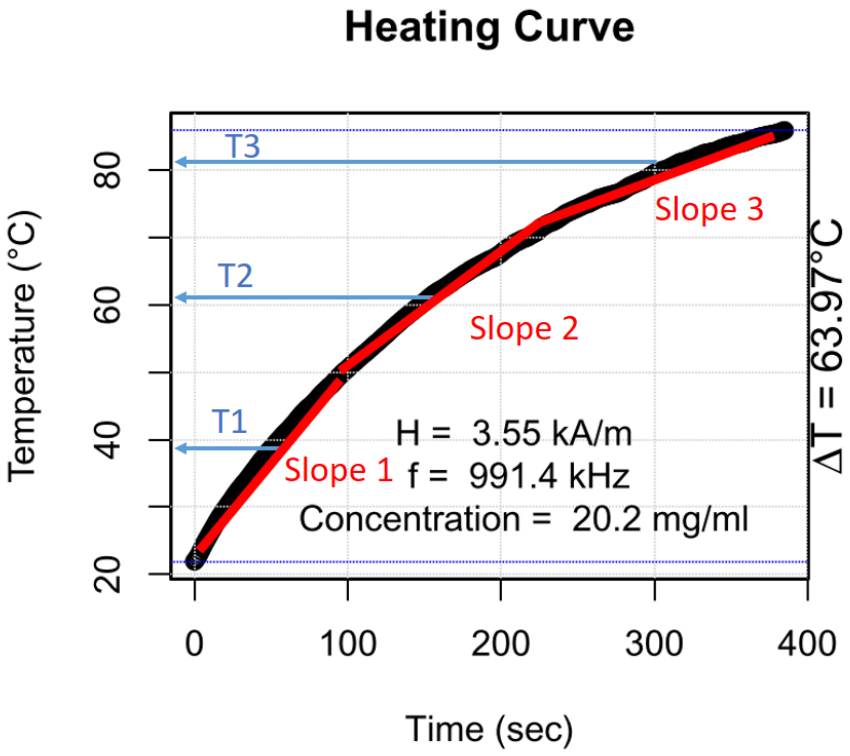

Figure B.2: Illustration of corrected slope method. The heating curve is divided into 3 regions. The slope of each region is denoted as Slope 1, 2 and 3. The average temperature at each region is denoted as T1, T2 and T3.

As illustrated in Fig. B.2, a heating curve can be divided into different regions. The slope of each region decreases with time. It is because the heat loss rate L increase with the temperature difference. Say the average temperature of each region is denoted as T1, T2 and T3, then it suggests that:

$$C \times Slope1 + T1 \times L = C \times Slope2 + T2 \times L = C \times Slope3 + T3 \times L \qquad \text{(B.1)}$$

In which, the C means the heat capacity of the medium.

Once the heat loss rate is attained, the Eq. B.1 suggests that the slope at each region can be corrected by adding the product of its average temperature, e.g., T1, and the heat loss rate L. As a result, the initial slope is calculated. Afterwards, based on Eq. 2.18 and Eq. 2.19, the ILP of an MNP suspension at each region can be calculated, as shown in Fig. B.3. The average and the standard deviation of all the ILP are regarded as its ILP value and its uncertainty. For instance, the ILP of an MNP would be expressed as 5.71 ± 0.3 nHm^{2}kg^{-1}.

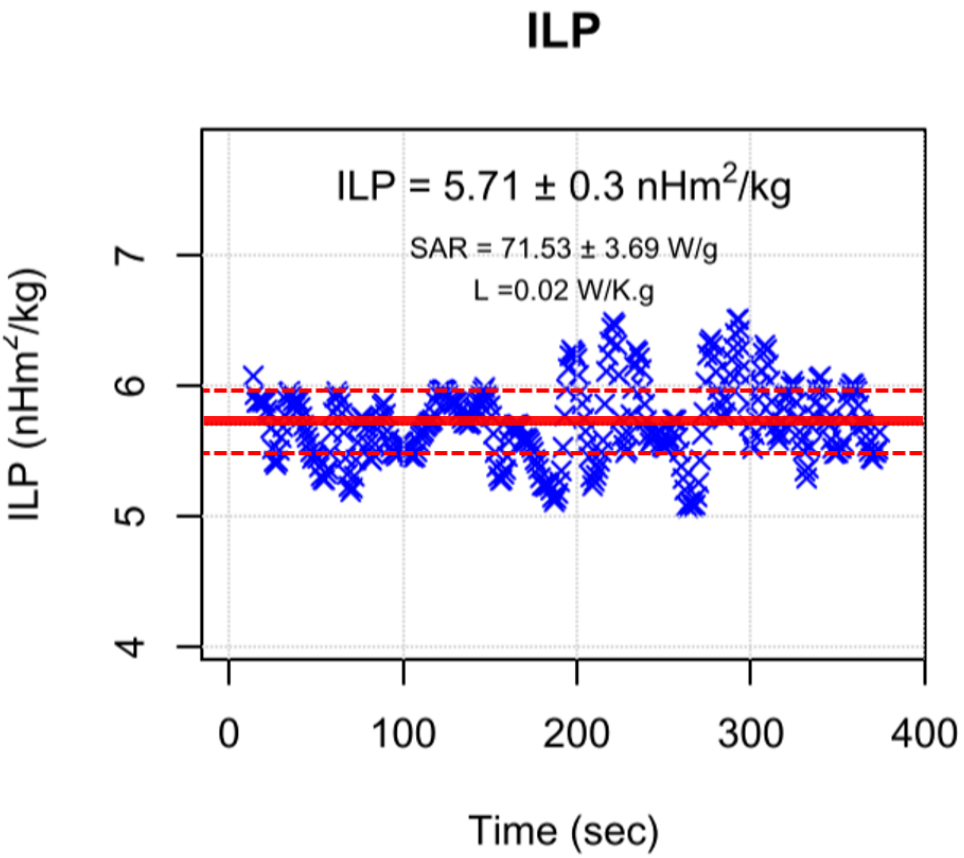

Figure B.3: The corrected ILP of Perimag®-COOH at each second during the measurement.

Appendix C

Parameters of Magnetic Nanoparticles

Label	Name	Composition	Surface	Size (nm)	Neat Concentration (mg_{Fe}/ml)	Manufacturer
			MNP used in **Chapter 1**			
	Nanomag®	Magnetite	plain	100	73.00	micromod
	Sienna^{+}®	Magnetite/maghemite [122]	plain	60	28.00	Endomagnetics
			MNP used in **Chapter 3**			
	Perimag®	Magnetite	plain	130	20.00	micromod
			MNP used in **Chapter 4**			
	Perimag®COOH	Magnetite	COOH	130	50.00	micromod
			MNP used in **Chapter 5**			
A0	fluidMAG/C11-D Lot:180916 (denoted as C180916)	Magnetite	plain	100	60.00	Chemicell
B0	RCL-01	Magnetite	plain	130	11.26	Resonant Circuit Ltd
B1	Perimag®	Magnetite	plain	130	20.20	micromod
B2	RCL-01	Magnetite	plain	130	10.00	Resonant Circuit Ltd

Table C.1: Parameters of main MNPs used in this thesis.

Appendix D

The Concept of Permeability - Darcy's Law

Darcy's law is a fundamental equation in hydrodynamics. This equation analyses the phenomenon that a fluid flows through a porous medium (e.g. sand), which is depicted in Fig. D.1. The symbols of L and A in the figure represent the length and the cross section area of the porous medium, respectively. Q is a quantity which indicates how much volume of the fluid passes through the hydrodynamic system per second, and thereby Q is termed as the discharge rate, or Darcy velocity, of flow.

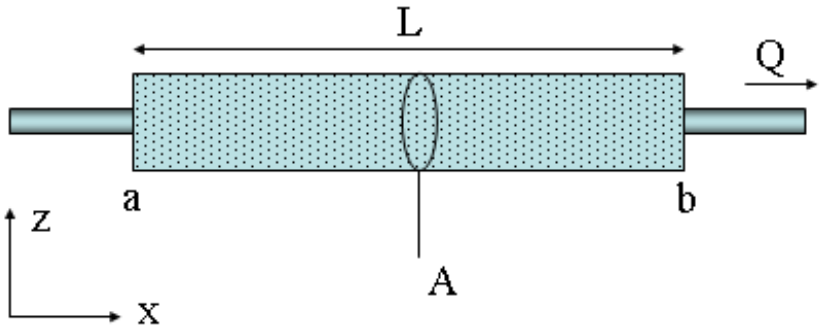

Figure D.1: Fluid flows through a porous medium. L (m) is the length of the medium; A (m^2) is the cross section area of the medium; Q (unit volume per time; m^3/sec) is discharge rate or flux of flow.

Intuitively, the larger difference between the fluid pressure at the point a (denoted as P_a) and the pressure at the point b (denoted as P_b), the faster the Darcy velocity (Q) would be. On the other hand, high viscosity, μ, of the fluid would increase the

resistant to flow and thereby decrease the Darcy velocity, Q. In addition to the pressure and viscosity of fluid, the geometrical properties of the medium, e.g. A and L, also affect Q. The relationship can be described by Eq. D.1.

$$Q = \frac{-\kappa A}{\mu} \frac{(P_b - P_a)}{L} \tag{D.1}$$

In this equation, there is another parameter, κ, the permeability of the porous medium. The high permeability of a medium implies that the medium has strong porosity, which facilitate the fluid flows through it. By rearranging the Eq. D.1, another more neat equation, Eq. D.2 , is obtained.

$$q = \frac{-\kappa}{\mu} \nabla P \tag{D.2}$$

In this equation, ∇P is the pressure gradient of flow, and q is the flux of fluid as defined in the Eq. D.3, which is:

$$q = \frac{Q}{A} \tag{D.3}$$

This concept of flux does not only simplify the calculation in hydrodynamics, but also help to interpret the principle of magnetic field.

Appendix E

The Simulation of Langevin Equation

```
# Author: Fang-Yu Lin
# This script is used to simulation the Langevin equation.
# The Langevin equation describes the temperature dependence of magnetic
magentisation.
# It was initially proposed to described the MH curve of paramagnet.
# It has also been used to describe the MH curve of superparamagnetic materials.
# More discussion can be found in Weaver et. al.'s article:
# J. B. Weaver, A. M. Rauwerdink, and E. W. Hansen, "Magnetic nanoparticle
temperature estimation," Med. Phys., vol. 36, no. 5, pp. 1822-1829, 2009.

rm(list=ls())
library(stats)
library(svDialogs) # pop out box for user input
library("tcltk")

EnterPara <- T

while (EnterPara == T){
  biasedB<- as.numeric(dlgInput("What is the bias magnetic field (unit: A/m) ?",
0)$res)
  appliedB <- as.numeric(dlgInput("What is the strength of the AMF (unit: A/m)
?",2000)$res)
  appliedfreq <- as.numeric(dlgInput("What is the frequency of the AMF (unit: Hz)
?",1)$res)
  initialT <- as.numeric(dlgInput("What is the initial temperature of the MNPs
(unit: K) ?",50)$res)
  finalT <- as.numeric(dlgInput("What is the final temperature of the MNPs (unit:
K) ?",50)$res)
  dTemp <-  as.numeric(dlgInput("what is the incremental temperature (unit: K)
?",100)$res)

  Description <- paste0("Alternating Magnetic Field : ", appliedB, " A/m and ",
appliedfreq," Hz", "; ",
                        "Temperature Range: between ", initialT, " (K)
and",finalT," (K)", "; ",
                        "Incremental Temperature: ", dTemp, " (K)")

  Answer <- tkmessageBox(message =Description,
                         icon = "question", type = "yesno", default = "yes")
  GoodPara <- (tclvalue(Answer) == "yes")
  EnterPara <-!GoodPara
}
#########################
######functions()#########
#########################
coth = function(X){
  new <- {}
  for (i in 1:length(X)){
    if (X[i] <= 710 & X[i] >= -710){
      new[i] <- cosh(X[i])/sinh(X[i])}
    else if (X[i] > 710){
      new[i] <- 1}
    else if (X[i] < -710){
      new[i] <- -1}
    else{}
  }
```

```
B0.all <- 10e3 # The range of the MH plot. Unit: A/m.
B.all <- B0.all*sin(2*pi*freq*t) # for MH curve.

#CREATE OUR FREQUENCY ARRAY
f <- 1:length(t)/T

#Parameters initialisation
i<-1
All.T <- seq(initialT,finalT,dTemp)
ratio.H3.H5 <- 0
H3<-0
H5<-0
chi.T <-0

#########################
# pre-assumed parameters:
#########################
   # diameter of an individual core: 130 nm
   # (Tay, Zhi Wei et al. "In vivo tracking and quantification of
   # inhaled aerosol using magnetic particle imaging towards inhaled
   # therapeutic monitoring." Theranostics vol. 8,13 3676-3687. 8 Jun. 2018,
   # doi:10.7150/thno.26608), then
   # the volume of a particle v would be:
   v <- (4/3)*((130e-9/2)^3) # unit: m3

   # assume the concentration of MNP suspension is 20 mg/ml
   # assume the particle density is 1.4 g/cm3
   # assume the volume of MNP suspension is 0.5 ml
   # then, the number of particle n can be estimate

   ###unit conversion:###
     #particle density rho:
     rho = (1.4/1000)/((1/100)^3) # unit: kg/m3
     #the weithg of all particles:
     mass_sample <- 0.5*20/1000000 # unit: kg
     #the overall volume of particles nV:
     nv <- mass_sample/rho #unit: m3
     n<- nv/v

   # The amplitude of Langevin Function (AL is the ratio of the magnetic energy
and thermal energy):
   # To calculate the magnetic energy loss, it is important that the unit of M
and H is correct so that
   # their product would have an unit of J.
     H_tesla <- B*4*pi*1e-7 # convert the unit of A/m to T


   # The coil volume (coil diameter: 29.33 mm; height; 33.32 mm):
   # V_sample = (pi*(29.33e-3/2)^2)*33.32e-3 #unit: m3
   V_sample = 0.5e-6 # unit: m3

   # assume the Saturation magnetisation to be: 90 (A·m2/kg)
   # Convert the mass magnetisation to volume magnetisation
   M_0_mass <- 90 #unit: A·m2/kg
   M_0 <- M_0_mass*rho # unit: A/m
```

```
par(mfrow=c(2,2)) # 2x2 plots

############################## 1st figure - MH curve
##############################
col<-0
for (Temp in All.T ){
  #index k:
  k<-Temp
  AL<- (v*M_0*H_tesla)/(4*pi*kB*Temp)    # unitless
  M <- (nv/V_sample)*M_0*(coth(AL)-(1/AL))  # A/m
  M <- M[2:length(M)]
  t_M <- t[2:length(t)]

  H_tesla.all <- B.all*4*pi*1e-7
  AL.all<- (v*M_0*H_tesla.all)/(4*pi*kB*Temp)
  M.all <- (nv/V_sample)*M_0*(coth(AL.all)-(1/AL.all))
  M.all <- M.all[2:length(M.all)] # for MH curve
  M.all[is.na(M.all)] <- 0

     #PLOTTING
  col<-col+1
  if (col ==1){
     plot(B.all[2:length(B)],M.all, type="l",lty = col,lwd=2, col = col)
     grid()

  }else{
    lines(B.all[2:length(B)],M.all, type="l",lty = col,lwd=1, col = col)
    grid()

  }
     grid()
     Sys.sleep(0.1)
     print(Temp)
}

############################## 2nd figure - M output
##############################
col<-0
for (Temp in All.T ){
  k<-Temp
  AL<- (v*M_0*H_tesla)/(4*pi*kB*Temp)    # unitless
  M <- (nv/V_sample)*M_0*(coth(AL)-(1/AL))  # A/m
  M <- M[2:length(M)]
  t_M <- t[2:length(t)]

  H_tesla.all <- B.all*4*pi*1e-7
  AL.all<- (v*M_0*H_tesla.all)/(4*pi*kB*Temp)
  M.all <- (nv/V_sample)*M_0*(coth(AL.all)-(1/AL.all))
  M.all <- M.all[2:length(M.all)] # for MH curve
  M.all[is.na(M.all)] <- 0

  #PLOTTING
  col<-col+1
  if (col ==1){
    plot(t_M,M,  type="l",lty = col,lwd=2, col = col+3,
         ylim = c(-max(M.all),max(M.all)))
```

```
  grid()
  Sys.sleep(0.1)
  print(Temp)
}
############################## 3rd figure - H input
##############################
col<-0
for (Temp in All.T ){
  k<-Temp
  AL<- (v*M_0*H_tesla)/(4*pi*kB*Temp)    # unitless
  M <- (nv/V_sample)*M_0*(coth(AL)-(1/AL))  # A/m
  M <- M[2:length(M)]
  t_M <- t[2:length(t)]

  H_tesla.all <- B.all*4*pi*1e-7
  AL.all<- (v*M_0*H_tesla.all)/(4*pi*kB*Temp)
  M.all <- (nv/V_sample)*M_0*(coth(AL.all)-(1/AL.all))
  M.all <- M.all[2:length(M.all)] # for MH curve
  M.all[is.na(M.all)] <- 0


  #PLOTTING
  col<-col+1
  if (col ==1){
    plot(B,t,  type="l",lty = col,lwd=2, col = col+1, ####
         xlim = c(-B0.all,B0.all))
    grid()
  }else{
    lines(B,t,  type="l",lty = col,lwd=1, col = col,
          xlim = c(-B0.all,B0.all))
    grid()
  }
  grid()
  Sys.sleep(0.1)
  print(Temp)

}
############################## 4th figure - M Harmonics
##############################
col<-0
for (Temp in All.T ){
  k<-Temp
  AL<- (v*M_0*H_tesla)/(4*pi*kB*Temp)    # unitless
  M <- (nv/V_sample)*M_0*(coth(AL)-(1/AL))  # A/m
  M <- M[2:length(M)]
  t_M <- t[2:length(t)]

  H_tesla.all <- B.all*4*pi*1e-7
  AL.all<- (v*M_0*H_tesla.all)/(4*pi*kB*Temp)
  M.all <- (nv/V_sample)*M_0*(coth(AL.all)-(1/AL.all))
  M.all <- M.all[2:length(M.all)] # for MH curve
  M.all[is.na(M.all)] <- 0
  #FOURIER TRANSFORM WORK
  fftM <- fft(M)
  mag <- abs(fftM)*(2/length(M))

  ..
```

```
         xlim = c(0,6*freq),ylim = c(0,2100)) ####
  }else{

    lines(f[1:(fft_data_length)],mag[2:(fft_data_length+1)], type="l",lty =
col,lwd=1, col = col,
          xlim = c(0,6*freq))
  }

  grid()
  Sys.sleep(0.1)
  print(Temp)

  H3[col] <- sort(mag, decreasing = TRUE)[3]
  H5[col] <- sort(mag, decreasing = TRUE)[5]
  ratio.H3.H5[col] <- sort(mag, decreasing = TRUE)[5]/ sort(mag, decreasing =
TRUE)[3]

}

############################### 5th figure - Ration of H3 and H5
###############################
plot(All.T, ratio.H3.H5,type = "o")
grid()
```

Appendix F

Estimation of the Volume of MNP suspension

The volume of an MNP suspension is estimated based on three assumptions:

1. The labelled concentrations on the product of MNP suspensions are correct and uniform.

2. The volume of MNP suspension is independent of the mass of MNPs. i.e. the volume of the suspension is only decided by the volume of water.

3. Based on (1) and (2), the volume of MNP suspension, $V_{MNP}(ml)$, is calculated by:

$$V_{MNPsuspension} = \frac{M_{MNPsuspension}}{1 + (Concentration/1000)} \tag{F.1}$$

   In which, the mass and concentration of MNP suspension (i.e., $M_{MNPsuspension}$ and $V_{MNPsuspension}$) have units of g and mg/ml, respectively.

For instance, if the concentration of an MNP suspension is 10 mg/ml, then it suggests that for 1 ml of the MNP suspension, there is 1 g of water and 10/1000 g of MNP particles. Then, provided that there is 0.35 g of MNP suspension being poured into a mould, the volume of MNP suspension can be estimated base on Eq. F.1. The estimated volume of MNP suspension would be 0.347 ml. That is, because of the low concentrations of those MNP suspensions used in Table 3.13, the weight of MNP suspension (unit: g) can indicate its volume (unit: ml).

Appendix G

The Measurement of Phase Shift in AC Susceptometer

There are two ways to measure the phase shift of a susceptometer. The first is to use a reference sample. The second is to generate a reference signal.

G.1 Reference Sample

If there is a reference sample that could be magnetised and its induced magnetisation is always in phase with the excitation field, then the phase difference between the magnetisation and shifted excitation field can be derived. Because the reference sample's magnetisation is in phase with the excitation field, the measured phase shift would only be associated with the Rogowski coil.

In literature, a paramagnetic material, dysprosium oxide Dy_2O_3, is commonly used as a reference material for the calibration of a susceptometer [123]. Nevertheless, the susceptibility of Dy_2O_3 is much weaker than that of MNPs.

For instance, according to [123], the DC susceptibility of Dy_2O_3 at 300K is 0.000206 $(emu/Oe \cdot g)$, while the DC susceptibility of the aforementioned C180916 (see Section 5.3.1) at 300K is 0.24 $(emu/Oe \cdot g)$[1]. The latter has over a thousand times stronger susceptibility than the former. For the simplified susceptometer presented in this study, the intensity of excitation field ranged only between 25 Oe and 125 Oe. This was not strong enough for inducing a detectable magnetic moment in Dy_2O_3.

In short, because of the not-strong-enough excitation field and the small capacity

[1]The value of which was measured by Quantum Design SQUID-VSM Magnetometer (MPMS SQUID VSM-7T, Quantum Design, California) at 50 Oe.

of sample holder, i.e., 2 ml glass vial, to contain samples, the Dy_2O_3 cannot be used as a reference material in this experimental setup.

G.2 Reference Signal

Take a step back, the fundamental concept of phase correction is to have a detectable signal in the detection coil[2] and the phase of which follows the excitation field. Instead of using a reference material, one could use a coil to generate such a signal. As shown in Fig. 6.1B, if the detection coil only consists of a pick-up coil, when exposing to an excitation field, a periodic voltage would be induced in the pick-up coil even if no sample is present in the coil.

More importantly, the associated magnetic field would be in phase with the excitation field. By comparing this induced field with the shifted excitation field that was detected by the Rogowski coil, the unwanted phase shift could be determined and thus corrected.

[2]Either a pair of balancing coil or a pick-up coil only.

Appendix H

Phasor and Correlation

H.1 Why Phasor?

We have described the periodic voltage that induced in the pickup coil as $V_0 cos(\omega t)$, which was a cosine wave without a phase shift. It was reasonable to assume that the phase shift of such a signal was zero because a phase shift is a relative value. That is, a phase shift is only meaningful when more than one signal is considered.

In the experiment in Chapter 6, two signals were measured (see Fig 6.2). Although one could found the phase difference between those two signals, the phase difference between the induced voltage and the shifted excitation field had no clear physical meaning; hence, knowing the phase difference between them could not facilitate the calculation of susceptibility.

Alternatively, to facilitate the calculation, one may compare each detected signal with a reference signal. Provided that the reference signal had the same angular frequency with the excitation field, i.e., ω, and its magnitude peaked at 1, then the reference signal u_{ref} could be written as $cos(\omega t)$.

For the convenience of explanation, the phase difference between the induced voltage and u_{ref} was termed as θ_{pickup}, and that between the shifted excitation field and u_{ref} was termed as $\theta_{shiftedH}$. The maximum magnitudes of the former and the latter were respectively denoted as V_0 and H_0.

Overall, the induced voltage V_{pickup} and the shifted excitation field $H_{shifted}$ could be written as $V_{pickup} = V_0 cos(\omega t + \theta_{pickup})$ and $H_{shifted} = H_0 cos(\omega t + \theta_{shiftedH})$, respectively. The aforementioned signals, V_{pickup}, $H_{shifted}$ and u_{ref} were all periodic scalar signals. For manipulating signals that involve phase shifts, the mathematical manipulation of scalars can be complicated.

H.2 What is Phasor?

To simplify the calculation of such signals, C. P. Steinmetz (1865-1923) introduced a notion called **phasor**, which allows one to express a periodic scalar signal with its amplitude and its phase relative to a reference signal.

A phasor can be stated in any of the three equivalent forms, i.e., the rectangular form, the polar form and the exponential form. Furthermore, the expression of phasor can be easily visualised on such a diagram in Fig. H.1A.

To avoid possible confusion, the phasors of V_{pickup}, $H_{shifted}$ and u_{ref} are denoted as $\mathbb{V}_{pickup}$, $\mathbb{H}_{shifted}$ and $\mathbb{U}_{ref}$, respectively. In Fig. H.1A, the reference signal $\mathbb{U}_{ref}$ sits on the x-axis, its phase is zero as its phase is regarded as the reference. The phase shift of another signal could then be defined to be the phase difference between the signal and $\mathbb{U}_{ref}$.

For a signal with a non-zero phase like $\mathbb{V}_{pickup}$, the orientation of which on the phase diagram would be rotated accordingly. Similarly, Fig. H.1B depicts both the $\mathbb{U}_{ref}$ and $\mathbb{H}_{shifted}$. If we regard the x-axis as the real axis and the y-axis as the imaginary axis, we can further decompose a phasor into the real part and imaginary part of a complex number, which often refers to a phasor's rectangular form. Consequently, the phasors can now be re-expressed as $\mathbb{V}_{pickup} = V'_{pickup} + iV''_{pickup}$ and $\mathbb{H}_{shifted} = H'_{shifted} + iH''_{shifted}$.

More discussions on the advantages of Phasor is given in Appendix H.

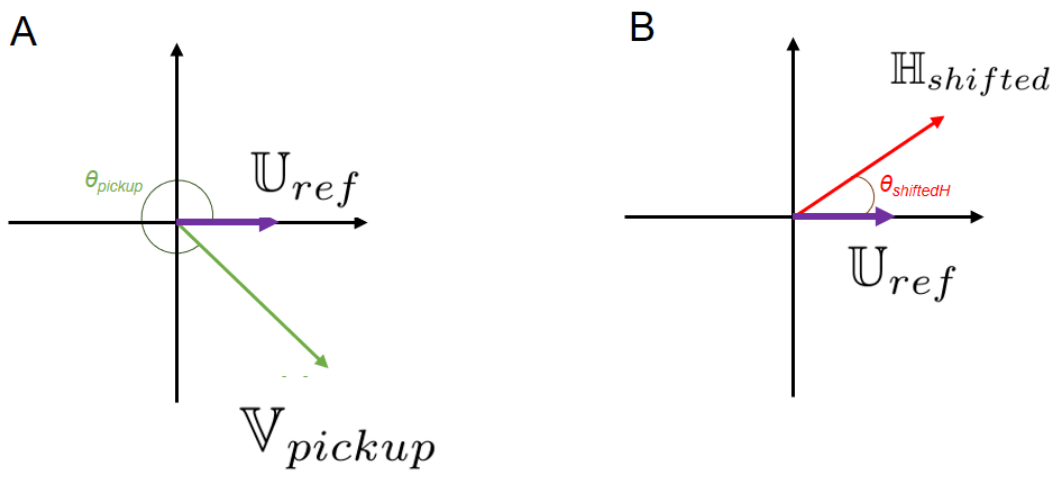

Figure H.1: (A) Phasor diagram of V_{pickup} relative to u_{ref}. (B) Phasor diagram of $H_{shifted}$ relative to u_{ref}.

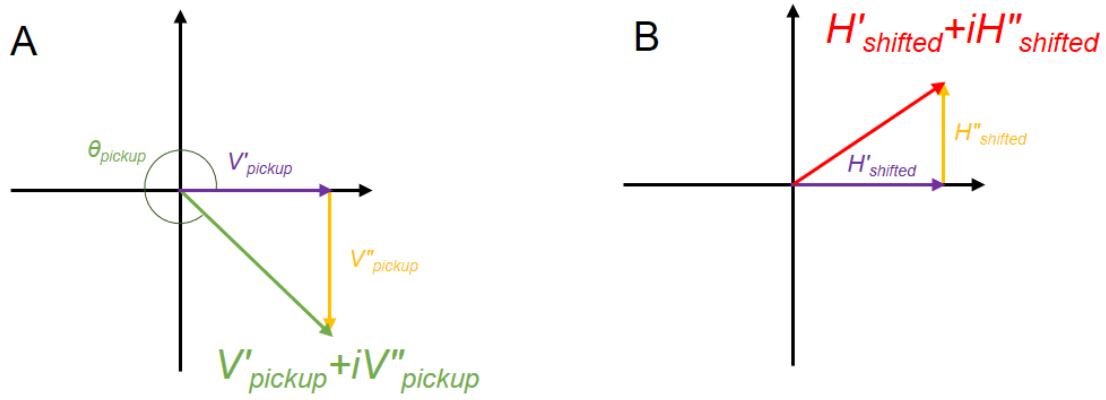

Figure H.2: A phasor can be decomposed into a real part and an imaginary part, which is termed as the rectangular form of a phasor. (A) The rectangular form of $\mathbb{V}_{pickup}$. (B) The rectangular form of $\mathbb{H}_{shifted}$.

H.3 Advantages of a Phasor

Expressing a signal by the rectangular form of its phasor is beneficial. The expression of complex number facilitates the analysis of signal. For instance, it could be practically difficult to attain the phase difference between two signals through the scalar manipulation of sequential data that collected from the oscilloscope.

However, if the sequential data is periodic and can be expressed as a complex number, one could then easily attain the phase through manipulations such as *dot product* and *division*. In fact, the core of discussion presented here is to elaborate a method for converting a periodic sequential data, e.g., V_{pickup}, to a phasor in the form of complex number, e.g. $V'_{pickup} + iV''_{pickup}$.

From one perspective, if the rectangular form of the phasor is known, to obtain the real part of the phasor, i.e., V'_{pickup}, one could simply calculate the dot product of $\mathbb{V}_{pickup}$ and $\mathbb{U}_{ref}$ (see Fig. H.1A). The result of the dot product is the value of V'_{pickup}, because the amplitude of $\mathbb{U}_{ref}$ has been defined to be 1. Or it can be mathematically described as below:

$$V'_{pickup} = \mathbb{V}_{pickup} \cdot \mathbb{U}_{ref} = |\mathbb{V}_{pickup}||\mathbb{U}_{ref}|cos(\theta_{pickup}) \tag{H.1}$$

Because $|\mathbb{U}_{ref}|$ is 1, and thus:

$$V'_{pickup} = |\mathbb{V}_{pickup}|cos(\theta_{pickup}) \tag{H.2}$$

From another perspective, as the recorded signals, i.e., V_{pickup} and $H_{shifted}$, were sequential scalars, one cannot perform the dot product as described above. Fortunately, there is another equation for evaluating the correlation between two sets of variables, and the correlation between two sets of data is equivalent to the notion of dot product.

H.4 Correlation of Two Signals

The notion of correlation has been widely used in statistics. To be more clear, the correlation of two periodic signals, $f(t)$ and $g(t)$, is stated as below:

$$corr(f(t), g(t)) = \frac{\int_0^T (f(t) - \overline{f})(g(t) - \overline{g})dt}{\sqrt{(\int_0^T (f(t) - \overline{f})^2 dt)}\sqrt{(\int_0^T (g(t) - \overline{g})^2 dt)}} \tag{H.3}$$

In which, the t and T represent the time and the period of signal. The $\overline{f}$ and $\overline{g}$ are the average of each signal over a whole period. The result of $corr(f(t), g(t))$ is equivalent to $cos(\theta)$ in which the θ is the phase difference between $f(t)$ and $g(t)$. The proof of the equivalence is stated in Appendix I.

H.5 Convert Measured Signals to Phasors by Correlation Equation

In the case presented in Fig. H.1A, the correlation of V_{pickup} and u_{ref}, denoted as $corr(V_{pickup}, u_{ref})$, is equivalent to $cos(\theta_{pickup})$. In addition, as there was no DC offset signal involved, the average of a sinusoidal signal, e.g., V_{pickup} or u_{ref}, over a full period would be 0. That is, both $\overline{f}$ and $\overline{g}$ were 0. Therefore, by comparing Eq.H.2 and Eq. H.3, one attains:

$$\frac{V'_{pickup}}{|\mathbb{V}_{pickup}|} = \frac{\int_0^T V_{pickup} u_{ref} dt}{\sqrt{\int_0^T (V_{pickup})^2 dt)} \sqrt{\int_0^T (u_{ref})^2 dt}} \tag{H.4}$$

By expanding both V_{pickup} and u_{ref}, the Eq. H.4 becomes:

$$\frac{V'_{pickup}}{|\mathbb{V}_{pickup}|} = \frac{\int_0^T V_{pickup} cos(\omega t) dt}{\sqrt{\int_0^T V_0^2 cos^2(\omega t + \theta_{pickup}) dt} \sqrt{\int_0^T cos^2(\omega t) dt}} \tag{H.5}$$

Because the integral of $cos^2(\omega t)$ equals to the integral of $sin^2(\omega t)$ over a full period and the sum of $cos^2(\omega t)$ and $sin^2(\omega t)$ is 1, the integral of $cos^2(\omega t)$ over a period would then equal to $\frac{T}{2}$. Similarly, $\int_0^T cos^2(\omega t + \theta) dt$ would also be $\frac{T}{2}$. In addition, in our case, the amplitude of phasor $|\mathbb{V}_{pickup}|$ is V_0. As a result, the Eq. H.5 becomes:

$$V'_{pickup} = \frac{2 \int_0^T V_{pickup} cos(\omega t) dt}{T} \tag{H.6}$$

Similarly, to obtain the imaginary part of $\mathbb{V}_{pickup}$, i.e., V''_{pickup}, one can simply rotate the phase of u_{ref} with 90° and make the reference signal to be $sin(\omega t)$. Repeat the above calculation, one can then obtain:

$$V''_{pickup} = \frac{2 \int_0^T V_{pickup} sin(\omega t) dt}{T} \tag{H.7}$$

To conclude, a periodic signal can be converted to the rectangular form of its phasor as long as the frequency of which is known[1]. In our case, the ω was measured

[1] A simulated example of converting a periodic signal to a phasor is presented in Appendix J

by Rogowski coil, so both $sin(\omega t)$ and $cos(\omega t)$ could be generated when handling the data. Through Eq. H.6 or Eq. H.7, the real and imaginary parts of both V_{pickup} and $H_{shifted}$ can be derived. Once these periodic signals were re-expressed with complex numbers, the calculation of susceptibility could be more easily handled. More details on the calculation will be further described in the next section.

Appendix I

The Equivalence of Correlation and Dot Product

In Section 6.1.3, the equivalence of correlation and dot product has been described. This paragraph below provides a proof of the equivalence.

From the qualitative perspective, the cosine of phase difference between two phasors can be used to describe their correlation. To be more specific, if two signals overlap, the phase difference θ between them would be $0°$, which leads to $cos(\theta) = 1$. Then, one can describe that there is high correlation between those two signals, or one can quantitatively describe the correlation between them is 1. To be more clear, let us describe this equivalence in equations.

Assume that there are two periodic signals, $X(t)$ and $Y(t)$; the phasors of which are denoted as $\mathbb{X}$ and $\mathbb{Y}$. Then, by definition, the $cos(\theta)$ can be derived from their dot product (see Eq.I.1).

$$cos(\theta) = \frac{\mathbb{X} \cdot \mathbb{Y}}{|\mathbb{X}||\mathbb{Y}|} \tag{I.1}$$

Here the question to be answered is that whether or not $corr(X(t), Y(t))$ equals to $cos(\theta)$. To answer this, one can assume $X(t)$ and $Y(t)$ to be $X_0 sin(\omega t)$ and $Y_0 sin(\omega t + \theta)$. Substituting these two signals into Eq. H.3, then one would obtain:

$$corr(X(t), Y(t)) = \frac{\int_0^T (X_0 sin(\omega t))(Y_0 sin(\omega t + \theta))dt}{\sqrt{(\int_0^T X_0^2 sin^2(\omega t)dt)}\sqrt{(\int_0^T Y_0^2 sin^2(\omega t + \theta)dt}} \tag{I.2}$$

Because of the fundamental trigonometric formula:

$$sin(\theta_1)sin(\theta_2) = \frac{1}{2}(cos(\theta_1 - \theta_2) - cos(\theta_1 + \theta_2)) \tag{I.3}$$

The numerator of Eq. I.2 becomes:

$$\int_0^T \frac{X_0 Y_0}{2}(cos(\theta) - cos(2\omega t + \theta))dt = \frac{X_0 Y_0 T}{2} cos(\theta) \tag{I.4}$$

Also, the integral of $sin^2(\theta)$ equals to the integral of $cos^2(\theta)$ over a whole period; hence:

$$\int_0^T X_0^2 sin^2(\omega t)dt = \int_0^T X_0^2 \frac{(sin^2(\omega t) + cos^2(\omega t))}{2} dt = \frac{T X_0^2}{2} \tag{I.5}$$

Similarly:

$$\int_0^T Y_0^2 sin^2(\omega t + \theta)dt = \frac{T Y_0^2}{2} \tag{I.6}$$

Substituting Eq. I.4, Eq. I.5 and Eq. I.6 into Eq. I.2, then the equation below is attained, which proves the aforementioned equivalence.

$$corr(X(t), Y(t)) = cos(\theta) \tag{I.7}$$

Appendix J

The Simulation of Periodic Signals Correlation

The Matlab script below was for demonstrating the Eq. H.6 and Eq. H.7, which were used to convert a scalar periodic signal to the rectangular form of a phasor. Through correlating the signal with cosine and sine waves individually, one could obtain the real and imaginary components of the phasor of the signal. In the picture below, an signal M, which peaks at M_0 with an phase shift θ_M relative to a cosine wave is presented for the demonstration. The Matlab script of which is presented in the following pages.

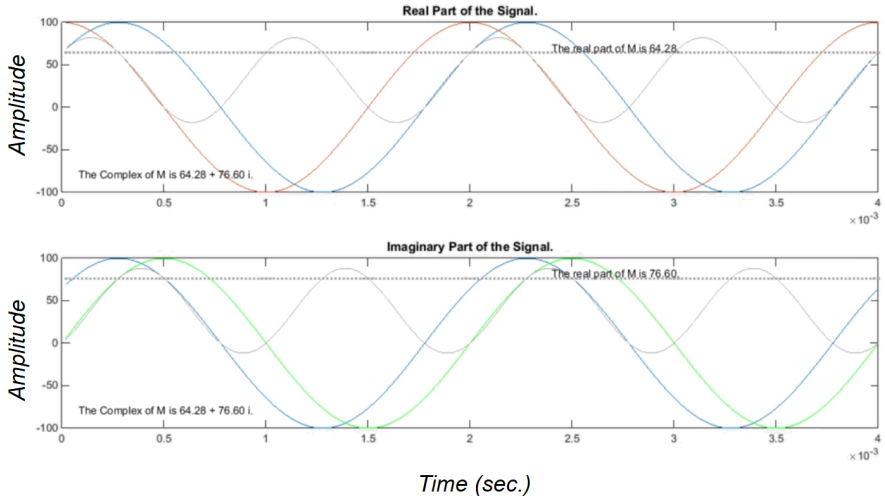

Figure J.1: The top graph is the correlation of a periodic signal M (denoted with blue colour) with a cosine wave (denoted with red colour) that has the identical frequency to M. The grey curve represents $M_0 cos(\omega t + \theta_M) cos(\omega t)$, and the dashed line is the correlation coefficient, which also is the real part of the phasor of M. Similarly, the bottom graph is the correlation of M with a sine wave (denoted with green colour). Both the $M_0 cos(\omega t + \theta_M) sin(\omega t)$ and the correlation coefficient are illustrated with grey colour.

```
% Technique: Correlation Purpose: Expressing a waveform on a phasor
% diagram.
%
% Scenario: A waveform was captured in Labview. We want to compare
% its phase with other waveforms. The phasor diagram makes the phase
% tracking easier since the phase of a waveform is fixed.
%
% Condition: We need to know the frequency of the waveform. Let's say the
% frequency of which is w.
%
% Principle: While the average level of
% Waveform*cos(wt) can represent real part of the complex, the average
% level of Waveform*sin(wt) represents the imaginary part of the complex.

%%
clear all;clc;

%% Define a wave
    index= 1:200;

for angle = 0:5:360
    clf('reset')
    theta = (angle/180)*pi();
    f = 500;
        samplingRate = 100*f; % 100Xfrequency
        samplingPeriod = 1/samplingRate;
    t = index.*samplingPeriod;
        w = 2*pi()*f;


    M0 = 100;
    M = M0*cos(w*t-theta)
%% 1.0 Plot Input and Cos
subplot(2,1,1);
    plot(t,M);hold on;
    plot(t,M0.*cos(w*t));

%% 1.1 Correlation, i.e. Converting a wave to a complex

    w = 1*w;
%   Real Part of the Complex Number
    plot(t,M.*cos(w*t),'Color',[169/256,169/256,169/256])
    rm_M = 2*(sum(M.*cos(w*t))./length(t));
    plot(t, rm_M*ones(length(t)), '.','Color',[169/256,169/256,169/256]);
    text(0.6*max(t),rm_M+0.05*M0, sprintf('The real part of M is
%0.2f.',round((rm_M),2)));
    title('Real Part of the Signal.')
```

```
%% 1.2 Calculate the Complex number based on theta

    text(0.02*max(t),-0.8*M0, sprintf('The Complex of M is %0.2f + %0.2f i.',...
    round(M0*cos(theta),2),round(M0*sin(theta),2)));

%% 2.0 Correlation, i.e. Converting a wave to a complex
%   Imaginary Part of Complex Number
subplot(2,1,2);
    plot(t,M);hold on;
    plot(t,M0.*sin(w*t),'g');
%% 2.1 Correlation, i.e. Converting a wave to a complex
%   Real Part of the Complex Number
    plot(t,M.*sin(w*t),'Color',[169/256,169/256,169/256])
    Im_M = 2*(sum(M.*sin(w*t))./length(t));
    plot(t, Im_M*ones(length(t)), '.','Color',[169/256,169/256,169/256]);
    text(0.6*max(t),Im_M+0.05*M0, sprintf('The real part of M is
%0.2f.',round((Im_M),2)));
    title('Imaginary Part of the Signal.')
%% 2.2 Calculate the Complex number based on theta

    text(0.02*max(t),-0.8*M0, sprintf('The Complex of M is %0.2f + %0.2f i.',...
    round(M0*cos(theta),2),round(M0*sin(theta),2)));

    pause(0.1)
end
```

Appendix K

Features of Simplified Susceptometer

To better utilise the susceptometer, it is important to understand its features. Discussions on the intrinsic limitations of simplified susceptometer will be presented below. With the limitations in mind, meaningful signals could be more easily distinguished from other interferences when performing data analysis.

The limitations of the simplified susceptometer lies on two aspects. **One is related to the correlation calculation** used for converting a signal to a phasor, while **the other is in relation to the accuracy**. Each limitation will be be individually described in detail below.

K.1 The issue in Calculation of Correlation

It would not be an issue if the assumption made at the beginning of Section 6.1.3 is true for the measurement. In the section, the author assumed that either V_{pickup} or $H_{shifted}$ is a pure sinusoidal signal, e.g., $cos(\omega t)$; that is, there are no harmonics in them.

This is usually true for the excitation field, as it is designed to be like that. However, very often, the magnetisation of a material is non-linear to the excitation field; in other words, harmonics exist in the magnetisation. An issue here is that, during the calculation of correction (calculation of complex number), those harmonics would be discarded, or to be more precisely, they would not be seen. To explain this, it may be helpful to describe the notion of correlation qualitatively.

K.1.1 Missing Information during the Phasor Calculation.

Take Eq. H.6 as an example, what the correlation equation tries to do is to define how many portions of V_{pickup} are identical to $cos(\omega t)$. Only those portions have the same frequency and phase as those of $cos(\omega t)$, those portions would be detected. Thus, $cos(\omega t)$ is sometimes termed as a detector in the literature. Similarly, the Eq. H.7 withdraws a part of V_{pickup} that is identical to another detector, i.e., $sin(\omega t)$, in terms of frequency and phase. For other portions in V_{pickup} that are not at the same frequency as those detectors, i.e., harmonics of V_{pickup}, they cannot be detected and will be discarded after the correlation.

Fortunately, this limitation would not affect the experiment presented here, which aimed at validating the proposed MPT. The author points out this issue here is mainly because a susceptometer is sometimes used for visualising the hysteresis loop of a material [80]. The simplified susceptometer presented in this chapter is however not able to assess this effect. It was designed mainly for measuring the AC susceptibility in the same conditions of proposed MPT.

Appendix L

The Simulation of Frequency Dependency of Susceptibility

The R script for the simulation of frequency dependence of susceptibility is presented in the following pages. The script is based on the Eq. 9a and Eq. 9b in Rosensweig's work in [48]. The script was first built by the author's colleague, Francesca Brero, then later modified by the author for the purpose of explaining the difference between the empirical and theoretical data in Section 6.2.2.

```
## Simulation of Susceptibility based on the paper given by Rosensweig 2002
## Initial Script on particle distribution written by Francesca Brero
## Modified by FY Lin on 22/Apr/2019
## Modified by FY Lin on 08/Sept/2019


rm(list=ls())

###########################################
##########function of chi.rosencalc  #######
###########################################
"chi.rosencalc"<-function(k.eff=14000,Md=446e3,
                          nu=1e-3,tau0=1e-9,temp=300,
                          phi=0.5,H=5000,sig=0.15,R0=6e-9,
                          delta=2e-9,radius=seq(1e-9,100e-9,0.1e-9),
                          frequency=seq(1,1e+8,500),verbose=F){
  i<-0
  kb<-1.38e-23
  mu0<-4*pi*1e-7
  chi.p<-double(length(frequency))
  chi.pp<-double(length(frequency))
  power<-double(length(frequency))


  R<-radius
  ### Gaussian Distribution ###
  #create the distribution gR and step dr
  if(sig==0){
    g.R<-rep(0,length(radius)) #Gaussian Function, when sigma == 0.
    index_median <- median(1:length(radius))
    g.R[index_median] <- R0
    dr<-1/R0#mean(diff(radius)) # interval between two data
  }else{
    g.R<-1/(sqrt(2*pi)*sig*R)*exp((-(log(R/R0))^2)/(2*sig^2) ) # number of cases
per interval
    dr<-mean(diff(radius)) # the interval
  }

  ###
  Anorm<-sum(g.R*dr) # check both g.R and dr. The Anorm should be 1.
  if(round(Anorm,2) != 1){
    print("Error!!! Anorm does not equal to 1.")
  }



  ### Values when R is a serial of number ###
  vol.m<-(4/3)*pi*((R)^3)#*g.R*dr #particle volume
```

```
  #example of using Gaussian equation, e.g., V_effective <- sum(vol.m*g.R*dr)
  vol.h<-((4/3)*pi*((R)^3)*(1+delta/(R))^3)#*g.R*dr #hydrodynamic volume


  vol.m.eff <-vol.m #sum(vol.m)
  vol.h.eff <-vol.h #sum(vol.h)
  ###
  epsilon<-mu0*Md*H*vol.m.eff/(kb*temp) #Langevin term
  chi.i<-mu0*phi*Md^2*vol.m.eff/(3*kb*temp) #Initial Susceptibility
  chi.0<-3*chi.i*(1/tanh(epsilon)-1/epsilon)/epsilon #static Susceptibility
  ## relaxation time when R = R0 ###
  gamma<-k.eff*vol.m.eff/(kb*temp)
  tau.b<-3*nu*vol.h.eff/(kb*temp)
  tau.n<-(sqrt(pi)/2)*tau0*exp(gamma)/sqrt(gamma)
  tau.eff<-1/(1/tau.b+1/tau.n)
  ######################

  for (freq in frequency){
    i<-i+1
    w<-2*pi*freq # angular frequency
    chi.p[i]<- sum(chi.0/(1+(w*tau.eff)^2)*g.R)*dr # Real Susceptibility
    chi.pp[i]<- sum(chi.0*w*tau.eff/(1+(w*tau.eff)^2)*g.R)*dr #Imaginary
susceptibility

power[i]<-sum(pi*mu0*chi.0*H^2*freq*(2*pi*freq*tau.eff/(1+(2*pi*freq*tau.eff)^2))*g
.R)*dr # Effective Power
  }


  return( data.frame(frequency, chi.p, chi.pp, power,
tau.eff,tau.b,tau.n,radius,g.R,dr))
}



##############################################
##############################################
##############################################


## Independent variable
radius<-seq(0.1e-9,20e-9, length.out = 100)
R0<-6.5e-9
temp <- 300

## Animation of plots with a verity of Sigma#
for(sig in 0.3)
  print(sig)
```

```
tmp.sig0<-chi.rosencalc(sig=sig,R0=R0,H=5000,nu=8.9e-4,
                        frequency=seq(1,1e+6,length.out = 500),
                        verbose=F,radius=radius,temp=temp )

frequency <- tmp.sig0$frequency/1000
chi.p <- tmp.sig0$chi.p
chi.pp <- tmp.sig0$chi.pp
chi.amp <- sqrt(chi.p^2 + chi.pp^2)

radius <- tmp.sig0$radius
g.R <- tmp.sig0$g.R
dr<-tmp.sig0$dr
R_particle <- radius*g.R*dr

#################################################
### Plot Result ############
############################

plot(frequency,chi.p/chi.amp[1],
     xlab = "Frequency (kHz)",
     ylab = expression(paste('|',chi,'/',chi['0'],'|')),
     log='x',
     col = "green",
     lty=5,
     ylim
=c(min(range(chi.p/chi.amp[1]),range(chi.pp/chi.amp[1])),max(range(chi.p/chi.amp[1]
),range(chi.pp/chi.amp[1]))),
     type="l",lwd= 5, cex.lab=1.5, cex.axis=1.5)


lines(frequency,chi.pp/chi.amp[1], col = "red",lwd= 5, lty=5)
lines(frequency,chi.amp/chi.amp[1], col = "black",lwd= 2,lty=1)

grid()
legend(0.001,0.9, c( "Real Susceptibility, X'",
                    "Imaginary Susceptibility, X''",
                    'Amplitude of Susceptibility' ),
       lty=c(5,5,1),
       lwd=c(2.5,2.5,2.5),col=c("green","red",'black'))

text(0.01,0.3, paste0("Core Radius: ",
                      round(R0*1e9,2),
                      " nm \n Sigma: ",
                      round(sig,2),
                      " \n Temperature: ",
                      round(temp,2), " K",
                      " \n H: ", 5, "kA/m"))
```

Appendix M

The Details of Samples Applied in Figure 6.8

Measurement	ID
1	Apr05_Measurement_C180916_15mgml
2	Apr05_Measurement_C180916_30mgml
3	Apr05_Measurement_C180916_60mgml
4	Apr05_Measurement_CSICDTU01-1
5	Apr05_Measurement_CSICDTU01-2
6	Apr05_Measurement_CSICMM0801-2
7	Apr05_Measurement_MM0801-1
8	Apr05_Measurement_MMDTU01-1
9	Apr05_Measurement_MMDTU01-2
10	Apr05_Measurement_Nanomag_new_
11	Apr05_Measurement_NanoPowder
12	Apr05_Measurement_NM15mgml
13	Apr05_Measurement_NM36mgml
14	Apr05_Measurement_NM73mgml
15	Apr05_Measurement_PM_new_
16	Apr05_Measurement_PM20_2
17	Apr05_Measurement_PMcooh
18	Apr05_Measurement_PMcooh_2nd
19	Apr05_Measurement_RCbeforeG
20	Apr05_Measurement_RCLafterG
21	Apr05_Measurement_Synomag_
22	Apr05_Measurement_Synomag_D_
23	Apr07_Agar_C180916_1Percent_beforeGel_5_5kAm
24	Apr07_Agar_C180916_1Percent_Gel_5_5kAm
25	Apr07_Agar_C180916_2Percent_beforeGel_5_5kAm
26	Apr07_Agar_C180916_2Percent_Gel_5_5kAm
27	Apr07_Agar_C180916_3Percent_beforeGel_5_5kAm
28	Apr07_Agar_C180916_3Percent_Gel_5_5kAm
29	Apr07_Agar_C180916_4Percent_beforeGel_5_5kAm
30	Apr07_Agar_C180916_4Percent_Gel_5_5kAm
31	Apr07_C180916_1Percent_Gel_gel_8kAm
32	Apr07_C180916_1Percent_Gel_gel_10kAm
33	Apr07_C180916_2Percent_Gel_gel_8kAm
34	Apr07_C180916_2Percent_Gel_gel_10kAm
35	Apr07_C180916_3Percent_Gel_gel_8kAm
36	Apr07_C180916_3Percent_Gel_gel_10kAm
37	Apr07_C180916_4Percent_Gel_gel_8kAm
38	Apr07_C180916_4Percent_Gel_gel_10kAm
39	Apr07_C180916_4Percent_Gel_gel_10kAm_2nd
40	Apr07_C180916_6kAm
41	Apr07_C180916_30mgml_6kAm
42	Apr07_C180916_30mgml_10kAm_2nd
43	Apr07_C180916_60mgml_7kAm
44	Apr07_C180916_60mgml_8kAm
45	Apr07_C180916_60mgml_9kAm
46	Apr07_C180916_60mgml_10kAm
47	Apr07_C180916_60mgml_B_6kAm
48	Apr07_C180916_60mgml_C_6kAm
49	Apr07_Nanamag_36_mgml_10kAm
50	Apr07_Nanomag_36_5mgml_6kAm
51	Apr07_nanomag_36_5mgml_7kAm
52	Apr07_Nanomag_36_5mgml_8kAm
53	Apr07_Nanomag_36_5mgml_9kAm
54	Apr07_Nanomag_36_5mgml_9kAm_B
55	Apr07_PM_nh2_5_5kAm
56	Apr07_PM_plain_5_5kAm
57	Apr07_PM20_2_9kAm
58	Apr07_PM20_2mgml_9kAm_B
59	Apr07_PMcooh_6kAm
60	Apr07_PMcooh_7kAm
61	Apr07_PMcooh_8kAm
62	Apr07_PMcooh_9kAm
63	Apr07_PMcooh_10kAm
64	Apr07_PMnh2_8kAm
65	Apr07_PMnh2_9kAm
66	Apr07_PMnh2_10kAm
67	Apr07_PMplain_8kAm
68	Apr07_PMplain_9kAm
69	Apr07_PMplain_10kAm
70	Apr07_RCL1_afterG_9kAm
71	Apr07_RCL1afterG_6kAm
72	Apr07_RCL1afterG_9kAm_B
73	Apr07_RCL1afterG_10kAm
74	Aprl06_BNF_2kAm
75	Aprl06_BNF_5_5kAm
76	Aprl06_C180916_15mgml
77	Aprl06_C180916_15mgml_2kAm
78	Aprl06_C180916_30mgml
79	Aprl06_C180916_30mgml_2kAm
80	Aprl06_C180916_60mgml
81	Aprl06_C180916_60mgml_2kAm
82	Aprl06_CSIC-DTU01-1
83	Aprl06_CSICDTU01-1_2kAm
84	Aprl06_CSIC-DTU01-1_B
85	Aprl06_CSICDTUo1-2_2kAm
86	Aprl06_CSICMM0801-1
87	Aprl06_CSICMM0801-1_2kAm
88	Aprl06_CSICMM0801-2
89	Aprl06_CSICMM0801-2_2kAm
90	Aprl06_MMDTU01-1
91	Aprl06_MMDTU01-2
92	Aprl06_MMDTU01-2_2kAm
93	Aprl06_MMDTUO1-2_2kAm
94	Aprl06_nanomag_15mgml
95	Aprl06_Nanomag_15mgml_2kAm
96	Aprl06_nanomag_36_5mgml
97	Aprl06_Nanomag_36_5mgml_2kAm
98	Aprl06_Nanomag_73mgml_2kAm
99	Aprl06_NanomagD_2kAm
100	Aprl06_NanomagD_5_5kAm
101	Aprl06_NanoPowder_2kAm
102	Aprl06_nanopowder_5_5kAm
103	Aprl06_Perimag_new_5_5kAm
104	Aprl06_Perimag20_2
105	Aprl06_PM20_2mgml2kAm
106	Aprl06_PMcooh
107	Aprl06_PMcooh_2kAm
108	Aprl06_PMcooh_cooling_2kAm
109	Aprl06_PMnew_2kAm
110	Aprl06_RCL1_afterG_2kAm
111	Aprl06_RCL1_beforeG_2kAm
112	Aprl06_RCL1afterGl
113	Aprl06_RCL1beforeG
114	Aprl06_RMMCSIC12-2
115	Aprl06_RMMCSIC12-2_2kAm
116	Aprl06_synomag_2kAm
117	Aprl06_Synomag_5_5kAm
118	Aprl06_Synomag_5_5kAm_maybeD
119	Aprl06_synomagD_2kAm

Figure M.1: The ID of each measurement.

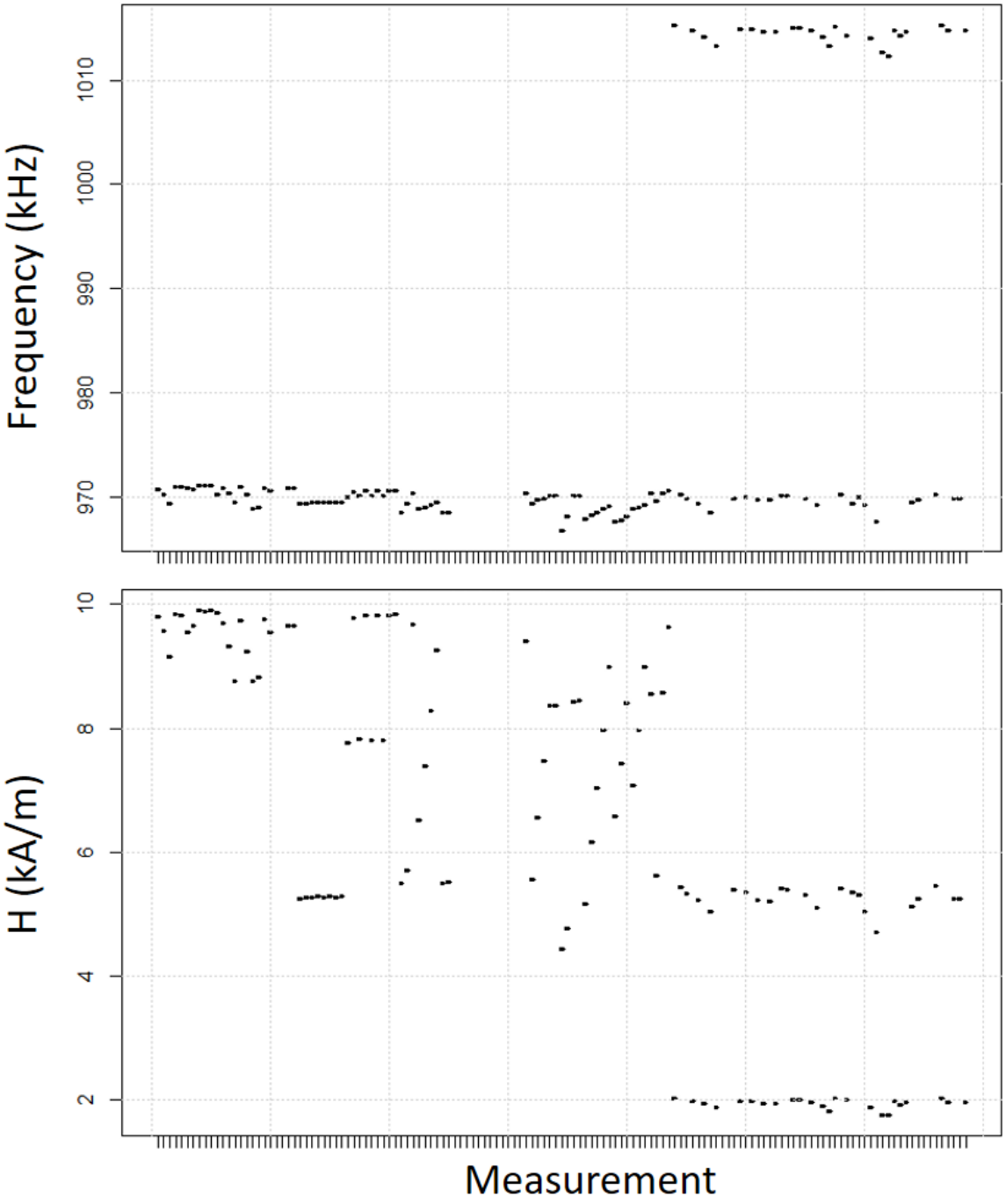

Figure M.2: The field strength and frequency applied in each measurement.

Name	Surface	Size (nm)	Fe Concentration (mg_{Fe}/ml)
Perimag P1.2	plain	130	74
Perimag P1.2	plain	130	7.4
CSIC-DTU01-1	Coating Nature:Citric acid	10.2	8.6
CSIC-DTU01-2	Coating Nature:Citric acid	11.3	7.03
R-MM-CSIC12-1		19	1.19
R-MM-CSIC12-2		19	4.09
Perimag 20.2		130	20.2
MM-DTU01-1		~10	3.58
MM-DTU01-2		~10	3.59
CSIC-MM0801-1	Coating Nature:Citric acid	27	6.2
CSIC-MM0801-2	Coating Nature:Citric acid	25	6.95
Perimag COOH	COOH	130	50
C180916		100	60
C180916		100	30
C180916		100	15
RCL1 after G	plain	130	14.65
RCL1 before G	plain	130	11.28
synomag	plain	30	5.5
synomagD	plain	50	5.5
Nanomag-D	plain	250	5.6
Perimag(new)	plain	130	5.5
BNF-starch	plain	100	5.2
Nanomag	plain	100	73
Nanomag	plain	100	36.5
Nanomag	plain	100	18.25

Name	Surface	Size (nm)	Weight (mg_{Fe})
NanoPowder(Fe3O4)		20-50	72.2
Dy2O3 Powder			895.7